MICROSTRUCTURE EVOLUTION OF METALS THROUGH THERMO-MECHANICAL PROCESSES (TMP), MECHANICAL PROPERTY OF TMP SAMPLES, AND SMALL SCALE TEST SAMPLES

by

Ying-Liang Lee

A dissertation submitted in partial fulfillment
of the requirements for the degree of
Doctor of Philosophy
(Materials Science and Engineering)
in The University of Michigan
2010

Doctoral Committee:

Professor Amit K. Ghosh, Chair
Professor William F. Hosford
Assistant Professor Samantha H. Daly
Research Scientist Kai Sun.

TABLE OF CONTENTS

LIST OF TABLES

Table

LIST OF FIGURES

Figure

Chapter 1

GENERAL INTRODUCTION

1.1 Grain refinement and Hall-Petch effect

Grain refinement is an important field of study in metal processing. Through grain refinement, properties such as strength and hardness of the metals can be substantially improved. Unlike cold working, which trades strength of the metals with ductility, grain refinement of the metals usually increases the ductility as well, especially in superplastic deformation. The focus of this work is on the grain refinement of metal materials through various thermo-mechanical processes. To study the nature of grain refinement, the fundamental understanding of the hardening mechanism behind the grain refinement must first be elucidated. Hall [1] and Petch [2] first discovered the hardening in polycrystalline metals with smaller grain size and relayed the famous Hall-Petch relation as follow:

$$\sigma = \sigma_0 + KD^{-1/2} \quad (1)$$

where σ is the flow stress of polycrystalline material, K is constant and D is the grain size. The principle of the hardening effect in Hall-Petch relation was well explained by the review of Li and Chou [3]. A gliding dislocation propagating into another grain is blocked by the surrounding grain boundaries and forms a dislocation pile-up near the grain boundary. With the increasing numbers of the pile-ups near the grain boundary, the stress concentration of the tip increases. When a critical stress is reached, another dislocation in the neighboring grain is activated and glides until it meets another grain

boundary. With the decreasing size of the grains, the total grain boundary area is substantially increased and more obstructions would be encountered by the dislocations. Higher flow stress is thus required for the dislocations to move through the grain boundaries.

Another explanation of the hardening effect in Hall-Petch relation was provided by Professor J.C.M. Li [4]. Instead of explaining the hardening effect by the dislocation pile-up mechanism, Li proposed that ledges in the grain boundaries pump dislocations into the grain during deformation, and the yield stress of a metal is corresponding to the stress that required overcoming the stress-fiend around the dislocations near the ledges or stress that required to activate new ledges. Many studies have reported that dislocations were generated from the grain boundary ledges at the onset of yielding [5-7], which provide strong supports to the hardening mechanism proposed by Li.

1.2 Common grain refinement practices

Grain refinement in polycrystalline materials can be achieved by many methods. One common practice of grain refinement on polycrystalline material is adding nucleants (grain refiner) to the base material before or during the casting process. The result from Zhang et al. [8] work shows that by adding 0.3wt% of JR-6 nano-grain refiner, the grain size of the cast A356 decreased from 44 μm to 23 μm and had 30MPa, 24 MPa and 4.1% increase in tensile strength, yield strength and elongation, respectively. Common grain refiners for magnesium alloys include carbon [9], ferric chloride ($FeCl_3$) [10], Zr [11,12], Sr [13] and SiC [14]. These additives are believed to serve as heterogeneous nucleation sites during the cooling which promotes the fine grain structure or as obstacles which

hinder the grain growth. Superheating is also used to refine the grain structures of polycrystalline magnesium alloys [15]. The process involves superheating the alloy 150-260ºC [16] above the liquidus temperature and cool back to pouring temperature. The mechanism of superheating grain refinement was explained by Wood [10] and Hall [17]. According to Wood, iron precipitates forms during cooling and these precipitates serve as the nuclei for new grains. In Hall's theory, it was magnesium or aluminum oxides formed during the cooling instead of iron.

Another common grain refinement method is severe plastic deformation (SPD), which was first introduced by Valiev et al. [18]. SPD process can easily produce metals with fine grains, sometimes even ultra-fine grain structures (ie. grain size range from few microns to nano-meter). Ultra-fine grain (UFG) materials usually have promising properties in strength, ductility and even superplastic behavior. Extensive researches have been conducted to establish different SPD routes to fabricate UFG metals with enhanced mechanical properties [19-25]. UFG metals are usually processed with high pressure and extensive amount of strain under relative low temperature. The crystal structure developed by SPD is usually dominated by high angle grain boundaries with equiaxed granular type grains [26]. Equal channel angular extrusion (ECAE) is by far the most popular SPD process. It was first introduced by Segal et al. [27] in 1981. The ECAE process is implemented by repeat pressing ingot in a special die with two intersecting channels usually at an angle of 90º. The two channels have equal cross-sections so the strain put on the ingot is nearly pure shear and the shape of the ingot does not change. This unique processing technique enables the ingot to accumulate strains through many

pressings. Different processing routes can be applied by ECAE with different insertion angles of the ingot between passes. In process route A, no rotation is applied to the ingot between passes. In route B and C, 90 and 180 degrees rotations is applied to the ingots in between passes. Extensive studies of ECAE process were done on pure or alloy metals such as titanium [28-31], magnesium [32-36], aluminum [37,38], steel[39,40], copper[41], and gold[42]. Though the microstructure morphology may vary with different processing conditions and materials, it has shown that homogeneous UFG microstructure can be obtained after 4-6 ECAE passes by route B with equiaxed grains and high angle grain boundaries [43]. The simple design and promising outcome of ECAE process makes it the most common SPD practice. Many metal processing studies nowadays are still depending on the ECAE processes.

Another popular SPD process, namely high pressure torsion (HPT), was first introduced in 1984 by Zhorin et al. [44]. The process of HPT is applying high pressure and torsion to a small disk-shaped metal work piece and induce tremendous amount of shear strain in the work piece. The HPT device is usually consisted of one cylindrical plunger and one cup-shaped holder. The work piece is held in between the plunger and holder under high pressure (several GPa). The holder rotates and the friction on the sample forces it to shear. The hydrostatic compression applied to the sample stops the sample from breaking apart under high shear strain. The sample size is usually 10-20mm in diameter and 0.2-0.5mm thick. High pressure torsion has been successfully used to refine microstructures in many applications [45-48]. The advantage of using HPT is the ability to control the applied pressure, cumulative strain and the strain rate to the sample. The resulting grain size is

usually in nano-meter range with high angle grain boundaries. However, due to the limited sample size, the HPT processes are still confined to the laboratory experiments. Also, strains obtained by the samples are non-uniform from zero in the center to high strain near the surface.

Accumulative roll bonding (ARB) is also used for obtaining refined crystal structures. The principal of the ARB is to simultaneous roll two sheets of metal together into one sheet. The rolled sheets were bounded together from rolling and the thickness of original sheets was reduced in half. The rolled sheet was then cut into two halves and stack together for the next rolling. The operation was repeated several times to impart large strains into the rolled sheets. Several reports have been made on ARB processes with substantial grain refinement [49-51].

Grain refinement is the key to achieving better mechanical properties. From the various studies listed above, it is suggested that SPD process is the best way to give fine or Ultra-fine grain structures. In light of this, this study is dedicated to find a better SPD route to achieve grain refinement and study the accompanying mechanical improvements. The detailed processing techniques and procedures would be described in Chapter 2-5.

1.3 Superplasticity and related deformation mechanisms

Superplastic deformation is an importance field of study especially in hard-to-deform metals. One important criterion to achieving superplastic deformation is refined grain size. With ultra-fine grain structures, several hundred or even thousands percent of elongations could be achieved in the samples tested at elevated temperature. The first superplastic

behavior of metallic material was reported back at 1912 by Bengough [52] on the brass sample pulled to 163% at 700ºC. In 1964 Backofen et al. [53] demonstrated superplasticity in Zn-Al alloy and suggested the commercial potential of superplasticity, the report started intense superplastic- associated researches. With elongation more than 300%, most complex shapes of the parts can be made by superplastic deformation, and the savings of weight and costs on the superplastic productions gives much of incentive in commercial manufacturing to change from conventional to superplastic forming. The most important trait of the superplastic materials is the high strain-rate sensitivity (m values) derived from the equation $\sigma = C\acute{\varepsilon}^m$, where σ is the true flow stress , C is constant , and $\acute{\varepsilon}$ is the strain rate. Most metals have m value less than 0.2. Superplastic materials usually have m greater than 0.5. The high m values help promote the uniform deformation of the samples for the flow stress of high flow rate regions is higher than the flow stress of low flow rate regions. The most common way to achieve superplasticity is through grain refinement, namely fine-structure superplasticity [54]. The rate-control mechanism of the fine-structure superplasticity is grain boundary sliding (GBS) and GBS only takes place in fine grain materials. In fine-structure superplasticity, the grain size is usually on the order of 1-5 μm and this is the reason why ultra-fine grain materials drew so much attention in the past few decades. Also, the flow stress of the fine-grain structures at elevated temperature is relatively lower than the coarse grained structures. Therefore it is more energy efficient to process the fine-grain structure materials.

The superplastic deformation mechanisms can be explained in three modes; namely diffusion flow (Nabarro-Herring and Coble creep), grain boundary slip accommodated by

diffusion flow and grain boundary slip accommodated by slip. Many experiments have been conducted to explore the most probable deformation mechanisms for superplastic deformation. By far, the grain boundary sliding (GBS) accommodated by slip is believed to be the most probable mechanism in superplastic deformation [57]. In this mechanism, GBS is accommodated by slip in the mantle area of the grains or grain boundaries, while little or no slip is occurred at the core of the grains. Fine grain structure is essential in GBS mechanism since most of the slips occur in or near the grain boundaries and fine grain structure provides high volume fractions of grain boundaries. In other words, if the grains are coarse, it is not likely to have superplastic deformation in the material.

From the analysis of various deformation mechanisms provided above, it is clear that fine grain structure is essential in both room temperature and elevated temperature deformations. Thus it is worth devoting our efforts into the discovery of new and efficient processing routes that leads to fine-grained metal materials. In light of this, current study is dedicated to practice new thermo-mechanical processes on hard-to-deform materials (ie. magnesium and titanium) and analyze the resulting microstructure and mechanical properties of the work pieces in hope to discover a processing technique that betters the existing thermo-mechanical processes.

1.4 Experimental studies

The followings briefly introduce the experimental works and analysis that have been done regarding the thermo-mechanical processes in metals. Different processing techniques are divided in different chapters. Besides the thermo-mechanical processes of

metals, a new tensile test procedure was adopted for testing micro-scale tensile samples and is described in chapter 6.

In chapter 2, efforts have been made to impart severe plastic deformation on ZK60 and gallium containing Mg alloy (3%Al, 2%Ga and Mg balance) with ABRC process at elevated temperature. The ABRC route is different than the convention SPD process and can impart heavy deformation on sheet metals without drastically alter its form. This technique was first developed by Ghosh and Yang[60] for processing AZ31 Mg alloy. In current study, the same processing route was used on ZK60 and gallium containing Mg alloy with processing temperature ranged from 450ºC to 275ºC. Microstructures of processed Mg alloys were studied on different processing passes and show substantial grain refinements along the processing stages. Tensile tests done on the processed sheet show improvements in strength at room temperature and ductility at high temperature. Also, the analytical studies were made on the growth dynamic and strain rate sensitivity at various strain rate regions to evaluate the optimum deformation conditions.

In chapter 3, Ti-6Al-4V was processed through a series of thermo-mechanical deformations include forging in a special designed angle die and hot rolling. The tapered design in the angle die helped resolve the applied compressive stress registered on the punch to both compressive and shear stresses and provide an efficient way to impart severe deformation to high strength materials. The microstructure analysis of the processed Ti-6Al-4V showed substantial grain refinement and equiaxed grain structure. High temperature tensile testes were performed on the processed Ti-6Al-4V sheet and superplastic behaviors were found on the test samples with elongation up to 450%. The

strain rate sensitivity (m) calculated from jump strain rate tests indicated the deformation is superplastic (m >0.5) in the strain rate range from 10^{-4}/s to 10^{-3}/s. Dynamic grain growth and static grain growth kinetics of the processed Ti-6Al-4V were studied through the microstructure analysis of the tested tensile samples.

Chapters 4 and 5 concentrate on a novel thermo-mechanical process, namely biaxial extrusion process. The biaxial extrusion process is different from the conventional SPD processes and can apply severe plastic deformation to hard-to-deform material and convert billet form to sheet form in one processing step. Biaxial extrusion process was tested on many materials (Ti-6Al-4V in Chapter 4, magnesium and Mg based alloys in Chapter 5). All processed materials showed great grain refinement with improved mechanical properties such as enhanced yield strength in Ti-6Al-4V (564MPa increment), in ZK60 (200MPa increment) , increase in hardness (Mg-Al composite, chapter 4) and good ductility (252% elongation in ZK60).

In Chapter 6, efforts were put on the study of mechanical behaviors of the small tensile specimens in the of micron-meter scale (with sample cross-sectional area ~100μm^2). Ti-1100 and Inconel 625 sheets were choose for base materials. A strong increase in yield strength in the small specimens was observed with respect to the large samples. The microstructure of the tested specimens was studied. Many strain steps were found in both Ti-1100 and Inconel 625 specimens. These strain steps were believed to be the cause of the strain bursts found in the stress-strain curves of the small sample tests. The deformation mechanism of the materials in micro-meter range is proven to be different than the bulk materials. Detailed studies will be described in chapter 6.

References

[1] E.O. Hall: *Proc. Phys. Soc*. B64. 747. (1951)

[2] N.J. Petch: *Iron Steel inst*. 74. 25 (1953)

[3] J.C.M Li, Y.T. Chou: *Metal. Trans*. 1145. (1958)

[4] J.C.M Li: *Trans. TMS-AIME* 227. 239. (1963)

[5] E. S. Venkatesh, L.E. Murr: *Scripta Metall*. 10(1976) 477

[6] E.S. Venkatesh, L.E. Murr: *Mater. Sci. Eng*. 33(1978) 69

[7] L.E. Murr: *Appl. Phys*. Lett. 24(1974) 533

[8] Y. Zhang, N. Ma, Y. Le S. Li. And H. Wang: *Material Letters* 59 (2005) 2174-2177.

[9] J.A. Davis and L.W. Eastwood: *Trans. AFS,* 1945, vol. 53, pp. 352-62

[10] R.T. Wood: *The Foundryman*, 1953, pp. 98-99 and 256-61

[11] E.F. Emley: *Principles of Magnesium Technology*, Pergamon, Elmsford, NY, 1966, P. 260

[12] E.L. Glasson and E.F. Emley: *The Solidification of Metals*, Iron and Steel Institue, London, 1968, pp. 1-9

[13] J.E. Gruzleski and C.A. Aliravci: U.S. Patent No 5,143,5564, 1992.

[14]A. Luo: *Metall. Q*, 1996 vol 221, pp. 540-46

[15] C.E. Nelson: *Trans. AFS*, 1948, vol. 56 pp. 1-23

[16] Y.C. Lee, A.K. Dakhle and D.H. Stjohn: *Metall Trans* vol 31A, 2895, 2000.

[17] H.T. Hall: *Magn. Rev. Abs*., 1945, vol. 3, pp. 68-72

[18] R.Z. Valiev, A.V. Korznikov, and R.R. Mulyukov: *Mater. Sci*. Eng. A, 186 (1993), p.141.

[19] Y.T. Zhu, T.G. Langdon, R.Z. Valiev, S.L. Semiatin, D.H. Shin, T.C. Lowe: *Ultrafine Grained Materials III* (2004)

[20] T.G. Langdon, F. Minoru, N. Minoru, H. Zenji: *JOM*, v 52, n 4, p 30-33, 2000.

[21] Y.R. Kolobov, G.P. Grabovetskaya, K.V. Ivanov, R.Z. Valiev, Y.T. Zhu: *Ultrafine Grained Materials 3 Symposium*, p 621-8, 2004

[22] I.P. Semenova, Y.T. Zhu, G.J. Raab, T.C. Lowe, R.Z. Valiev: *Ultrafine Grained Materials 3 Symposium*, p 463-8, 2004

[23] S.M Kim, J. Kim, D.H. Shin, Y.G. Ko, C.S. Lee, S.L. Semiatin: *Scripta Materialia*, v 50, n 7, p 927-30, April 2004.

[24] G.G. Yapici, I. Karaman, Z.P. Luo, H. Rack: *Scripta Materialia*, v 49, n 10 SPEC., p 1021-1027, November 2003.

[25] I.P. Semenova, G.I. Raab, L.R. Saitova, R.Z. Valiev: *Materials Science and Engineering A*, v 387-389, n 1-2 SPEC. ISS., p 805-808, December 15, 2004.

[26] R.Z. Valiev, R.K. Islamgaliev, I.V. Alexandrov: *Materials science* 45(2000) 103-189

[27] V.M. Segal: *Russ Metall*,1(1981), p99

[28] S.L. Chong, G.K. Young , H.S. Dong, K. Park: *Scripta Materialia*, v 54, n 10, p 1785-9, May 2006

[29] E. Tabachnikova, V.Z. DBengus, A.V. Podolskiy, S.N. Smirnov, K.M. Csach, J.S. Miskuf, R. Lilya R, I.P. Semenova, R.Z. Valiev: *International Journal of Mechanics and Materials in Design*, v 4, n 2, p 189-195, June 2008

[30] L.I. Saitova, H.W. Höppel, R. Valiev, M. Göken: *Materialwissenschaft und Werkstofftechnik*, v 39, n 4-5, p 367-370, April/May 2008

[31] H. Watanabe, T. Mukai, K. Ishikawa, K. Higashi: *Scripta Materialia*, v 46, n 12, p 851-6, 14 June 2002

[32] A. Yamashita, Z. Horita, T.G. Langdon: *Materials Science and Engineering A*, v 300, n 1-2, p 142-147, Febrary 28, 2001

[33] R.B. Figueiredo, T.G. Langdon: *Materials Science and Engineering A*, v 503, n 1-2, p 141-144, March 15, 2009

[34] T.G. Langdon, R.B. Figueiredo: *Materials Science & Engineering A* ,v 430, n 1-2, p 151-6, 25 Aug. 2006

[35] H. Watanabe, T. Mukai, K. Ishikawa, K. Higashi: *Scripta Materialia*, v 46, n 12, p 851-6, 14 June 2002

[36]G. Hamu, D. Ben Eliezer, L. Wagner: *Journal of Alloys and Compounds*, v 468, n 1-2, p 222-229, January 22, 2009

[37] T. Mukai, T.G. Nieh, H. Watanabe, K. Higashi: *Materials Science Forum*, v 304-306, p 109-14, 1999

[38] H.G. Salem, R.E. Goforth, K.T. Hartwig: *Journal of Materials Science and Technology*, v 12, n 1, p 45-64, 2004

[39] A. Yanagida, K. Joko, A. Azushima: *Journal of Materials Processing Technology*, v 201, n 1-3, p 390-4, 26 May 2008

[40] N. Saito, M. Mabuchi, M. Nakanishi, I. Shigematsu, G. Yamauchi, M. Nakamura: *Journal of Materials Science*, v 36, n 13, p 3229-3232, July 1, 2001

[41] L.L. Gao, X.H. Cheng: *Tribology Letters*, v 27, n 2, p 221-5, Aug. 2007

[42] W.Y. Yeung, R. Wuhrer, M. Cortie, M. Ferry: *Materials Forum*, v 31, p 31-35, 2007, Materials Forum

[43] C.L. Terry and R.Z. Valiev: *JOM* .October 2004

[44]V.A. Zhorin, D.P. Shashkin, N.S. Yenikoponyan: *DAN SSSR* 1984;278:144

[45] F. Wetscher, R. Pippan: *Philosophical Magazine*, v 86, n 36, p 5867-5883, December 21, 2006

[46] A.P. Zhilyaev, S. Lee, G.V. Nurislamova, R.Z. Valiev, T.G. Langdon: *Scripta Materialia*, v 44, n 12, p 2753-2758, June 8, 2001

[47] D. Arpacay, Y. Sangbong, M. Janecek, A. Bakkaloglu, L. Wagner: *Materials Science Forum*, v 584-586, pt.1, p 300-5, 2008

[48] A.P. Zhilyaev, T.R. McNelley, T.G. Langdon: *Journal of Materials Science*, v 42, n 5, p 1517-28, March 2007

[49] Y.T. Zhu, T.G. Langdon, R.Z. Valiev, S.L. Semiatin, D.H. Shin, T.C. Lowe: *Ultrafine Grained Materials III* (2004)

[50] D. Terada, S. Inoue, N. Tsuji: *Journal of Materials Science*, v 42, n 5, p 1673-1681

[51] N. Tsuji, N. Kamikawa, H.W. Kim, Y.Minamino: *Ultrafine Grained Materials III*, p 219-226, 2004

[52] G.D. Bengough: *Inst. Metals* 7, 123 (1912)

[53] W.A. Backofen, I.R. Turner and D. H. Avery: *Trans. Am. Soc. Metals* 57, 980 (1964)

[54] X.J. Xing, H. Yang, S.T. Miura: *Materials Transactions*, v 48, n 6, p 1406-11, 2007

[55] K. Kitazono, R. Hirasaka, E. Sato, K. Kurtbayashi, T. Motegi: *Acta Materialia*, v 49, n 3, p 473-86, 8 Feb. 2001

[56] R.S. Mishra, A.K. Mukherjee: *Superplasticity and Superplastic Forming* 1995. Proceedings of a Conference, p 171-8, 1996

[57] O.D. Sherby and J. Wadsworth: *Progress in Materials Science* Vol. 33. pp. 169-221, 1989

[58] Y. Maehara: *Trans. Iron and Steel Inst. Japan*, 27, 705 (1987)

[59] W.J. Kim, G. Frommeyer, O.A. Ruano, J.B. Wolfenstine and O.D. Sherby: *Scr Metall.* 23, 1515(1989)

[60] Q. Yang, A.K. Ghosh: *Acta Material*(2006)

Chapter 2

Grain refinement of ZK60 alloy and gallium-containing magnesium alloy through ABRC process

Abstract

The present work is focused on the processing and properties of two magnesium alloys, ZK60 and a gallium-containing magnesium alloy (Mg-3Al-2Ga). The aim of this work was to achieve superplasticity through a new severe deformation technique, namely alternate biaxial reverse corrugation (ABRC). Mechanical properties and microstructure transformations were evaluated side-by-side along each step of the experimental process. Fine grain distributions of 6.39 μ m and 3.58 μ m of the ZK60 and the gallium-containing magnesium alloy respectively, were observed after the ABRC process. A tensile elongation of 207% was observed in processed ZK60 under strain-rate of $2x10^{-4}$ /s at 400^{o}C. High m-value of 0.46 of ZK60 was obtained under strain-rate of 10^{-3}/s at 300^{o}C.

2.1 Introduction

Due to its light weight, high specific strength, high stiffness and good damping capacity, magnesium is used in many industrial applications such as aerospace and automobile body parts. However, because of its hexagonal close pack (HCP) structure, few slip systems can be activated during the room temperature deformation thus limited the formability and ductility of magnesium. Due to its low ductility, most fabrication of magnesium alloys is limited to casting or semisolid processing (thixomoulding). Many Mg parts are used in automobile components or sports ware to reduce weight. However, these cast parts, unlike wrought materials, don't have good strength and ductility. A new technique is essential to improve the properties of the magnesium and widen the usage of Mg alloys. Early studies suggested that severe plastic deformation could effectively induce grain refinement in the polycrystalline materials and increase the strength and ductility of the material [1-4]. In the past decades, various techniques had been developed to introduce sever plastic deformation (SPD) into the metallic alloys such as hot extrusion [5, 6], equal channel angular extrusion or pressing (ECAE/ECAP) [7-9] and alternate biaxial reverse corrugation (ABRC) [10] process. In this study, the ABRC process would be introduced to ZK60 and magnesium-gallium alloy and the microstructure evolution and mechanical properties of the processed work pieces would be studied.

The reason ZK60 is chosen for the target material is because ZK60 magnesium alloy (Mg- 6% Zn -0.6% Zr) is favored in the commercial use due to its relative higher yield strength among the Mg alloys. The finely dispersed MgZn, $MgZn_2$, and Zn_2Zr_3 precipitates [4] in the ZK60 alloy hinder the movements of the dislocations inside the

grains, thus increase the stress required to further dislocation propagation or activation of new dislocations. The ductility of ZK60 could also be improved by grain refinement through SPD process. The early study of Galiyev et al. [11] showed significant tensile elongations in processed ZK60 magnesium alloy (1330% at 250° C with the strain-rate of $1.4x10^{-4}s^{-1}$). Galiyev's thermo-mechanical processes include three-steps; extrusion, compression and isothermal rolling. The resulting microstructure of the processed ZK60 showed refined grain size ~3.7 μ m.

Another common practice to increase the strength of the Mg alloys is solid solution strengthening. Additives of SiC [12], lithium [13] and rare earth [14] were usually added into magnesium to improve the mechanical behaviors. C.J Ma et al. [14] found that by adding the rare earth elements such as Ce, La and Nd into the ZK60 alloy, second phases particles were formed in the Mg matrix and helped refine the grains during the solidification. The strength of ZK60 was both enhanced by the refined grain size and also by the entanglement of dislocations around the second phase particles. In this study, gallium was used as additive in the Mg alloy for its good wetting property.

ABRC process and hot rolling was introduced to the magnesium-gallium alloy and ZK60 billet consolidated from machined chips. The processing temperature is progressively decreased from 450ºC to 300ºC to enhance the grain refinement and slow down the grain growth during the process. The microstructures of the processed magnesium-gallium alloy and ZK60 would be studied and the mechanical properties would be tested. Jump strain-rate tests were conducted to obtain the strain rate sensitivity (m-value). The detailed processing procedures would be described in the following sections.

2.2 Material preparation

One of the target materials, ZK60 billet, was obtained from consolidating ZK60 machined chips. Another material, magnesium-gallium billet, was obtained from melting Ga and Mg in high-temperature induction heat furnace. The chemical composition of the ZK60 magnesium alloy and gallium containing magnesium (magnesium-gallium) alloy is shown in Table 2.1. The ZK60 chips provided by Thixomat Inc. were about 0.13 inch long, 0.11 inch wide and 0.02 inch thick as illustrated in Fig 2.1. The chips were poured into a closed cylindrical die and pressed with a Forney FX700 hydraulic press machine under the pressure of 17000 psi at 450° C. During the process, the ZK60 Mg chips were consolidated into a 2.23inch in diameter, 0.59inch in thickness ingot. The ingot was then taken out and flattened down to a 3.5"x3.5"x0.188" plate with a square die. The magnesium-gallium alloy was prepared by melting pure Mg , Al, Ga powders in the induction heat furnace at 950° C for 90 minutes then air cooled to room temperature. The molded ingot, 1.55inch in diameter and 0.31 in thickness, was flattened down to a 2.22 inch in diameter, 0.15inch in thickness plate with a 3.5”x3.5” squared die.

2.3 Thermo-mechanical processing

ABRC processes [10] were done on the as consolidated ZK60 and magnesium-gallium alloy for grain refinement. The work piece was first corrugated between two sinewave dies as shown in Fig 2.2(b). The beaded sinewave dies applied tension and compression in different areas of the work piece. After the first corrugation, the work piece was rotated 90 degrees to its original position and corrugated again. The deformation lines intersected each other and formed a checkerboard-like shape. The work piece was then

turned over (flipped) to push the peaks of the waves to the reverse direction. The original tensioned area became compression area and the original compression area became tensioned area in one direction of the checkerboard-like work piece. At last, the work piece was turned 90 degrees to its orthogonal direction and pressed in the other direction of the checkerboard to finish a cycle of the ABRC process. A total of 2 cycles of ABRC was applied to the magnesium-gallium ingot and 3 cycles to the ZK60 plate. The deformation temperature was progressively lowered from 300° C to 275° C for magnesium-gallium ingot and from 450° C to 350° C for ZK60 plate. After the ABRC process, the work pieces were flattened in the square die to remove the wavy shape in the surface. The processed magnesium-gallium and ZK60 plates were put into steel jackets and hot rolled to 0.015 inch and 0.03inch at 300° C and 320° C respectively. The cumulative strain was about 6 in the magnesium-gallium work piece and 7.5 in the ZK60 work piece.

2.4 Mechanical testing and microstructure equipments

Tensile samples, 1.378inch (32mm) gauge length and 0.118inch (3mm) gauge width, and high-temperature tensile samples, 0.25inch (6.35mm) and 0.125inch (3.175mm) gauge width, were directly machined from the rolled pieces. Room temperature tensile tests were performed with Instron universal testing machine (model 5505). High-temperature tensile tests were performed ranging from 250° C to 400° C with strain-rate ranging from 10^{-3} /s to $2x10^{-4}$/s by Instron testing machine (model 4505) equipped with a three-zone high-temperature furnace. Microstructures of samples were examined with an olympus Pme3 optical microscope. . Acetic-picral solution with the composition of 4.2g

picric acid, 10m acetic acid, 10ml deionized water and 70ml ethyl alcohol was used for etching the Mg samples. Philips-Xl30 SEM in the electron analysis laboratory (EMAL) was used to provide higher resolution photos. The microstructure evolution and mechanical properties of the processed Mg alloys are discussed in the following sections.

2.5 Microstructure evolution

Fig.2.3 shows the microstructure of the magnesium-gallium alloy and the ZK60 before and after ABRC process and rolling. The grain size of the as cast magnesium-gallium alloy and as consolidated ZK60 are 266 μm and 87μm. With 2 cycles of ABRC (8 passes) and hot rolling (cumulative strain=6), the grain size of magnesium-gallium alloy has reduced to 3.58μm. With 3 cycles of ABRC (12 passes) and hot rolling (cumulative strain=7.5), the grain size of the ZK60 has reduced to 6.39μm. It's worth noticing that during the processing, some droplet-like particles emerge from the grain boundary of the magnesium-gallium work piece as shown in Fig 2.3e. With the energy dispersive x-ray (EDX) analysis, these particles are rich of Zn and Ga, thus are believed to be the Ga rich second phase. The as-consolidated ZK60 (Fig 2.3b) has many inherent voids. Those voids were greatly reduced after the subsequent thermo-mechanical ABRC and rolling processes. With the increasing strain along the passes of thermo-mechanical process, the grains became progressively uniform and refined. It is believed recrystallization is the main mechanism for the grain subdivision since heavy deformation took place at ambient temperature (>300ºC). The dislocations pile-up around second phase particles (gallium rich dispersoids) provided great locations for nucleation of new grains in magnesium-gallium alloy. Recrystallization is also found in ZK60 along the grain boundaries where

high dislocation density encourages the new grains to form as shown in Fig. 2.4. The ZK60 processed by ABRC showed homogeneous fine grain structure with grain size = 6.39μm, unlike the ZK60 processed by ECAE which usually show bimodal grain structure with mixture of large and small grains. In Lapovok et al. [16] study on ECAE processed ZK60, large grains with grain size ~25μm still remains even after 8 passes in route A and route C. In the ZK60 sheet processed by hot rolling by Gong et al. [17], bimodal grain structure is still shown after 45% reduction with elongated large grain size ~30μm. The uniformly distributed fine grain structure found in ABRC processed ZK60 in current study is believed to be attributed to the repeated recrystallizations induced by the high local strain during the ABRC process.

Twinning is also believed to play an important role in subdividing the coarse grains in the early stage of deformation in magnesium [16] because the interaction between dislocations and twins often serve as nucleation sites for new grains. Twinning was observed in both magnesium-gallium and ZK60 work pieces as indicated by the black arrows in Fig 2.3c and Fig 2.3d. A study by Yang and Ghosh [18] reported that with the process temperature higher than 250° C or lower than 170° C with cumulative strain greater than 4.0, no twinning could be found in the AZ31 magnesium. Lapovok et al. [16] also reported that no twins were found in the ECAE processed ZK60 with deformation temperature higher than 300° C. The rarity of twinning at high-temperature is because the stress required to activate secondary slip plane (slip on prismatic or pyramidal planes) is lowered. However, many twins were observed in the ZK60 work piece with the process temperature higher than 400° C and strain more than 4 as shown in Fig 2.3d. The

twinning found in ZK60 in the current study is attributed to the high local dislocation density induced by ABRC process.

2.6 Mechanical behavior

Elevated temperature tensile tests were done on ZK60 and magnesium-gallium specimens at strain-rate ranging from 10^{-3} to $2x10^{-4}$ $s^{-1}$and temperatures ranging from 250° C to 400° C. The true stress-strain curves of the tests are tabulated in Fig.2.5. The stress peak of ZK60 shifted to the higher strain with higher temperature during the same strain-rate ($2x10^{-4}s^{-1}$). Strain hardening was observed at the beginning of most of the tests but some strain softening is observed at 250° C with the strain-rate of $2x10^{-4}s^{-1}$. Under the same test conditions (300ºC, $2x10^{-4}$/s), magnesium-gallium alloy has higher strain hardening rate and higher flow stress than ZK60 (Fig 2.5(b)) with lower elongation (Table 2.2). This result is consistent with the work done by C.J Ma et al. [14] on the rare earth-containing Mg alloy where low ductility was found. It is believed that the large gallium second-phase particles reside on the grain boundaries in the magnesium-gallium alloy impeded the sliding between relative grains and caused difficulty to grain boundary sliding, which lead to the subsequent low ductility. Room-temperature tensile tests show higher yield strength in ZK60 (274MPa) compared to magnesium-gallium alloy (190MPa) as shown in Fig 2.6. The high strength in ZK60 is expected since the MgZn dispersoids are much finer and uniformly distributed in the Mg-matrix in ZK60 than the coarse gallium second phase particles in the magnesium-gallium alloy.

Strain rate sensitivity (m-values) of ABRC processed magnesium-gallium alloy and ZK60 were measured by jump strain-rate tensile tests with strain-rate ranging from 10^{-5}/s to 10^{-3}/s at 300ºC. The magnesium-gallium alloy has a strain rate sensitivity of m= 0.35 and ZK60 has m=0.35-0.38 at lower strain-rates (10^{-5}/s-$5x10^{-4}$/s) and m=0.5 at higher strain-rates ($5x10^{-4}$/s-10^{-3}/s) as shown in Fig 2.7. A high strain rate sensitivity is essential to the superplastic deformation. Therefore it is important to find the highest m-value by optimizing the test temperatures and strain-rates. The elevated temperature tensile tests done by Figueiredo et al.[19] on ECAE processed ZK60 showed m-values varied from <0.1 at 300K to 0.5 at 450K with strain-rate =10^{-4}/s. The highest ductility (1140% elongation) was found on the sample tested at 450K (highest m-value). In Yan et al. [20] tests on SiC/ZK60 composite, highest m-value (m=0.35) was found at test temperature = 613K with strain-rate = $1.67x10^{-2}$/s. For temperature higher than 613 K or strain-rate lower than 10^{-2}/s, the maximum m was no more than 0.25. It is believed that the grain size has an important effect on the distributions of m-values. Smaller grains would have high m at higher strain-rates. In Hiroyuki et al.[21] tests on ZK60, samples with grain size 6.5μm have highest m(m=0.5) at 10^{-5}/s and samples with grain size 3.3μm have highest m (m=0.5) at ~$5x10^{-2}$/s. Mukai et al.[22] reported m-value = 0.5 at strain-rate (> 0.1/s) in their SiC/ZK60 composite with test temperature 350ºC-500ºC. This high m-value at high strain-rate is attributed to their fine grain size (~0.5μm) SiC/ZK60 attained by the PM method. The m-values of ZK60 processed by ABRC varies from lowest 0.36 at strain-rate = $5x10^{-4}s^{-1}$ to highest 0.5 at strain-rate = 10^{-3}/s, but m-value in magnesium-gallium alloy is not temperature or rate sensitive and has a constant value m = 0.35. The m-values found in ZK60 and magnesium-gallium in this study correspond well to their

elongations to failures since higher m (0.36-0.5) was found in ZK60 with larger elongations (136~207%) and lower m (0.35) was found in magnesium-gallium alloy with lower elongations (80%).

To observe the mechanisms during plastic deformations, it is important to obtain the activation energy Q. A constitutive equation for determining the activation energy is

$$\dot{\varepsilon} = A\,\sigma \exp(-Q/RT) \text{ [20]} \quad (1)$$

where $\dot{\varepsilon}$ is strain-rate, A is material constant, Q is activation energy, R is gas constant and T is temperature.

The activation energy of ABRC processed ZK60 can be calculated from the slope in the $\ln\sigma$ vs T^{-1} plot as shown in Fig 2.8. The data were collected from elevated temperature tensile tests at strain = 0.4 with strain-rate = $2\text{x}10^{-4}\text{s}^{-1}$. The calculated activation energy of ZK60 is 68 kJ/mol. The calculated activation energy is much lower than the activation energy found in the most common superplastic deformation mechanisms, grain boundary sliding accommodated by grain boundary diffusion [20,21,23], which has activation energy ~92 kJ/mol. In ECAE processed ZK60 done by Chuvil'deev et al.[24], low activation energy (75 kJ/mol) was also reported. He attributed the low activation energy to the enhanced grain boundary diffusion caused by the non-equilibrium grain boundaries created by ECAE process. Since the activation energy found in ABRC-processed ZK60 in this work is close to the activation energy found in ECAE-processed ZK60 in Chuvil'deev's work. It is believed the ABRC process also created non-equilibrium grain boundaries like ECAE and cause the main deformation mechanism at elevated temperature to be enhanced grain boundary diffusion.

Substantial grain growth usually took place in structures with high internal energy and causes lowered ductility. Therefore, it is of interest to study the grain growth mechanism of processed ZK60 and magnesium gallium alloy to evaluate their structural stability. The microstructures of ZK60 and magnesium-gallium alloy tensile samples pulled at elevated temperature are shown in Fig 2.9. Inter-linkage of voids appears in near the fracture surface along the tensile direction, which suggested plasticity-controlled cavity growth [25]. Also, both extensive dynamic grain growth and static grain growth took place in the tensile samples (gauge section and grip section) during the tensile deformation. The average grain size of magnesium-gallium increased from 3.58μm (as processed) to 14.63μm after pulling at 300°C. The average grain size of ZK60 increased from 6.39μm (as processed) to largest 36.62μm in the grip section of tensile sample pulled at 400°C. The corresponding grain sizes of different pulling temperature and areas are tabulated in Table 2.3. Little or no grain growth was observed in ZK60 tensile specimens pulled under 250ºC but with temperature higher than 300ºC, extensive grain growth took place both statically and dynamically. The grain growth occurred during the plastic deformation increased the flow stress of the specimens, as shown in the stress-strain curves in Fig 2.5 where large amount of strain hardening in the tests done at 300-400ºC. It is also believed that dynamic growth rates are higher than static growth rate at temperature 300-350ºC, where average grain sizes of the gauge sections (dynamic growth) are larger than the grip sections(static growth). In Galiyev et al. [26] work, extensive grain growth were found in processed ZK60 at temperature higher than 300ºC and little/no grain growth were observed at temperature under 275ºC. So it is believed the optimal processing

temperature of ZK60 is ~ 250-300ºC where grain growth would not obstruct the superplastic deformation.

2.7 Summary and conclusions

ABRC processes have been done on both magnesium-gallium alloy and consolidated ZK60 followed by hot rolling. Extensive grain refinement was found in both samples with homogeneous grain distribution. The recrystallization during the corrugation processes is believed to be the main attribute to the grain refinement in ZK60, while fine dispersed gallium particles assisted the fragmentation of the grains in magnesium-gallium alloy. ABRC processed magnesium-gallium alloy and ZK60 both exhibit good strength at room temperature (Y.S. = 190 MPa and 274 MPa). However, the ductility of magnesium-gallium alloy is not satisfactory. The lack of superplasticity in magnesium-gallium may be caused by the gallium particles which reside on the grain boundaries and impede the relative boundary sliding. The low activation energy, Q, of 68kJ/mol indicates that the deformation mechanism of ZK60 is grain boundary diffusion enhanced by the non-equilibrium grain structure created by ABRC process. The study of ABRC process on ZK50 and magnesium-gallium alloy could be summarized by the following:

1. Grain refinement was obtained through elevated temperature ABRC processes in ZK60 and magnesium-gallium alloy.
2. High yield strength and U.T.S are found in processed ZK60 and magnesium-gallium alloy.
3. Elevated temperature tensile tests showed highest elongation 207% at 400ºC and $2x10^{-}$

$^{4}s^{-1}$ in ZK60 and 80% at 300ºC and $2x10^{-4}s^{-1}$ in processed magnesium-gallium alloy.

4. Low ductility in magnesium-gallium may be attributed to the hindrance of grain boundary sliding due to its large gallium precipitates.
5. The deformation mechanism in ABRC processed ZK60 is believed to be enhanced grain boundary diffusion.

Table 2.1 Chemical Composition of ZK60 and Gallium-containing Magnesium Alloys

	Mg	Zn	Zr	Ga	Al
ZK60(wt%)	93.4	6	0.6	0	0
Ga-Mg(wt%)	95	0	0	3	2

Table 2.2 Elongation to Failure of Ga-Mg and ZK60 Samples in Different Temperature and Strain rate.

	Temperature(°C)	Strain rate(/s)	% Elongation
ZK60	300	$2x10^{-4}$	136%
	350	$2x10^{-4}$	168%
	350	10^{-3}	136%
	400	$2x10^{-4}$	207%
	250	$2x10^{-4}$	152%
Mg-3Ga-2Al	300	$2x10^{-4}$	80%

Table 2.3 Grain size of the tensile specimens before and after pulling at elevated temperature in Gauge section (dynamic growth) and grip section (static growth).

Unit (μm)	Do	250˚C Gauge section	250˚C Grip section	300˚C Gauge section	300˚C Grip section	350˚C Gauge section	350˚C Grip section	400˚C Gauge section	400˚C Grip section
ZK60	6.39	7.7	6.4	19	10.27	18.3	13.2	32.88	36.62
Mg-Ga	3.58	-	-	14.63	-	-	-	-	-

Figure 2.1 ZK60 chips provided by Thixomat.Inc..

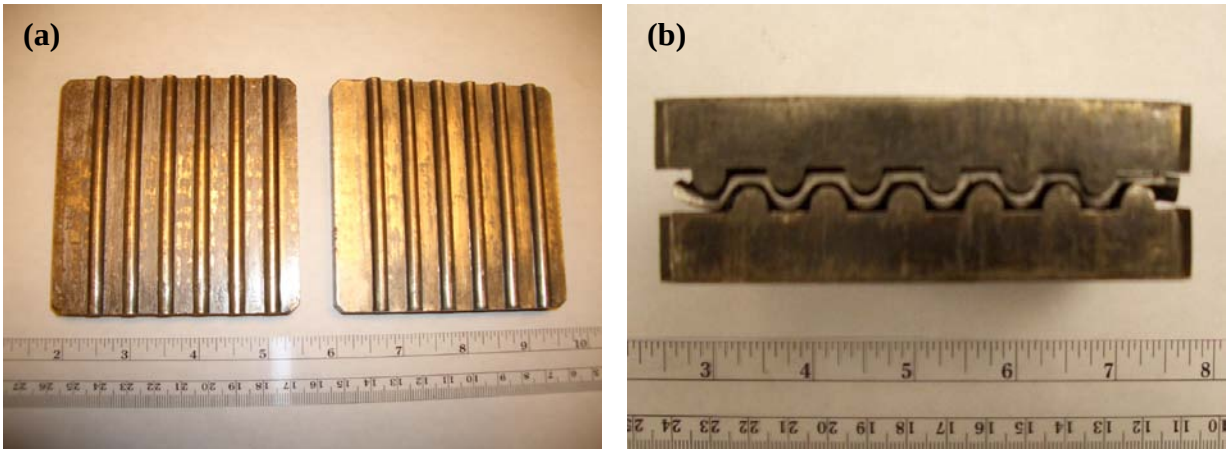

Figure 2.2 (a) Sine wave dies (b) work piece deformed between 2 sine wave dies

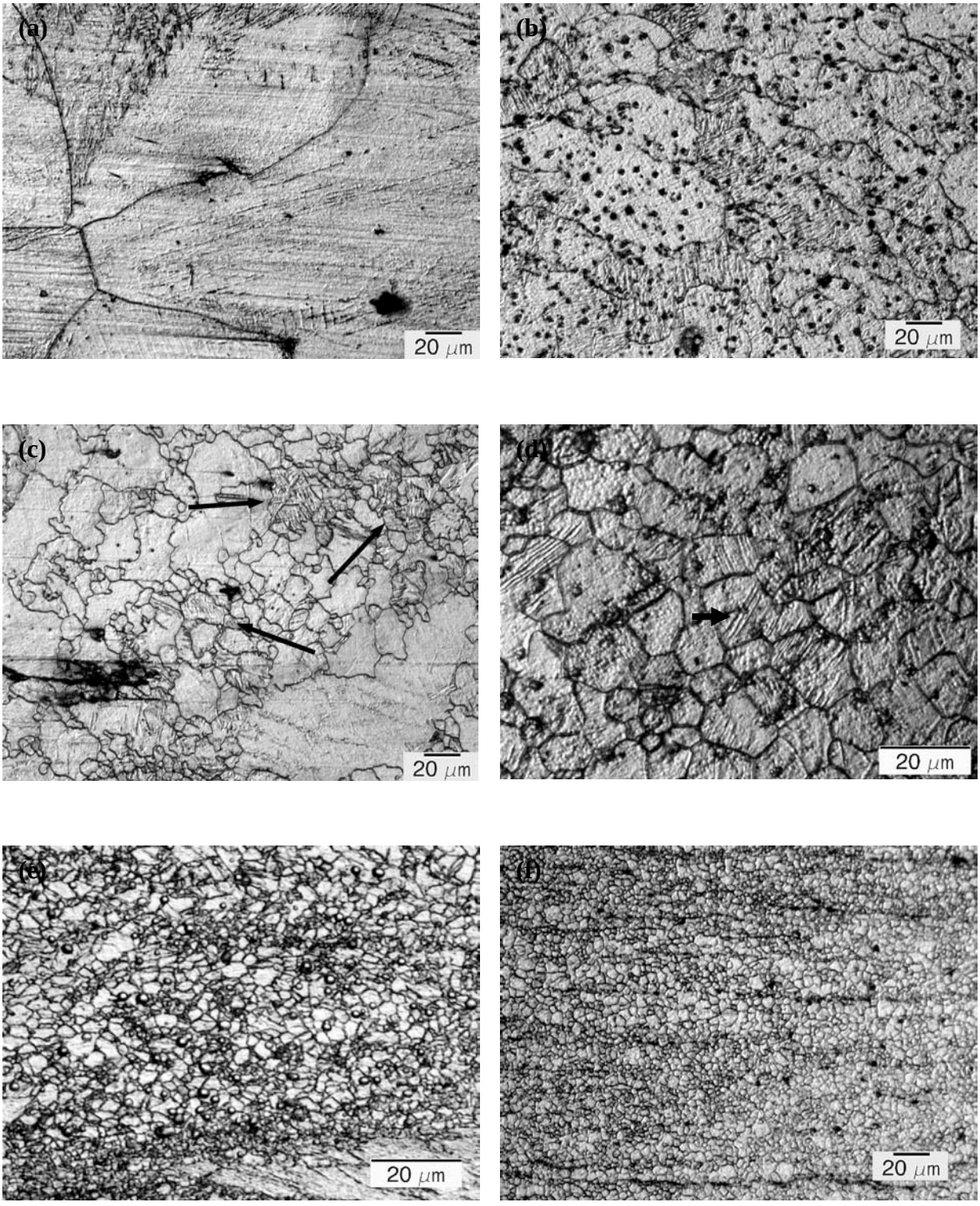

Figure 2.3 (a) Mg-Ga from cast ingot (b) As consolidated ZK60 (c) Mg-Ga processed by ABRC 1 cycle, strain = 2.15 (d) ZK60 processed by ABRC 2 cycles, strain = 4 (e) Mg-Ga processed by ABRC 2 cycles and rolled, strain = 6 (f) ZK60 processed by ABRC 3 cycles and rolled, strain = 7.5

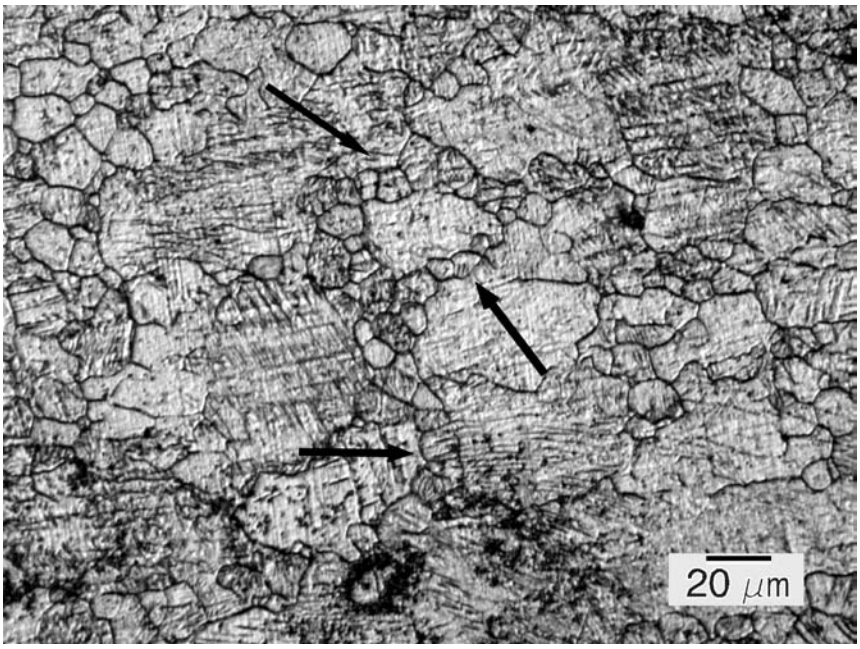

Figure 2.4 ZK60 Necklace like grain structure indicates that the new grains emerge in the grain boundary of the original grains

(a)

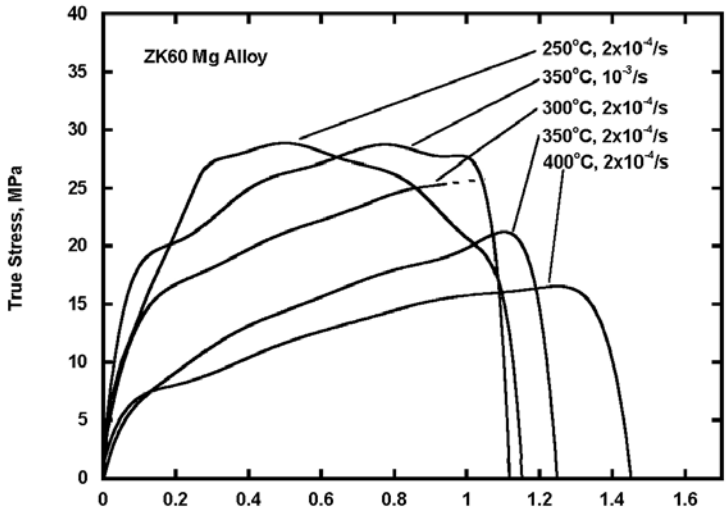

(b)

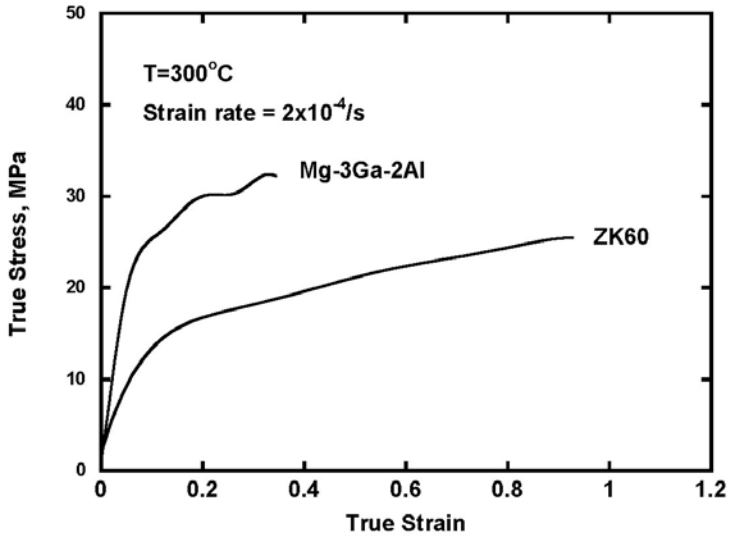

Figure 2.5 (a) Effect of temperature and train rate on the true stress-strain curves on the ZK60 Mg alloy. (b) Stress-Strain curve of the Mg-Ga alloy and ZK60 at 300° C with the strain rate $2x10^{-4}s^{-1}$.

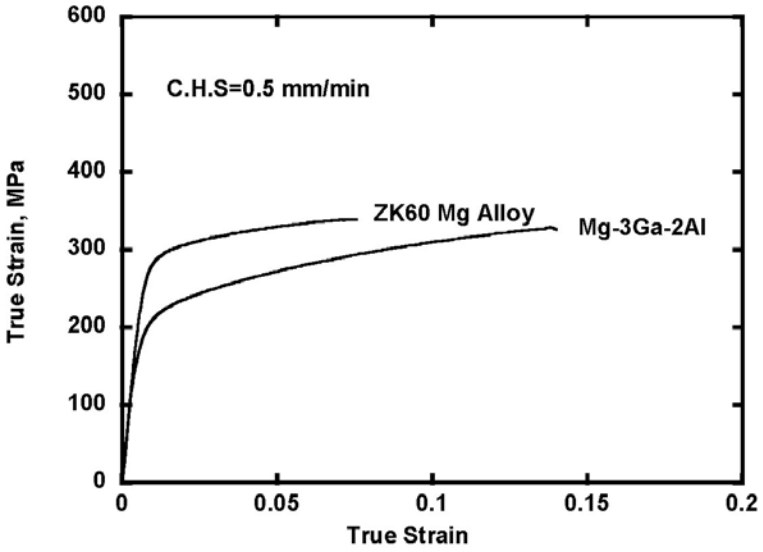

Figure 2.6 Room temperature stress-strain relationship of ZK60 and Mg-Ga alloy. ZK60 has the yield strength of 274MPa and 7.8% elongation. Mg-Ga has the yield strength of 190 MPa and 15% elongation.

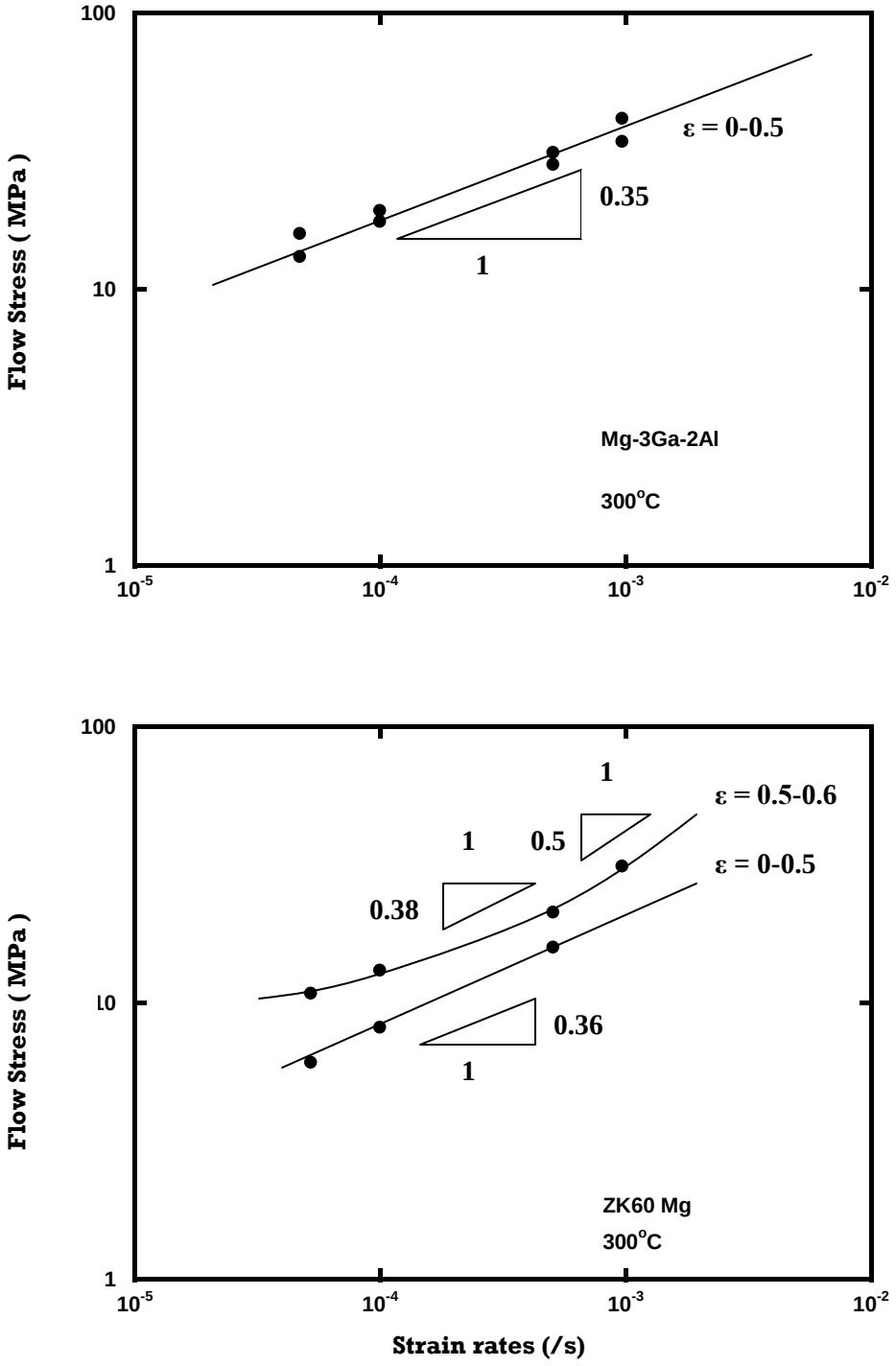

Figure 2.7 Strain rate sensitivity (m values) of ABRC processed Mg-Ga alloy and ZK60**.**

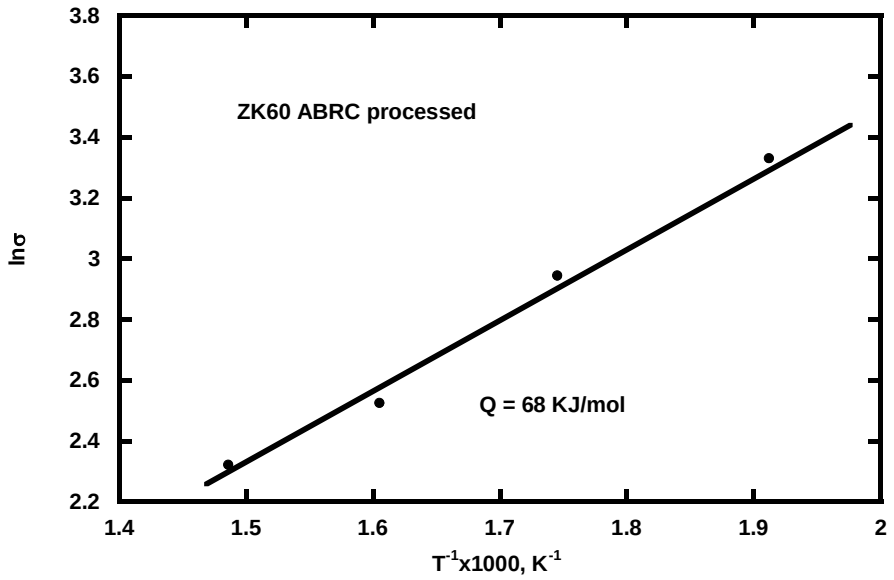

Figure 2.8 Relationship between ln σ and 1/T in ZK60 processed by ABRC. Test strain rate = $2x10^{-4}s^{-1}$.

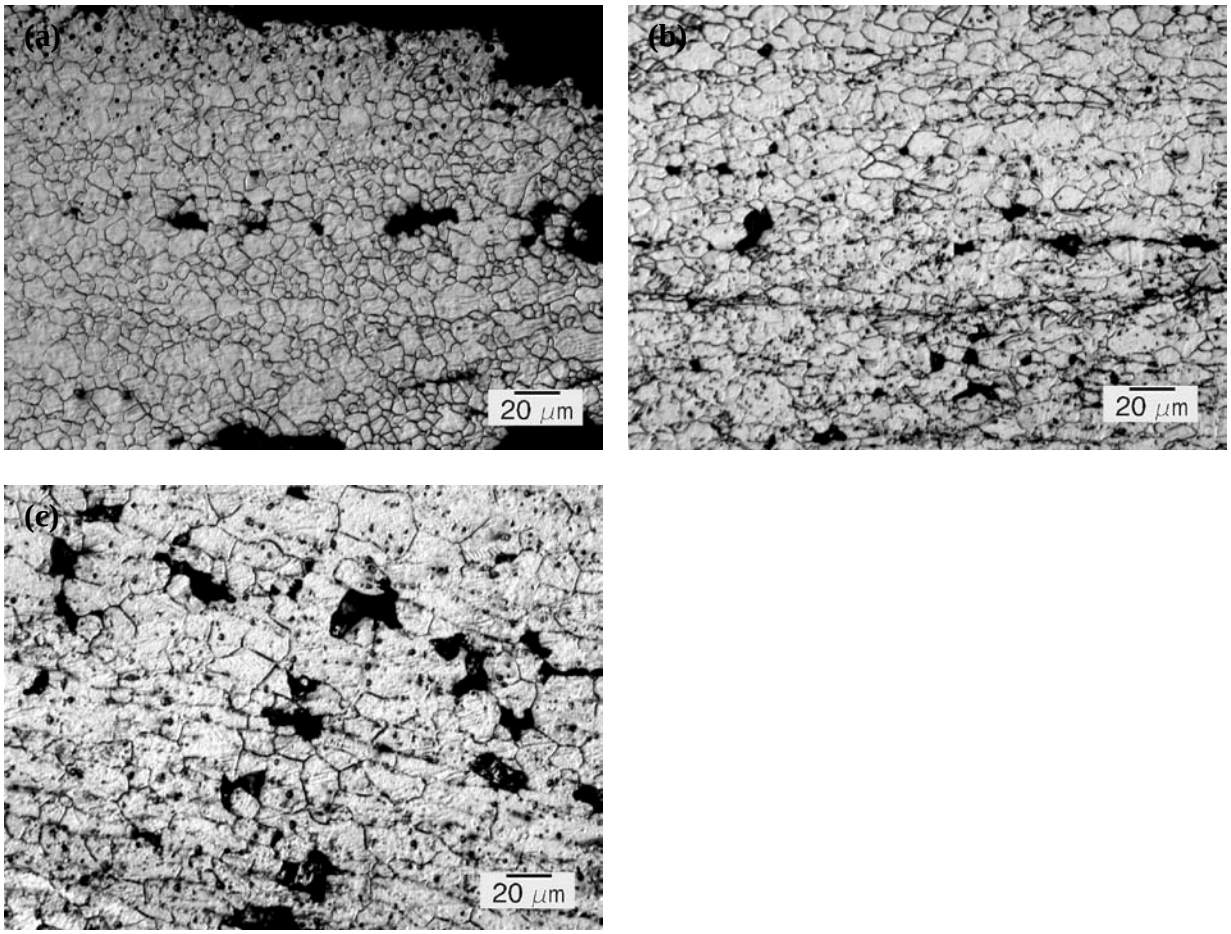

Figure 2.9 Microstructures of pulled tensile samples under the same strain rate = $2x10^{-4}$ s^{-1}(a) Mg-Ga alloy in 300° C (b) ZK60 in 300° C (c) ZK60 in 400° C.

References

[1] K. Shigeharu, A. Tatsuya,Y. Hideaki, S. Kou, and K. Yo: *Material Science Forum vols*. 350-351 (2000) pp. 65-72

[2] J.A.Valle, M.T. Perez-Prado, O.A. Ruano: *Materials Science Forum vols*. 4260432 (2003) pp. 637-642

[3] T. Mohri, M. Mabuchi, N. Saito, M. Nakamura: *Materials Science and Engineering* A257 (1998) 287-294

[4]A.Galiyev, R. Kaibyshev: *Acta material*. 49 (2001) 1199-1207

[5] A. Bussiba, A. Ben Artzy, A .Shtechman, S. Ifergan, M. Kupiec: *Material Science nad engineering* A302 (2001) 56-62

[6]K. Matsubara, Y. Miyahara, Z. Horita, T.G. Langdon: *Acta material* 51(2003) 3073-3084

[7]K. Mathis, J. Gubicza, N.H. Nam: *Journal of Alloys and Compounds* 394(2005) 194-199

[8]M. Mabuchi, H. Iwasaki, K. Yanase, K. Higashi: *Scripta Material*, Vol 36, No. 6, pp. 681-686, 1997

[9] M. Furukawa, Z. horita, T.G. Langdon: *Materials Science Forum*, v 539-543, pt.3, 2007, p 2853-8

[10] Q. Yang, A.K. Ghosh: *Acta Materialia*, v 54, n 19, Nov. 2006, p 5147-58

[11] A. Galiyev, R. Kaibyshev: *Scripta Material* 51 (2004) 89-93

[12] A. Ma, J. Jianq, Y. Nishida, T. Imai, P.S. Chen, T. Imura, M. Takaqi: *Materials Science Forum*, v 304-306, 1999, p 285-90

[13] A. Sanschagrin, R. Tremblay, R. Angers, D Dube: *Material Science and Engineering*. A220(1996) 69-77

[14] C. J. Ma, M. Liu, G. Wu, W. Ding, Y. Zhu: *Material Science and Engineering* A349(2003) 207-212

[15] S.M. He, L.M. Peng, X.Q. Zeng, W.J.Ding, Y.P. Zhu: *Materials Science & Engineering A*, v 433, n 1-2, p 175-81, 2006

[16] R. Lapovok, P.F. Thomson, R. Cottam: *Journal of Materials Science 40* (2005) 1699-1708

[17] X. Gong, S.B. Kang, S. Li, J.H. Cho: *Materials and Design* 30 (2009) 3345–3350

[18] Q. Yang, A.K. Ghosh: *Acta Material* (2006)

[19] R.B. Figueiredo, T.G. Langdon: *Mat Sci & eng* A 503 (2009) 141-144

[20] F. Yan, K. Wu, G.L. Wu, B.L. Lee, M. Zhao: *Materials Letters* 57 (2003) 1992-1996

[21] H. Watanabe and T.Mukai: *Scripta Mat* Vol. 40. No.4, pp. 477-484 1999

[22] T. Mukai, T.G. Nieh, K. Hiqashi: *International Conference on Thermomechanical Processing of Steels and Other Materials*, p 1847-52 vol 1.2, 1997

[23] H.J. Frost, M.F. Ashby: *Deformation Mechanism Maps*, 1982, p44.

[24] V.N. Chuvil'deev: *Journal of Alloys and Compounds* 378 (2004) 253-257

[25] J. Pilling, N. Ridley: *The Institute of Metals*; 1989. p. 214.

[26] A. Galiyev, R. Kaibyshev: *Scripta Mat* (2004) 89-93

Chapter 3

Severe deformation in Ti-6Al-4V alloy through forging in an angle die and hot rolling

Abstract

A series of thermo-mechanical processes, including elevated temperature forging in angle die and elevated temperature rolling, were done on the Ti-6Al-4V alloy. The resulting Ti-6Al-4V has reduced grain size to 0.31μm with enhanced mechanical properties. Superplasticity was also developed in the Ti-6Al-4V with maximum elongation of 450% at 800ºC. An equiaxed grain structure was obtained after the processing. The flow stress of the processed Ti-6Al-4V rose with the increasing strain rate and the strain rate sensitivity (m) was around 0.5 at high strain rate ($10^{-3}s^{-1}$) region. The grain growth exponent (n) was found to be 0.26 and 0.29 in the dynamic and static growth of the processed Ti-6Al-4V.

3.1 Introduction

Titanium and its alloys are well known for their high specific strength (100-200 MPa-cc/g) [1], good corrosion resistance [2] and high formability associated with superplasticity [3]. This explained why titanium alloys are wildly used in the aerospace, chemical industry and medical engineering. The mechanical properties of the Ti alloys depend very much on their chemical composition and microstructure. Ti alloys are usually exhibit in two forms; lamellar and equiaxed structures. The lamellar structure provides better rupture resistance while the equiaxed structure gives higher strength and ductility [4]. Among more than 100 titanium alloys known today, the classic Ti-6Al-4V covers more than 50% of commercial usage. Despite its success in commercial applications, the superplasticity is still limited to Ti-6Al-4V with fine grain size (<10μm) and equiaxed structure. For this purpose, a way to achieve fine and equiaxed grain structure of the Ti-6Al-4V is required. Several severe plastic deformation (SPD) techniques have been developed recently which showed promise to the production of material with ultra-fine grain sizes [5-7]. The SPD techniques include hot extrusion [8, 9], equal channel angular extrusion or pressing (ECAE/ECAP) [10-12], high-pressure torsion (HPT) [13] and alternate biaxial reverse corrugation (ABRC) [14]. Rolling process is also a popular SPD process often used in the industry for mass production of sheet metals. The alternating roll-bonding (ARB) technique used by Daisuke et al. [15] imparted heavy strain on the commercial purity titanium (CP-Ti). During a series of rolling and continuous bonding, the grain subdivision [16, 17] induced grain refinement of CP-Ti was observed and the SEM metallographic photos showed lamella structures with volume fraction of equiaxed grains increased with the increasing ARB cycles. The final grain size

of the ARB processed CP-Ti has achieved 100nm. Although ARB and other processes [18-21] had successfully produced ultra-fine grained Ti-alloys, there is still a need of systematic study on the grain refinement of the Ti-6Al-4V by thermo-mechanical processing. The goal of this work is to study the microstructural evolution as well as mechanical behavior of the Ti-6Al-4V processed by the hot forging and rolling. Since rolling Ti-6Al-4V billet at room temperature may lead to cracking and pre-heating Ti-6Al-4V in furnace for long period of time before rolling may result in grain growth, a new rolling method was applied to minimize the exposure time of Ti-6Al-4V to elevated temperature. The new rolling method is to sandwich the Ti-6Al-4V billet in a hot steel jacket (~900ºC) and quickly send to the roller when Ti-6Al-4V billet is heated up to ~700ºC in a short period of time (~5 seconds). By applying this rolling technique, the unnecessary grain growth during hot rolling of Ti-6Al-4V is avoided. The metallographic microstructures of Ti-6Al-4V in every stage of the thermo-mechanical process was taken and examined. The tensile tests were performed on the thermo-mechanical processed Ti-6Al-4V samples to evaluate the change in mechanical properties.

3.2 Thermo-mechanical process

Thermo-mechanical processing was followed in two separate steps: (1) β heat treatment following by pressing in angle die and (2) hot rolling. In the following paragraphs, these are discussed.

1A β treatment

The microstructure of the raw Ti-6Al-4V material is shown in Fig 3.1. One 0.9345 x 1.088 x 0.67 $inch^3$ Ti-6Al-4V piece was sectioned from the raw Ti-6Al-4V block by wire

EDM. To facilitate later grain refinement, a high temperature β treatment was employed before starting the thermo-mechanical process of the Ti-6Al-4V. The Ti-6Al-4V piece was first coated with a layer of boron nitride and encapsulated in a quartz tube. The tube was then vacuum sealed to prevent surface oxidation of the piece during the heat treatment in a rapid heat furnace. The quartz sealed piece was sent to a pre-heated furnace and held at 1010 ºC for 30 minutes then quench in water. The β treated Ti-6Al-4V microstructure formed a Widmanstätten structure which comprised of long orthogonally oriented martensitic transformed β with acicular ά morphology as shown in Fig 3.2.

1B Forging in angle die

The heat-treated block was then given several thermo-mechanical processes to impart a heavy strain into the material. The first stage of the thermo-mechanical deformation of the block was forging. A special designed angle pressing die was used here to forge the piece. Fig 3.3 shows the schematic of how the piece was forged in the angle pressing die. The load was applied on the 12-degree angled punches of the angle pressing die and resolved into shearing and compression stressed on the sample. The shear stress facilitated the flowing of material and reduced the excess load concentrated on the surface of the punch and reduced the chance of die damaging. Three different punches were used in the angle pressing die; each differs in pressing (contacting) area. In each pressing step, two of the punches would be used and the difference in contact areas between punches allowed the work piece to flow such that more strain could be attained during forging. The pressing areas of the lower punch, upper punch A and upper punch B are 1.59 x 1.59 $inch^2$,1.53 x 1.47 $inch^2$ and 1.47 x 1.47 $inch^2$, respectively. The detailed forging procedures are described in the following: A β heat-treated Ti-6Al-4V piece was

first machined to a 0.9345 x 1.088 x 0.27 inch^3 block and put in between the lower punch and upper punch A (punch set 1) in the angle pressing die. The angle pressing die were then heated to 550ºC by using band heaters. When temperature was homogeneous and stable throughout the die, load was applied to the punches by hydraulic press and slowly increased to 250,000lbs. Upon reaching 250,000lbs, the block was taken out from the die and cooled in the air. Two steps forging were used to maximize the applied strain. The second forging was done in between the lower punch and upper punch B (punch set 2). The forging temperature was kept at 550ºC and the maximum load increased to 400,000lbs. After two steps of forging, the block became a 1.5 x 1.8 x 0.06 inch^3 plate with flashes on each side as shown in Fig 3.4. Flashes were cut off from the plate before hot rolled.

2 Hot rolling

After forging in the angle die, the Ti-6Al-4 V plate became thin enough for the hot rolling. A steel jacket was used for heat retaining for the plate during the rolling. As shown in Fig 3.5, two 0.06 x 4 x 7 inch^3 rectangular high strength steel sheets were spot welded together on three sides. The fourth side of the jacket was left open so the plate could be slid in. Before hot rolling, the steel jacket was first heated to 950ºC in the furnace. The plate was quickly slid into the hot jacket from the open side and the heat was quickly transferred from the jacket to the plate. The temperature between jacket and plate became homogeneous at ~700ºC. The opening of the jacket was immediately hammer closed and the whole pack was quickly sent to a 5"x8" Stanant rolling mill and rolled to 50% reduction with 25 rpm feeding rate. After hot rolling, the pack was quenched in the water to stop the grain growth. The rolling process took less than 1

minute and the grain growth of the plate during the process was minimized. Secondary rolling was done for another 50% reduction with the same procedure and rolling direction. Another rolling with 30% reduction was done after on the perpendicular direction. The final thickness of the rolled sheet was 0.028inch.

3.3 Metallographic specimen preparation

The microstructure examinations were done on the as-received, as-forged, and as-rolled samples. The samples were mounted in the self-curing resin, and mechanically ground by silicon carbide papers (up to grit 4000 grade) and polished with 0.06μm colloidal silica and later etched with Kroll's reagent (2ml HF, 10ml Nitric acid, and 88ml water). XL30 Philips SEM was used for the microstructure examination with working voltage between 10-17 V.

3.4 High temperature tensile test

The elevated temperature tensile samples with gauge length 0.25" and gauge width 0.125" were machined from the rolled sheets. The elevated temperature tensile tests were performed by Instron 4505 frame and test temperature was set between 700ºC ~ 800ºC with strain rate ranged from $10^{-3}s^{-1}$ to $2x10^{-4}s^{-1}$. Elevated temperature tensile test was done following the subsequent procedures to ensure test consistency. A clam shell furnace equipped on the Instron 4505 frame was first preheated to a selected temperature (700-800ºC) for 15 minutes and test sample was inserted to the furnace and heated for 15 minutes. A stainless steel tube continuously blew argon gas onto the surface of the sample to keep the sample from oxidation during the test. Computer controlled constant

strain rate was applied to the test samples with temperature variation less than ±2ºC. The test results will be compared and discussed in the following sections.

3.5 Microstructure evolution

Fig 3.1 showed the SEM photo of the microstructure of unprocessed Ti-6Al-4V material. The grain sizes of α grains and β grains of the raw Ti were 7.87 μm and 1.07 μm, respectively. To calculate the average grain size, the area-base grain size average was used:

$$d_{ave} = A_{\alpha} * d_{\alpha} + A_{\beta} * d_{\beta} \qquad (1)$$

where A_α and A_β are the area fractions of the α grains and the β grains shown in the SEM photo and d_α and d_β are the mean grain sizes of α and β grains. Computer software Scion Image was utilized to measure the area fractions and the individual grain sizes. The area fraction of α grains and β grains are 89.8% and 10.2% and the average grain size of the raw Ti is 7.19 μm. After the Ti block was β heat-treated at 1010ºC for 30 minutes and water quenched, famous "widmanstätten" structure was observed. The average grain size of the heat-treated Ti was 254 μm. After two passes of forging in angle pressing die at 700ºC, the widmanstatten structure was broken into two phase structure (α+β) as shown in Fig 3.6a. The mean grain sizes of α and β grains (d_α and d_β) were calculated individually by averaging the grain sizes of α grains and β grains circled by the dotted lines in Fig 3.6b and 3.6c. The individual grain size distributions of α and β grains are shown in Fig 3.6d and 3.6e. Area fraction of α grain is 93.8 % and the area fraction of β grain is 6.2 %. The average grain size of the Ti after forging is 0.66μm. Fig 3.7a shows the microstructure of the work piece after hot rolling (cumulative strain = 9.6). Again α

and β grains were circled individually by dotted line in Fig 3.7b and 3.7c and the grain sizes of α and β grains are 0.34 μm and 0.22 μm, respectively. Area fractions of α grains and β grains are 80% and 20%, respectively and the average grain size is 0.31 μm. By comparing the grain sizes of the as-rolled sheet and as-forged billet, we can see that both α grains and β grains are more refined in the as-rolled sheet and the area fraction of the β grains also increases. The grains of the as rolled sheet remained equiaxed with no sign of elongation from the rolling process. It is believed that by rolling at high temperature (700ºC) with large deformation strain (~80% reduction), original large grains recrystallized into fine and equiaxed grains. The grain sizes of the Ti-6Al-4V processed in each stage are tabulated in Table 3.1.

.

3.6 Mechanical behavior

The stress-strain curves of the as-processed Ti samples tested in 700ºC and 800ºC with various strain rates are shown in Fig 3.8. Samples tested in 800ºC have lower flow stress but higher strain. Substantial strain-hardening was observed in each test condition. This suggested that grain growth might have taken placed during the tensile test at the elevated temperature. The tested tensile samples are compared in Fig 3.9 with different test conditions. The tensile elongations of the as processed samples tested at 700ºC with strain rates of $10^{-3}s^{-1}$ and $2x10^{-4}s^{-1}$are 270% and 325% respectively. The samples tested at 800ºC reached higher elongation of 404% and 450% with the strain rates of $10^{-3}s^{-1}$ and $2x10^{-4}s^{-1}$ respectively. It seemed higher strain rate leads to lower elongation in between 700ºC and 800ºC. Table 3.2 listed the tensile elongations in different test conditions of the pulled samples. Two two-step strain rate tests were done at 800°C with the starting

strain rate of $10^{-3}s^{-1}$ pulled to strain 0.9 and 1 then followed by lowered strain rate of $2x10^{-4}s^{-1}$ untill failure. Higher elongations were expected in two step strain rate tests for less time spent in higher strain rate region so that less grain growth took place. However, as can be seen in Fig 3.8, the second part of the two step strain rate tests had a higher strain hardening rate than the 800°C, $2x10^{-4}s^{-1}$ test and samples failed earlier than expected. The higher strain hardening rate indicated higher grain growth rates happened in the second part of the two step strain rate tests and lead to less elongation. The maximum elongation of the two step strain rate test was 434%.

3.7 Strain rate sensitivity

To determine the strain rate sensitivity (m values) of the as-rolled sample, a decrement step-strain rate tensile test was performed. The test was conducted at 700ºC with starting strain rate of $10^{-3}s^{-1}$. The strain rate decreased 50% to $5x10^{-4}s^{-1}$ when strain reached 0.15; decreased 50% again to $10^{-4}s^{-1}$ when strain reached 0.25 and decreased 50% again to $5x10^{-5}s^{-1}$ when strain reached 0.28. After strain reached 0.3, the strain rate jumped back to $10^{-3}s^{-1}$ and another cycle of strain rates decrement took place from strain 0.3 to 0.6. After pulled to strain 0.6, the strain rate went back to $10^{-3}s^{-1}$ and kept untill failure. The saturating stresses at each step were measured and plotted against each corresponding strain rate in a log-log plot as shown in Fig 3.10. The strain rate sensitivity (m) of the as processed Ti is calculated by measuring the slopes of the flow stress-strain rates curve and plotted in Fig 3.11. In lower strain rate region (~$5x10^{-5}s^{-1}$), both m values measured from 700ºC and 800ºC tests are small(less than 0.1). With the increasing strain rates, the m values increased and went up to around 0.6 when the strain rate rose to $10^{-3}s^{-1}$. The

relatively high m value in higher strain rates indicated that the deformation mechanism had changed from diffusion creep at low strain rate to the grain boundary sliding which accommodated by the dislocation creep [22].

3.8 Bulge testing

A 25mm diameter circular sample was cut from the as processed Ti sheet for the biaxial bulge tests with argon. The surface of the sample was mechanical ground to remove defects and deformation marks from the previous thermo-mechanical process. The circular sample was clamped in a circular die with 13mm inner diameter and sent to the preheated 700ºC furnace. After temperature was homogeneous and stable (around 5 minutes), high pressure argon gas was applied to the Ti sample from the inside the die and forced the sample to bulge to another side and form a dome. Different pressures were applied to the sample and the corresponding holding time and dome height were tabulated in Table 3.3. A photo of gas formed dome is shown in Fig 3.12.

3.9 Static/Dynamic Grain growth

Fig 3.13 shows the microstructure of the Ti sample after tensile tested at 800ºC with strain rate of $2x10^{-4}s^{-1}$(3.13a. and 3.13b.) and with two step strain rates of $10^{-3}s^{-1}$ and $2x10^{-4}s^{-1}$ (3.13c, 3.13d and 3.13e.). SEM images took from the grip section of the tested samples, as shown in Fig 3.13a and 3.13c, exhibited an equiaxed grain structure. In the grip section, no strain was imposed, so the growth of the grains was considered statically. SEM image taken from the gauge section of the tested samples, as shown in Fig 3.13b, 3.13d and 3.13e, also showed an equiaxed grain structure. The strain at the gauge section

was around 2.1 and the evolution of the grains at the gauge section was considered dynamical. Compared to the grain size of the sample before the test (0.31 μm), substantial amount of grain growth was evident in both grip (static) and gauge (dynamic) sections. The overall time the sample pulled in the high temperature (800 ºC) was 200 minutes (Fig 3.13a and 3.13b) and 82 minutes (Fig 3.13c, 3.13d, and 3.13e) . The grain sizes of the tested samples were tabulated in Table 3.4. Equation of classic grain growth kinetics deduced by Burke and Turnbull [24] is as follow:

$$R^{\frac{1}{n}} - R_0^{\frac{1}{n}} = K' \gamma \, t \qquad (2)$$

Where R is the grain size at time t and R_o is the initial grain size. K' is constant. γ is grain boundary free energy which is proportional to boundary pressure P due to surface curvature. n is the grain growth exponent. Since the grain growth of the Ti is extensive and grain size of the annealed sample is much lager than the as processed sample, the initial grain size R_o is negligible and a more general form [25] as:

$$\boldsymbol{R = Kt^n} \qquad (3)$$

In a simplified case which only the geometric factor is considered (growth of the soap foam model, Fisher and Fullman, 1952), the n value (grain growth exponent) is equal to 0.5. Fig 3.14a shows the static/dynamic grain growth of the processed Ti at 800ºC .The square blocks in Fig 3.14a are the measured values and the two polynomial curves are growth behaviors extrapolated to fit the measured data. By plotting the growth curves in log-log scale, we can find the growth exponent n by measuring the slope of the converted curves as shown in Fig 3.14b. The initial dynamic grain growth is faster than static grain growth. This stress-assisted grain growth was often observed in high temperature deformation of the Ti alloys [23]. The enhanced n value (0.48) in the beginning of the

dynamic grain growth is believed to be caused by faster grain boundary movement which was aided by the applied stress. The dynamic grain growth slowed down fast and came to a steady state (n = 0.26) after around 100 seconds. The static grain growth had a constant n value (0.29) through this time range. The grain growth kinetics of the two phases Ti are more complicated than the single phase material. Several researches [26-29] have been made to explain the growth mechanism of the microduplex Ti alloys. The n values measured in from the dynamic/static grain growth curves (n=0.26 and 0.29) are close to n value of the bulk diffusion [28] (n=0.33). So the main growth mechanism of the processed Ti is believed to be diffusion through bulk.

3.10 Conclusions

By applying forging at 550ºC and rolling at higher temperature to the Ti-6Al-4V, ultra-fine equiaxed grain structure was obtained with superplasticity. The high temperature tensile test gave a 450 % elongation of the as processed Ti. The growth mechanism of the processed Ti was believed to be bulk diffusion. Several conclusions could be drown as follow:

-Ultra-fine and equiaxed grained Ti-6Al-4V could be obtained through a series of thermo-mechanical process including high temperature forging and rolling.

-The angle pressing die facilitated the flowing of the material and reduced the possibility of damage to punch.

-Higher strains could be attained by allowing material to flow into the sides of the punch with smaller contacting area in the angle pressing die.

-By controlling the time Ti-6Al-4V was exposed to the high temperature surroundings

during the hot rolling process, the grain growth was limited and the ultra-fine grain structure of the Ti-6Al-4V was retained.

-Superplasticity of the thermo-mechanical processed Ti-6Al-4V was achieved with the tensile elongation up to 450%.

- Extensive grain growth was observed in the Ti-6Al-4V samples after the high temperature tensile test.

- Substantial strain hardening was observed during the testing of the as-processed Ti-6Al-4V samples. It is believed to be attributed to the grain growth of the test samples.

- Dynamic grain growth of the processed Ti-6Al-4V was enhanced by the applied tensile stress in the beginning of the test then gradually slowed to a steady state close to the static growth rate.

Acknowledgement

The raw Ti-6Al-4V block was kindly provided by Dr. Semiatin of U.S Air force research lab.

Table 3.1 Grain sizes comparison of Ti-6Al-4V in different thermo-mechanical process stages.

Thermomechanical process	**As Received**	**As Beta Heat Treated(1010°C)**	**After Forging in Angle die**	**After Rolling in Steel Jacket (50% reduction)**
Cumulative strain	0	0	4.5	9.6
Grain size (μm)	7.19	254	0.66	0.31

Table 3.2 Percent elongation of the High temperature tensile tested Ti-6Al-4V samples

	Strain Rates (s^{-1})	**Test Temperature (°C)**	
		700ºC	**800°C**
Tensile Elongation (%)	**10^{-3}**	270%	404%
	2×10^{-4}	325%	450%

Table 3.3 Dome Height of Ti-6Al-4V sample formed in 13mm diameter circular die

Pressure / time	Dome Height
300 psi / 8 minutes	2.42 mm
400 psi / 8 minutes	2.44 mm
500 psi / 8 minutes	2.6 mm
600 psi / 8 minutes	3.09 mm
900 psi / 8minutes	3.16 mm

Table 3.4 Individual α and β grains sizes, volume fractions of each phases and average grain sizes of the Ti-6Al-4V samples taken from each thermo-mechanical process.

Thermomechanical Process	α Grain Size(μm)	β Grain Size (μm)	Volume Fraction of α Grains (%)	Volume Fraction of β Grains (%)	Average Grain Size (μm)
As Received	7.87	1.07	89.8	10.2	7.19
As Beta Heat Treated(1010°C)		254	0	100	254
After Forging in Angle Die	0.68	0.35	93.8	6.2	0.66
After Rolling in Steel Jacket	0.34	0.22	80	20	0.31
Tensile Tested at 800ºC (Grip Area) for 200 mins	4.31	1.86	76	24	3.73
Tensile Tested at 800ºC (Gauge Area) for 200 mins	7.83	1.74	78	22	6.5
2 Step Strain Rate Tensile Tested at 800°C (Gauge Area) for 82 mins	5.36	1.4	93.2	6.8	5.1
2 Step Strain Rate Tensile Tested at 800°C (Grip Area) for 82 mins	3.1	1.13	88	12	2.87

`

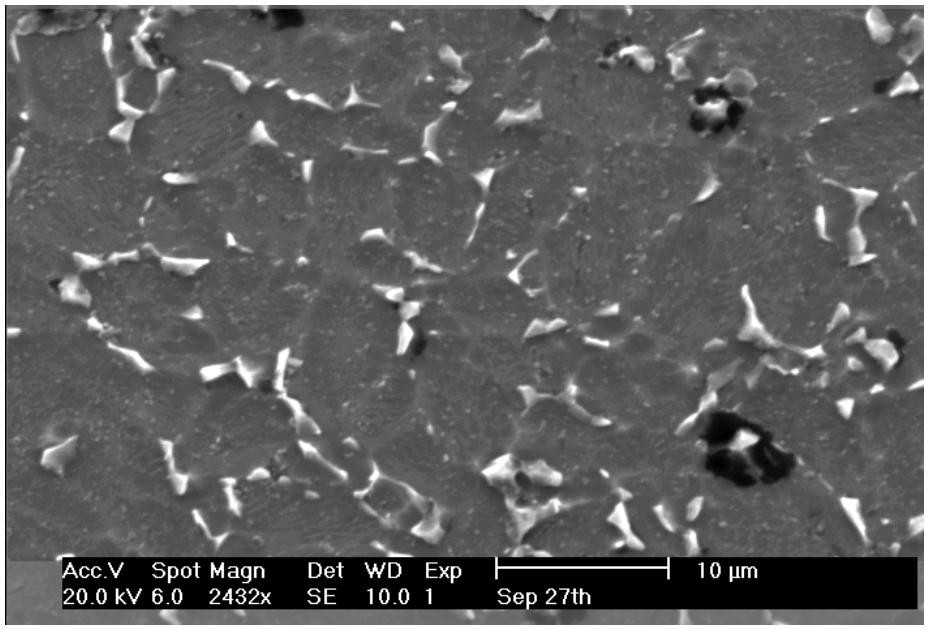

Figure 3.1 Microstructure of as-received Ti-6Al-4V. β grains are dispersed around the grain boundaries of the α grains. Some voids are visible in the structure. The average grain size is 7.19 µm.

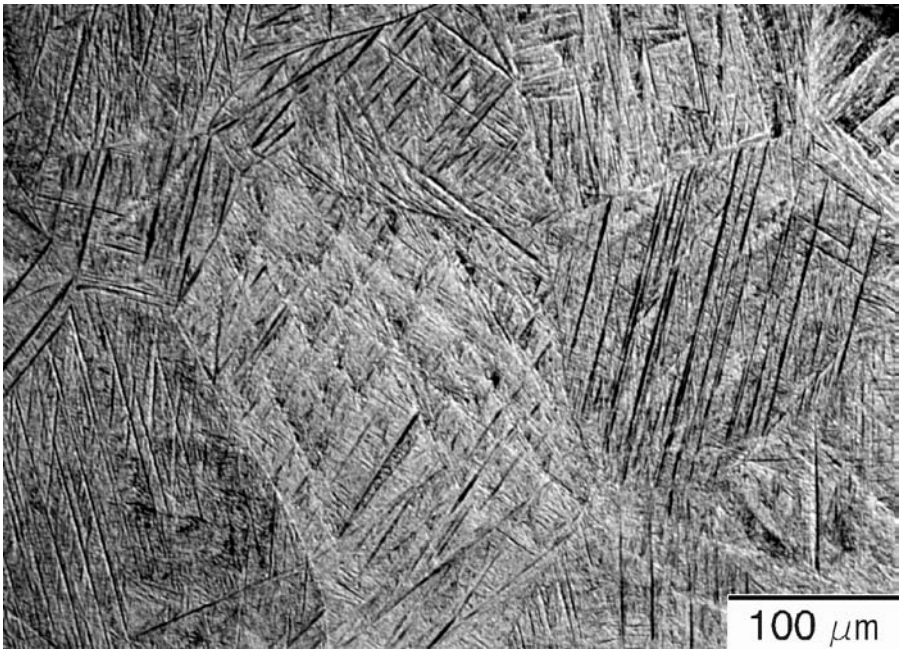

Figure 3.2 Microstructure of Ti-6Al-4V after heat treated at 1010ºC for 30 minutes. The Widmenstätten structure is observed with acicular ά inside the coarse transformed β grains. The average grain size is 254µm.

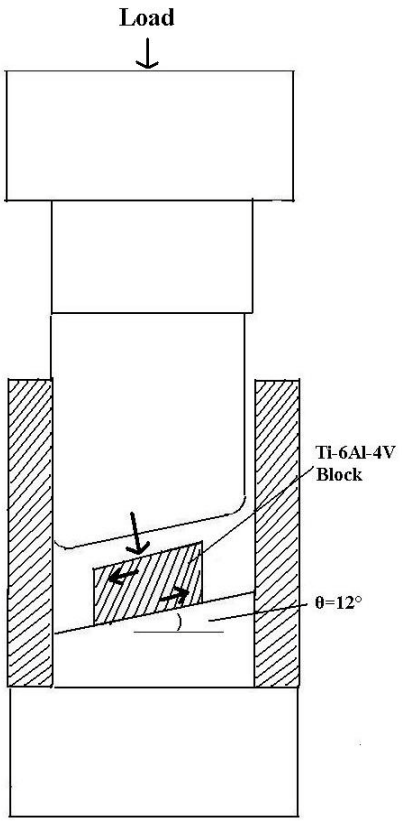

Figure 3.3 Schematic diagram of the 12º angle pressing die. Vertical load is resolved into compression and shearing directions on the work-piece

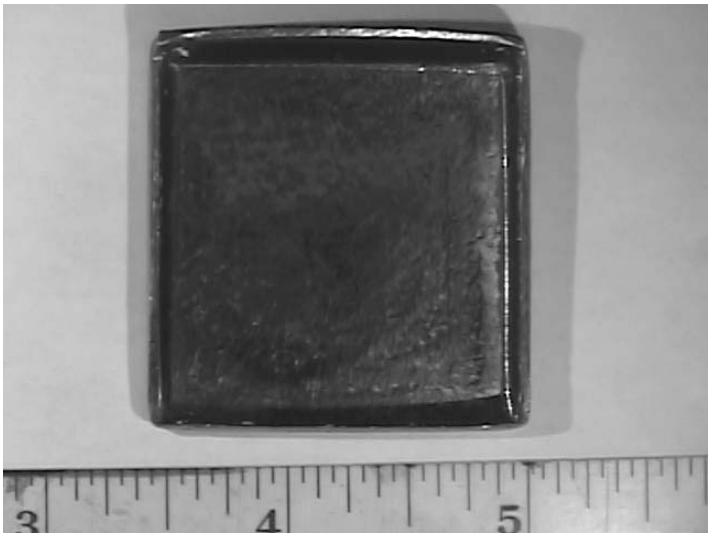

Figure 3.4 Photo image of as-forged Ti-6Al-4V piece. Thin vertical flashes (2mm thick) on the sides of the piece would be later removed before hot rolling.

Figure 3.5 The steel jacket used to protect the Ti piece during heating and retain heat during rolling. Three sides of the bag were spot welded and the fourth side was opened so that the Ti-6Al-4V piece could be easily slid in.

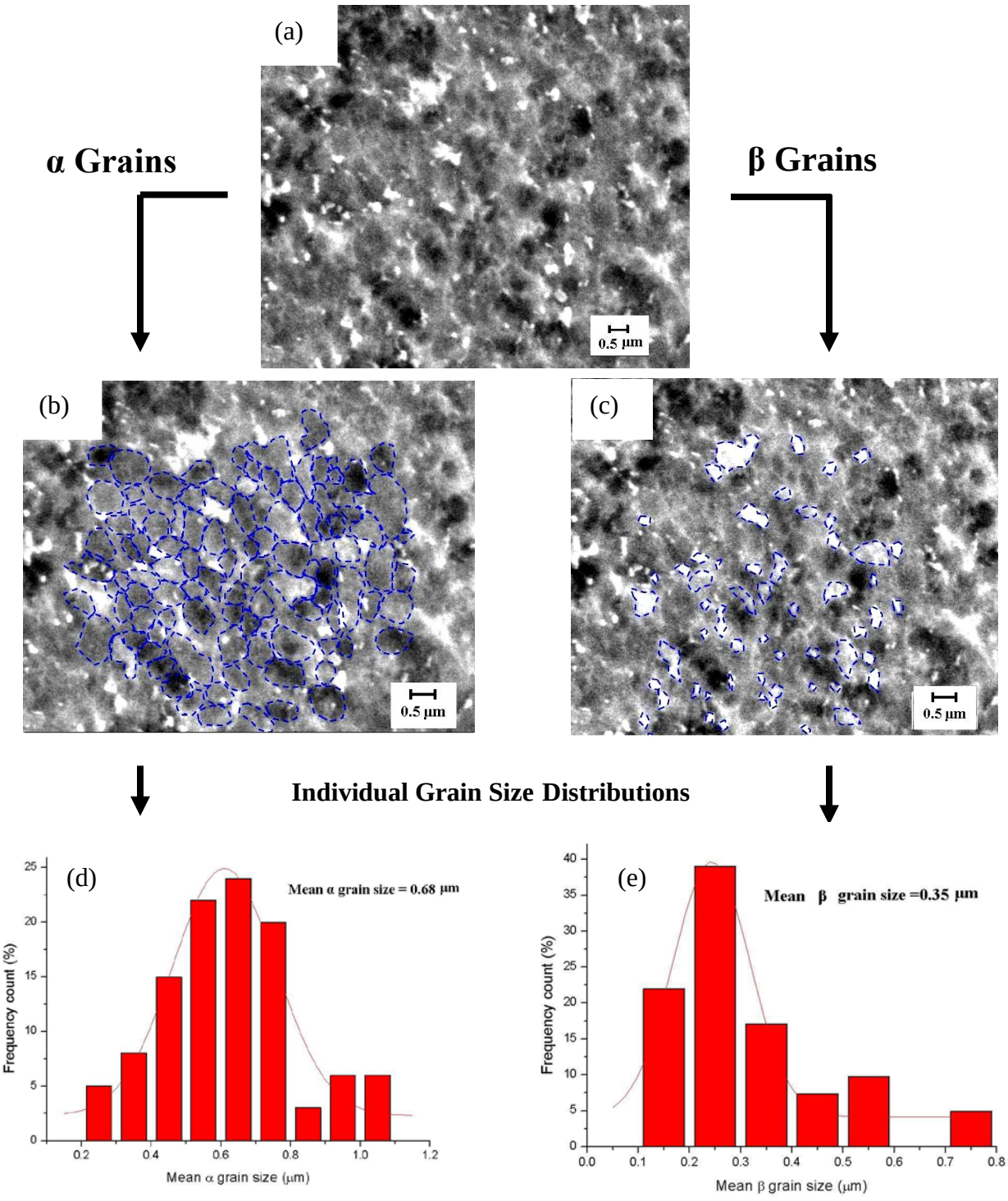

Figure 3.6 Microstructure and grain size analysis of Ti-6Al-4V alloy after forged from the angle pressing die. a) the original grain structure, b) α-grains of the structure, c) β-grains of the structure, d) α-grain size distribution, e) β-grain size distribution.

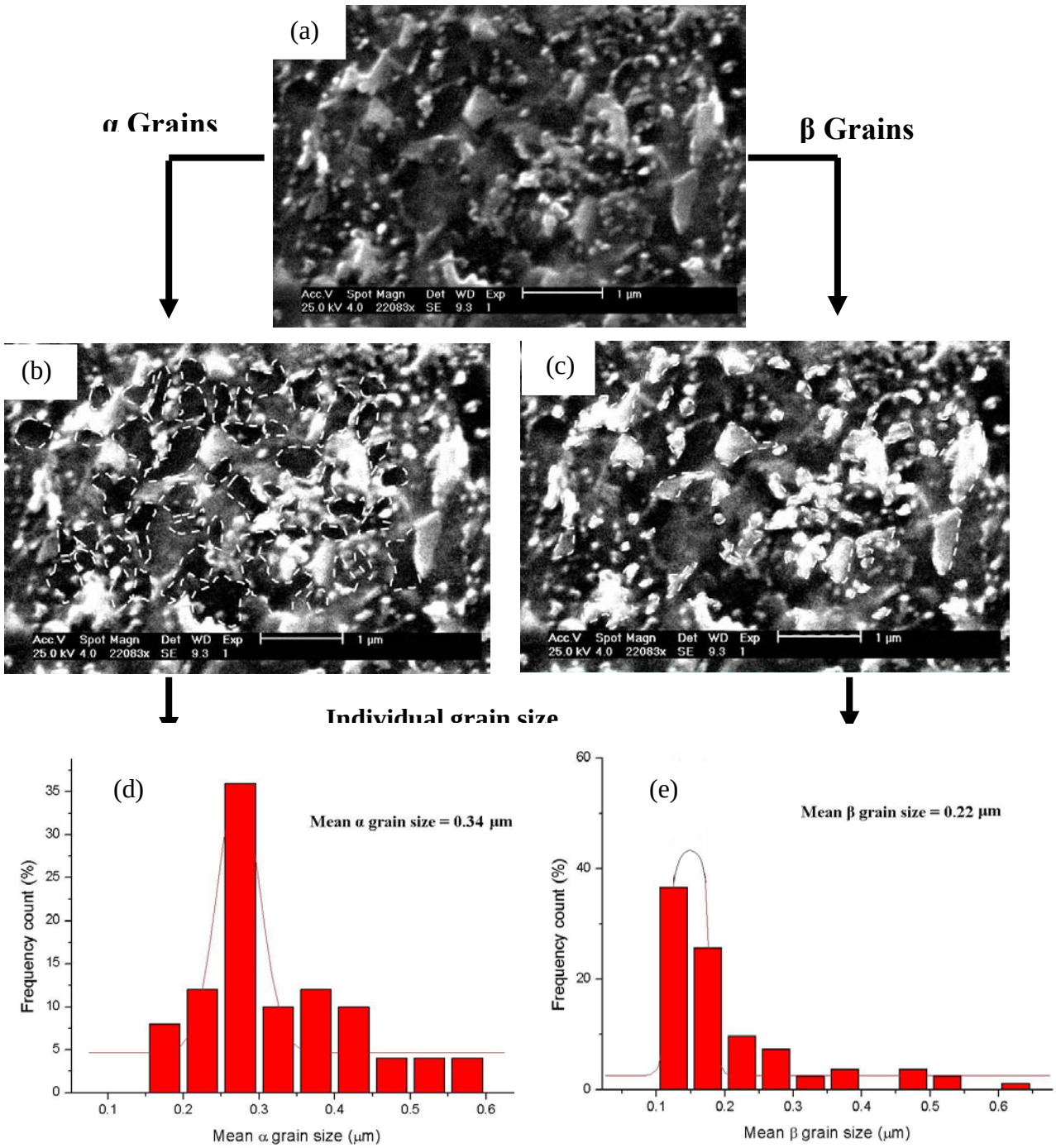

Figure 3.7 Microstructures and grain size analysis of the Ti-6Al-4V after rolled in the steel jacket. a) the original grain structure, b) α-grains of the structure, c) β-grains of the structure, d) α-grain size distribution, e) β-grain size distribution.

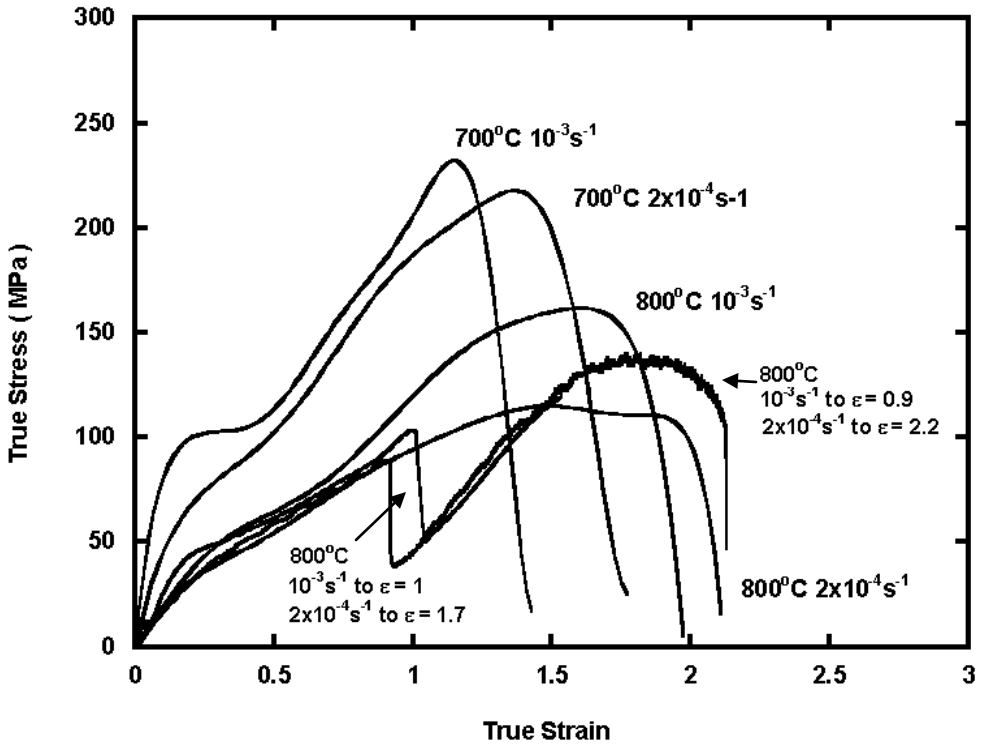

Figure 3.8 Stress-Strain curves of as processed Ti-6Al-4V. The tests were conducted at 700ºC and 800ºC with strain rates of $10^{-3}s^{-1}$ and $2x10^{-4}s^{-1}$. Two two-step strain rate tests were also conducted at 800ºC with initial strain rate of $10^{-3}s^{-1}$ pulled to strain 0.9 and 1 and lowered strain rate of $2x10^{-4}s^{-1}$ pulled to failure. Extensive strain hardening was observed in each test condition.

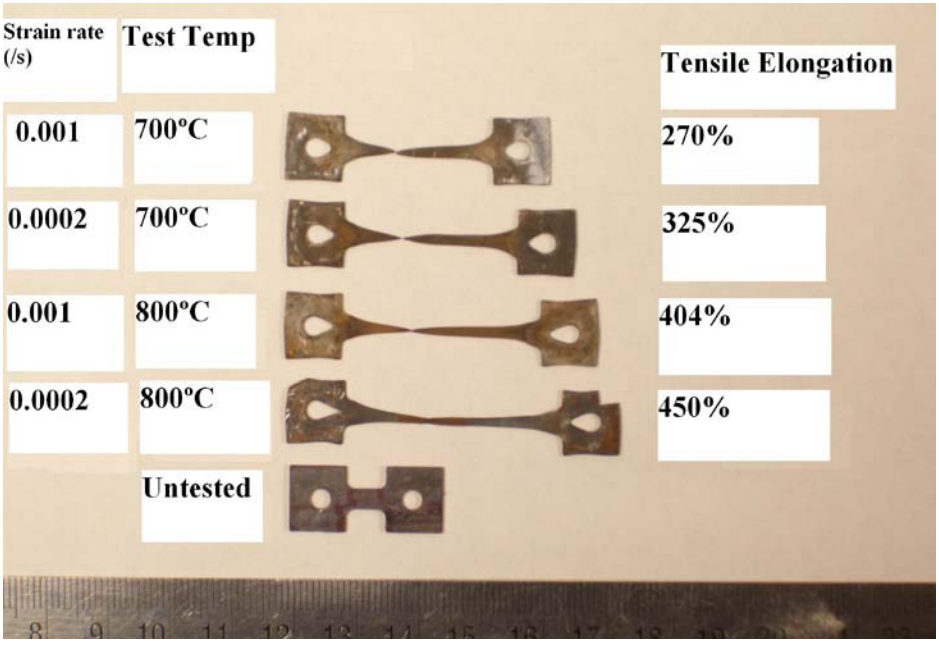

Figure 3.9 Ti-6Al-4V tensile tested samples compared with the original(untest) sample. Test conditions are tabulated on the left side and the tensile elongations are tabulated on the right side.

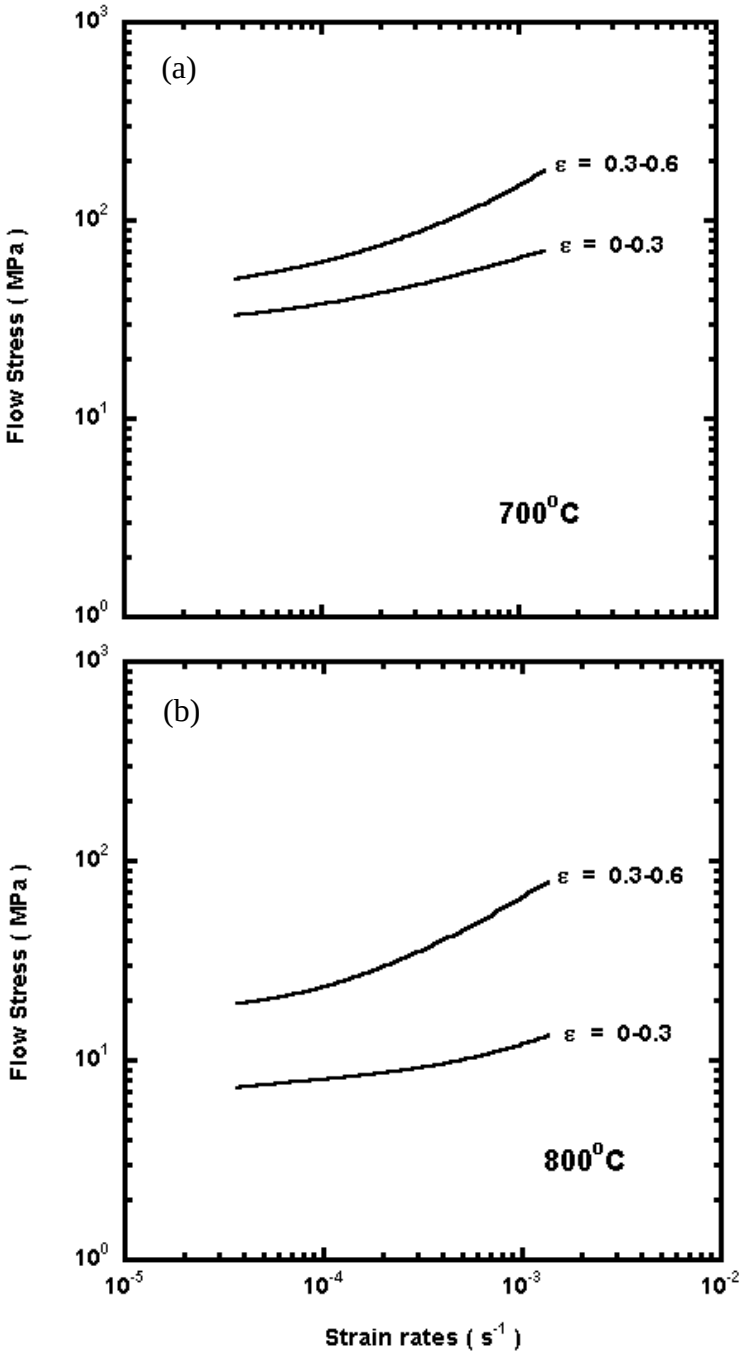

Figure 3.10 Flow stress versus strain rate curves of as processed Ti-6Al-4V at a) 700°C and b) 800°C in different strain ranges.

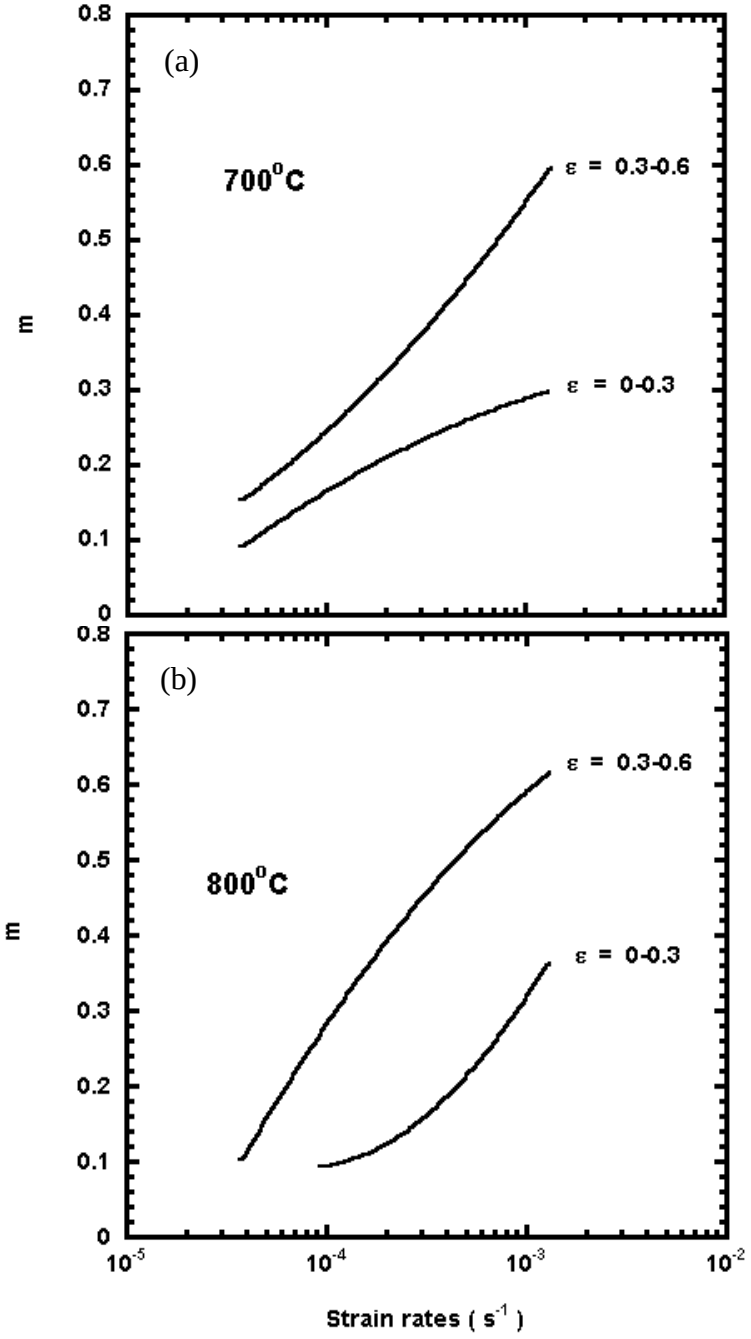

Figure 3.11 The value of m of the as-processed Ti-6Al-4V in different tensile strain rates tested at a) 700ºC and b) 800°C in different strain ranges.

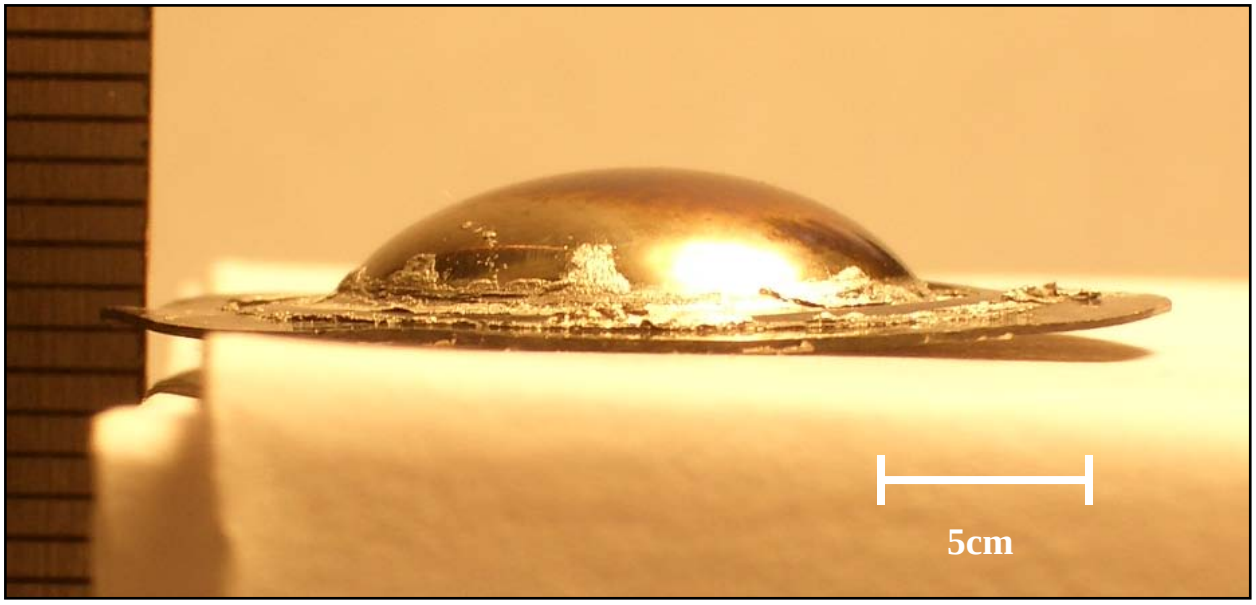

Figure 3.12 Photo of the dome formed on theTi-6Al-4V thin sheet at 700ºC. The diameter of the Ti-6Al-4V disc is 25mm and the diameter of the dome formed in the center is 13.5mm.

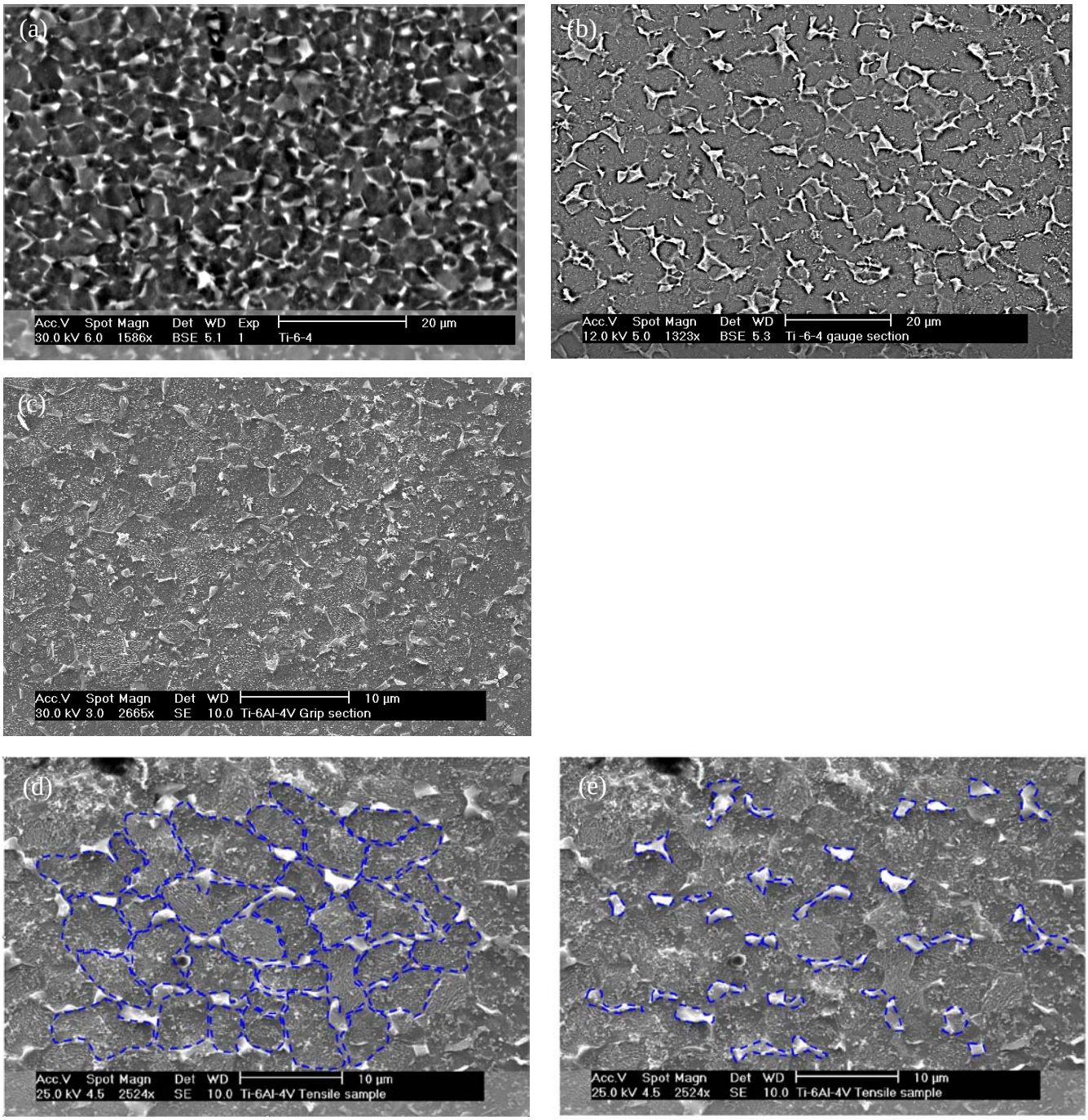

Figure 3.13 SEM images of the microstructure of the Ti-6Al-4V tensile samples. a) and c) the grip area of the samples tested at 800°C for 200 and 82 minutes, which represented the static grain growth of the material. b) the gauge section of the sample tested at 800ºC at strain rate of $2x10^{-4}s^{-1}$ for 200 minutes which shows the dynamic grain growth. d) and e) the gauge sections of the sample tested at 800°C with 2 step strain rates ($10^{-3}s^{-1}$ to $\varepsilon = 0.9$ then $2x10^{-4}s^{-1}$ to failure). The alpha and beta grains are circled by the dotted lines.

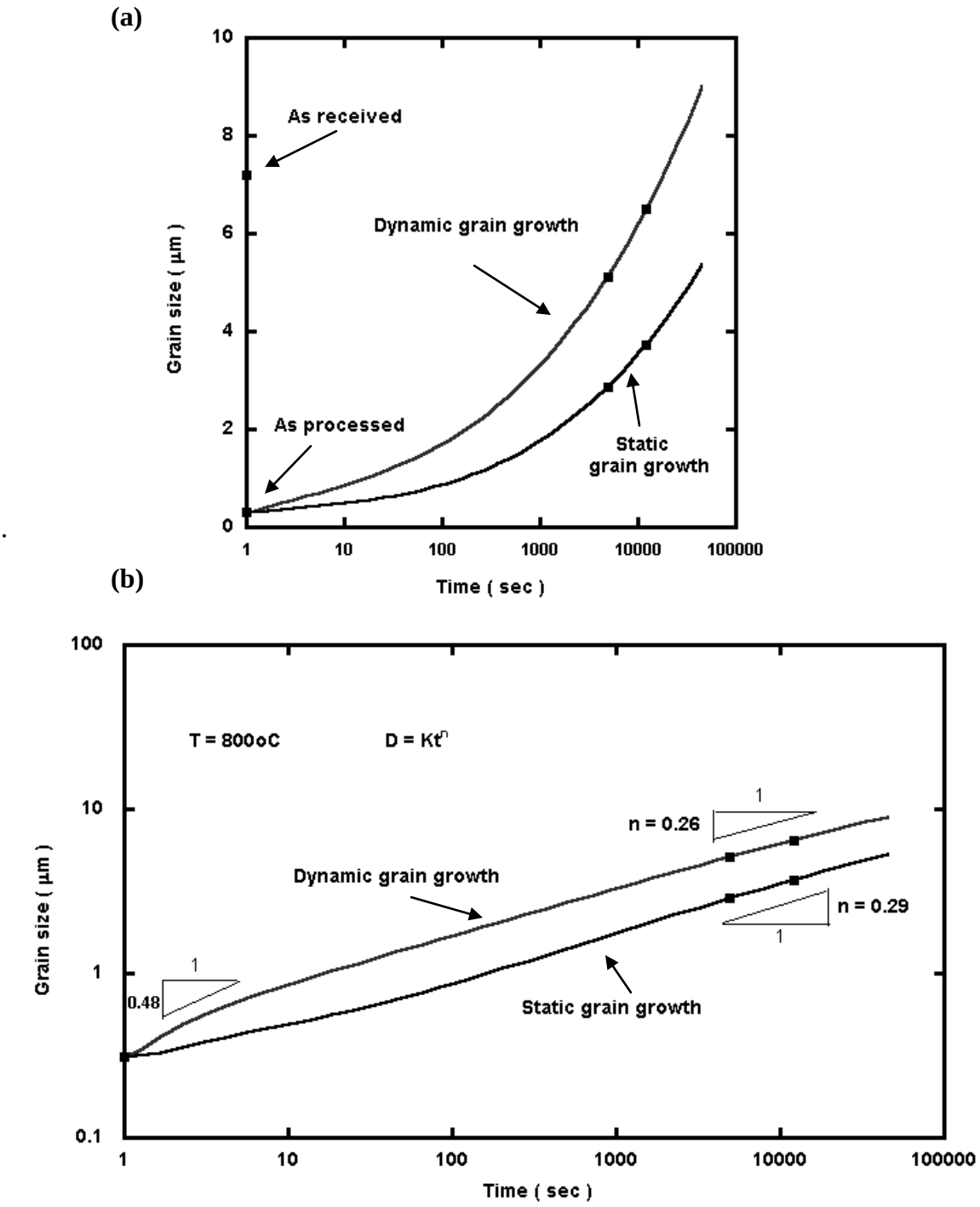

Figure 3.14 (a) Static and dynamic grain growth in the grip(static) and gauge(dynamic) sections of Ti-6Al-4V tensile sample after tested at 800ºC .The grain sizes of as-received and as-processed Ti-6Al-4V are plotted as t=0.(b) Log-log plot of the grain size versus time curves. The slopes of each growth line give the dynamic/static growth exponent (n) of the material.

References

[1] M. Petters, J. Hemptenmacher, J. Kumpfert and C. Leyens: *Advanced Engineering Materials*, v 5, n 6, Jun 1, 2003, p 419-427

[2] A. Balyanov, J. Kutnyakova, N.A Amirkhanova: *Scripta Materialia*, v 51, n 3, August, 2004, p 225-229

[3] R. Boyer, G. Welsch, and E.W. Collings: *Materials Properties Handbook*: Titanium Alloys, *ASM INTERNATIONAL*, 1994, pp. 483-636

[4] T. Seshacharyulu, S.C. Medeiros, J.T. Morgan, J.C Malas, W.G.Frazier: *Scripta Materialia* Vol 41 (1999)

[5] A. Belyakov, R. Kaibyshev: *Nanostructured Materials*, v 6, n 5-8, 1995, p 893-6

[6] Y. Iwahashi, M. Furukawa, Z. Horita, M. Nemoto, T.G. Langdon: *Metallurgical and Materials Transactions A* (Physical Metallurgy and Materials Science), v 29A, n 9, Sept. 1998, p 2245-52

[7]V.M. Segal: *Materials Science & Engineering A* (Structural Materials: Properties, Microstructure and Processing), v A197, n 2, 1 July 1995, p 157-64

[8] A. Bussiba, B. Artzy, A .Shtechman, S. Ifergan, M. Kupiec: *Materials Science and Engineering A*, v 302, n 1, Apr 15, 2001, p 56-62

[9] K. Matsubara, Y. Miyahara, Z. Horita, T.G Langdon: *Acta Materialia*, v 51, n 11, 27 June 2003, p 3073-84

[10]K. Mathis, J. Gubicza, N.H. Nam: *Journal of Alloys and Compounds*, v 394, n 1-2, May 17, 2005, p 194-199

[11]M. Mabuchi, H. Iwasaki, K. Yanase, K. Higashi: *Scripta Materialia*, v 36, n 6, Mar 15, 1997, p 681-686

[12]M. Furukawa, Z. horita, T.G. Langdon: *Materials Science Forum*, v 539-543, pt.3, 2007, p 2853-8

[13]R.S Mishra, V.V. Stolyarov, C. Echer, R.Z. Valiev, and A.K. Mukherjee: *Materials Science & Engineering A* (Structural Materials: Properties, Microstructure and Processing), v A298, n 1-2, 31 Jan. 2001, p 44-50

[14] Q. Yang, A.K. Ghosh: *Acta Materialia*, v 54, n 19, Nov. 2006, p 5147-58

[15] D. Terada, S. Inoue, N. Tsuji: *Journal of Materials Science*, v 42, n 5, March, 2007, Special Issue: Nanostructured Materials-Processing, Structures, Properties and Applications, p 1673-1681

[16] Y.U.A Vinogradov, V.V. Stolyarv, S. Hashimoto, R.Z. Valiev: *Materials Science & Engineering A* (Structural Materials: Properties, Microstructure and Processing), v A318, n 1-2, Nov. 2001, p 163-73

[17] V.V. Stolyarov, Y.T. Zhu, I.V. Alexandrov, T.C. Lowe, R.Z. Valiev: *Materials Science and Engineering A*, v 343, n 1-2, Feb 25, 2003, p 43-50

[18]C.C. Chen, J.E. Coyne: *Metallurgical Transactions A* (Physical Metallurgy and Materials Science), v 7A, n 12, Dec. 1976, p 1931-41

[19] Y.G. KO, C.S. Lee, D.H. Shin, and S.L Semiatin: *Metallurgical and Materials Transactions A* (Physical Metallurgy and Materials Science), v 37A, n 2, Feb. 2006, p 381-91

[20] A.V. Sergueeva, V.V. Stolyarov, R.Z. Valiev, and A.K Muhkerjee: *Scripta Materialia*, v 43, n 9, Oct, 2000, p 819-824

[21] A.V Sergueeva, V.V. Stolyarov. R.Z. Valiev, and A.K Mukherjee: *Mater. Sci. Eng*, 2002 Vol A323 p318-25

[22] Y.H. Wei, Q.D. Wang, Y.P. Zhu, H.T. Zhou, W.J. Ding, Y. Chino, M. Mabuchi: *Materials Science & Engineering A* (Structural Materials: Properties, Microstructure and Processing), v A360, n 1-2, 15 Nov. 2003, p 107-15

[23] A.K. Ghosh and C.H. Hamliton: *Metallurgical Transactions A* (Physical Metallurgy and Materials Science), v 10A, n 6, June 1979, p 699-706

[24] J.E. Burke, D. Turnbull, Prog: *Progress in Metal Physics*, v 3, 1952, p 220-292

[25] J.G. Byrne: *Recovery, recrystallization, and grain growth* 1965

[26] F.J. Gil, J.A. Planell: *Journal of Materials Science Letters*, v 19, n 22, Nov, 2000, p 2023-2024

[27] E. Levine, I. Greenhut and H. Margolin: *Metallurgical Transactions*, v 4, n 11, Nov, 1973, p 2519-2525

[28] G. Grewal and S.Ankem: *Metallurgical Transactions A (Physical Metallurgy and Materials Science)*, v 21a, n 6, Jun, 1990, p 1645-1654

[29] C.H. Johnson, S.K. Richter, C.H. Hamilton and J.J Hoyt: *Acta Materialia*, v 47, n 1, Dec 11, 1998, p 23-29

Chapter 4

Improved plasticity and strengthening in Ti-6Al-4V via biaxial extrusion

Abstract

A novel deformation technique, namely biaxial extrusion, is applied to the Ti-6Al-4V billet to convert the original billet form into sheet form. The deformation includes shearing and extrusion along all radial directions of the extrudate. The strain input in the work piece is variable and depends upon the ratio of radius of the billet and thickness of extrusion gap and to some extent how much material extruded. Microstructure of the extruded Ti-6Al-4V showed equiaxed fine grains with diameter ~0.7μm. Tensile tests done on the processed Ti-6Al-4V sheet showed improved yield strength (1513MPa) over conventional alloys and high ductility (724% elongation at 800ºC, $2x10^{-4}$/s).

4.1 Introduction

Several severe plastic deformation (SPD) techniques have been developed in past few decades and showed great promise to improving mechanical properties of metal materials. The idea of SPD is to impart heavy strain into materials and promotes grain subdivision thus refines the microstructure of the material. The grain boundary subdividing the grains in the process of deformation can be categorized into two types; geometrically necessary boundaries and incidental dislocation boundaries [1]. In severe plastic deformation, many geometrically necessary boundaries were created and helped refine the grains. Common SPD techniques include hot extrusion [2, 3], equal channel angular extrusion or pressing (ECAE/ECAP) [4-14], high-pressure torsion (HPT) [15, 16, 17], alternating roll-bonding (ARB) [18], and conventional rolling [19, 20, 21]. In those processes, ECAE is the most promising technique since it could repeatedly impart plastic deformation into materials without changing the original shape of the sample. However, this is also the limitation of the ECAE since it could only produce samples in billet forms. Some studies have been made in the ECA-rolling [22-24], or ECAR, which can produce samples in sheet forms and eliminates the labor-consuming reloading processes in the conventional ECAE process for ECAR's semi-continuous nature. This new technique creates an opportunity to obtain ultra-fine grained materials in sheet forms but still, could not directly transform billets into sheets. High pressure torsion usually gives very fine grains in materials down to nano-meter scale. In Sergueeva et al. study, Ti-6Al-4V samples with grain size of 200-300nm is produced via HPT process, which poses very high ductility at elevated temperature (676% elongation at 725ºC). Although the success of HPT in improving the

material property is unquestionable, owing to its high pressure necessity, HPT can only produce samples with limited sizes (< 20mm in diameter). Large samples which meet the industrial needs is still unavailable. Rolling is often used in the industry for mass production of sheet metals and can also impart heavy deformation in the material. Textures, however, are often introduced into the material from the rolling process [19, 21] and lead to anisotropy. The ARB process adapted by Daisuke et al. [18] can eliminate the texture build-up and property anisotropy from the conventional rolling process. The processed C.P Ti has very fine grained microstructure (~100nm) with high yield strength (~900 MPa). Nevertheless, the process requires many steps and is very time-consuming.

The authors recently developed a novel SPD process, namely Biaxial Extrusion [25], which can overcome the limitations faced by the conventional SPD techniques mentioned above. With the biaxial extrusion route adapted in this new technique, work piece in sheet form could be produced from billets/rods in a single extrusion process with very high strain input and extensive grain refinement. The shear strain experienced from the process is no less than 5 in one extrusion and the extrusion direction is biaxial, which means the shear is in 360º. In other words, the strain input in one biaxial extrusion would equal to strain input in 5~10 runs of ECAE in route B and route C. A two-pieces circular die set is used in the extrusion process. As shown in Fig 4.1a, Two 5 inch diameter H-13 steel round blocks (upper block, 5 inch diameter x 3.5 inch tall and lower block, 5 inch diameter x 1.5 inch tall) were clamped together by six high strength steel bolts with a thin gap kept in between blocks to allow the work piece to flow. The thickness of the gap is controlled by the thickness of the washers put on the steel bolts and could be varied to

adjust the thickness of the sheets to be formed. In the extrusion, work piece is put at the bottom of the hole in the upper block and load is gradually applied to the work piece through several one-inch diameter punches. In the loading process, work piece would flow into the gap in 360º directions and forms a round disk/sheet with the thickness of the gap. To keep the edge of the work piece from cracking, a sacrificial washer is required to constrain the work piece in order to provide hydrostatic compression force during the extrusion process. This washer is very ductile and softer than the work piece so it can expand to a greater extent and still provide enough hydrostatic compression to the work piece. Fig 4.1b. shows the top view of the lower block of the biaxial extrusion die. The work piece sits in the one inch circle in the center and flows to 360º directions upon extrusion. Six shaded round circles represent where the bolts sit and these bolts would constrain the flow of the work piece. The limit of the flowing path of the work piece in the current die design is 3.5 inch (distance between the two pairing bolts). Further expansion of the work piece is blocked by the surrounding bolts; this limitation can be improved if larger die is used. The unique biaxial extrusion route could promote the activations of various slip planes parallel to the extrusion directions in 360 degrees. These slip planes were activated when work piece exited from the center hole and slips in different directions would intersect each other, as illustrated in the schematic in Fig 4.2. The multi-slips planes activated from the biaxial extrusion are different from the ECAE process where only one pair of slip planes are activated from each extrusion process (details shown in Appendix 4A). These biaxial slip motions help promote uniform strain distribution and lead to finer equiaxed grain structure.

4.1.1 Numerical calculation of deformation strain in biaxial extrusion

Samples experience both shear and expansion strains in biaxial extrusion process. The shear strain can be calculated by analyzing the strain of a single element of the work piece shown in the schematic in Fig 4.3. Element given by abcd represents the sample before extrusion. Element given by aefb represents the sample after extrusion. Notice line gb and bi are perpendicular to lines dc , ab and ef. r =the radius of the sample and t = thickness of the gap. The shear strain experienced by the sample is given by $\gamma = dc/gb$, where $dc = r\sec\theta$ and $gb = r\sin\theta$. Therefore, the shear strain is:

$$\gamma = 1/\sin\theta\cos\theta \tag{1}$$

Where $\theta = \tan^{-1} t / r$.

Consider the von Mises effective strain, the strain from the extrusion is:

$$\varepsilon_1 = 1/\sqrt{3}\ \sin\theta\cos\theta \tag{2}$$

The strain from the expansion can be simply determined by the radius difference of the sample in two directions.

$$\varepsilon_2 = 2\ln(r / r_o) \tag{3}$$

where r = final radius of the extruded disk, r_o = original radius of the sample

Assume Δh of the original sample has been pressed down, a corresponding disk with equal amount of volume should be extruded out:

$$\Delta h \pi r_0^2 = \pi r^2 t \tag{4}$$

So

$$\frac{r}{r_0} = \sqrt{\frac{\Delta h}{t}} \tag{5}$$

Plug equation (5) into equation (3) then we have

$$\varepsilon_2 = \ln (\Delta h / t) \quad (6)$$

The total strain experienced in one extrusion run is simply the summary of ε_1 and ε_2

$$\varepsilon_{total} = \varepsilon_{1} + \varepsilon_2 = 1/ \sqrt{3} \ \sin\theta\cos\theta + \ln (\Delta h / t) \quad (7)$$

Plots of $\varepsilon_{1,}$ ε_2 and ε_{total} with different r, t and h values are shown in Fig 4.4. It is clear that with higher r / t ratio, higher shear strain could be obtained (Fig 4.4 (a)). The strain from expansion ε_2 is plotted in Fig 4.4(b) with different sample height and gap thickness. It appears that strain increases with the sample height but decreases with larger gap. Though the ε_{total} is combined with ε_1 and $\varepsilon_{2,}$ the final strain is mostly contributed from ε_1 since its value is much greater than $\varepsilon_{2.}$ In the current study, the gap is kept at 0.04 inch and the radius of the sample is 0.5 inch. For the sample with original height of 0.5 inch, the overall strain input is 9, based on the plot (Fig 4.4(c)). Fig 4.4(d) shows the final strains of the extruded disks with different initial sample radius.

The strain input in work piece in ECAE is about 1.15 per pass and is relatively lower than the strain input in the biaxial extrusion. Detailed strain calculation of ECAE is tabulated in Appendix 4A.

Titanium is favored in a large variety of applications from aerospace to sports wares for its high specific strength and good corrosion resistance. However, like other HCP metals, titanium lacks ductility at room temperature and most of the Titanium products are formed by casting and mechanical machining. In order to enhance the formability and strength of Titanium, extensive studies [4-24] have been made to introduce severe plastic deformation into Titanium alloys which lead to fine grained structure and enhanced

ductility or even superplasticity in elevated temperature. Many techniques were used to impart SPD into raw titanium alloys; among those, ECAE [4-14] is the most common and successful technique for its design simplicity and experimental repeatability. Other severe deformation techniques includes high pressure torsion [15-17], isothermo compression [18] and rolling [19]. In this study, we tried to apply SPD into Ti-6Al-4V via biaxial extrusion process since up to date, no SPD process has been made to directly transform billet Ti-6Al-4V into sheet form. The reason Ti-6Al-4V was chosen here is that it is the most common Ti alloys used in the titanium industry and it can acquire large varieties of microstructures with different α morphologies, depending on thermal-mechanical treatments. Also, the fine plate-like α phase in β heat treatment Ti-6Al-4V helps break up the coarse grains into fine equiaxed grains during the elevated temperature SPD process. Metallographic analysis has been done on the raw and extruded Ti-6Al-4V to understand the microstructure evolution. Room temperature tensile tests were also done on the processed Ti-6Al-4V to obtain mechanical properties.

4.2 Experiment.

A 0.75 inch diameter x 0.65 inch tall Ti-6Al-4V rod was used in this study. The Ti-rod was first heat treated to 1050ºC for 1 hour and water quenched. After heat treatment, the Ti-rod was put into a 0.125 inch thick soft steel tube with height same as the Ti-rod and with 1 inch out side diameter as shown in Fig 4.5. Two washers were attached to the bottom of the tube to provide hydrostatic pressure during the extrusion; one steel washer with 1.5 inch inner diameter and 2 inch outer diameter and one aluminum washer with 2.5 inch inner diameter and 3 inch outer diameter, both washers have the same thickness

of 0.1 inch. The extrusion was done at 500ºC with very high load (~330,000lbs). One problem commonly faced by the extrusion processes is the friction between work piece and the inner wall of the die. Large friction force may result in local shearing which favors the goal, however, in the processing of high strength materials such as Ti-6Al-4V, too much load on the punches and dies may cause unwanted deformations. To avoid the friction problem, proper lubrication is needed. To allow the lubricant to flow into the die and separate the sample and punches from the die, a 0.003 inch gap is created in between the sample, punches and the die. Fig 4.6 shows how the Ti-6Al-4V work piece and punches were assembled in the die. Due to the nature of high temperature processing environment, PVA and boron nitride powder mixture was used for lubricant.
After biaxial extrusion, a two inch diameter x 0.11 inch thick Ti-6Al-4V round disk was obtained as shown in Fig 4.7. The cumulated strain of the extruded Ti-6Al-4V disk is 4.13.

4.3 Microstructure evolution

Metallographic pictures were taken from the as heat treated and as extruded Ti work piece. The samples were first mounted in the Kold mount self curing resin and ground with sand paper to grit 4000. A 0.3 μm colloidal silica was used for polishing.
Titanium is categorized in three classes due to its unique dual phase composition; alpha alloys, alpha-beta alloys and beta alloys. Alpha alloy have mostly alpha phase with little or no beta grains. Alpha-beta alloys have both alpha and beta phases in the alloy with different volume fractions, the volume of alpha and beta phases could be controlled by heat treatment or alloy additions. Beta alloys have mostly beta phase retained from the

solution treatment. The phase compositions or the classes of the alloys heavily depend on the element additions to the alloy. Elements like Zr, niobium, and iron are known as beta stabilizers. Addition of these elements to the titanium lowers the alpha-beta transformation temperatures and thus, more beta phase could be retained. Elements like Aluminum, Sn are well known alpha stabilizers and could raise the alpha-beta transformation temperatures and lead to higher alpha content in the resulting alloy. Ti-6Al-4V contains 6 wt% aluminum and 4 wt% Zr, which are alphas and beta stabilizers, and make Ti-6Al-4V an alpha-beta alloy with mixed alpha and beta phases in the matrix. The microstructure manipulation of Ti alloys mainly depends on the beta → alpha transformation while cooling from the alpha-beta transformation temperature. Many different phases take various forms in metallography and also effect the alloy properties. For examples, equiaxed morphologies would have the advantage in ductility and formability. Acicular morphologies have the advantage in fracture-toughness and stress-corrosion resistance [27]. Fig 4.8a shows the microstructure of Ti-6Al-4V after β treated at 1100ºC for 1 hour. The heat treated Ti-6Al-4V showed a famous widmenstätten structure with transformed β phase (acicular α). The thin plate-like ά are well distributed inside the large β grain. These dual phase structure is beneficial for the further thermal mechanical processing since the plate-like ά phase is already very thin and would help break down the large β grains. The transformation mechanism from widmenstätten structure into fine equiaxed α+β structure can be categorized into two types as suggested by Ding et al. [26]. The first mechanism involves the formation of both low and high angle grain boundaries across α plate and followed by the penetration of β phase along the sub-boundaries. The second mechanism is associated with the localized shearing and

rotation in the α plates and β phase would penetrate along the shearing band in the α plates and break them into smaller segments. Fig 4.8b shows the break downs of original α plates and the protrusion of β phase into α dendrites. In higher strain level, most of the α phase arms have been turned into rounded segments as shown in Fig 4.8c. Long acicular α were sheared into small segments and would later on turned into fine equiaxed grains. With highly imposed strain and continuous breaking up of α plates and β grains during the extrusion process, very fine equiaxed α+β phase could be obtained as shown in the SEM image in Fig 4.8d.The average grain size of the biaxial processed Ti-6Al-4V is ~0.7μm.

In the TEM image, as shown in Fig 4.9, many individual grains show high angle grain boundaries as circled by dotted lines. The grain fragments shown in the figure are no more than 200-300nm. The circled α grains are believed to be the segments of the original α plates broken up by the surrounding β grains and have distinct orientations and sharp boundaries. The surrounding β grains have a high dislocation density, which indicates that more severe deformations have been imparted in the β grains during the segmentation of the α phase. The higher dislocations density in the β grains suggested that more deformation strain have been accommodated by the softer β phases than α phases [25] or more slip systems are readily activated in BCC β phase than HCP α phases. The volume fraction of β phase content calculated from the TEM images is ~21 vol%.

4.4 Mechanical test

Room temperature tensile samples with 3mm wide x 12.7mm long gauge section were machined from the as-extruded Ti-6Al-4V work piece. The tensile samples were ground and polished before testing to eliminate any defects on the gauge section. Instron 450 machine was used for the tensile test with constant strain rate of 0.5 mm/minute. Strain was directly measured from the gauge section of the sample with the 0.5 inch extensile meter. The test result is tabulated in Fig 4.10. It can be clearly seen that the work piece after biaxial extrusion has much higher yield strength (1513MPa) than the commercial grade Ti-6Al-4V. The elongation of the extruded work piece is however, little less than the commercial grade Ti-6Al-4V. The increase in strength is most likely attributed to the grain refinement during the extrusion process.

High temperature tensile tests were conducted at 800ºC and 700ºC with constant strain rate equals $2x10^{-4}$/s. The samples were machined from the extruded Ti-6Al-4V disk with gauge width=3mm and gauge length=6.35mm (0.25 inch shoulder to shoulder distance). Tests were done with the Instron 4505 test machine with a clamshell 3-Zone heating furnace. Temperature variation of the tests was controlled within ± 3ºC. Boron Nitride was coated on the samples before tests to avoid contact with air. Surfaces of the samples were polished to remove damages from machining. Fig 4.11 shows the stress-strain curves of the tests. Low flow stress was found in the sample tested at 800ºC with maximum flow stress less than 15 MPa. The sample tested at 700ºC has much higher flow stress, up to 150 MPa and showed strong strain hardening before the flow stress reached its peak. Superplasticity were found in both samples tested at 800ºC and 700ºC

with 724% and 425% elongation, respectively as shown in Fig 4.12. Both samples showed diffusion necking with no sign of brittle fracture.

The high ductility of extruded Ti-6Al-4V can be attributed to its high m value determined by the decrement strain rate test with starting strain rate $10^{-3}s^{-1}$ and lowest strain rate $5x10^{-5}s^{-1}$. The following equation is used to calculate m values.

$$m = d\log(\sigma)/d\log(\dot{\varepsilon}) \quad (5)$$

The decrement strain rate test results are tabulated in Fig 4.13. Highest m value is measured at strain rate $\sim 10^{-4}s^{-1}$ where m = 0.42. The high m value in low strain rate region corresponds to high elongation (724%) in sample tested at strain rate $2x10^{-4}s^{-1}$.

4.5 Conclusion

Biaxial extrusion was successfully demonstrated on the Ti-6Al-4V work piece. The extrusion temperature was relatively low (500ºC) and the one step processing prevented Ti-6Al-4V work piece from heavy surface oxidation, which is usually encountered by the repetitive processing at high temperature. The microstructure of the extruded work piece showed equiaxed $\alpha + \beta$ phase with average grain size less than 1μm. The fine-grained structure of the biaxial extruded Ti-6Al-4V work piece is similar to the Ti-6Al-4V work piece processed by 4-8 passes by ECAE [10,14] (route B). Processed Ti-6Al-4V with fine grain size less than 1 μm usually exhibit improved strength and good ductility. The Ti-6Al-4V disk processed by Sergueeva [17] with HPT has fine grain structure with 100-200 nm grain fragments. The highest elongation reached 676% at 725ºC with test strain rate equals 10^{-3}/s. Ti-6Al-4V work piece processed by multi-stage forging by Patankar [28]

has grain size 0.3μm-0.8μm and exhibits high yield strength (1190MPa) and high Ultimate strength (1238MPa). An elongation of 474% was obtained on Ti-6Al-4V work piece processed by Ko et al. [7] after ECAE. The grain size of was refined to 0.3μm. Compared to the Ti-6Al-4V work pieces processed in different techniques listed above, the Ti-6Al-4V processed by the biaxial extrusion has higher yield strength exceeding 1513 MPa. Also, the elongation of biaxial extrusion processed Ti-6Al-4V have higher ductility (724%). The mechanical properties of biaxial extrusion processed Ti-6Al-4V demonstrated that this new processing technique is an efficient SPD method with good potential for metal processing technology.

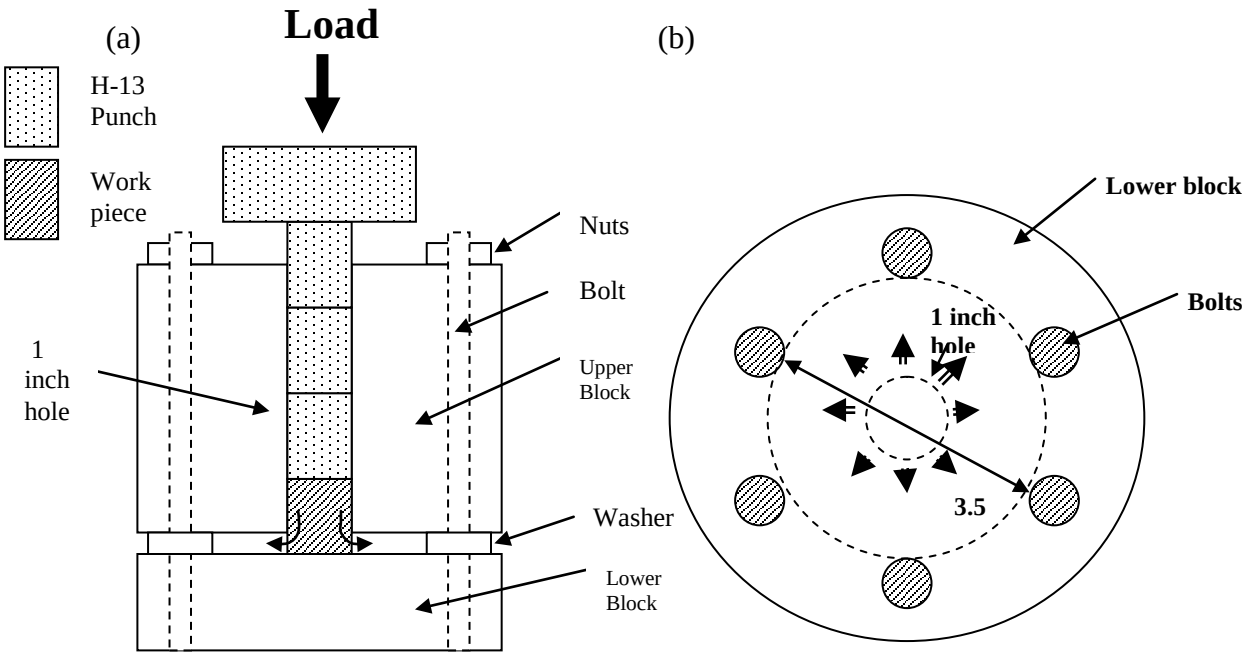

Figure 4.1 Schematic of (a) biaxial extrusion process and (b) cross section of the lower block. upper block is clamped with the lower block by the bolts and the gap in between is controlled by the thickness of the washers. The load is applied to the punches and the punches press on the work piece. Upon yielding, the work piece would flow from the center hole to the gap between the upper piece and the lower piece and form a circular disk. The black arrows in (b) indicated the flow directions of the work piece upon extrusion. The free flowing distance is 3.5 inch from the edges of two pairing bolts. The optimal size of the sample is 3.5 inch in diameter.

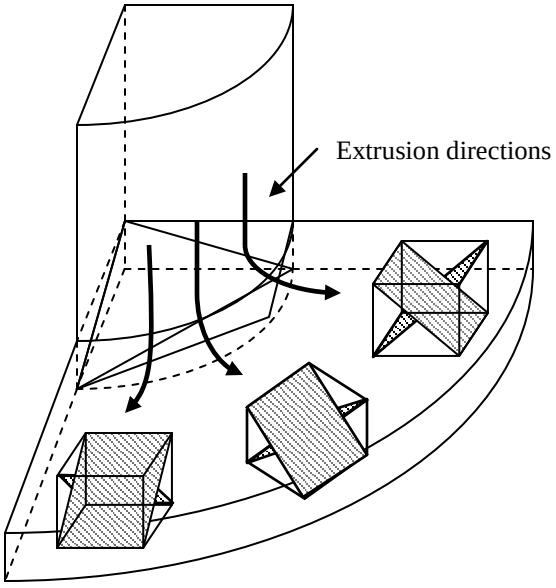

Figure 4.2 Schematic diagram of the work piece extruded from the biaxial extrusion die. Different shearing planes were activated and intersect each other along the extrusion process.

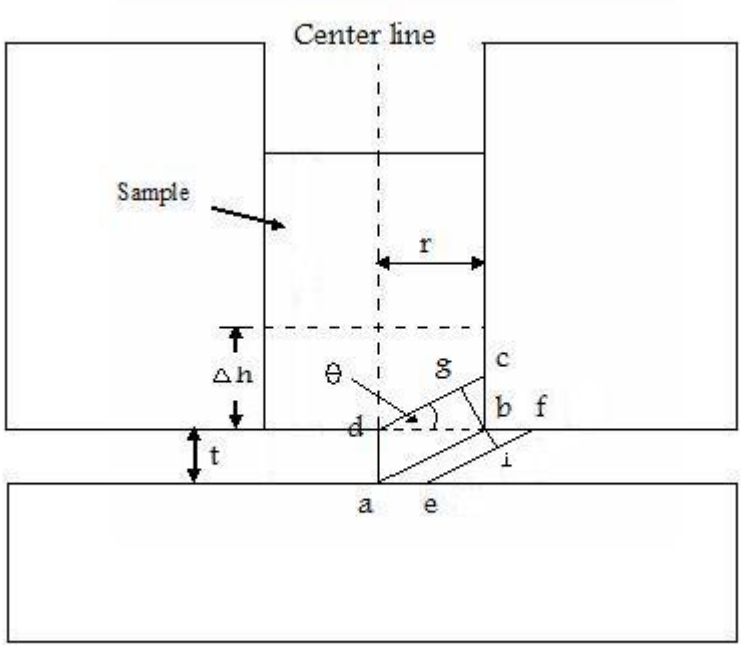

Figure 4.3 Schematic of the shear strain input of the biaxial extrusion die.

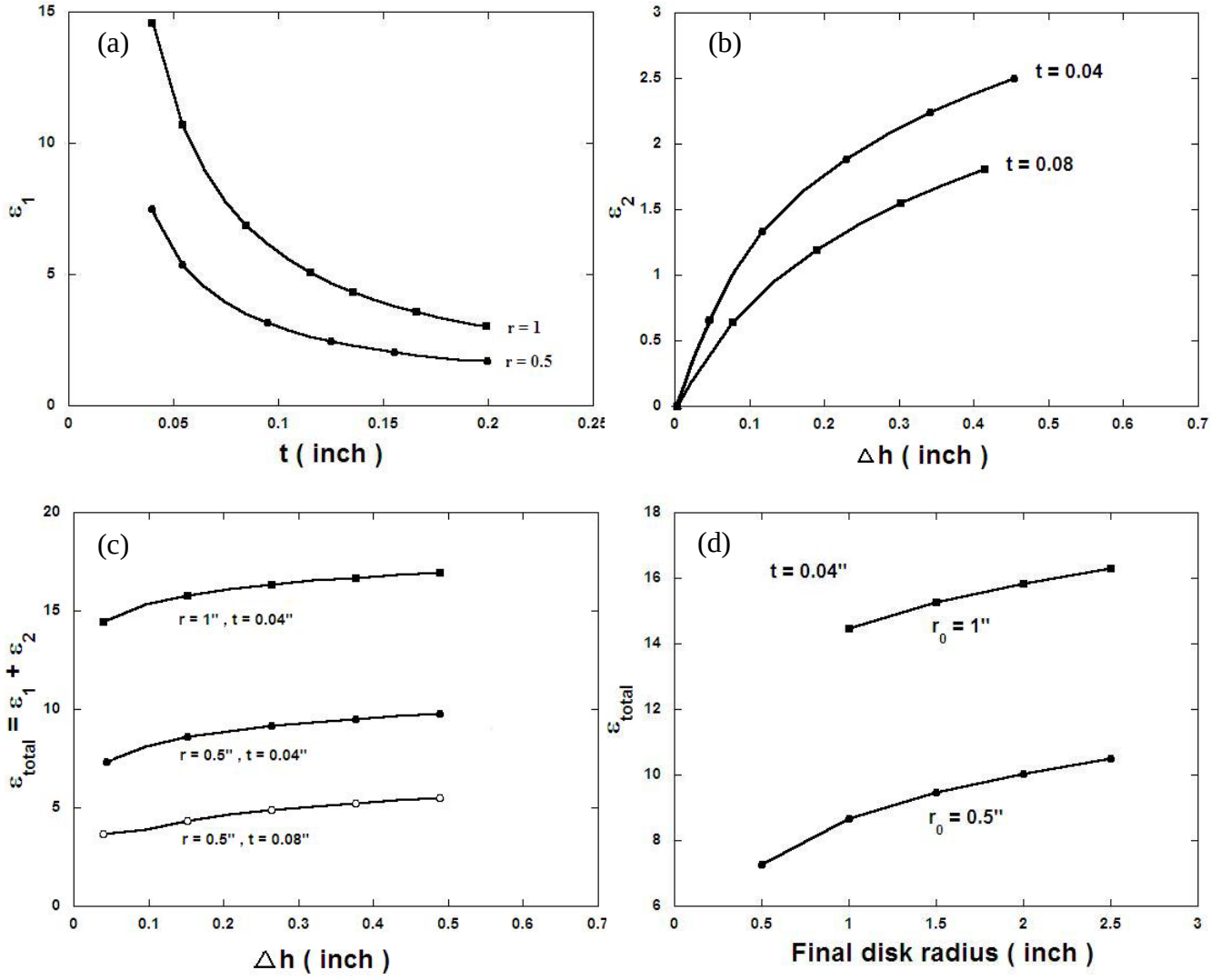

Figure 4.4 (a) Strain ε_1 (equation 2) applied to the extruded sample with different r (hole radius) and t (gap thickness) values. (b) Strain from extruded sample expansion ε_2 (equation 6) with different Δh (change in sample height) and t values. (c) Total strain input to the sample ε_{total} (equation 7).

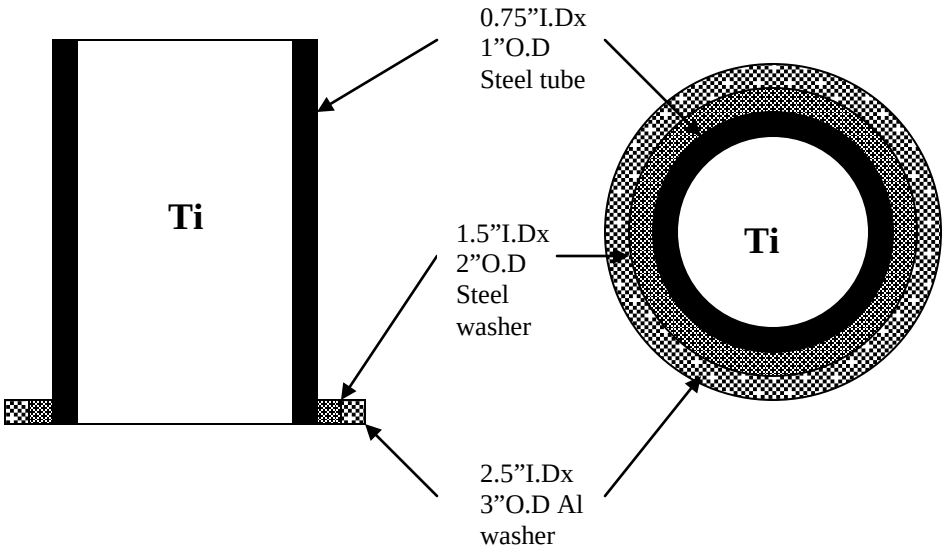

Figure 4.5 Schematics arrangement of the Ti work piece. A 0.75 inch I.D x 0.65 inch tall cylindrical Ti was encapsulated inside a 0.125 inch thick steel tube. Two pieces of 0.1 inch thick steel and Al washers were attached to the bottom of the tube to provide circumferential constraint to the Ti work piece and prevent the edge cracking.

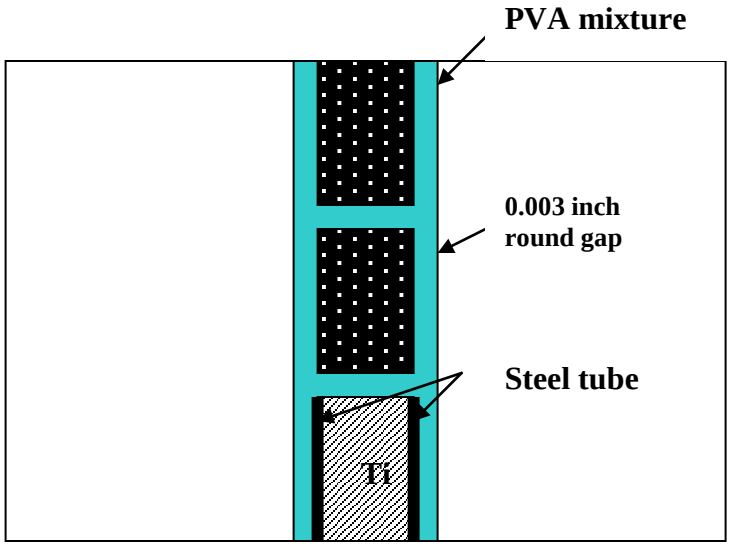

Figure 4.6 Schematic illustration of the arrangement of Ti-6Al-4V work piece in the biaxial extrusion die. The diameter of the punches and the work piece is reduced 0.003 inch to create a gap between them and the inner wall of the die such that PVA mixture could be filled in. The PVA-BN mixture works as lubricant during the extrusion process.

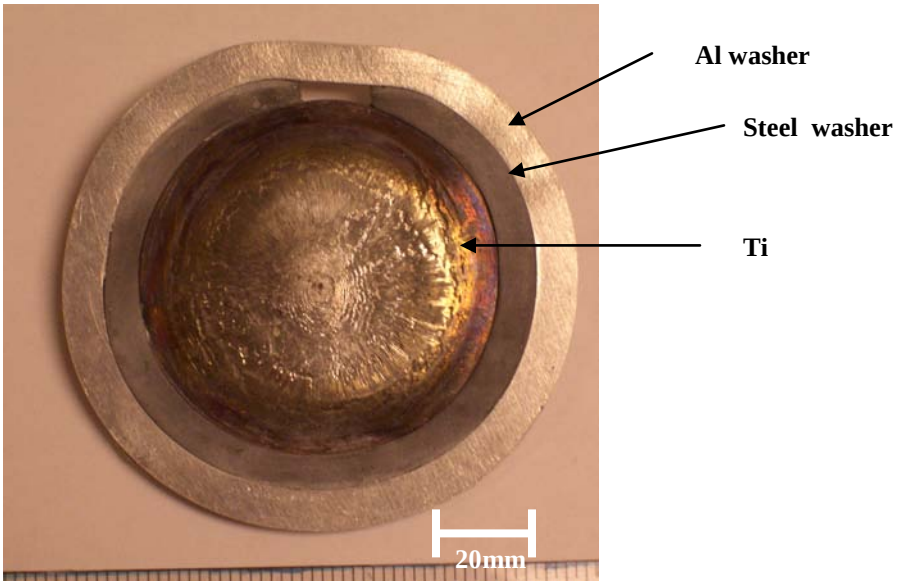

Figure 4.7 Photo image of Ti-6Al-4V piece after biaxial extrusion. An approximate 2 inch diameter Ti flat disk with thickness of 0.11 inch is clamped inside the steel and Al washers. Both steel and Al washers were stretched out by the extruded Ti. Steel washer failed at a certain point during the extrusion process while the Al washer held the most of the compression stress to the Ti-6Al-4V piece till the end of the run.

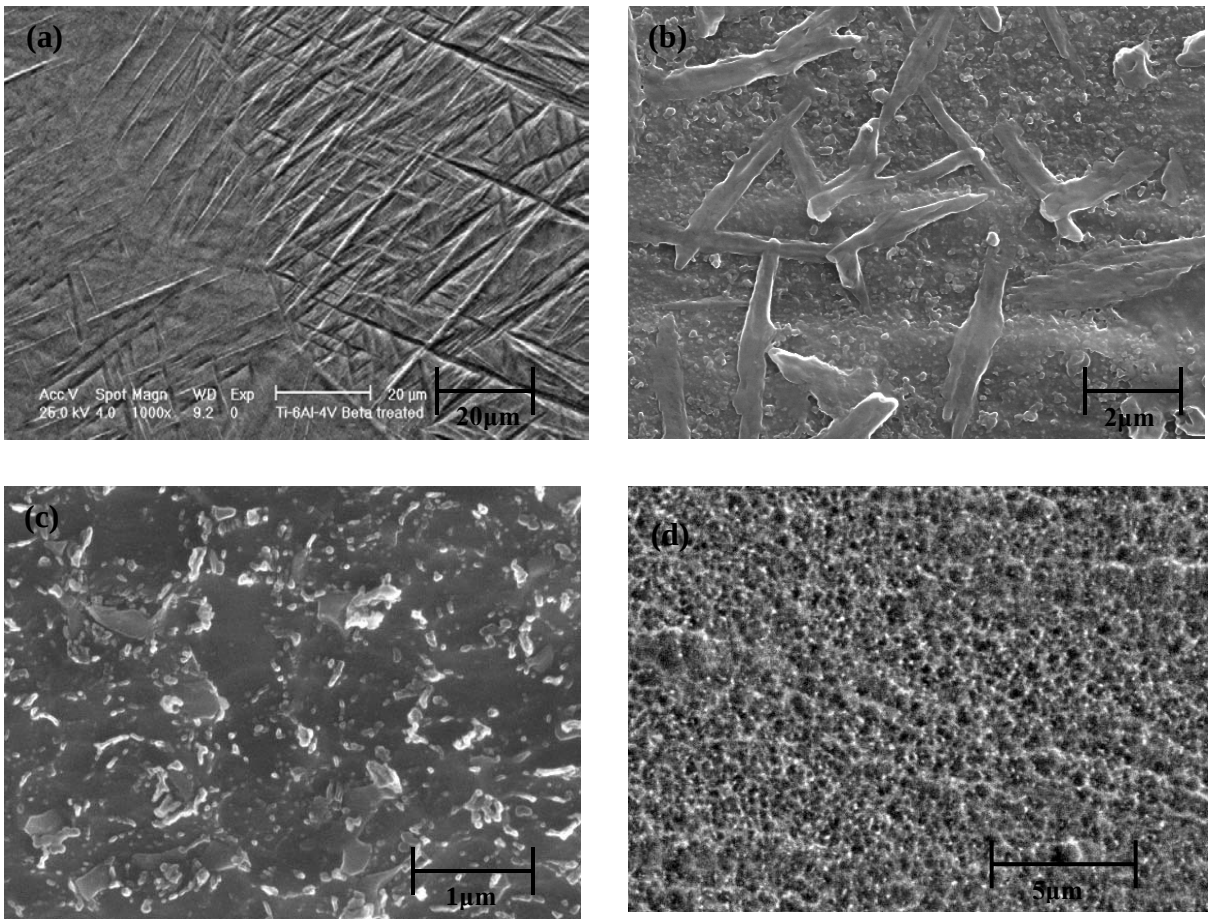

Figure 4.8 (a) SEM image of the heat treated Ti-6Al-4V. Widmenstätten structure with transformed β (acicular α) are shown in the matrix. (b) SEM image of processed Ti-6Al-4V shows the original acicular α started to break up.(c) Further thermo-mechanical deformation broke α dendrites into small round segments (d) SEM image of the extruded Ti-6Al-4V. The longitudinal strain is 2.7. A uniformly dispersed β and α grain are shown in the matrix. The average grain size is 0.7 µm.

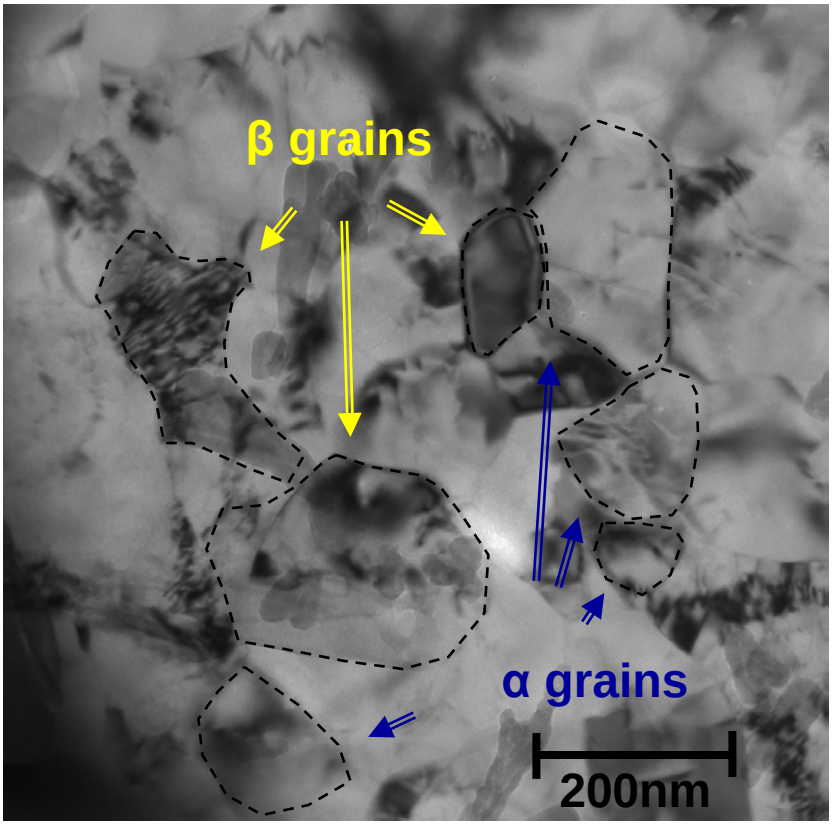

Figure 4.9 TEM image of extruded Ti-6Al-4V work piece. The β grains have higher dislocation intensity which indicates that higher deformation is attained in the softer β grains. Both α and β grains appear to be exuiaxed and uniformly distributed. The β grains occupied 75.2 % volume of the matrix. The TEM image only shows partial grains corresponding to its diffraction angle.

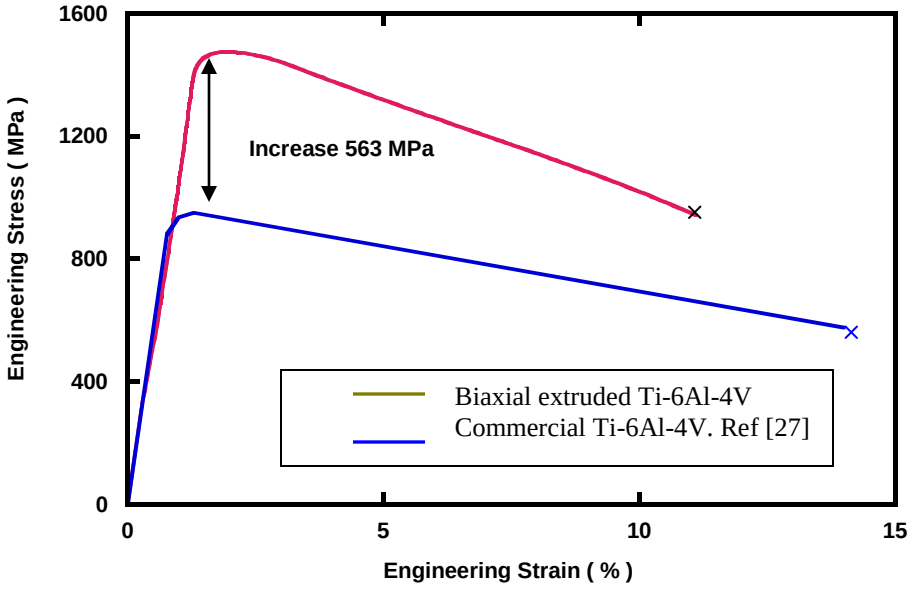

Figure 4.10 Room temperature tensile properties of commercial Ti-6Al-4V and Biaxial extruded Ti-6Al-4V. The yield strength of extruded Ti-6Al-4V increased 563 MPa than the commercial Ti-6Al-4V but has less ductility (strain = 12%).

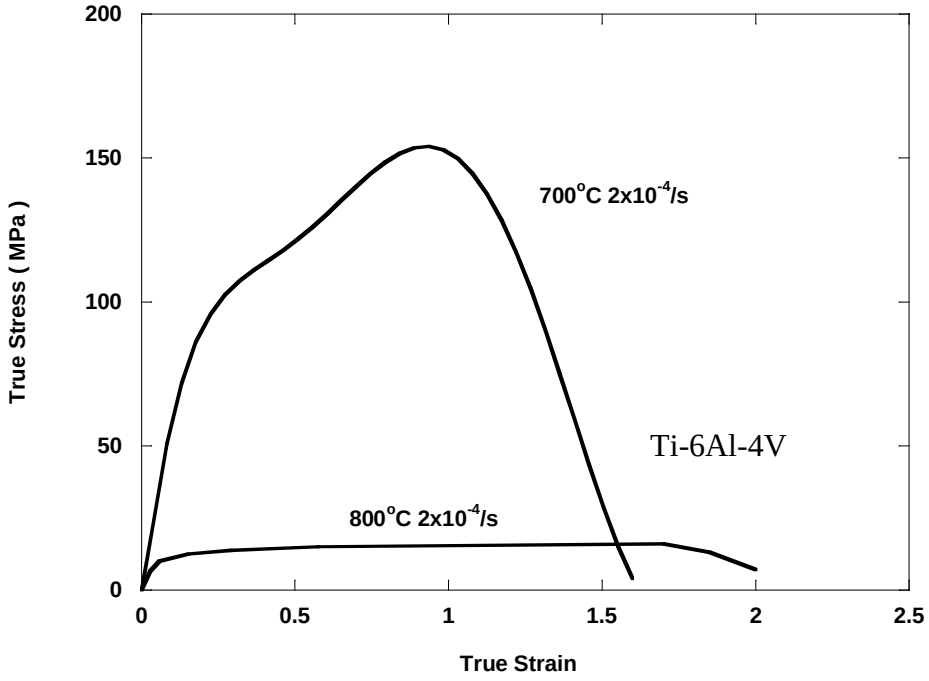

Figure 4.11 High temperature tensile tests on Ti-6Al-4V with strain rate equals $2x10^{-4}$/s. The flow stress of the sample tested at 800ºC is very low (<15MPa) compared to the 700ºC tested sample.

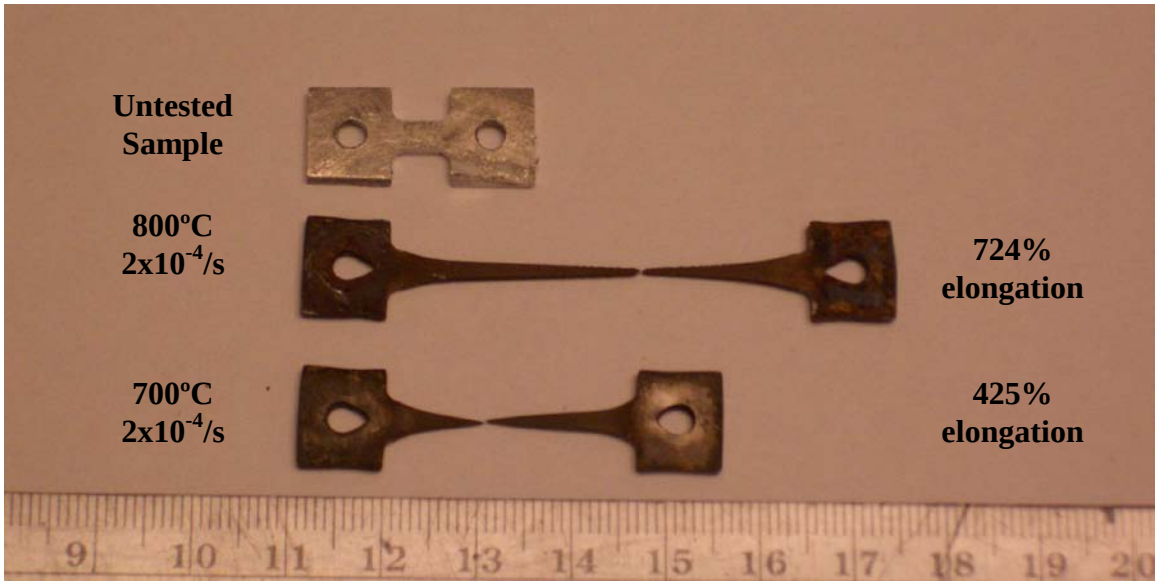

Figure 4.12 Photo image of the high temperature tensile tested Ti-6Al-4V samples.

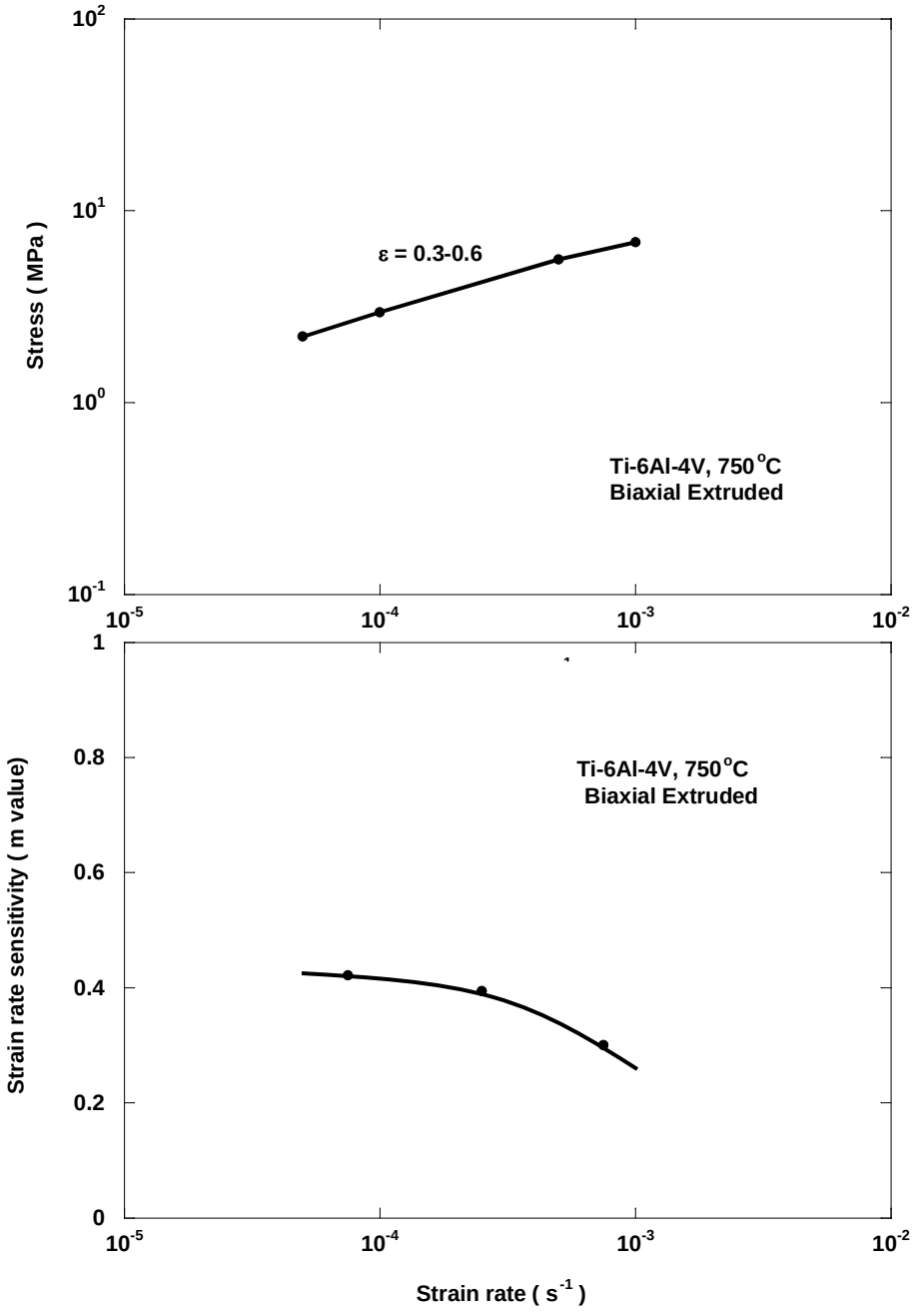

Figure 4.13 Measurement of strain rate sensitivity from decremented train rate test at 750ºC. m value of biaxial extruded Ti-6Al-4V show increased value in low strain rate region with highest m = 0.42 at strain rate $0.0001s^{-1}$.

Appendix 4A

Strain input in ECAE process.

ECAE is the most common SPD process used so far. The extrusion process is demonstrated in Fig 4A1. The billet abcd is pressed through the shear plane from original channel to the channel with the same cross section with angle 2φ to the original channel. The square shape of the billet abcd is turned to a diamond shape a′b′c′d′. The shear strain imparted in the billet would be:

$$\varphi=2 \cot \varphi \tag{A1}$$

The Von Mises effective strain is then:

$$\varepsilon = 2/\sqrt{3} \cot \varphi \tag{A2}$$

The angle φ is usually 45 degree and the strain per pass ECAE is 1.15.

However, there are still other factors still need to be counted for such as friction and radius of the die corner, which all have effects on final strain.

Different processing routes also triggers different slip planes in the billet as shown in Fig 4A2. In route A, the billet is not turned so two slip planes would be activated and intersect on the Y axis. In route B, the billet is turned 90 degrees between passes so different slip planes would be activated along the X axis. In route C, the billet would be turned 180 degrees between passes so basically only one slip plane would be activated but with alternating slip directions.

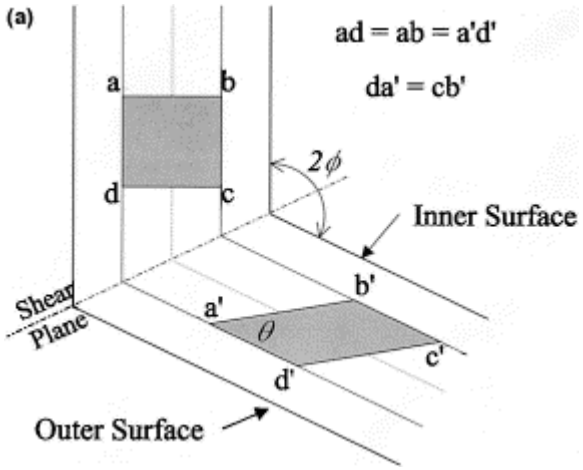

Figure 4A1. Schematic diagram of the ECAE process adopted from ref [29]. The element abcd is passed through the shear plane and become element a´b´c´d´with equivalent volume.

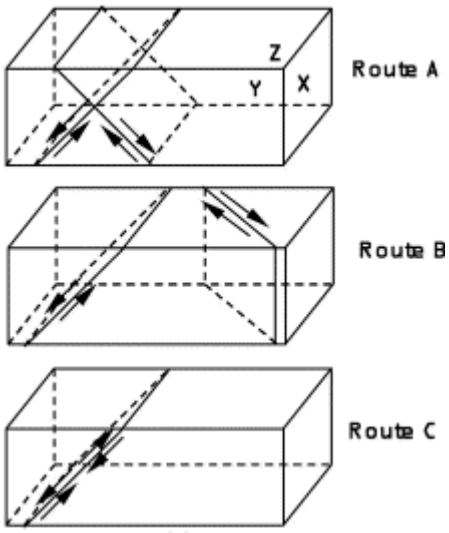

Figure 4A2. Schematic illustrations (adopted from ref [30]) of the slip planes activated in different routes during ECAE process.

References

[1] N. Hansen, D.J. Jensen: *Philosophical Transactions of the Royal Society London, Series A* (Mathematical, Physical and Engineering Sciences), v 357, n 1756, p 1447-69, 15 June 1999

[2] A. Bussiba, A. B. Artzy, A .Shtechman, S. Ifergan, M. Kupiec: *Materials Science and Engineering A*, v 302, n 1, Apr 15, 2001, p 56-62

[3] K. Matsubara, Y. Miyahara, Z. Horita, T.G Langdon: *Acta Materialia*, v 51, n 11, 27 June 2003, p 3073-84

[4] E.D. Tabachnikova, V.Z. Bengus, A.V. Podolskiy, S.N. Smirnov, K. Csach, J. Miskuf, L.R. Saitova, I.P. Semenova, R.Z. Valiev: *International Journal of Mechanics and Materials in Design*, v 4, n 2, p 189-195, June 2008

[5] C.S. Lee, Y.G. Ko, D.H. Shin, K. Park: *Scripta Materialia*, v 54, n 10, p 1785-9, May 2006

[6] L. Saitova, I. Semenova, H.W. Höppel, R. Valiev, M. Göken: *Materialwissenschaft und Werkstofftechnik*, v 39, n 4-5, p 367-370, April/May 2008

[7] Y.G. Ko, C.S. Lee, D.H. Shin, S.L. Semiatin: *Metallurgical and Materials Transactions A: Physical Metallurgy and Materials Science*, v 37, n 2, p 381-391, February 2006

[8] I. Karaman, Z.P. Luo, H. Rack: *Scripta Materialia*, v 49, n 10 SPEC., p 1021-1027, November 2003

[9] G.G. Yapici, I. Karaman, Z. Luo: *Acta Materialia*, v 54, n 14, p 3755-3771, August 2006

[10] I.P. Semenova, G.I. Raab, L.R. Saitova, R.Z. Valiev: *Materials Science and Engineering A*, v 387-389, n 1-2 SPEC. ISS., p 805-808, December 15, 2004

[11] Y.R. Kolobov, G.P. Grabovetskaya, K.V. Ivanov, R.Z. Valiev, Y.T. Zhu: *Ultrafine Grained Materials 3 Symposium*, p 621-8, 2004

[12] I.P. Semenova, Y.T. Zhu, G.J. Raab, T.C. Lowe, R.Z. Valiev: *Ultrafine Grained Materials 3 Symposium*, p 463-8, 2004

[13] S.M. Kim, J. Kim, D.H. Shin, Y.G. Ko, C.S. Lee, S.L. Semiatin: *Scripta Materialia*, v 50, n 7, p 927-30, April 2004

[14] Y.G. Ko, J.H. Kim, C.S. Lee, D.H. Shin, S.L. Semiatin: *Materials Science Forum*, v 475-479, pt.4, p 2955-60, 2005

[15] A.P. Zhilyaev, S. Lee, G.V. Nurislamova, R.Z. Valiev, T.G. Langdon: *Scripta Materialia*, v 44, n 12, p 2753-2758, June 8, 2001

[16] R.S. Mishra, V.V. Stolyarov, C. Echer, R.Z. Valiev, and A.K. Mukherjee: *Materials Science & Engineering A (Structural Materials: Properties, Microstructure and Processing),* v A298, n 1-2, 31 Jan. 2001, p 44-50

[17] V.V. Sergueeva, R.Z. Valiev, A.K. Mukherjee, V.V. Stolyarov: *Materials Science & Engineering A (Structural Materials: Properties, Microstructure and Processing),* v A323, n 1-2, p 318-25, 31 Jan. 2002

[18] D. Terada, S. Inoue, N. Tsuji: *Journal of Materials Science, v 42, n 5, March, 2007, Special Issue: Nanostructured Materials-Processing, Structures, Properties and Applications,* p 1673-1681

[19] M.R. Bache, W.J. Evans: *Materials Science & Engineering A (Structural Materials: Properties, Microstructure and Processing),* v A319-321, p 409-14, Dec. 2001

[20] T. Al-Samman, G. Gottstein: *Diffusion and Defect Data Pt.B: Solid State Phenomena*, v 105, p 201-206, 2005

[21] A.A. Sheikh: *Journal of Materials Science,* v 42, n 10, p 3621-6, May 2007

[22] C.Y. Nam, J.H. Han, Y.H. Chung, M.C. Shin: *Materials Science & Engineering A (Structural Materials: Properties, Microstructure and Processing),* v A347, n 1-2, p 253-7, 25 April 2003

[23] J.C. Lee, H.K. Seok, J.H. Han, Y.H. Chung: *Materials Research Bulletin,* v 36, n 5-6, p 997-1004, March/April 2001

[24] J. Han , H. Seok, Y. Chung, M. Shin, J. Lee: *Materials Science & Engineering A (Structural Materials: Properties, Microstructure and Processing),* v A323, n 1-2, p 342-7, 31 Jan. 2002

[25] A.K. Ghosh and Y. Lee: *USPO. Filing number 61223377*. Jul 6th 2009.

[26] R. Ding, Z.X. Guo, A. Wilson: *Mater Sci Eng A* 2002;327-233

[27] *ASM Metals handbook*. Vol 2. p 609.

[28] J.P. Patankar, D.P. Field, G. Salishchev, R.M. Galeyev, O.R. Valiakhmetov, F.H. Froes: *Journal of Alloys and Compounds*, v 345, n 1-2, p 221-227, October 28, 2002

[29] J.R. Bowen, A. Gholinia, S.S. Roberts, P.B. Prangnell: *Materials Science and Engineering* A287 (2000) 87-99

[30] D.H. Shin, I. Kim, J.Kim, Y.S. Kim, S.L. Semiatin: *Acta materialia* 51(2003) 983-996

Chapter 5

Processing of ZK60 and Fabrications of Mg-based materials through Biaxial Extrusion

Abstract

Biaxial extrusion is a novel severe plastic deformation (SPD) technique, by which materials in billet form is turned into round sheets. In this study, ZK60 billets processed through biaxial extrusion were turned into flat sheets with extensive grain refinements in relatively low deformation temperatures (150ºC-220ºC). The tensile tests done on the extruded ZK60 showed improved yield strength and good ductility. Also, with this unique processing technique, different types of Mg-based composite (Mg-Al) and alloys (Mg-Y_2O_3 and Mg-B) were successfully fabricated. Fine grain structures were observed in these Mg-based materials with good mechanical properties.

5.1.Introduction.

It is well known that the mechanical properties of metals can be improved through grain refinement. Of all grain refinement methods studied so far, severe plastic deformation (SPD) has been proved to be the most efficient way to achieving fine grain structure, or sometimes even ultra-fine grain structure (grain size < 1μm). Various SPD processing techniques have been developed in the past few decades such as equal channel angular extrusion (ECAE) [1-3], high pressure torsion (HPT) [4,5], and hot rolling[6]. It is always of interest to process metal sheets with good mechanical properties. However, ECAE processes could not give final products in sheet form and HPT could not produce samples in large scale (sample size ~15mm diameter). The only choice left for sheet processing is rolling, but strong textures are developed.

A novel technique, namely biaxial extrusion, is recently adopted to directly transform billets into sheets and impart heavy deformation along the process. With this new process technique, metal sheets with good mechanical properties can be produced with little texture developed. A schematic illustration of biaxial extrusion is shown in Fig 5.1.

A two-piece circular die set are used in the extrusion process. As shown in Fig 5.1a, Two 5 inch diameter H-13 steel round blocks(upper block, 5 inch diameter x 3.5 inch tall and lower block, 5 inch diameter x 1.5 inch tall) was clamped together with six high strength steel bolts. A thin gap was kept in between blocks to allow the work piece to flow and expand. The thickness of the gap was controlled by the thickness of the washers put in between the blocks. Thickness of the washers is adjustable, so the thickness of the extruded work piece is also changeable according to the thickness of the washers. In an

extrusion run, work piece was put at the bottom of the upper block while load was gradually applied to it. Work piece would be extruded into the gap between upper and lower block and flow into all directions, as shown in Fig 5.1b, and forms a round disk/sheet. The bolts around the edge of the blocks (gray circles in Fig 5.1b) limited the growth of the work piece since the work piece would touch the bolts while it expands out. The shortest distance between two facing bolts is 3.5 inch so the largest diameter a work piece can grow is 3.5 inch. This limitation could be improved if a larger die is used.

Fig 5.1c shows shear planes that were activated in work piece when work piece was extruded out from the upper block. Multiple shear planes were activated along their corresponding extrusion directions and intersected each other. A more uniform strain is believed to be developed from the slip intersections. Samples experience both shear and expansion strains in biaxial extrusion process. The shear strain can be calculated by analyze the strain of a single element of the work piece shown in the schematic in Fig 5.1(d). Element given by abcd represents the sample before extrusion. Element given by aefb represents the sample after extrusion. Notice line gb and bi are perpendicular to lines dc , ab and ef. r =the radius of the sample and t = thickness of the gap. The shear strain experienced by the sample is given by $\gamma = dc/gb$, where $dc = r\sec\theta$ and $gb = r\sin\theta$. Therefore, the shear strain is:

$$\gamma = 1/\sin\theta\cos\theta \qquad (1)$$

Where $\theta = \tan^{-1} t / r$.

Consider the von Mises effective strain, the strain from the extrusion is:

$$\varepsilon_1 = 1/\sqrt{3}\ \sin\theta\cos\theta \qquad (2)$$

The strain from the expansion can be simply determined by the radius difference of the sample in two directions.

$$\varepsilon_2 = 2\ln (r / r_o) \quad (3)$$

where r = final radius of the extruded disk, r_o = original radius of the sample

Assume Δh of the original sample has been pressed down, a corresponding disk with equal amount of volume should be extruded out:

$$\Delta h \pi r_0^2 = \pi r^2 t \quad (4)$$

So

$$\frac{r}{r_0} = \sqrt{\frac{\Delta h}{t}} \quad (5)$$

Plug equation (5) into equation (3) then we have

$$\varepsilon_2 = \ln (\Delta h / t) \quad (6)$$

The total strain experienced in one extrusion run is simply the summary of ε_1 and ε_2

$$\varepsilon_{total} = \varepsilon_{1 +} \varepsilon_2 = 1/ \sqrt{3} \ \sin\theta\cos\theta + \ln (\Delta h / t) \quad (7)$$

In the current study, the gap is kept at 0.04 inch and the radius of the sample is 0.5 inch. For the sample with original height of 0.5 inch, the overall strain input is 9 based on equation (7).

The goal of this study is to examine ZK60 magnesium alloy and Mg-based materials (Mg-Al, Mg-Y_2O_3 and Mg-B) processed through biaxial extrusion. Chapter 5A describes the process of ZK60 and chapter 5B describes the process of Mg-based composite and alloys.

5A. Severe deformation of ZK60 via biaxial extrusion.

ZK60 is a commercial magnesium alloy with high yield strength compared to the other Mg alloys. The high strength in ZK60 is mostly attributed to its well distributed Zn_2Zr_3 and Mg_2Zn_3 particles. The usual yield strength of cast ZK60 is close to 300MPa and can be increased by thermo-mechanical processing. Since magnesium is one of the lightest metals, it is desirable to use magnesium in applications that requires light weight. Also, with thermo-mechanical processes, magnesium parts can give good stiffness and strength and fit in applications that usually require uses of heavier metals. Many studies have been made to process magnesium alloys in hope to find a better processing route to increase the strength and ductility.

Severe plastic deformation (SPD) is one promising processing technique to increase the strength and ductility of metals. SPD process reduces the grain size of the original material and imparts heavy strain into the crystal hence the strength of the material could be greatly increased. Many SPD processes [7-9] have been done on ZK60 alloys to produce ultra-fine grained crystals with high strength and ductility. However, no study has yet been made to fabricate ZK60 sheets directly extruded from ZK60 billet. In this study, the biaxial extrusion process was done on the raw ZK60 billet (cut from cast ZK60 plate) with three different processing temperatures (150º, 180ºC and 220ºC). Microstructure evolution and mechanical properties of extruded ZK60 sheets were studied. The original grain size of raw ZK60 billet is 6.3 μm. After the extrusion process, the grain size of the extruded ZK60 sheets was reduced to ~ 1 μm, and the mechanical properties of extruded ZK60 was greatly improved. Superplastic behavior was also observed in the extruded ZK60 through high temperature tensile test.

5A.1 Experiment

Three 0.75 inch tall x 1 inch diameter ZK60 cylinders were machined from a 1 inch thick ZK60 plate (as shown in Fig 5.2) for the biaxial extrusion. Two 3003 Al sacrificial washers were used to provide hydrostatic forces to the work piece during the extrusion. Three different extrusion temperatures were used for processing; 150ºC, 180ºC and 220ºC. Fig 5.3 (a) shows the microstructure of raw ZK60 work piece,(b),(c)and (d) show the ZK60 work piece extruded at 150ºC, 180ºC and 220ºC, respectively. These extruded ZK60 have the same thickness of 0.08 inch with different diameters. The diameter of 150ºC, 180ºC and 220ºC extruded ZK60 pieces are 2.83 inch, 2.67 inch and 3.38 inch, respectively and the cumulative strains are 7.92, 7.8 and 8.27, respectively. Flow lines can be seen on the surfaces of the extruded ZK60 work pieces as shown in Fig 5.3. These flow lines are clear indications of flow directions of the work piece during the extrusion process, start from one inch center and radiate out in all directions. Work piece extruded at 180ºC showed a crack on the bottom edge. This edge crack happened at the place where the constraint Al washer had early failure during the expansion thus no hydrostatic pressure was applied to this region. Possible flow instability caused the work piece to crack along the edge.

5A.2 Microstructure evolution

Microstructure samples were sectioned from both extruded and raw ZK60 work pieces. The sectioned samples were mounted in the self-curing resin, ground with sand papers to 4000 grit and polished with 0.3μm colloidal silica. Picrial acid (1.26 mg picric acid, 3ml de-ionized water, 3ml acetic acid and 70ml ethyl alcohol) was used to reveal the grain

boundaries of the samples. The microstructures of the raw and as-extruded ZK60 samples in different extrusion temperatures are tabulated in Fig 5.4. The raw ZK60 shows bimodal grain structure with large grains sized more than 60 μm and small grains size about 6 μm. After biaxial extrusion, many large grains were broken into small grains. Heavy twinnings are shown in the samples with lower extrusion temperatures (150ºC and 180ºC as indicated by the arrows in Fig 5.4 (b) and (c)). It is believed that less recovery happened at lower temperature and forced twinning to accommodate the deformation strains. These twinnings happened mostly at the large grains at low deformation temperature. Also, more grain fragmentations were observed in the samples extruded at lower temperature. Volume percentage of the fine grained area in samples increased after the biaxial extrusion, as shown in the chart of Fig 5.5. The original small grain area constitutes 61% volume in the raw ZK60. After biaxial extrusion, the volume of the small grain area increased to 74%, 73% and 76% in 220ºC, 180ºC and 150ºC samples. The average grain size of the large grains reduced from 63μm in raw ZK60 to 36μm, 32μm and 29μm in 220ºC, 180ºC and 150ºC extruded samples. The average grain size of the small grains reduced from 6.3μm to 1.92μm, 1.86μm and 1.57μm in 220ºC, 180ºC and 150ºC extruded samples, respectively. From the numbers shown above, it is evident that lower extrusion temperature encouraged the grain subdivision and helped increase microstructural uniformity.

Fig 5.6 shows the TEM image of microstructure of ZK60 work piece extruded at 150ºC. Small individual grains were circled with dotted lines. Many small grains less than 500 nm were found in the microstructure and heavy dislocations can be seen in some of the

larger grains. These dislocations generated in larger grains increased the shear requirement in deformation, thus increased the overall strength of the sample. Heavy dislocations are usually generated in magnesium samples deformed at low temperature because with deformation temperature higher than 300ºC, recrystallizations are likely to happen and eliminate the dislocations in the grains.

(0002), $(10\bar{1}0)$ and $(10\bar{1}1)$ pole figures were done on both unprocessed ZK60 and 150ºC extruded ZK60 (as shown in Fig 5.7 and Fig 5.8) with Rigaku rotating anode X-ray diffractionmeter tilting from 15 to 85 degrees. The original diffraction patterns had been processed by "POPLA" to correct the misalignments and drop in intensity on the edge of the sample. The image processing details are postulated in Appendix 5A. The X-ray source was Cu-Kα radiation at 30Kv and 100mA. The unprocessed ZK60 has some texture developed from the previous forming process (extrusion) in both (0002), $(10\bar{1}0)$ and $(10\bar{1}1)$ poles. The highest intensity is 14.94. After biaxial extrusion, though the texture on (0002) basal pole was still developed parallel to the extrusion direction, the intensity dropped to 7.89 with broad texture pattern. Also, the textures on $(10\bar{1}0)$ and $(10\bar{1}1)$ poles have greatly been reduced and broadened out. It is believed that the biaxial extrusion with multiple slip directions develops very little texture on the sample or can even reduce the inherited textures from previous forming processes.

5A.3 Mechanical test

Room temperature tensile samples were machined from the extruded ZK60 sheets. The strain rate is set at 0.5mm/minute. Test results are tabulated in Fig 5.9. It is worth noticing that both specimens extruded at 150ºC and 180ºC showed very high yield strength (355MPa and 290MPa). Specimen extruded at 220ºC has relatively lower yield strength of 180MPa. The yield strength increases with lower extrusion temperature. The result matches the finding in the microstructures since lower temperature extruded work pieces have smaller grains and higher volume percentage of fine grained area.

Both 150ºC and 220ºC samples have good room temperature ductility (fracture strain ~15%). This high ductility is rarely seen in the commercial ZK60 (~7% fracture strain) and is believed to be attributed to the fine grained structure. The 180ºC sample failed at a much lower strain (~4%), which is believed to be caused by the pre-existing machine defects.

High temperature tensile tests were performed on the extruded work piece with different test temperatures. The tests were done on the work piece extruded at 150ºC. Tests were done at 300ºC and 250ºC with constant strain rate ($2x10^{-4}$/s) and the results are tabulated in Fig 5.10. The sample tested at 250ºC showed higher flow stress (~60MPa) but less ductility. Fig 5.11 shows samples used in the high temperature tensile tests. The top one is the untested sample with original 0.25 inch gauge length. The middle one is the sample tested at 300ºC and the bottom one is the sample tested at 250ºC; both tested samples showed very good ductility with 252% elongation and 244% elongation. Ductile fractures were observed with pointed fracture tips and uniform necking areas.

Micro-hardness tests were performed on both raw ZK60 and extruded ZK60 work pieces. Test load was set to 100g with 10 second dwell time in standard vicker's micro-hardness tester. The results are tabulated in Table 5.1 with average grain size of the processed samples and their tensile properties. Hardness of the unprocessed ZK60 is 72 and increased to 82, 86.5 and 90.6 after extruded at 220ºC, 180ºC and 150ºC. The increase in hardness in work pieces extruded at lower temperature is believed to be caused by the higher volume percentage of fine-grain area and smaller grains.

5A.4 Discussion

Raw ZK60 in billet form was successfully processed by biaxial extrusion at elevated temperature. Bimodal structures with mixed large-grain/small-grain areas were observed in both raw and processed samples. However, large grains in raw ZK60 were broken up during the extrusion process and average sizes of the large grains were greatly reduced after the extrusion. Also, the volume fraction of the fine grains increased after the extrusion. The extrusion temperature is essential in controlling resulting microstructures and the mechanical properties of the work pieces. Lower extrusion temperature has better effect in grain subdivision and inducing twinnings and dislocations into the crystal, hence has better increase in strength of the work piece. It is believed that dislocations generated at low temperature extrusion contributed a great portion of strengthening in the material. In Jinbao Lin et al. study [10], the yield strength of the ZK60 work piece reduces with the increasing numbers of extrusion processes at 230ºC from 261 MPa 1-pass extrusion to 215 MPa 4-passes extrusion. The grain size was refined in the first extrusion with large

amounts of dislocations. The following extrusions did not reduce the grain size by much. Decrease in strength with further extrusions is believed to be caused by the elimination of dislocations when dynamic recrystallizations occurred during the processes.
From the microstructural analysis and mechanical tests of the biaxial extruded ZK60 work pieces, it is safe to say that the optimal extrusion temperature is 150ºC.

Although the strength of ZK60 was greatly increased through biaxial extrusion, the ductility of the extruded ZK60 is still low. Many have reported processed ZK60 work pieces have elongation more than 1000% [11, 12]. The maximum elongation of biaxial extruded ZK60 did not exceed 300%. It is believed that the bimodal microstructure of the processed ZK60 is the cause of its low ductility. The dominant deformation mechanism in superplastic forming is grain boundary sliding, and it only occurs in samples with very fine grains (<1μm) and good structural uniformity. In the biaxial extruded ZK60, bimodal microstructure could not be eliminated and some coarse grains were still around 30μm. These coarse grains were believed to be the major obstructions for grain boundary sliding during high temperature deformation thus reduced the ductility. To reduce the overall grain size of the sample, processing at higher temperature is required to encourage dynamic recrystallizations to occur and break down the large grains. However, this would sacrifice the strength of the material since dynamic recrystallization could reduce the numbers of generated dislocations.

Biaxial extrusion can produce fine-grained materials in sheet form in one extrusion process, but it also limited the possibility for repetitive processing like ECAE. In ECAE,

strain could be cumulated from each extrusion pass and large amount of strain can be attained. It usually takes cumulative strain more than 6 to have uniform and fine-grained microstructure in work piece. In biaxial extruded ZK60, the cumulative strain is around 8 with set condition gap/radius ratios equals 0.16 (0.08 inch gap with 1 inch diameter extrusion hole). The thickness of the gap is adjustable so larger strain could be obtained.

5B. Processing of Mg base composites through biaxial extrusion.

Three different Mg-based composites were studied: Mg-Al composite, Mg-Y_2O_3 alloy and Mg-B alloy. The reason Mg is used for base material in these composites is because Mg is light weight and has high specific strength and stiffness. The first Mg-based composite fabricated through biaxial extrusion die is Mg-Al composite for both magnesium and aluminum are light weight and easy to acquire. The aluminum used here is 5754 Al. Commercial 5754 Al is strengthened by the solid solution formed by the addition of magnesium [13]. So it is believed that 5754 Al in the Mg-based composite would be stronger for forming solid solution with higher Mg concentration. The Mg alloy used in the Mg-Al composite is AZ31 Mg alloy. In AZ31 magnesium, the strengthening mechanism is from β phase ($Mg_{17}Al_{12}$) precipitates [14,15] located at the grain boundary. It is believed that by combining AZ31 and 5754Al, a light weight composite with better strength could be made. The chemical composition of AZ31 is Mg-3%Al-1%ZN-0.2%Mn and the chemical composition of 5754 Al is Al-0.4%Si-0.4%Fe-0.5%Mn-2.8%Mg. A detailed description of the fabrication processes of the composite will be given in the following section. The microstructure of the fabricated composite would be examined and mechanical property (micro hardness) would be tested.

The second Mg-based alloy fabricated through biaxial extrusion die is Mg-Y_2O_3 for Mg is light weight and has high specific strength, high specific stiffness, good wear resistance and high damping capacity. The addition of hard particles to magnesium usually gives better properties for the precipitates formed in the matrix [16-19]. The precipitates distributed in the matrix obstruct the movements of the dislocations during the plastic deformation thus higher stress is required for the further deformations. Many processing techniques have been developed to fabricate new Mg-base alloys, including powder metallurgy, squeeze cast, stir casting and spray forming. By far, the powder metallurgy method gives the best properties for having finest grain structures. However, the powder metallurgy usually requires high temperature. With biaxial extrusion process, the fabrication of Mg-base alloys with additives could be done at much lower temperature. Also, the grain size of the original Mg can be greatly reduced and the additives can be well distributed inside the matrix through the extrusion process. Two Mg-Y_2O_3 sheets with different Y_2O_3 concentrations were fabricated from the extrusion processes. Microstructure evolutions of the sheets were studied and high temperature tensile tests were done.

An Mg-B alloy was also processed by biaxial extrusion process for property enhancement. An Mg-B ingot was first fabricated by hot pressing then processed through biaxial extrusion to attain fine grain structure. Microstructural analysis and EDS was done on the work piece. Both elevated and room temperature tensile tests were done on the composite to evaluate its mechanical properties.

5B.1 Experiment procedures

The starting materials for the Mg-Al composite are five 1 inch diameter x 0.1 inch thick AZ31 and five 1 inch diameter x 0.04 inch thick 5754 Al disks. The assembling of Mg and Al in the biaxial extrusion die is shown in the schematic in Fig 5.12. The AZ31 disks and 5754 Al disks were stacked alternatively in the biaxial extrusion die. Two 0.02 inch thick 3003 Al washers were used to provide hydrostatic stress to the work piece to prevent edge cracking. The disks were extruded first at 375ºC to form a 3 inch diameter x 0.1 inch thick composite sheet. Five 1 inch diameter disks were then cut from the extruded composite sheet and stacked again in the biaxial extrusion die for the second extrusion. To ensure the bonding between the layers, the temperature of the second extrusion was kept the same at 375ºC. Two 3003 Al washers were again used in the second extrusion to prevent edge cracking.

Fabrication of Mg-Y_2O_3 in the biaxial extrusion die is similar to fabrication of Mg-Al composite. The AZ31 disks were alternatively stacked with Y_2O_3 powders inside the die. A total of five AZ31 disks with one inch diameter and 0.1 inch thick were used. To ensure uniform distribution of the Y_2O_3, Y_2O_3 powders were first mixed with PVA, and the mixture of PVA+ Y_2O_3 was then coated on the front and back sides of the AZ31 disks. The set-up of the AZ31 disks with Y_2O_3 / PVA coating in the biaxial extrusion die is shown in Fig 5.13. Two Mg-Y_2O_3 sheets were fabricated with different Y_2O_3 concentrations. The extrusions were done at 220ºC and the weight percentages of Y_2O_3 of two fabricated Mg-Y_2O_3 sheets are 0.2 wt% and 0.5 wt% respectively.

Mg-B ingot was made from hot pressing ZK60 chips with 10 volume % Boron powder. Chips and Boron powders were first ball milled for 3 hours before hot pressing to promote uniform mixture. After ball milling, the mixture were hot pressed in enclosed die at 450ºC to form a 2.5 inch diameter x 1 inch thick ingot. A second hot pressing was done on the ingot at 230ºC to reduce the porosity. The ingot was then processed by the biaxial extrusion at 200ºC for further property enhancement.

5B.2 Microstructure evolutions

Fig 5.14 shows the microstructure of the Mg-Al composite sheet after first extrusion. Thick layers of AZ31 were sandwiched in between thin Al layers. The average thickness of the AZ31 layers is 153 μm and the average thickness of the Al layers is 28 μm. However, the thickness of the layers is not uniform. Some AZ31 layers were more than 300 μm thick and some were less than 100 μm. To reduce the thickness and increase numbers of layers of the composite, a secondary extrusion was conducted. 5 one inch disks were cut from the first extruded composite sheet and stacked in the biaxial extrusion die for another extrusion. The microstructure of the secondary extruded sheet is shown in Fig 5.15. Thinner and more uniform layers of AZ31 and 5754 Al were formed. Also, due to the repeated extrusions and high cumulative strain, the grain size of AZ31 layers was much refined (3.4 μm) as shown in Fig 5.15 (b). Mg-Al intermetallic layers were formed after second extrusion, these Mg-Al intermetallic layers are believed to be Al_3Mg_2 + β phase magnesium ($Mg_{17}Al_{12}$) for its high hardness. Vickers micro hardness tests were done on the Mg-Al composite sheet after secondary extrusion. The hardness of

the composite is not consistent throughout the whole samples, but varied in layers as shown in Fig 5.16. The hardness of the AZ31 layers is between HV 63 to HV68 and the hardness of the 5457 Al layers is between HV 123 and HV147. Hardness of the Mg-Al intermetallic layers is much higher than Mg and Al layers, with hardness value of HV 155~182.

Fig 5.17 (a) and (b) show the microstructure of extruded AZ31 sheets with 0,2 wt% Y_2O_3 and 0.5 wt% Y_2O_3, respectively. The grain size seem to be affected by the concentration of Y_2O_3 since work piece with higher Y_2O_3 concentration has finer grains (4.2 μm) than work piece with lower Y_2O_3 concentration (6.4 μm). It is believed that dislocation pile-ups were formed at Y_2O_3 precipitates, and the local stress field from the dislocation pile-ups facilitated the fragmentation of the grains, thus higher Y_2O_3 content AZ31 work piece would have finer grains

Annealing was done on both low and higher Y_2O_3 content AZ31 work piece for 13 hours at 230ºC to study the grain growth mechanism of Mg-Y_2O_3. The microstructure of annealed work pieces are tabulated in Fig 5.17 (c) and (d). Abnormal grain growth took place in the AZ31 work piece with low Y_2O_3 concentration. However, no abnormal grain growth was observed in AZ31 with high Y_2O_3 concentration. The lack of abnormal grain growth in high Y_2O_3 concentration AZ31 work piece is believed to be attributed to the larger amount of Y_2O_3 precipitates which pinned the grain boundaries and stopped the abnormal grain growth.

Fig 5.18(a) shows the micro of the as consolidated ZK60 billet. Many elongated voids can be seen on the original chip boundaries. To eliminate the voids and increase the homogeneity of the alloy, a second hot press was done on the billet at 230ºC. The number of voids was greatly reduced after secondary press as shown in the microstructure in Fig 5.18(b). The grains were elongated perpendicular to the pressing direction. After secondary pressing, a 1 inch diameter cylinder was cut out from the billet for the biaxial extrusion. The extrusion temperature was set at 200ºC to optimize the grain refinement and increase the numbers of dislocations. After extrusion, the grains were greatly refined. Microstructure of the extruded work piece showed bimodal grain structures with some large grained areas as shown in Fig 5.18(c). Overall fine grain areas were up to 86 volume %. The average grain size of the fine grained area is 1.1 μm. Though the structure is fine grain dominant, there are still some bands filled with small flake-like congregates in the matrix as shown in the SEM image in Fig 5.19(a). Energy dispersive x-ray (EDX) analysis shows high oxygen content in these bands. Higher magnitude SEM image taken on these band regions in Fig 5.20 shows that these bands were constituted with many small white flakes/particles. These flakes/particles are believed to be the $Mg_2B_2O_5$ collects. These bands of $Mg_2B_2O_5$ collects are believed to be formed during the consolidation process when the entrapped oxygen in between chips reacted with Boron and Mg at elevated temperature.

5B.3 Mechanical properties

Two elevated temperature tensile tests were done on the biaxial extruded Mg-Y_2O_3 work piece with high Y_2O_3 concentration (0.5wt%). Test temperatures were set at 300ºC and

250ºC with strain rate $2x10^{-4}$/s. Test results are shown in Fig 5.21. The sample tested at 300º C strain hardened to 44 MPa, then gradually softened untill failure. The sample tested at 250ºC reached a higher flow stress of 48 MPa, then rapidly softened and failed.

Another two elevated temperature tensile tests were done on the biaxial extruded Mg-B with strain rate of $2x10^{-4}$/s and test temperature 300ºC and 250. The test results are tabulated in Fig 5.22. Both samples tested have very low flow stresses (6 MPa in 250ºC test sample and 3 MPa in 300ºC test sample). Both biaxial processed Mg-Y_2O_3 and Mg-B showed very low ductility at elevated temperature with brittle fractures. Table 5.2 shows the elongation to failure of each tested sample.

Room temperature tensile tests were performed on the samples machined from as consolidated Mg-B billet and as extruded Mg-B sheet. The test results are tabulated in Fig 5.23. The as consolidated Mg-B has very low yield strength (78 MPa) measured from 0.2% off-set strain. After one step of hot pressing and subsequent biaxial extrusion, the yield strength of the Mg-B increased to 280MPa with U.T.S 322 MPa. This increase in strength is believed to be caused by the grain refinement through hot pressing and biaxial extrusion processes. Also, the ductility of the extruded Mg-B alloy has been greatly increased due to the elimination of voids in the as- consolidated Mg-B ingot. Stronger strain hardening is found on the as consolidated Mg-B while little or no strain hardening is found on the as extruded Mg-B.

5B.4 Discussion

The Mg-Al composite formed via high temperature biaxial extrusion has a lamellar structure with alternative layers of AZ31, 5754 aluminum and Mg-Al intermetallic (Al_3Mg_2+ $Mg_{17}Al_{12}$). The average hardness of the AZ31 layer in the composite is HV65, which is higher than the hardness of the original (unprocessed) AZ31 (HV52) billet. This increase in hardness is believed to be caused by the grain refinement during the repeated compressing and shearing during the extrusion process. The hardness of 5754 aluminum layer in the composite is HV~130, which is also greater than the hardness in the raw 5754 Al sheet (~HV75). The possible strengthening mechanism in the Al layer in the composite is believed to be attributed to the higher Mg concentration solid solution formed during the high temperature extrusion process. Besides the increase in hardness in both Mg and Al layers in the composite, the intermetallic layer formed in between Mg and Al layers has a relatively much higher hardness. So it is believed that the overall strength of the composite is much higher than individual magnesium and aluminum alloys. However, the ductility of the composite is very poor according to the result of room temperature tensile tests (not shown here). The test sample failed at strain less than 0.015. This low ductility may have two possible reasons: First, the intermittent fractures of the individual layers; many Mg/Al layers in the composite were not continuous through out the sample and have fractures. Those fractures carried little or no load during the tensile tests and caused the premature failure. Second, the brittle intermetallic layers; the intermetallic layers are consisted of hard β phase magnesium ($Mg_{17}Al_{12}$) and Al_3Mg_2 , both are hard but fail at little strain.

The biaxial extrusion done on the Mg-B made boron particles more uniformly distributed in the Mg matrix and reduced the grain size of the Mg matrix. The boron particles in the matrix formed precipitates and obstructed the dislocation movement thus enhanced the overall strength. The grain refinement of Mg-B through biaxial extrusion also contributed to the increase in strength. Although the extruded Mg-B has good strength, low ductility was shown in elevated temperature tests. The lack of ductility of Mg-B is believed to be caused by the formation of $Mg_2B_2O_5$ bands in the matrix. These $Mg_2B_2O_5$ bands are believed to be hard and brittle, which may cause local stress concentration and forms cracks upon loading. To avoid the formation of $Mg_2B_2O_5$ particles, it is important to ensure that no oxygen is allowed in the hot pressing process so that no chemical reactions could be involved.

5.2 Summary

Biaxial extrusion has been proven to be a versatile technique which can impart severe plastic deformation into materials via unique shear extrusion route and fabricate various Mg-base composite and alloys. Sheets of ZK60, Mg-Al composite, Mg-Y_2O_3 and Mg-B were successfully fabricated with good mechanical properties. Conclusions drawn from the experimental are as follows:

1. ZK60 sheets with fine-grained structure (~1μm) and high strength (Y.S=343 MPa) were fabricated via biaxial extrusion process, the optimal extrusion temperature is 150ºC. Superplastisity was obtained in the extruded ZK60 with highest elongation 252%

($300^{o}C$, $2x10^{-4}/s$).

2. Mg-Al composites were fabricated via biaxial extrusion. Repeated extrusion runs were applied to promote more uniform layer thickness. Mg-Al composite exhibit high overall hardness with hardness variation between composite layers.
3. Mg-Y_2O_3 was fabricated at low temperature ($220^{o}C$) through biaxial extrusion. Fine dispersed Y_2O_3 precipitates in the Mg matrix helped break down the grains during the extrusion process and stopped the abnormal grain growth during annealing. Low ductility was found on the extruded Mg-Y_2O_3 work piece.
4. Substantial grain refinement was observed in Mg-B through biaxial extrusion process. Good tensile strength properties were obtained in the Mg-B laminates but ductility was poor after biaxial extrusion.

Table 5.1 Grain size and mechanical properties of ZK60 before and after biaxial extrusion.

ZK60	Grain Size (μm)	Hardness (HV)	Yield Strength (MPa)	U.T.S (MPa)
Raw	6.3	72	138	290
Extruded at 220ºC	1.92	82	182	277
Extruded at 180ºC	1.86	86.5	292	348
Extruded at 150ºC	1.57	90.6	343	350

Test temperatures	300ºC	250ºC
Y_2O_3 containing AZ31	189%	157%
Mg-Boron	181%	165%

Table 5.2 Elongation comparison of elevated temperature tensile test samples of biaxial extruded Y_2O_3 containing AZ31 and Mg-Boron.

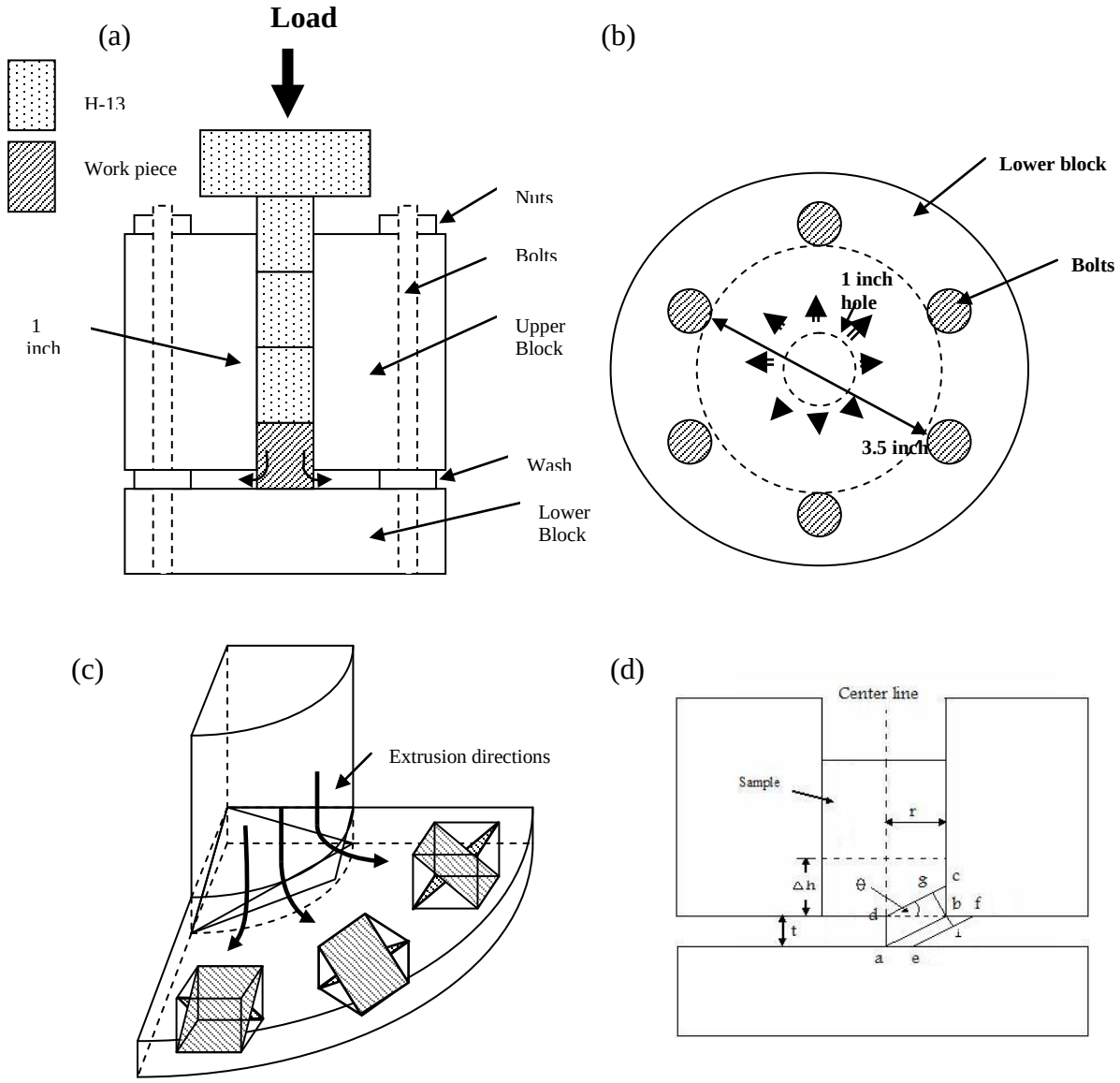

Figure 5.1 Schematic of (a) biaxial extrusion process, (b) cross section of the lower block. (c) extrusion directions and corresponding activated shearing planes (d) illustration of shear strain obtained by the element passed through the bottom exit. Schematic details are discussed in the text.

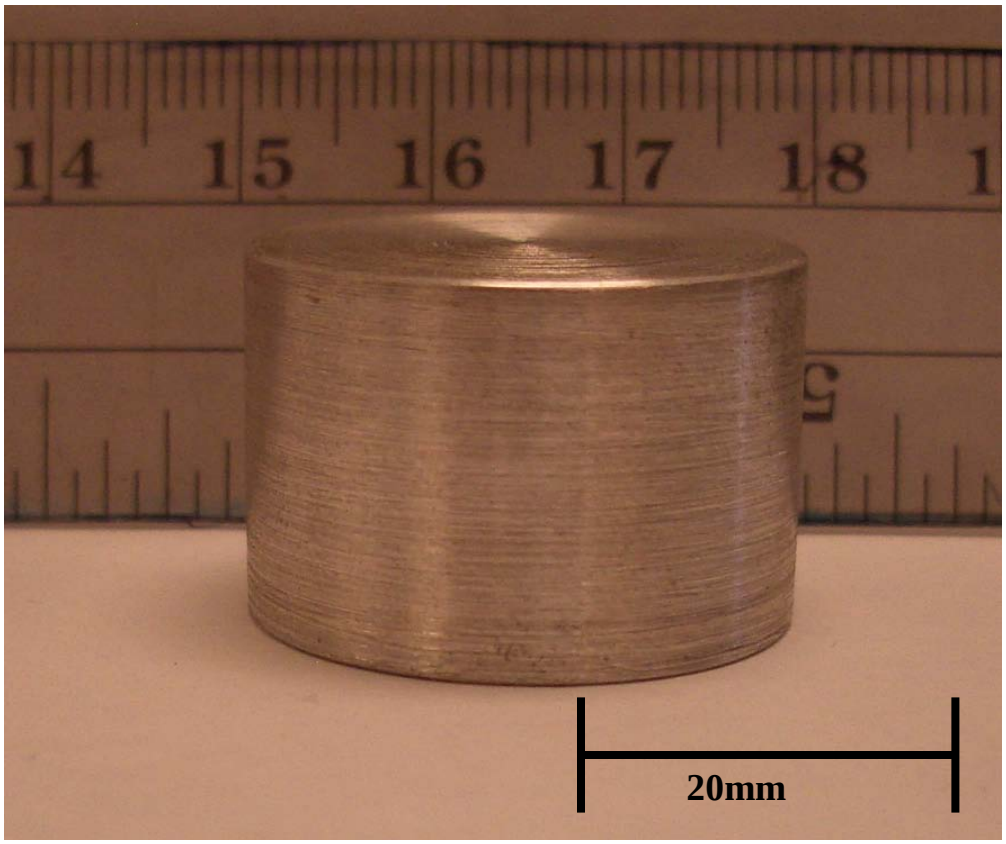

Figure 5.2 Photo image of ZK60 cylinder for biaxial extrusion. The dimension of the cylinder is 1 inch in diameter and 0.75 inch in height. Boron nitride would be sprayed on the cylinder before extrusion to avoid direct contact of Mg with steel die.

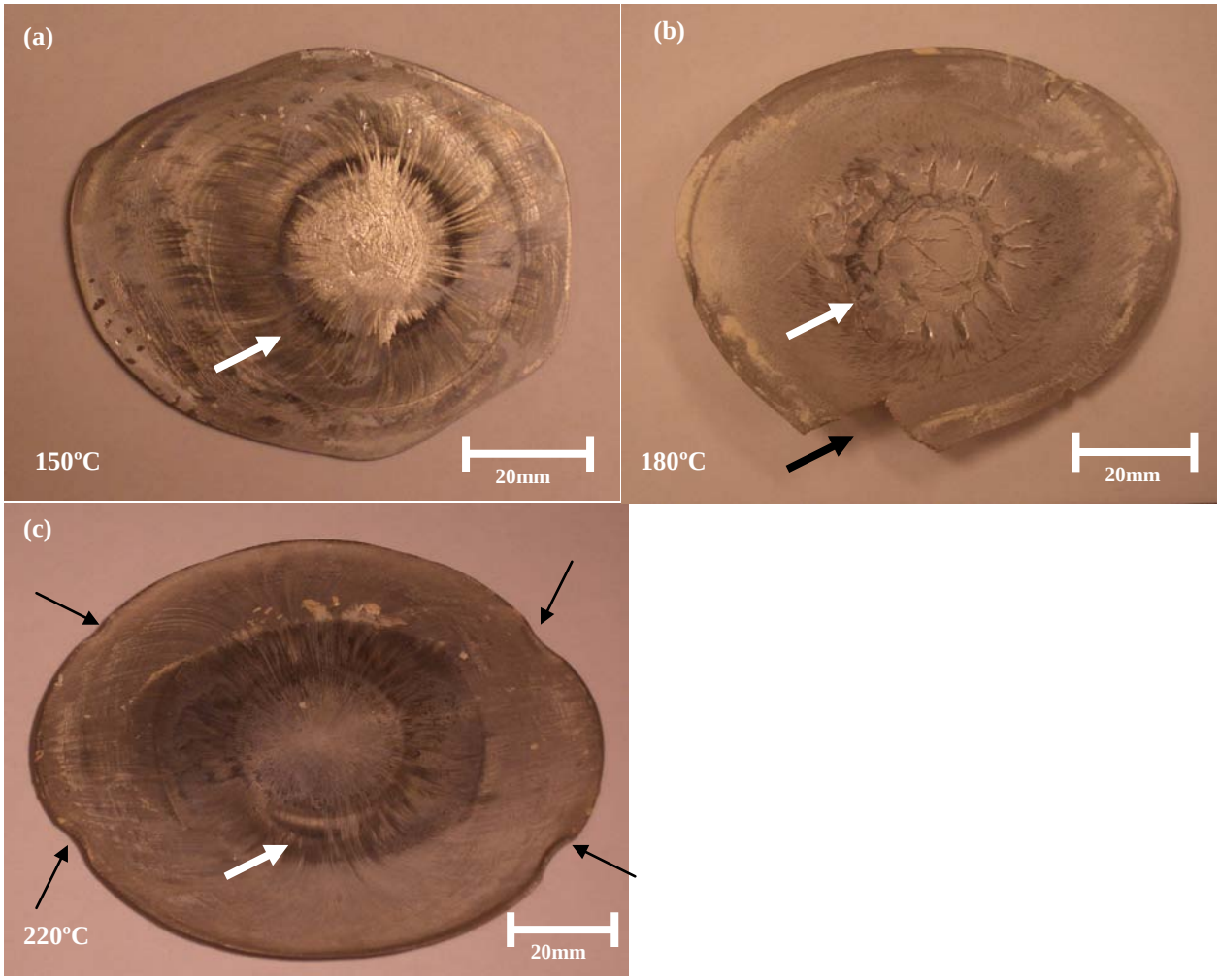

Figure 5.3 Photo images of extruded ZK60 disks. The extrusion temperatures are set at (a) 150ºC (b) 180ºC (c) 220ºC. Biaxial extrusion marks are clearly shown on the extruded disks as marked by the white arrows. All three disks have the same thickness of 0.08 inch. The one extruded at 180ºC has a crack near edge. Four round indents as marked by the black arrows in (c) indicated the place where ZK60 disk made contact with the bolts of the die set.

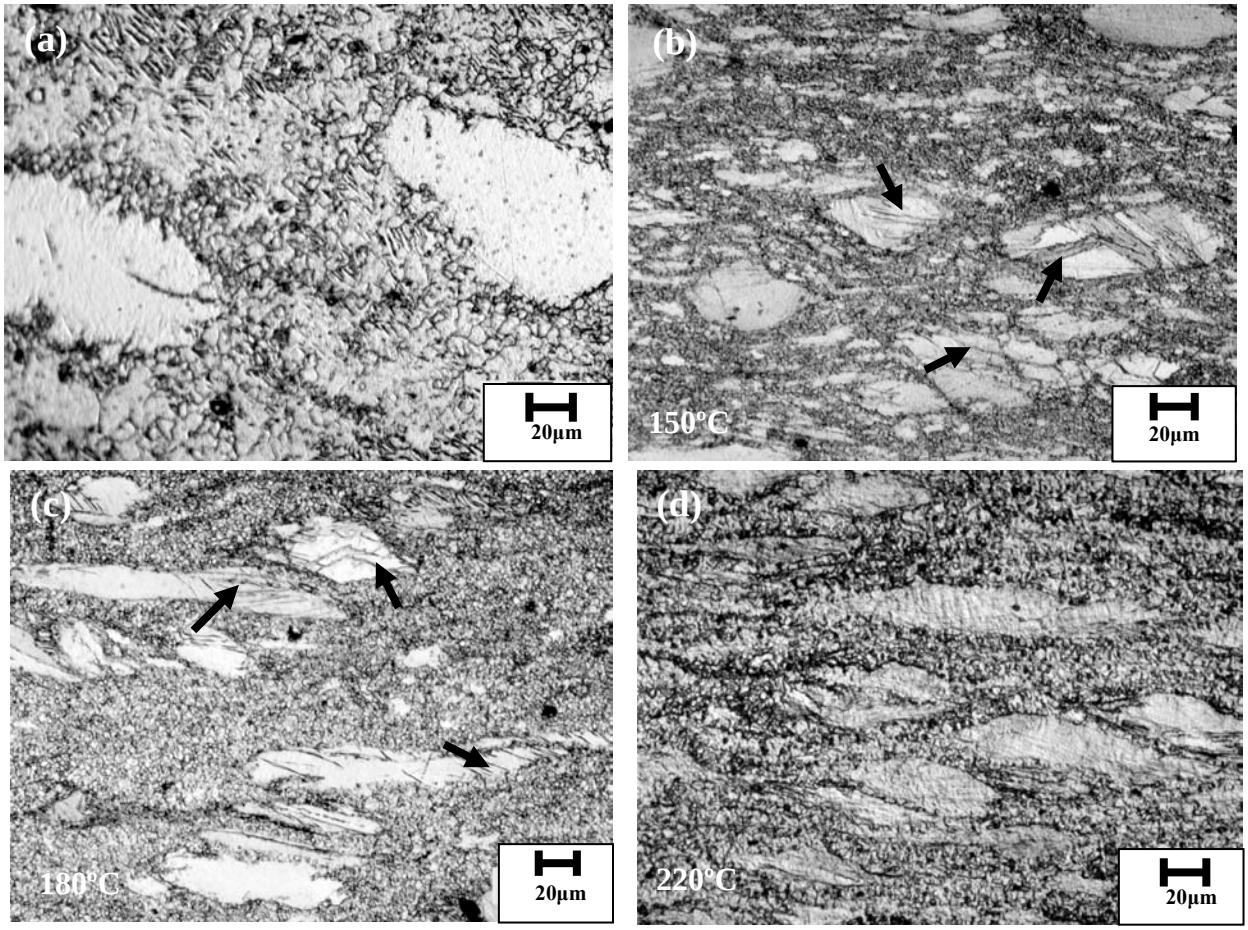

Figure 5.4 Photo images of the microstructures taken by the optical microscope of raw ZK60 (a), biaxial extruded ZK60 at (b) 150ºC (c) 180ºC (d) 220ºC. Heavy twins are found in the ZK60 extruded at 150ºC and 180ºC as indicated by the arrows. All the extruded disks show bimodal microstructures with large grains surrounded by the very fine grains. Extensive grain fragmentation can be seen in the 150ºC extrudate.

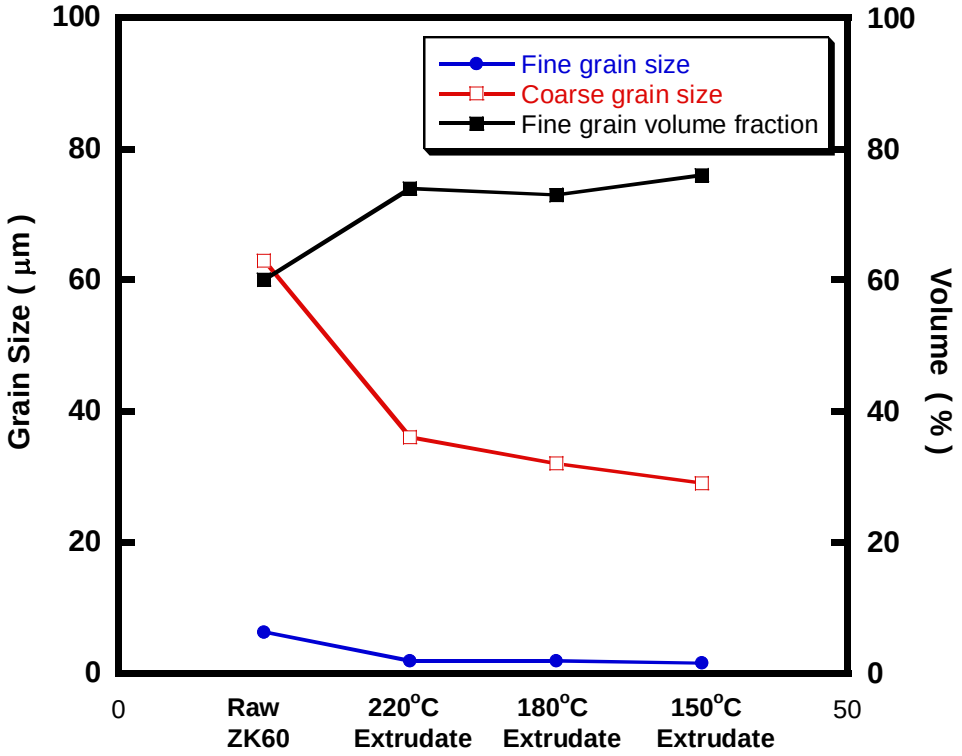

Figure 5.5 Grain distributions and grain sizes of raw and extruded ZK60 under different extrusion temperatures.

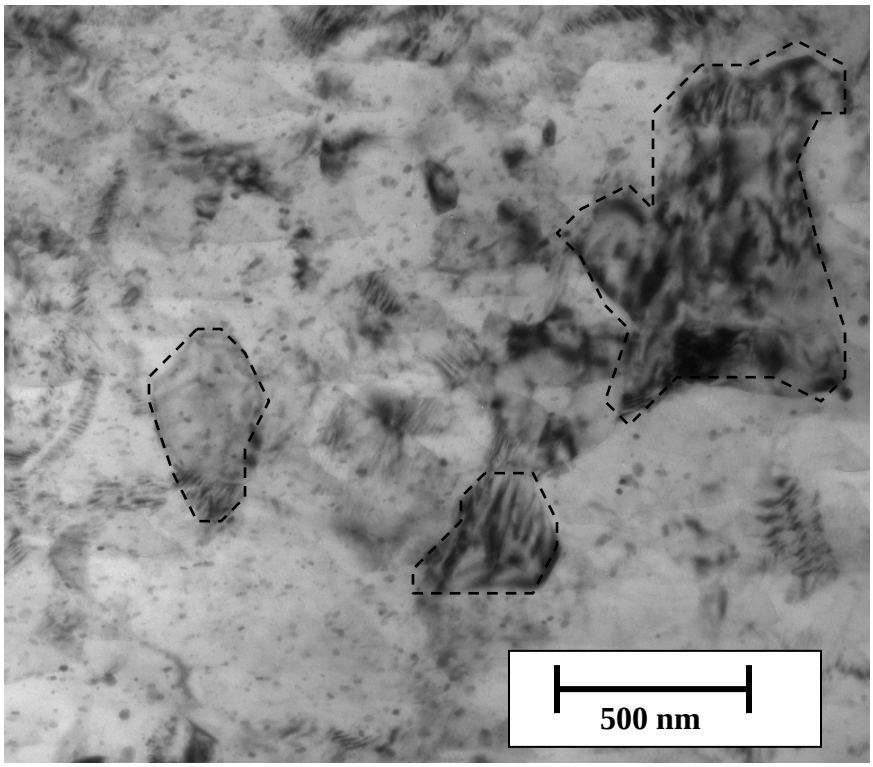

Figure 5.6 TEM image of 150ºC ZK60 extrudate. Many small grains less than 500nm can be seen around the sample. However, heavier dislocation lines were shown in the larger grains.

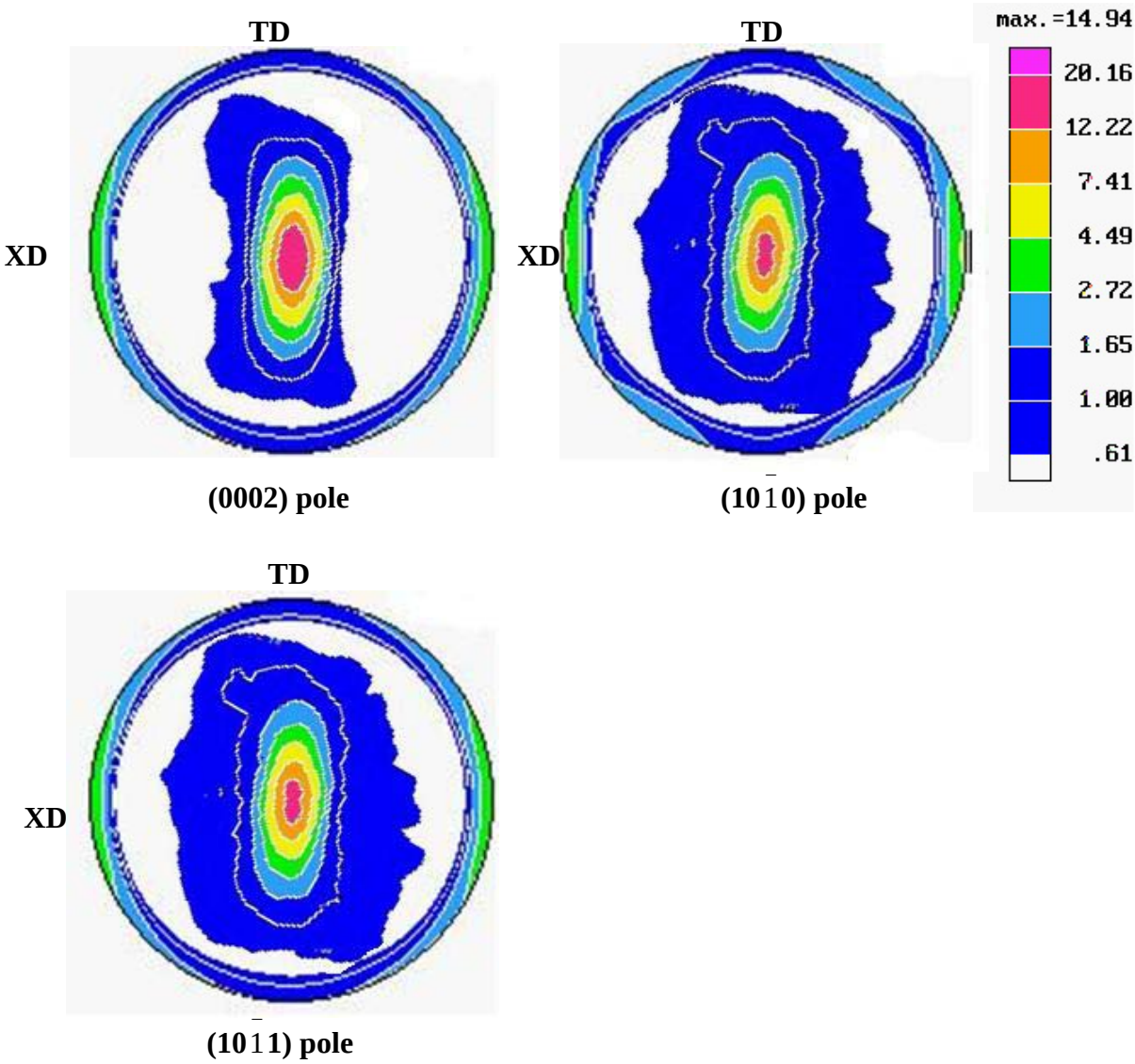

Figure 5.7 (0002), (10$\bar{1}$0) and (10$\bar{1}$1) pole figures of unprocessed ZK60

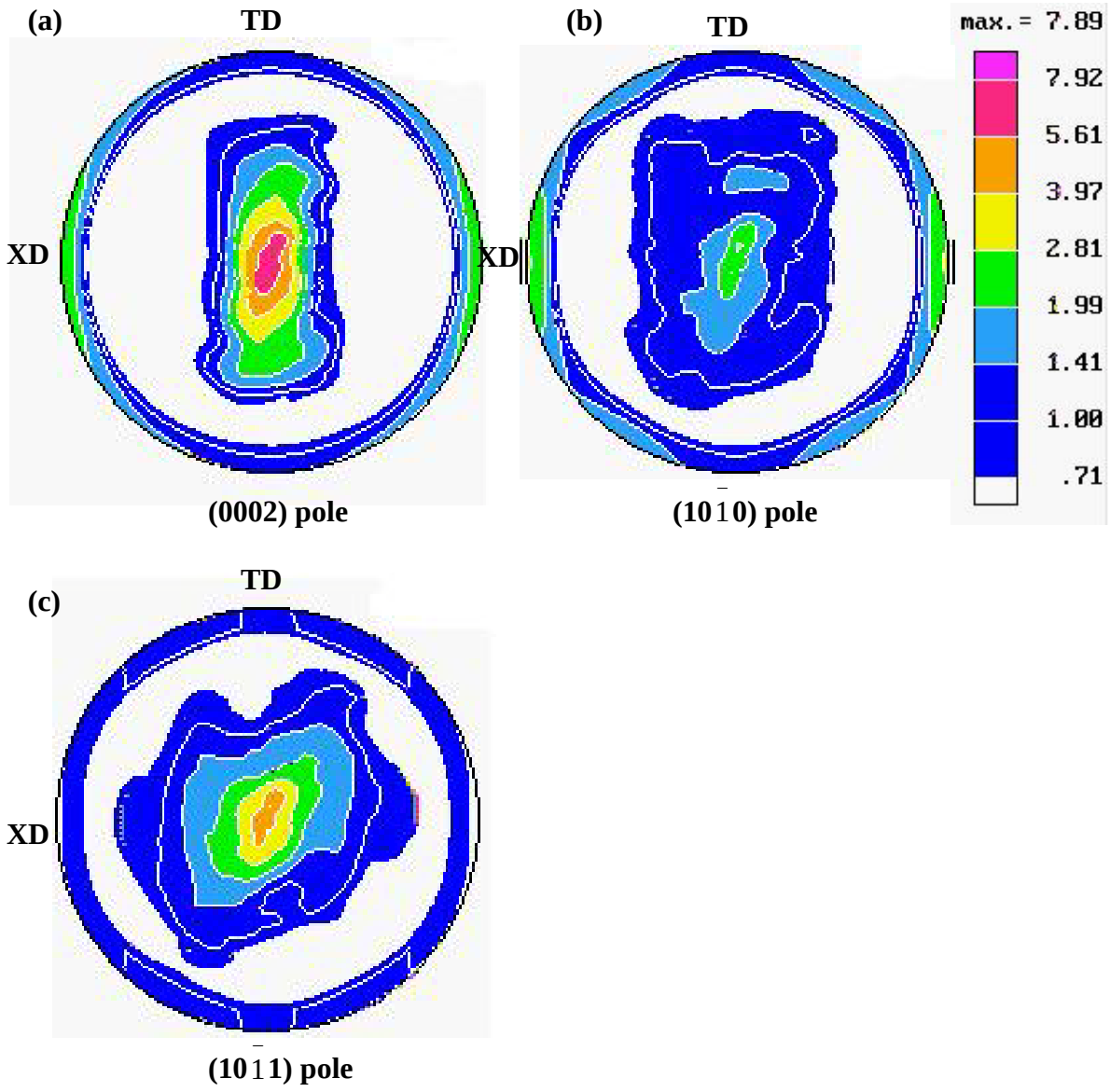

Figure 5.8 (0002), (10$\bar{1}$0) and (10$\bar{1}$1) pole figures of the biaxial extruded ZK60

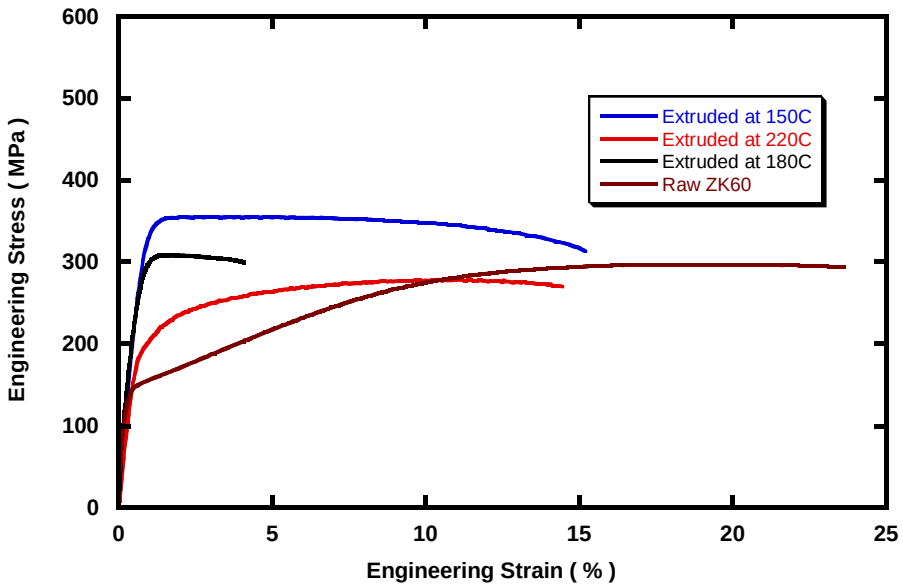

Figure 5.9 Tensile properties of the extruded ZK60 samples. High Y.S and U.T.S were attained by 150ºC and 180ºC extrudates. 220ºC extrudate has a relatively lower Y.S and U.T.S..

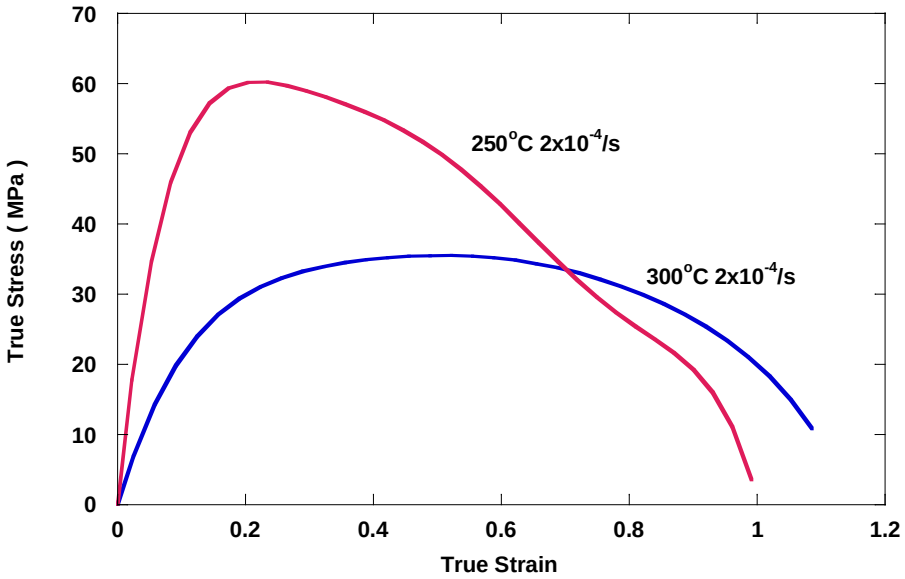

Figure 5.10 High temperature tensile properties of biaxial extruded ZK60 with different testing conditions.

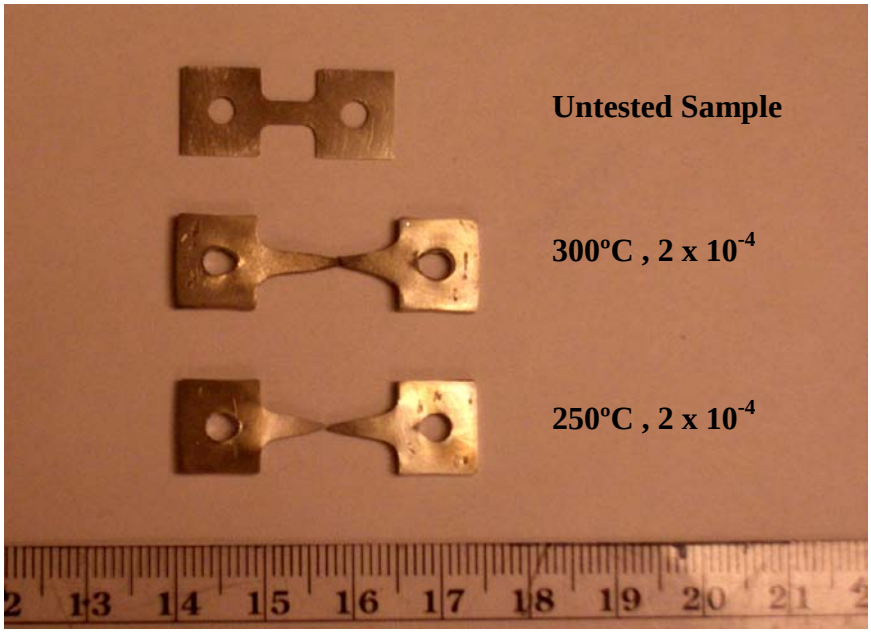

Figure 5.11 ZK60 tensile samples tested at elevated temperatures (300ºC and 250ºC). The strain rate was set at $2x10^{-4}$/s. Both samples show superplasticity which is evidenced by the pointed fracture tips. The 300ºC sample has 252% elongation and 250ºC sample has 244% elongation (shoulder to shoulder distance).

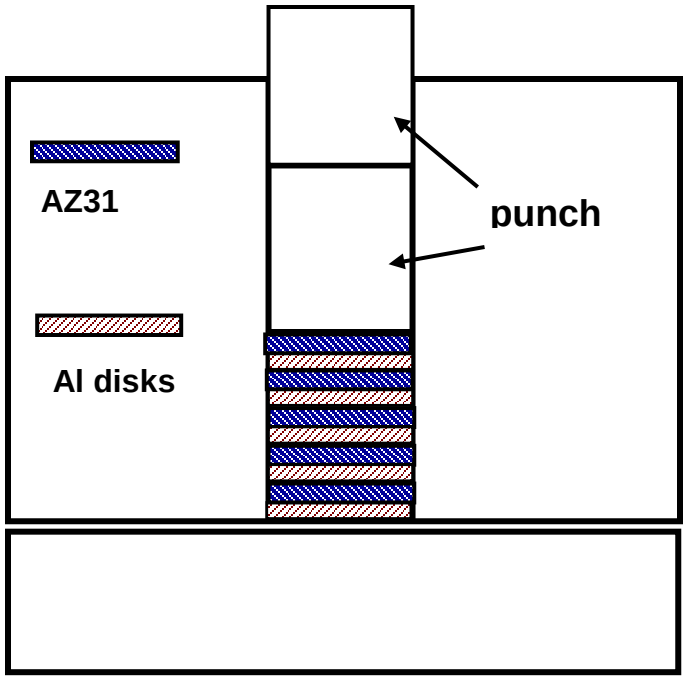

Figure 5.12 Schematic illustration of the assembling of Mg and Al disks inside the biaxial extrusion die. Five 1 inch diameter AZ31 disks and Al disks with 0.1 inch and 0.04 inch thickness, respectively, were stacked alternatively at the bottom of the die. Upon extrusion, Mg and Al were extruded out to become a single composite sheet.

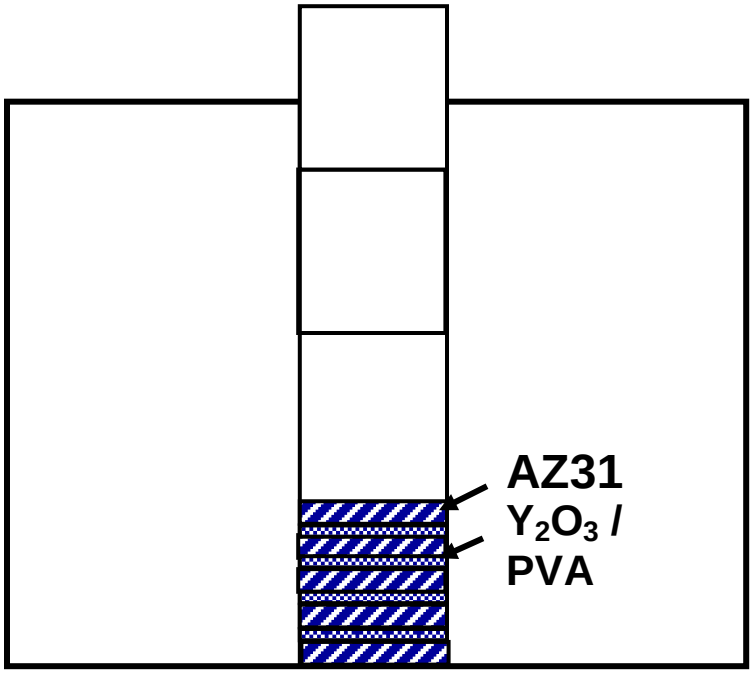

Figure 5.13 Schematic diagram of the set-up of AZ31 disks and Y_2O_3 powder inside the biaxial extrusion die. Each AZ31 disks were coated with Y_2O_3 powder in PVA in both front and back side. Extrusion was done at 220ºC.

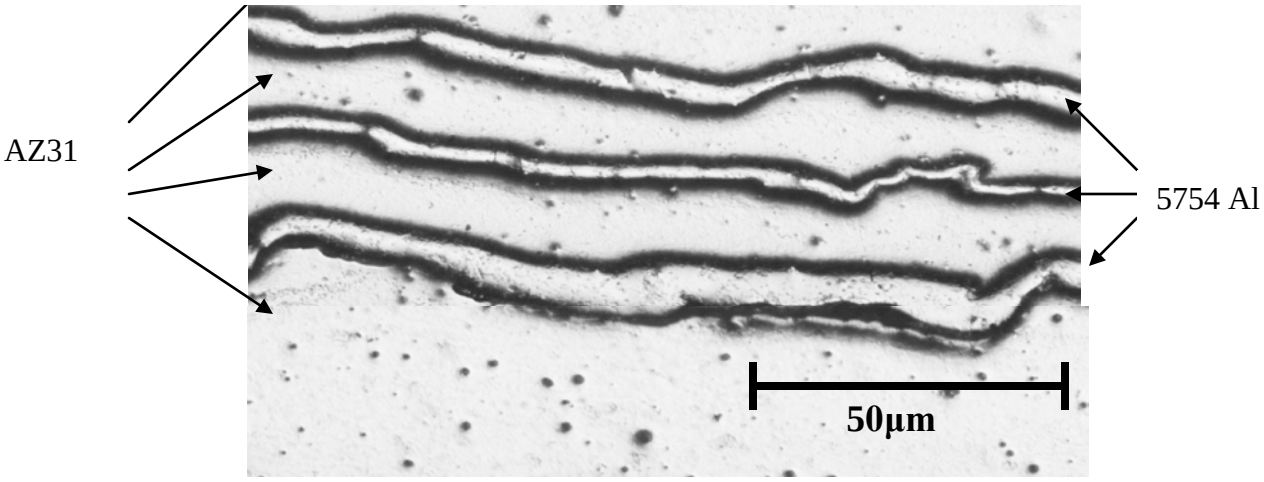

Figure 5.14 Microstructure of the extruded Mg-Al composite. Mg layers appeared to be much thicker than the Al layers.

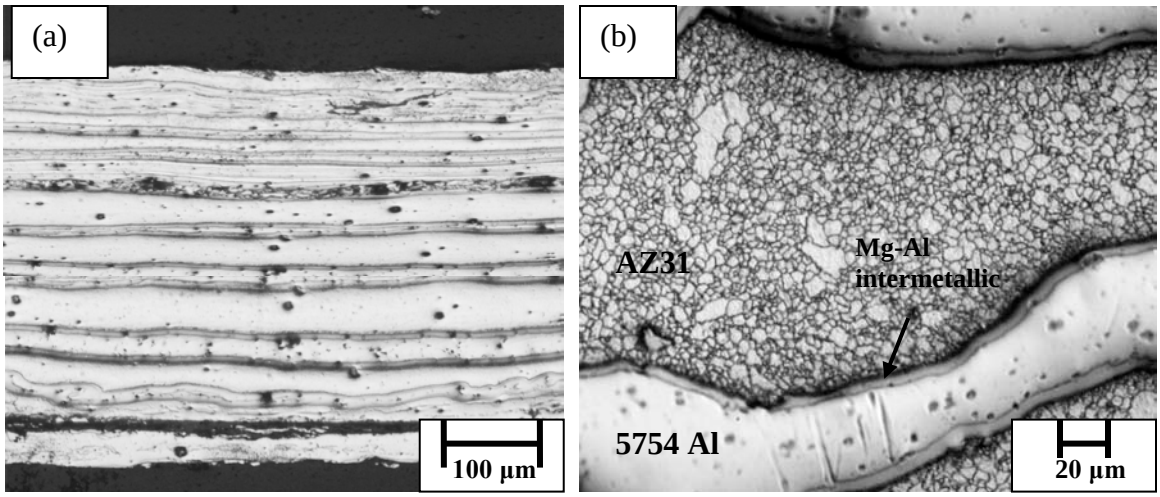

Figure 5.15 (a) Microstructure of composite sheet after 2nd extrusion. Many more layers of Mg and Al are shown in the sheet compare to the sheet in the first extrusion. (b) High magnitude picture shows fine grained AZ31 layer in between two 5754 Al layers. Mg-Al intermetallic is formed in between Mg and Al layers as indicated by the arrow.

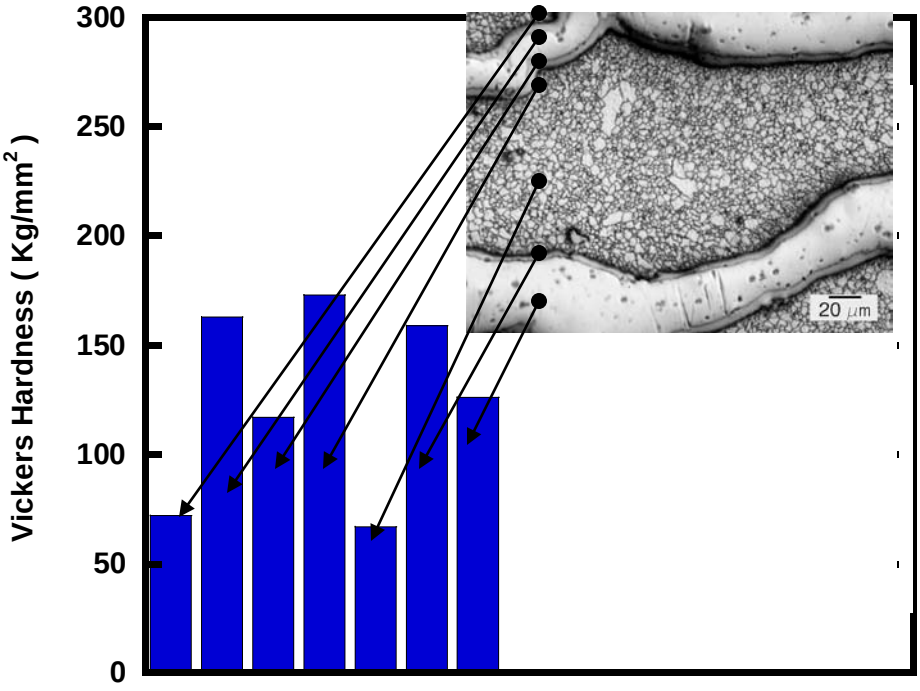

Figure 5.16 Hardness variation in the Mg/Al composite.

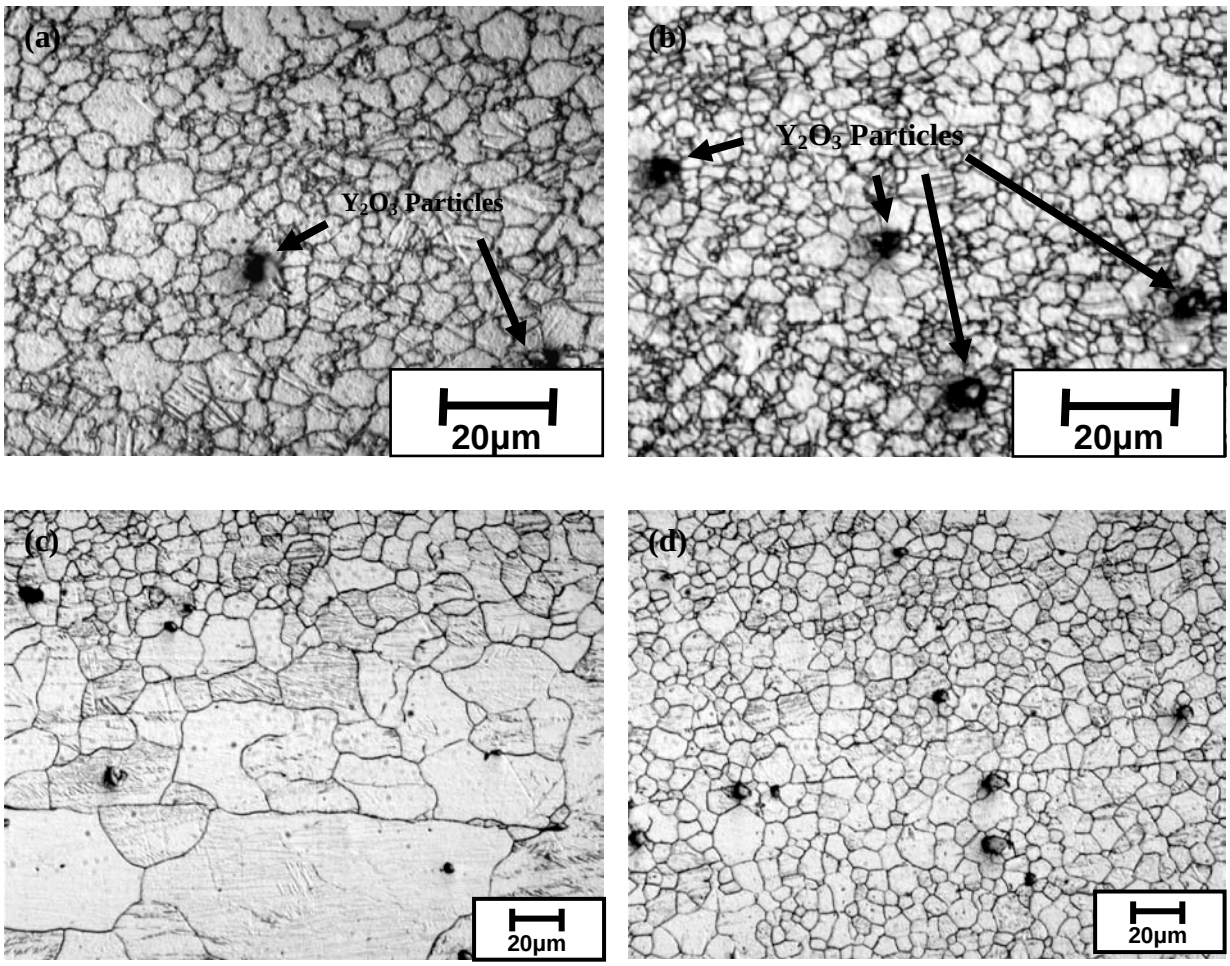

Figure 5.17 Microstructures of (a) Mg-Y_2O_3 with low Y_2O_3 content (0.2 wt%) after extrusion. Black dots shown in the microstructure are the Y_2O_3 particles. The average grain size is 6.4 μm. (b) Mg-Y_2O_3 with high Y_2O_3 content (0.5 wt%) after extrusion. More Y_2O_3 particles are shown with finer grain size of 4.2 μm. (c) Microstructure of low Y_2O_3 content AZ31 after annealing at 230ºC for 13 hrs. Some region with abnormal grain growth is seen at the bottom of the picture. (d) Microstructure of high Y_2O_3 content AZ31 after annealing. Higher Y_2O_3 content obstructed the movement of the grain boundaries hence no abnormal grain growth is shown in the sample.

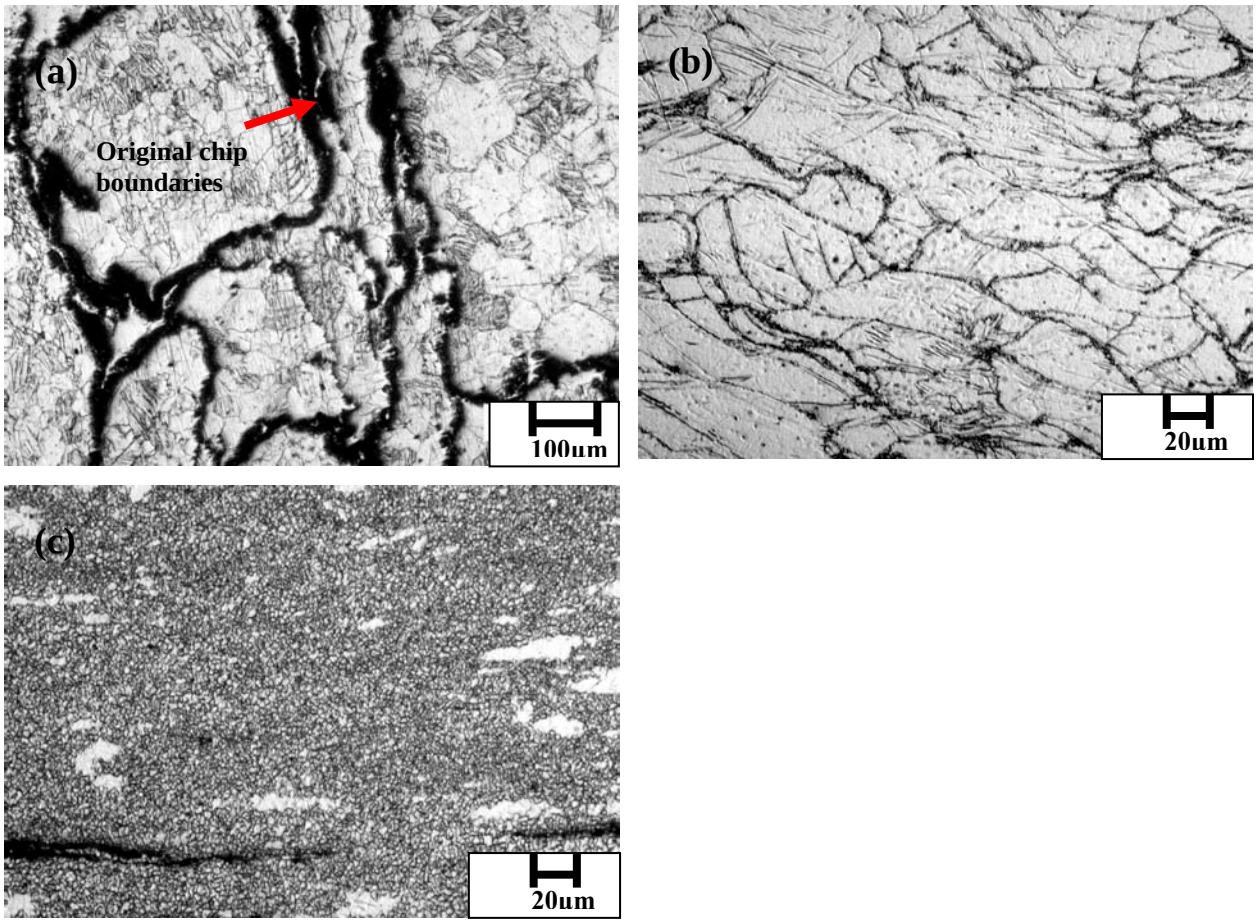

Figure 5.18 (a) As consolidated Mg-B. The ZK60 chips didn't seem to be bonded well due to the appearance of elongated voids around the original chip boundaries. (b) Mg-B alloy after first pressing. The voids seem to be greatly reduced after the pressing. Grains are elongated perpendicular to the pressing direction with many shearing lines. (c) Mg-B alloy after biaxial extrusion. It shows bimodal structure with 94 % fine grains and 6 % large grains. The average grain size of fine grains is 1.1 μm. Some long bands with width of 3~5μm are shown in the Mg matrix.

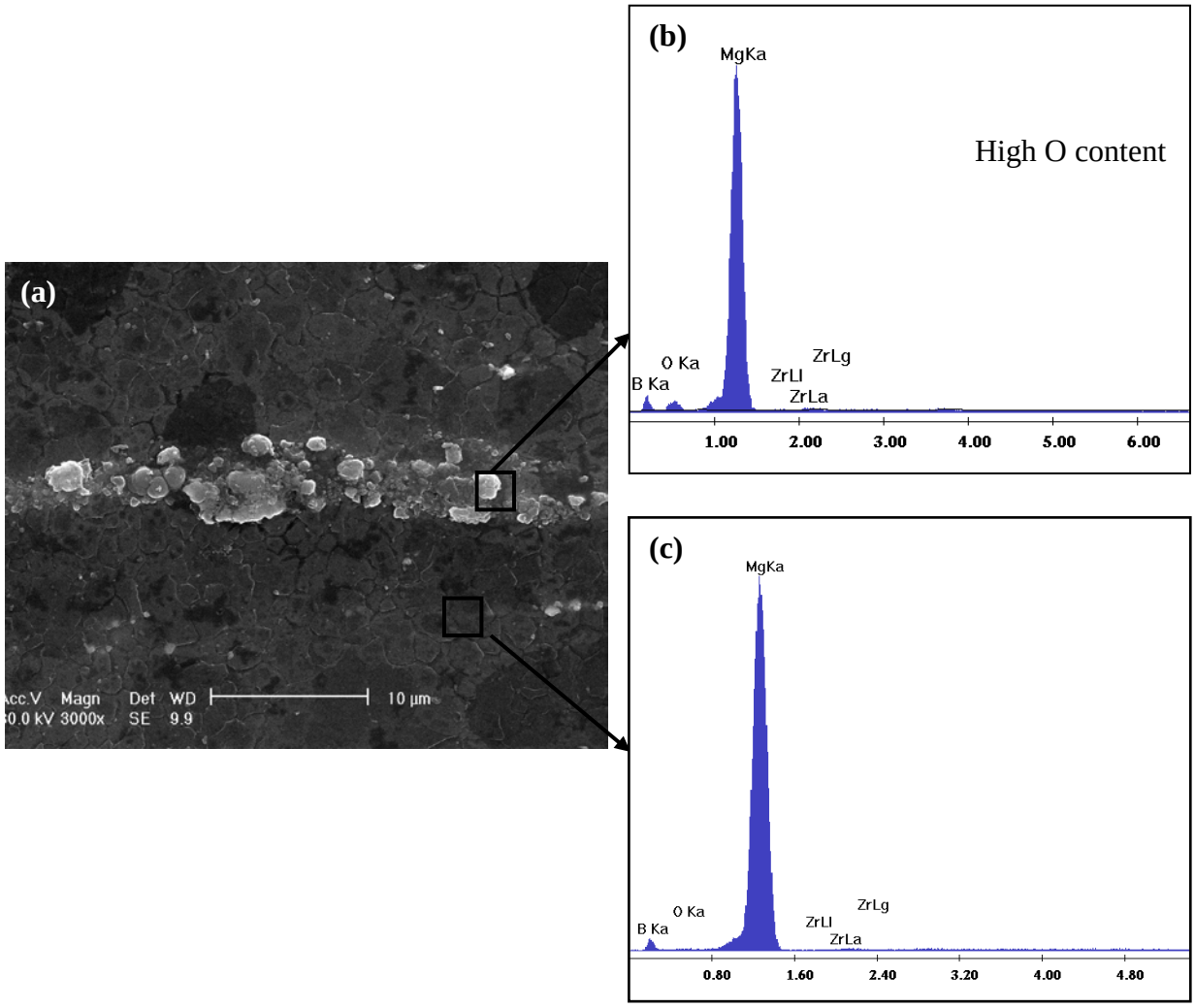

Figure 5.19 EDS analysis of the as extruded Mg-B. The white band observed in the SEM image in (a) has a high oxygen concentration and the Mg matrix doesn't have oxygen content as shown in the edax analysis in (b) and (c). This high oxygen concentration area (white band) is believed to be the magnesium-borate ($Mg_2B_2O_5$) collects.

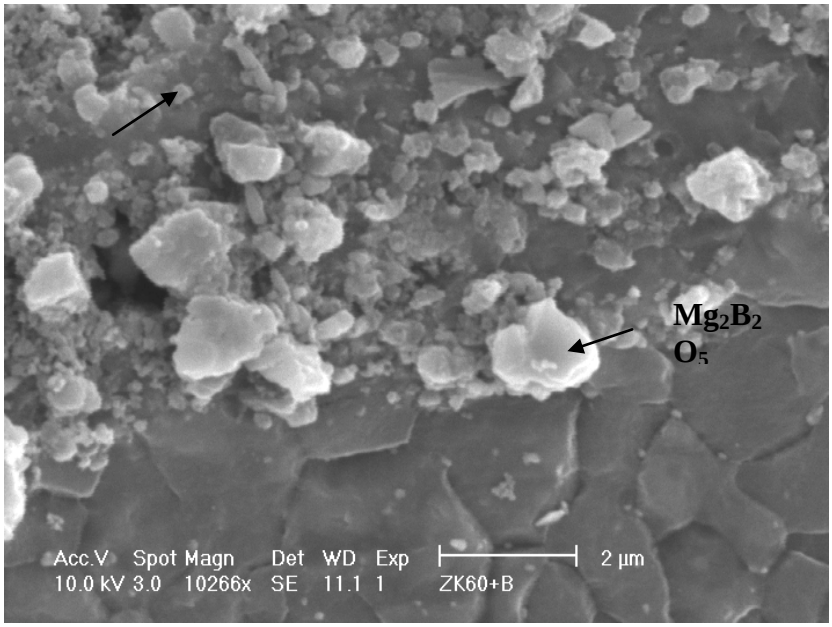

Figure 5.20 SEM image of extruded Mg-B. Band of $Mg_2B_2O_5$ is believed to be formed on the original chip boundaries where entrapped oxygen reacted with the boron and magnesium.

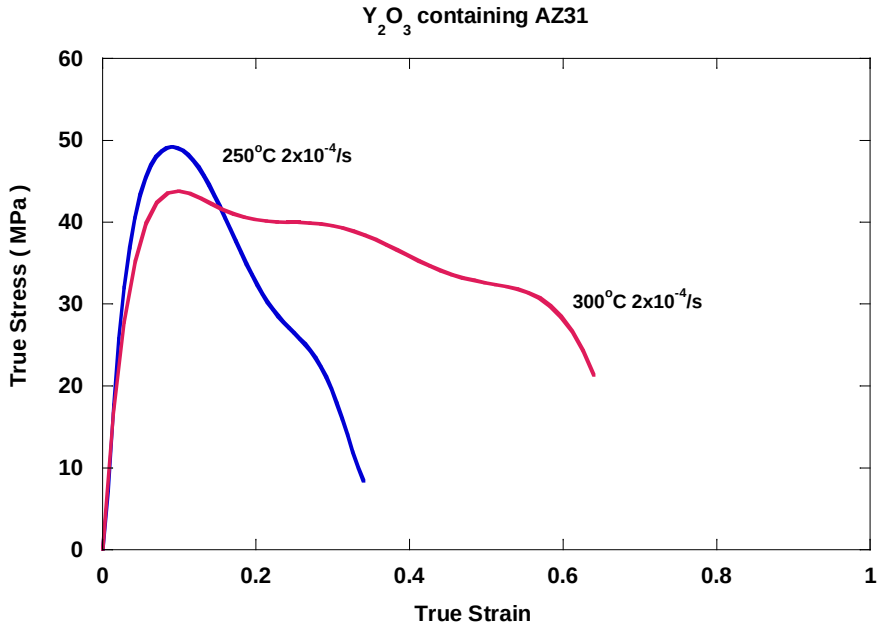

Figure 5.21 High temperature tensile properties of Mg-Y_2O_3.

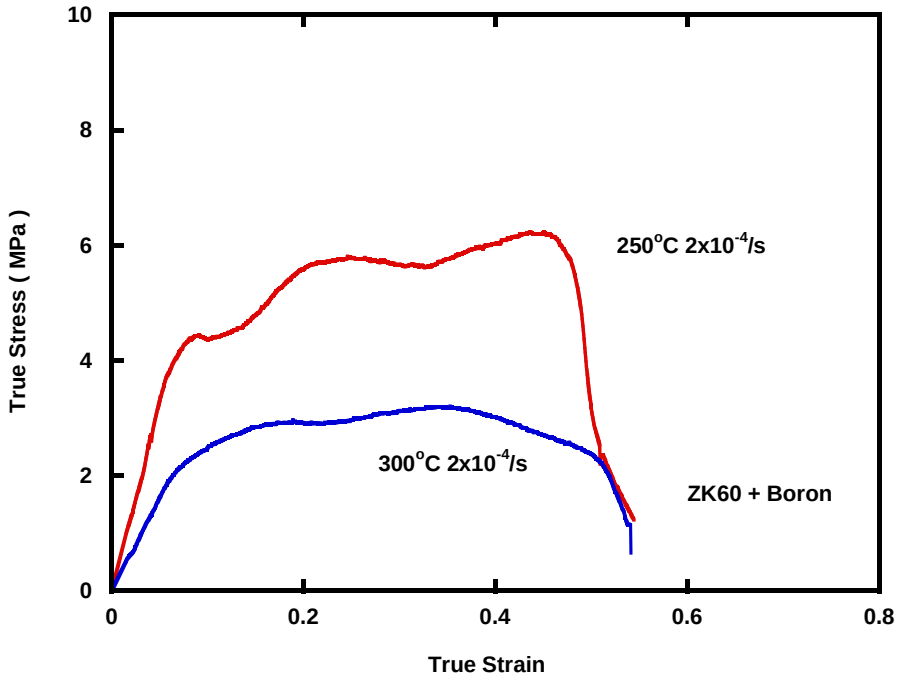

Figure 5.22 High temperature tensile properties of Mg-B.

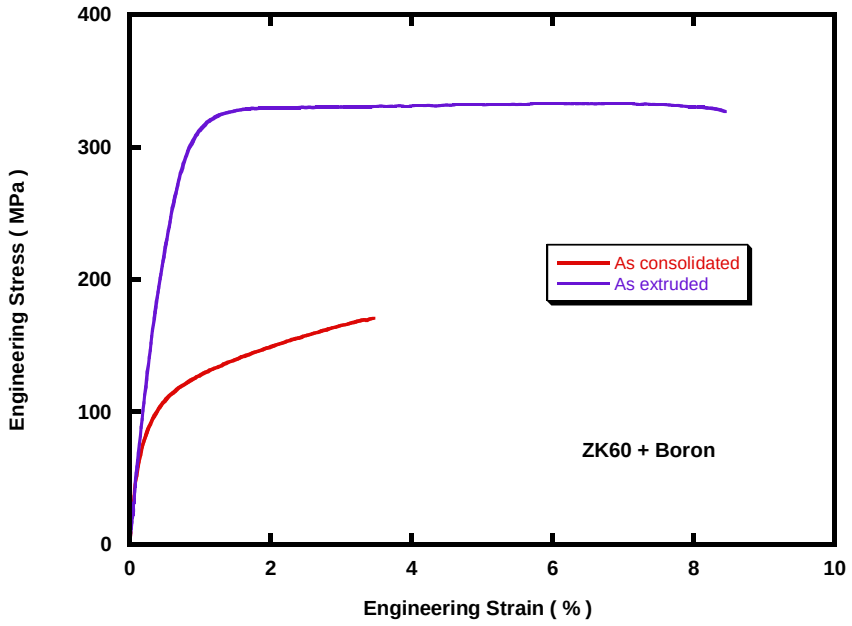

Figure 5.23 Plot of room temperature tensile properties of as consolidated and as extruded Mg-B. Both yield strength and ductility of extruded sample are much greater than the as consolidated sample.

Appendix 5A

Introduction to *popLA* and the processing tutorial
(adopted from popLA_manual provided by The Regents of the University of California and John S. Kallend.)

The computer program *popLA* is primarily designed to evaluate pole figures generated by 4-circle goniometer X-ray diffraction equipment but can also be used with pole figures generated from other sources (e.g. neutron diffraction). *popLA*'s data analysis programs correct pole figure data for background Xray counts, the drop in measured intensity which occurs at the edge of the sample due to geometric considerations, and sample misalignment. Two types of analysis, the harmonic method and the WIMV method,may be used to calculate the orientation distribution of the sample. Pole figures and orientation distribution determined by *popLA* may be displayed or printed on a variety of hardware. The tutorial of *popLa* is listed in the following pages.

TUTORIAL

This section gives a quick guide through a “standard procedure” for an easy case. It is assumed, for this exercise, that you already have an “experimental pole figure (.EPF)” file: with experimental corrections likedefocusing and background already incorporated, and in the right format. Appendix B2 will discuss how you getraw data into an .EPF file.The specimen name for this case is “demo”. All the files you will generate are already contained in`C:\X\DEMO`. In addition, this subdirectory contains a file TRY.EPF which is identical to DEMO.EPF and shouldbe used to regenerate a whole set of TRY.* files (without overwriting the DEMO.* files).The sequence in this tutorial does not follow the sequence in the *popLA* menu, but rather how you mightend up using *popLA* routinely later. References to the different screens are made by page number, to the optionon that page by #; e.g.: p.2#4, page 2 (in this case the Massage page) option number 4 (in this case the RotatePole Figures option).

BEFORE YOU START

• *popLA* must have been installed (from the yellow and blue disks, see Appendix A3) into `C:\X` on a PC (which
requires about 4 MB)
• Your AUTOEXEC.BAT file must have been augmented as suggested in AUTOEXEC.POP: put `C:\X` into thepath (preferably early); and (after the path statement) add the line: APPEND `C:\X /path:on`. There aresome problems with this recommendation; for other options, see Appendix A3.
• The computer must have been configured to have at least 540 MB of free memory (for some programs); this isthe last number given as an answer to ***CHKDSK***.

LOOK

At every stage, you will want to see what has been accomplished. We will use two instruments: p.1#1: lists a file (which we'll do later); andp.6#2: plots it on the screen and allows you to make hardcopies. The quickest way to make hardcopies (althoughnot WYSIWYG) is by downloading our special fonts (POPFONT?.HP) to an HP Laserjet II or better: do thisnow by entering ***popLA*** (from your work directory), opting for p.6#2, and answering `2` to the first question; itwill take a while but during any future use, skip this step by answering `0` to the first question.PlotNow stay within POD and merely `RETURN` upon every question (which selects default values), until it asks:`"Enter name of data file # 1": try.epf` and then again `RETURN` until you see that the calculations are running. Pretty soon, you'll see a pretty picture.Play
• Press `F1` repeatedly to see different colors and gray-shades; some have eight values, some fourteen (plus blackand white); however, the contour lines are drawn in at eight levels only, in either case.
• Look at the scale bar: there are numbers that go, in a logarithmic scale, from the minimum to the maximum.To get a nicer scale, press `F2`; when it asks you for a maximum, answer `400` (for this file), and then `3` to thenext question. To all other questions, `RETURN` to get the defaults. Eventually, you'll see a new picture. Notethat there are no contour lines (that was a default choice); that the region just above and just below randomdensity have the same shade; and that pure black and pure white (or pink) are used to show regions in whichthe density is beyond the limits you specified.(At this point, you should perhaps stop playing for now, and go on.)

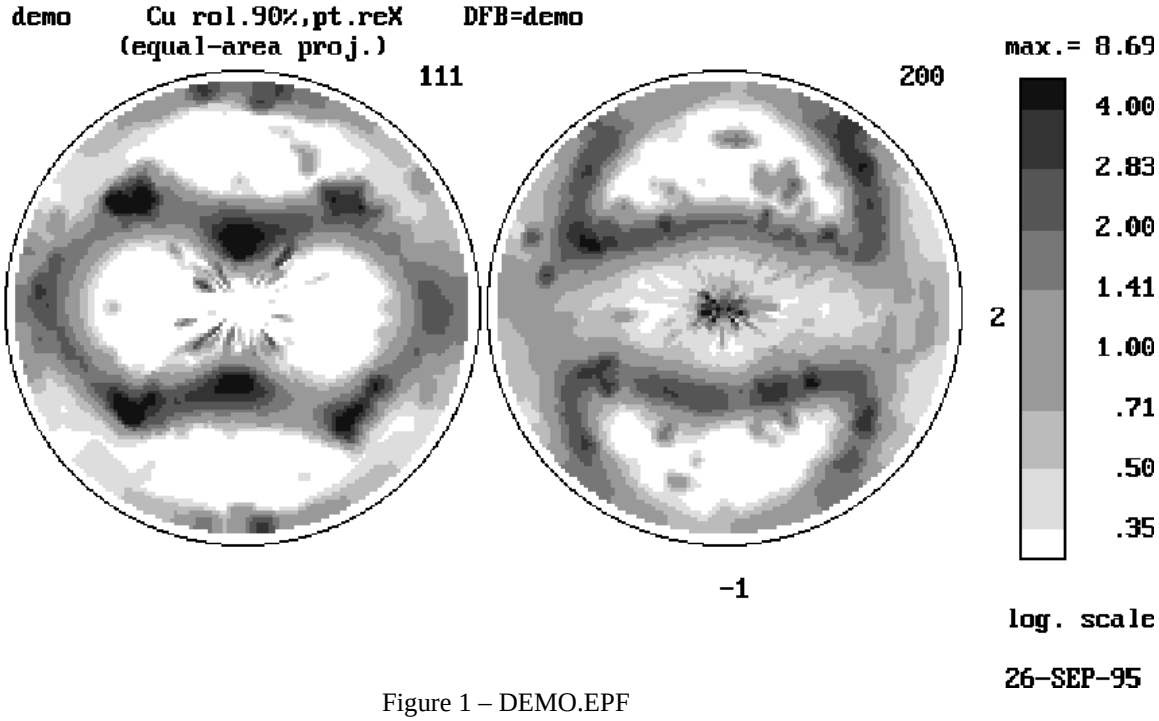

Figure 1 – DEMO.EPF

Print the plot

Now press F3: it will make a file copy (black/white and with lower resolution) which you will then be given anoption to print (hopefully self-explanatory). If the print doesn't come out right, restart the printer (therebydeleting all downloaded fonts) and then download ours again.Inspect the fileGet yourself to page 1 of the menu and select ***1***, then ***try.epf***. You will see the general format. (Press p to printout the file.) It will be worth your while to study Appendix B2 some time to understand all aspects of theformat. For now, we emphasize only a few things:

• The first line contains, in its first eight characters, the “specimen name” (here “demo”). This specimen namewill be used by some of the programs, with new extensions. (The rest of line 1 can be arbitrary comments –some of which may get overwritten later.)

• The second line has first an identifier ("(111)" in this case). Page down a few times to see that this file in factcontains 3 pole figures, identified with their indices, and separated by a blank line (and a repeat of the titleline).

•Go back home. In line 2, the next number is 5.0 (the angular increment in the radial direction) and then 80.0:this is the tilt to which measurements were made. Plots are always made to the angle listed in this position.Note, however, that the file contains numbers right up to 90°: these come from a simple extrapolationprocedure for the purpose of providing a preliminary normalization of the pole figures.

• In line 2, the second number from the end is 100: it is a scaling factor (multiplied by 100); if any of the datavalues would exceed 9999, the whole file is multiplied with a factor, and this factor (×100) is shown in line 2.(It would be less than 100.)

• Immediately preceding the 100 are 3 integers (" 2 1 3" in this case) which reflect your choice of axis nomenclature, in the sequence right-top-center on the figure. You will note that what you looked at before hada "2" on the right – reflecting our choice to call the rolling direction "1" and plot it on top. Exit by pressing X.NOTE: It is at this stage that you should edit your .EPF file, if you ever want to, because all the information in itis carried forward to all subsequent files!

MASSAGE

There are three common things that one may wish to do with experimental pole figures before proceeding with a

detailed analysis: rotate them, smooth them, and normalize them better. (Other "massaging" items will be discussed in the DETAILS section.)

Rotate
The experimental pole figures shown above seem to have some symmetry – except that it is not exactly alignedwith the axes. This could, for example, be due to a slight misalignment of the specimen on the goniometer. Iforthotropic symmetry were imposed on the data without first aligning them with the axes, some accuracy wouldbe lost.
• The program ROTATE (p.2#4, option 1) can analyze the data for this effect (by looking at sin terms in the harmonic expansion) and suggest an angle by which the pole figure should be rotated in order to make it as symmetrical as possible around the axes. In addition, you may wish to impose another rotation around the center of the pole figure; e.g., 90° if the way the specimen was mounted resulted in the rolling direction appearing on the right and you want it on top.(Other utilities in ROTATE are discussed in the DETAILS section.)The output file is called .RPF.SmoothSome data are very spotty; e.g., when only a few grains were covered. It is a matter of judgment in every casewhether this effect should be smoothed out in the beginning, or at the end of the analysis (or never).
• The program SMOOTH (p.2#8) provides an option to apply a Gaussian filter of arbitrary breadth to the data.We have found smoothing by 2.5° or 5° to be useful under some circumstances (remembering that this isabout the grid resolution). You may try the program now using .RPF as an input. Note, however, that the "maximum" values observed in the texture decrease. For this reason, we will not use the smoothed file for further analysis, only perhaps for plotting.• The output file is called .MPF ("Massaged Pole Figure" – even when you later use it to smooth whole ODs).Inspect it via p.1#1: note that the two last actions were recorded on the title line.Normalize using the harmonic methodThe orientation distribution (OD) analysis in terms of spherical harmonics may be used as the principal tool ofQuantitative Texture Analysis (QTA), or a discrete method may eventually be preferred by the user. Even in thelatter case, harmonic analysis brings a significant initial advantage: it predicts the intensities in the unmeasuredrim of all pole figures in a way that is consistent with all pole figures. In the process, all pole figures are renormalized,and this can be important (for example, in the WIMV program in *popLA*).
• Use p.4#2, with your .RPF as input. Answer defaults, and use only the output file .FUL: it is identical to theinput file except for the rim and the normalization. (The title line records this fact, but the two previous actions have now been dropped from being thus recorded.)This program is currently available only for crystal symmetries greater than orthorhombic and samplesymmetries that have at least one two-fold axis in the center of the pole figure.

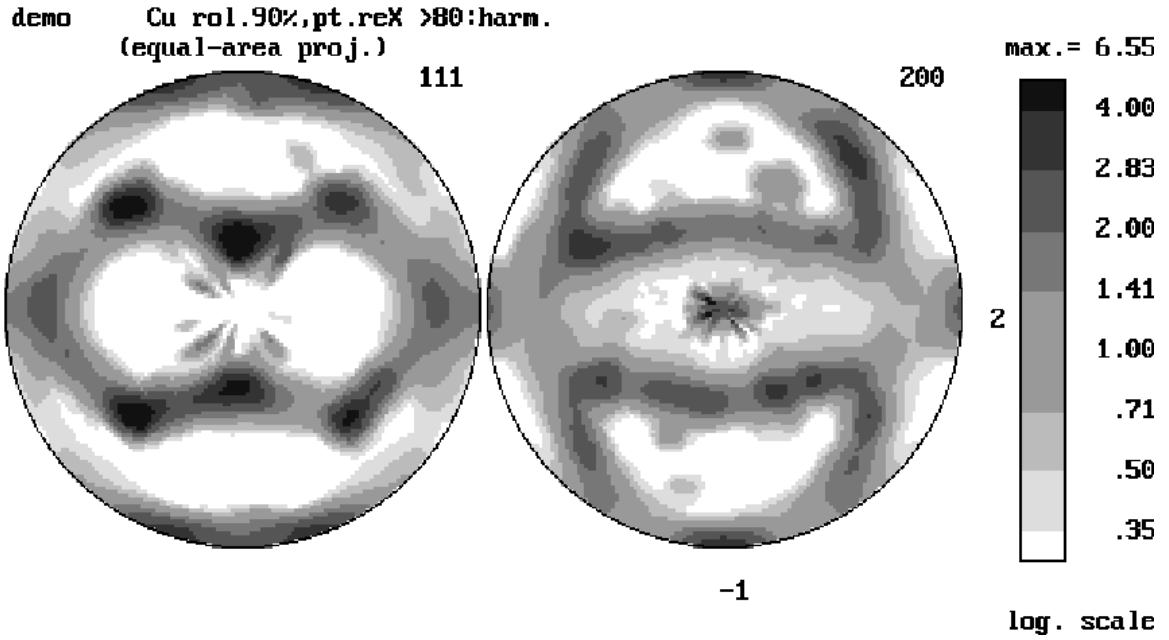

Figure 2 – DEMO.FUL

Analyze using the WIMV Method

For this, you need the .FUL pole figures just obtained; WIMV will ignore the values above a tilt of 80° (but needs the normalization obtained in the last step). You also need "pointer files". They have the extension .WIM,.BWM, or .WM3, depending on which level of WIMV you use. Use the default files supplied for now. (Lateryou can make your own on p.4#8.) There are three levels of the WIMV program in *popLA*, depending on thecomplexity of your problem: look at p.4 numbers 2, 3, and 4. We have the easiest case, so we will use the fastestprogram:

• Opt for p.4#2. Take the defaults on all options (especially the one on treating these as “incomplete” pole figures (even though they go to 90°). The progress will be displayed. The error estimates are listed for you to judge the rate of conversion. One may wish to stop when the change from one iteration to the next is onlya fraction of a percent. (For the DEMO. files, we have stopped after iteration 17. The number of iterations,the final error estimate, and the Texture Strength will all be listed on the title line of the resulting .SOD and.WPF files.At the end you have an option as to which Euler angles you wish to have the files sequenced in. Your choicewill be recorded in the output file, on the second line, position 5: B or R or K (for Bunge, Roe/Matthies, orKocks). Pick ***1*** for now.

• Before you look at the files, opt for p.4#7: make a file of WIMV-calculated inverse pole figures, .WIP. Sinceyou have just made it, you may as well look at it first:

• Opt for p.6#2 (for which you need to go back to p.1 first), answer `0`, then defaults until "...plots on page?" Ifyou answer `3`, you get the whole file; but answer `2` to get the Z- and Y-axis pole figures. (You can print only2 plots in higher resolution). Note that a whole quadrant is shown even though, for this case, just one of the“stereographic triangles” would have been sufficient. (You can cut it out...)

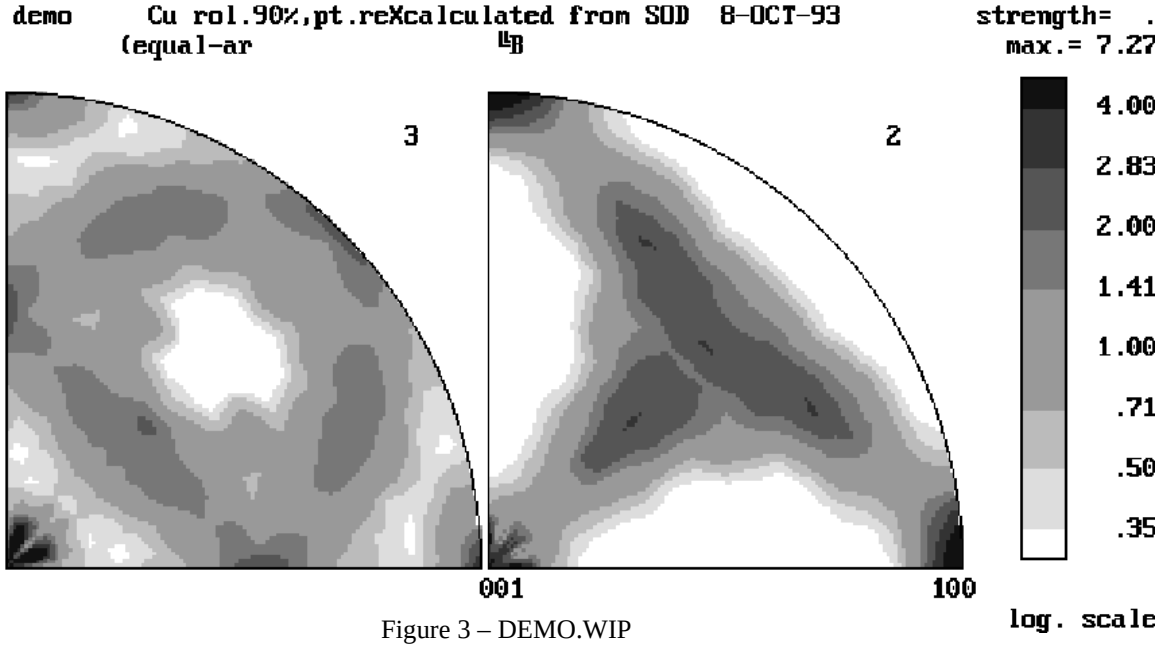

Figure 3 – DEMO.WIP

• Now you are back on p.6, opt again for #2, etc., but this time look at .WPF: the WIMV-recalculated pole figures; the first two suffice. Use scale `400/3` again. Do they look familiar? They should be similar to the original .EPF, only rotated a bit and symmetrized, and completed in the rim. Since we assumed orthotropic sample symmetry (as one of the default answers while WIMVing), the four quadrants of the pole figure contain the same, averaged information. Plotting only one quadrant allows a better resolution of the figure inthe same area.For a quantitative comparison of the recalculated and the input pole figures, we could either EXPAND the .WPF(p.2#7) or, which we suggest, SYMMETRIZE (p.2#6) the input pole figure. The actual input to WIMV was the.FUL pole figure, and we compare to it – firstly, because it has the rotation already built in, and second becauseit is properly normalized. As a fringe benefit, we get a comparison of the rim predictions from WIMV and fromthe harmonic method. Thus:

• Opt for p.2#6 (via p.1), using .FUL as input, getting .QPF as output. Now back to p.6#2 (via p.1). Try something new: the third question within POD asks whether you want all standard options, and you have answered "yes" ***(0)*** so far. Answer `1` "for any change". Now opt for the default of all options until the directive is "`Enter the number of FILES to open`": answer `2`. Now you know why it always asked you to "`Enter the name of date file #1`". This will be the next question and you pick .QPF. For the"maximum" you pick `400`, and for the next number enter `3`. When the question data file #2 comes up, enter.WPF, then later the same scale options. You will get the {111} pole figures side by side (and to the samescale: one good reason to pick the scale yourself rather than taking the defaults!) Inspect the similarities anddifferences by eye. (You may also wish to get rid of the net in the right figure, or put a net on both: you canplay using `F2`. But these nets don't print on the Laserjet by the procedure we are using now.)

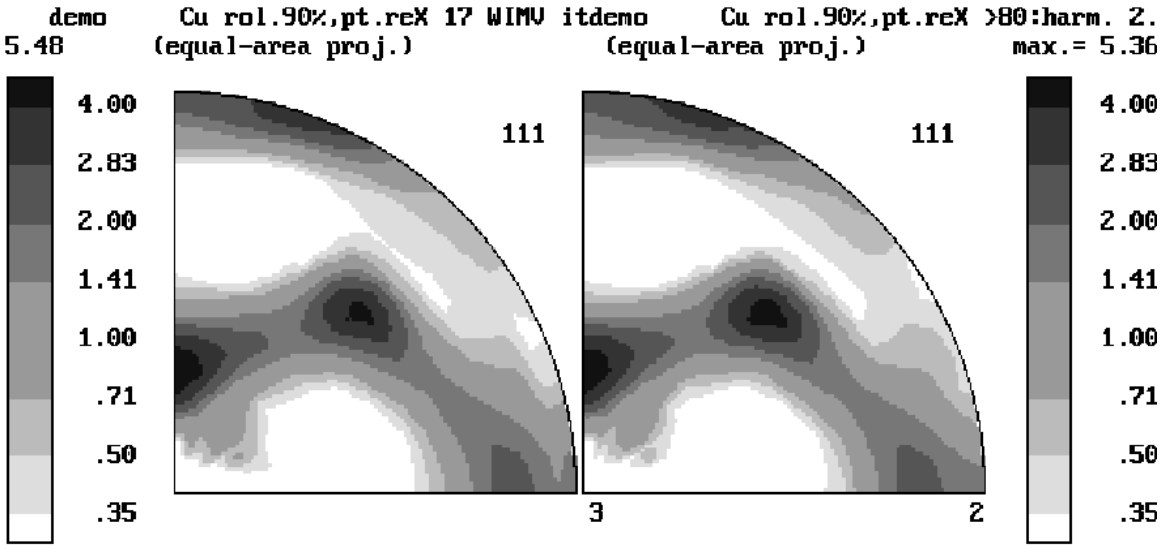

Figure 4 – DEMO.WPF and DEMO.QPF

• To do the comparison between the two files in a quantitative way, opt for p.2#9 (via p.1) and make a difference file (.DIF), subtracting the .QPF from the .WPF. It will do it for all three pole figures. (It will ask you whether the difference in second-line parameters is OK: it is.)

• Go to p.6#2 (you are already on p.6!), defaults, 2 plots, until it tells you "`THIS FILE CONTAINS NEGATIVEINTENSITIES`": answer `2` to make a scale symmetric around zero. For the amplitude, pick `140`. You willsee, for both the {111} and {100} pole figures, the actual difference between recalculated and experimentalvalues. Note that the differences are small everywhere but especially in the areas of very low density: thisgood fit is a consequence of the WIMV algorithm. It is also noteworthy that the peaks are higher(particularly, the "copper" and the "cube" orientations) than those predicted by the harmonic method.

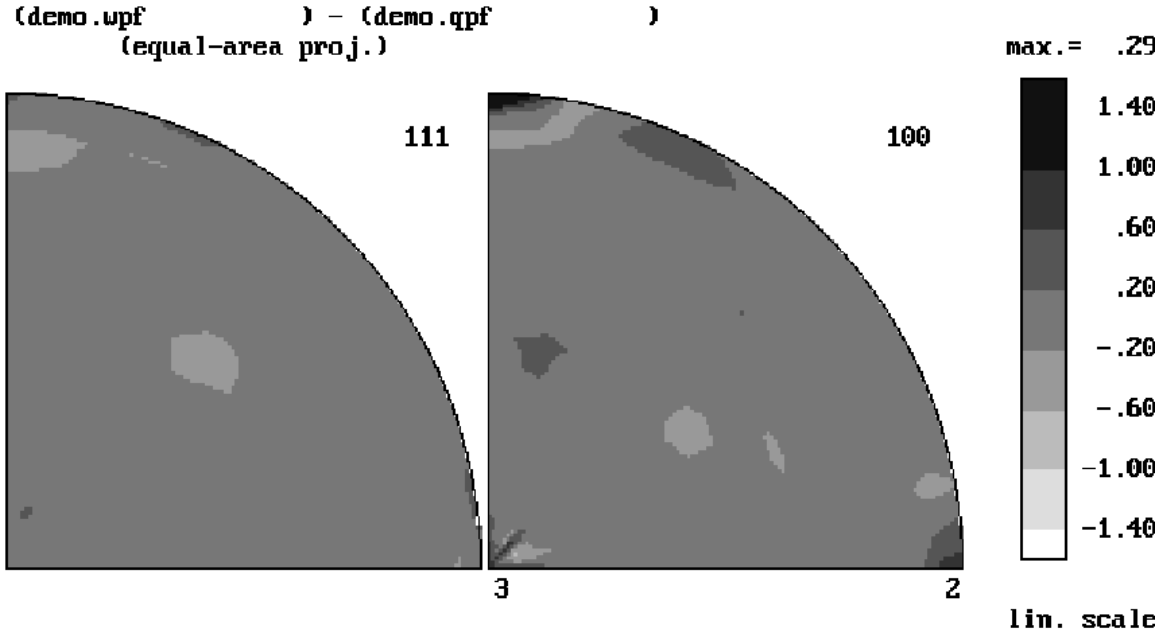

Figure 5 – DEMO_W-Q.DIF

Concerning Hardcopies

The prints you have been making are fast and adequate, but of lower resolution than the screen; and they do notcopy well. The figures in the document result from a different way of making hardcopies. We used a commercial screen-dump program (GRAFLASR) to make a .PCX file, then opened it in PAINTBRUSH (withinWINDOWS 3.1), and printed in the "coarse-dither" option. To get all eight gray-shades, you must have a 256-color monitor. The figure may not look pretty to you now: but copy it (it works) and then copy it to a reductionof less than 70%: it works, and it looks pretty. (If you want just a single figure, for example one transparency,you can print out in high resolution with a 600dpi printer – but it doesn't copy well.) Also try the regular Laserjet method (via `F3`), having loaded POPFONT?.HP when first entering POD). This works as expected for 2 plots; for more plots, the arrangement on the hardcopy will be different from thaton the screen. The option to use PostScript is similar (via `F4`).

DISPLAY the three-dimensional Orientation Distributions (ODs)

Now inspect your .SOD (p.1#1). The format looks much like the .EPF, but there are only 19 lines of data in eachblock. The OD (orientation distribution) files list the intensities in sections of 3-dimensional orientation space.In the .SOD, each section is a “partial inverse pole figure”: partial in that the third angle is constant; the sum ofall sections is the projection, which is the inverse pole figure for axis 3, which is appended as the last block.This file is only one way to arrange the derived densities in orientation space; it is the “Sample OrientationDistribution”, or. SOD (with respect to crystal coordinates).Each section ontains one quadrant (for cubic crystal symmetry): 19 lines. The sections are given at every 5° ofthe section angle. There are 19 of them (because we chose orthotropic sample symmetry). This is too many to plot and inspect comfortably.• Let us pare the file down to sections every 10°: p.5#5 will let you do this. Call the output file .SOS (the last Sfor Selected sections). Plot it (p.6#2): 11 plots per page. If you use the scale `400/3` again, the last plot (theprojection) should look quantitatively like the .WIP plotted out before (only smaller in size). However, sincethe densities in 3-D orientation space are usually higher than in the projections, it is better to plot it to adifferent scale: try it now, using `F2`, (put a net on every plot for a change, but leave out the contours), thenchoose the maximum `1600`, next `3`.A different way to section orientation space is as "partial pole figures" or a "crystal orientation distribution", or.COD (with respect to sample coordinates).

• To rearrange the OD that WIMV gave us from an .SOD to a .COD, use p.5#3, then again pare to somethingyou can plot: p.5#5, call .COS. Plot the 11 sections: the last one is the projection, which is the {001} polefigure, and thus should be the same as the second plot on .WPF.

• Now plot the .COD again, but in square sections. From within POD, opt for non-standard options: the first one is for `ksquare`. The best scale (which defaults to linear) is `700/0`. The resulting plot is on a very coarsescale, but it should be recognizable to people who have worked with rolled FCC materials.

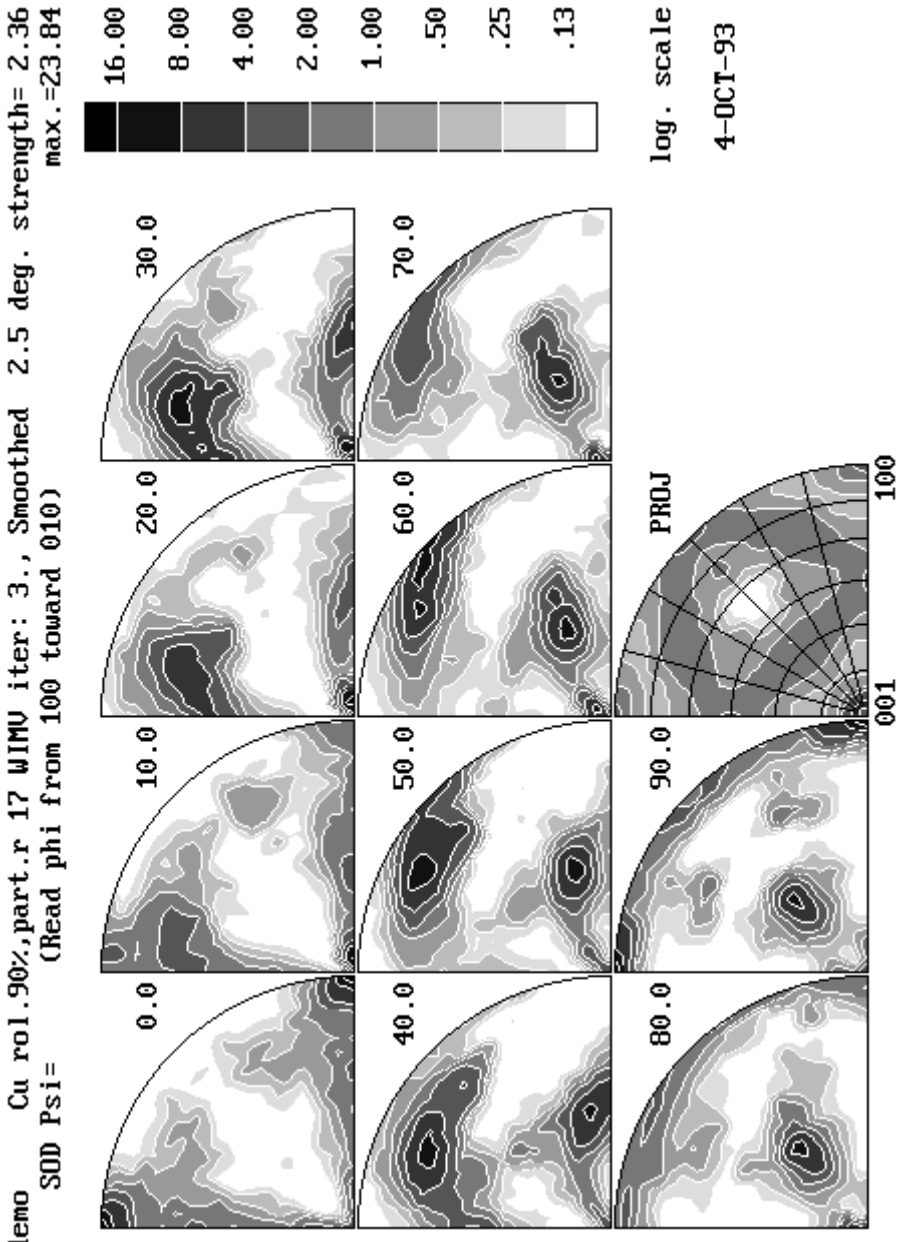

Figure 6 – DEMO.SOS

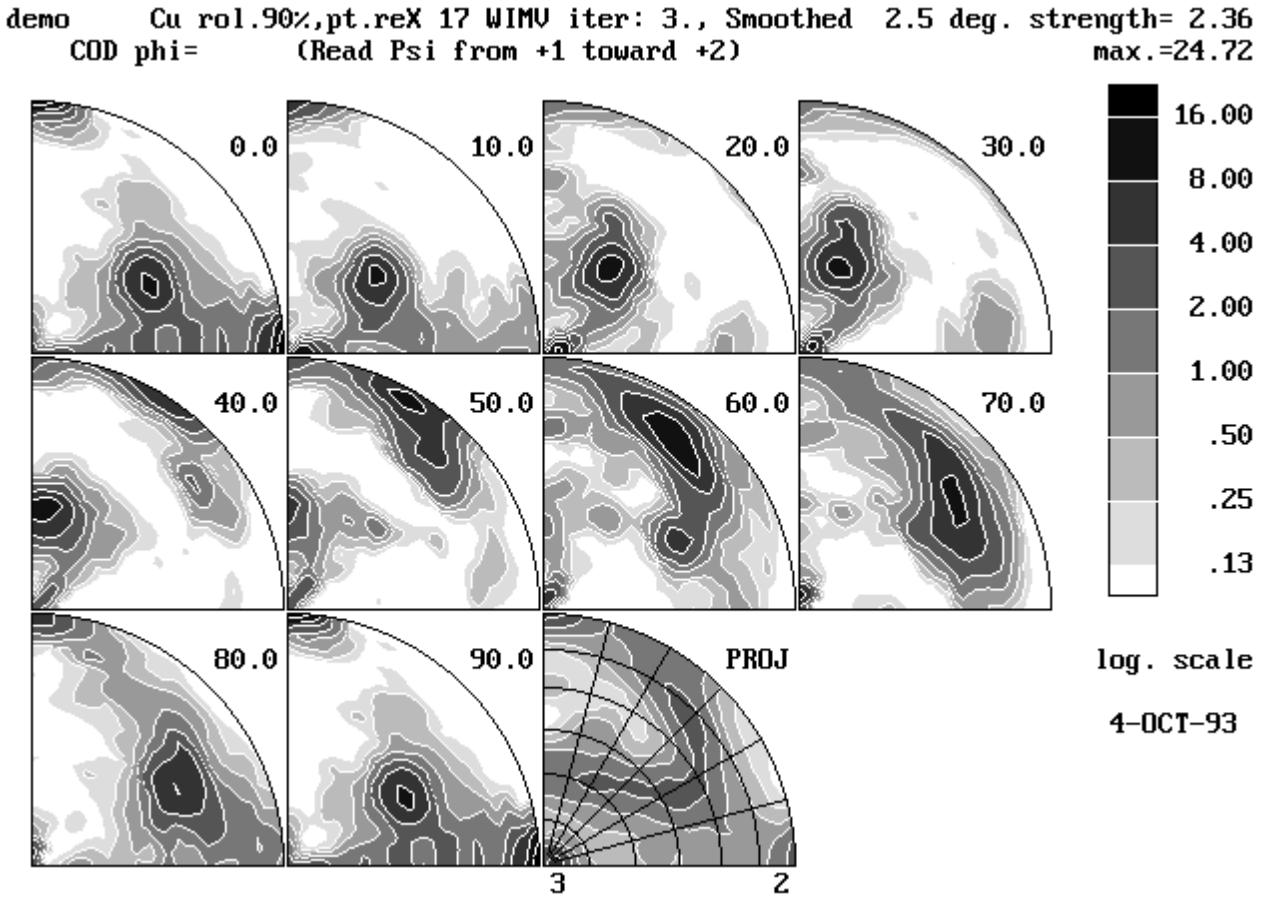

Figure 7 – DEMO.COS

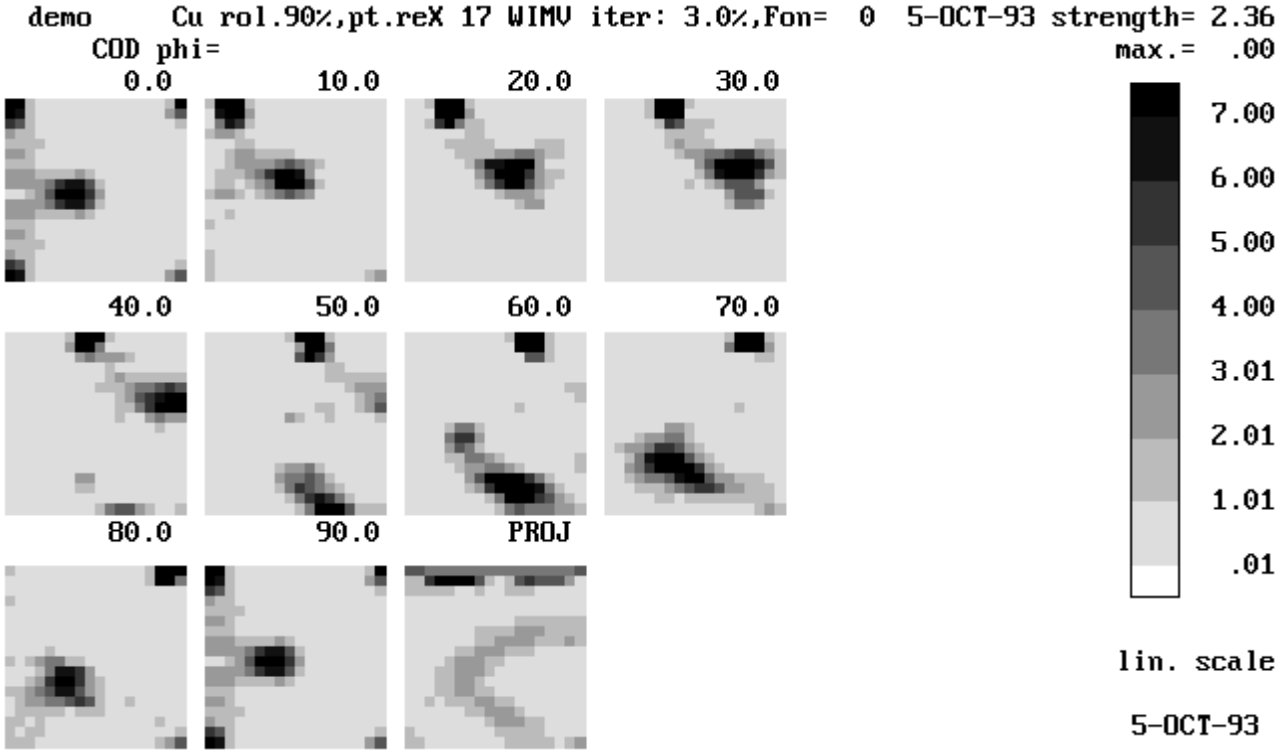

Figure 8 – DEMO.COS Square sections

In all the polar figures, there is some concentration near the origin of many sections. (This is a cube componentdue to partial recrystallization.) In the square plot, the concentrations at the top line (at various places in thevarious sections) all correspond to this one component. The best way to avoid any degeneracies for thisorientation is to use oblique sections.

• Run p.5#4, take option 2, angles from 0 to 45°. The output is .CON. For the benefit of some improvement inthe plots themselves, let us also smooth this file: go to p.2#8, range ***5.0***, do not treat as "INCOMPLETE polefigures". The resulting file is called .MPF (and overwrote the smoothed .RPF you may have made early on.The best is to rename it to .CMN, which you can do by escaping to DOS (p.1#8), then type exit to come backto *popLA*.

• Now plot (.MPF or .CMN): 10 sections. (The projection from this is the {001} pole figure again, but it is notplotted because, under some circumstances, the projections contains more, symmetrically equivalent components than are shown in the sections.) Scale `1600/3`.

• Try a few visual changes: `F2,` rewrite the first line to something descriptive, put a net on all plots, delete theEuler-angle information, stay with high resolution, but eliminate the contours (default!), finally change tovertical stacking (which allows you easier pasting for a "column figure").

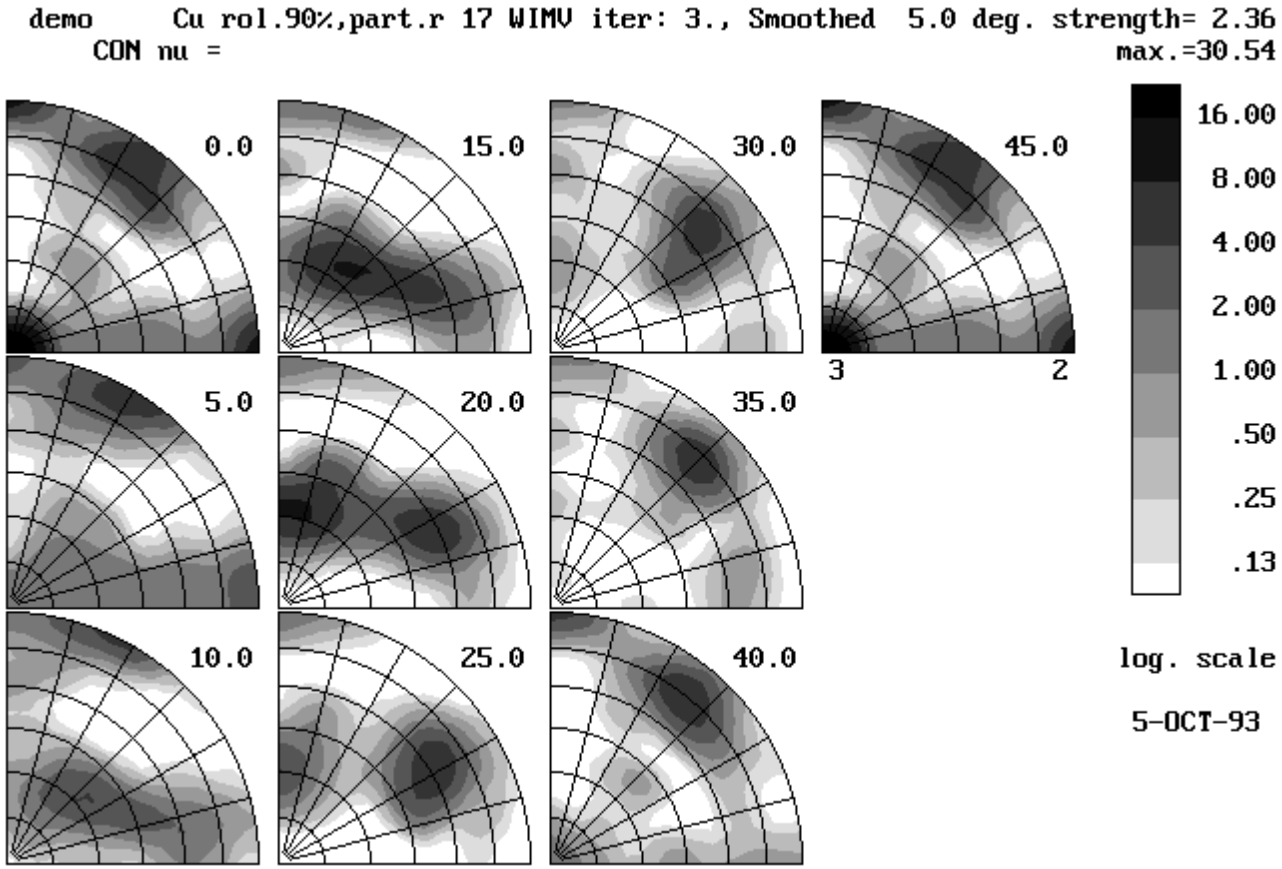

Figure 9 – DEMO.CMN

References

[1] E.D. Tabachnikova, V.Z. Bengus, Z. Vladimir, A.V. Podolskiy, V. Aleksey, S.N. Smirnov, K. Csach, J. Miskuf, L.R. Saitova, I.P. Semenova, R.Z. Valiev: *International Journal of Mechanics and Materials in Design*, v 4, n 2, p 189-195, June 2008

[2] C.S. Lee, Y.G. Ko, D.H. Shin, K Park: *Scripta Materialia*, v 54, n 10, p 1785-9, May 2006

[3] L. Saitova, I. Semenova, H.W. Höppel, R. Valiev, M. Göken: *Materialwissenschaft und Werkstofftechnik*, v 39, n 4-5, p 367-370, April/May 2008

[4] A.P. Zhilyaev, S. Lee, G.V. Nurislamova, R.Z. Valiev, T.G. Langdon: *Scripta Materialia*, v 44, n 12, p 2753-2758, June 8, 2001

[5] R.S Mishra, V.V. Stolyarov, C. Echer, R.Z. Valiev, and A.K. Mukherjee: *Materials Science & Engineering A (Structural Materials: Properties, Microstructure and Processing),* v A298, n 1-2, 31 Jan. 2001, p 44-50.

[6] T. Al-Samman, G.Gottstein: *Diffusion and Defect Data Pt.B: Solid State Phenomena*, v 105, p 201-206, 2005

[7] A. Galiyev, R. Kaibyshev, G. Gottstein: *Acta Materialia*, v 49, n 7, p 1199-1207, April 19, 2001

[8] A. Galiyev, R. Kaibyshev: *Materials Transactions*, v 42, n 7, p 1190-9, July 2001

[9] H. Watanabe, T. Mukai, K. Ishikawa, K. Higashi: *Scripta Materialia*, v 46, n 12, p 851-6, 14 June 2002

[10] J. Lin, Q, Wang, L. Peng, H.J. Roven: *Journal of Alloys and Compounds*, v 476, n 1-2, p 441-5, 12 May 2009

[11] R.B. Figueiredo, T.G. Langdon: *Materials Science and Engineering A*, v 503, n 1-2, p 141-144, March 15, 2009

[12] A. Bussiba, A.B. Artzy, A. Shtechman, S. Ifergan, M. Kupiec: *Materials Science & Engineering A* (Structural Materials: Properties, Microstructure and Processing), v A302, n 1, p 56-62, 15 April 2001

[13] C.B. Fuller, A.R. KrauseD.C. Dunand, D.N. Seidman: *Materials Science & Engineering A (Structural Materials: Properties, Microstructure and Processing)*, v A338, n 1-2, p 8-16, 15 Dec. 2002

[14] F. Czerwinski: *Acta Materialia*, v 53, n 7, p 1973-84, April 2005

[15] M. Zhang, F. Ye: *Metallurgical and Materials Transactions A: Physical Metallurgy and Materials Science*, v 36, n 7, p 1681-1688, July 2005

[16] A. Martin, J. LLorca: *Materials Science and Engineering A,* v A201, n 1-2, p 77-87, Oct 1995

[17] K.U. Kainer, J. Schroeder, B.L. Mordike: *Proceedings of the International Conference on Advanced Composite Materials*, p 1061-1065, 1993

[18] W. Kun, M. Zheng, M. Zhao, C. Yao, J. Li: *Scripta Materialia*, v 35, n 4, p 529-34, 15 Aug. 1996.

[19] R.A. Saravanan, M.K. Surappa: *Materials Science & Engineering A (Structural Materials: Properties, Microstructure and Processing)*, v A276, n 1-2, p 108-16, 15 Jan. 2000

Chapter 6

Plasticity in small tensile specimens

Abstract.

Tests have been done on Ti-1100 and Inconel 625 tensile specimens with cross-sectional area of ~400 μm^2 to ~2000 μm^2 directly machined from metal sheets. The machining processes including mechanical machining, chemical etching and focus ion beam (FIB) cutting. A small scale tensile testing fixture was special designed to test the specimens in micrometer size. SEM images have been taken to examine the deformation mechanisms of the small samples. Test results show strong increase in strength in the small samples relative to the conventional large samples.

6.1. Introduction

On the design of mechanical systems or developing new structures, understanding of the mechanical properties of materials is essential. It is common practice to test materials by the conventional mechanical tests such as tensile, compression, torsion or bending tests. From these tests the general understanding of the material properties is very well established in the past few decades. However, when the sizes of the materials come down to a very small scale (e.g. less than 100μm), the mechanical properties of the materials start to deviated from their bulk counterparts. This phenomenon was first discovered by Fleck et al.[1] in 1994 by conducting a series of torsion tests on the copper wires. In his tests, the strength of the copper wires increased with reducing diameters (volume). This finding rose interest to the material scientists and many started to test small volume samples in different test apparatus. Dimiduk[2] performed compression tests on the micro-scale Ni pillars and found small pillars hardened with reducing diameter. The detail of Dimiduk's experiment is described in the Appendix 6A. Fig 6.1(a) shows the flow stress vs sample diameter plot of Greer et al. experiment [3] by conducting compression tests on the micro-scale gold pillars. The flow stress of the smallest gold pillar (~400nm) in Greer's test is about 120 times larger than the pillars with diameter larger than 1000nm. Similar stress vs sample size plots was constructed by Kiener et al. [4] as shown in Fig 6.1(b), by conducting series of bending and compressing tests on the micro-scale copper beams. The shaded area at the bottom of the plot is the tensile stress of the copper single crystal. The curves have the same power low trend as Greer's plot and have the exponents of -0.8 for the micro-bending samples and -0.4 for the micro-compression samples. However, the power law behaviors in the plot in Fig 6.1(b) are

restricted in the micron-scale and would not apply to larger volumes. (ie, flow stresses would not change with the sizes of the conventional specimen). To compare the relationship between increase in strength and size of the samples of different materials, a modification is made using (σ-σ_0) in Y axis instead of σ. σ is the flow stress obtained from small samples, σ_0 is the tensile stress of the conventional specimens (large samples). A reconstruction using data acquired from Fig 6.1(a) and 6.1(b) is plotted in Fig 6.1(c). The reconstructed plot clearly illustrates the strengthening phenomenon of the specimens in small sizes. Higher strengthening (deeper slopes) are found in specimens with smaller sizes in both copper and gold in plot 6.1(c). Besides the tests done on the small copper and gold specimens, several other small sample tests were done with different apparatuses and changes in mechanical properties of the small samples were also reported. Yield strength 33 times larger than the bulk value of the thin aluminum film was observed by Haque et al.[5] by performing the micro-tensile tests inside the SEM chamber on the 200nm thick, 23.5μm wide and 185μm long sputter deposited aluminum samples. The load was applied by a piezo-actuator and the strain was measured by the sensor beam which directly connected to the specimen. Ruud and Josell [6] tested the Cu, Ag and Ni thin films of 1 cm long, 3.3 μm wide and 1.9-2.6μm thick in gauge area. The poisson ratios of the thin films tested by Ruud were found different than the calculated bulk values. Some more tests were done on the thin films [7-15]. After these findings through testing samples in micron-scales, various theories for explaining the change in strength in small size specimens, or size scale plasticity, were raised. In the Artz's overview literature[16] and Burghard et al. report[17] , size scale plasticity found in the thin films were attributed to the dimensional constraint of the films and/or the substrates.

According to the model proposed by Artz, it is the passivation layers on the film surface and grain boundaries that obstructed the advance of the dislocations. Dislocations nucleated from the source continued to pile up at the surfaces and the grain boundaries thus increased the shear stress required to generate new dislocations. Greer [3] proposed a dislocation starvation mechanism that explained the size effect found in his compression tests on gold pillars. The dislocations inside the gold pillars could not multiply (e.g. intersecting with other dislocations) before leaving the surface due to short moving distance in the small sample. With dislocations continuously leaving the sample, shear stress required to nucleate new dislocations from the lattice is increased so that total strength of the material is increased. Small size indentation tests also showed an increase in strength of small samples [18,19]. The indentation created geometrical necessary dislocations that accommodate the strain gradients formed during the deformation [20]. However, the hardening effect found in the indentation tests is not depending on the size of the sample but the profile of the test indenter and the strain gradient it created. So the hardening effect due to the strain gradient is not size scale plasticity. Another size effect found in the small volume beam bending tests was reported by Sedlacek [21]. He attributed the increase in strength of the small beams to the dislocation pile-ups formed near the neutral plane. This model is similar to Arzt's thin film model, except the passivation layers is in the middle of the sample rather than on the sample surface. Besides the above mentioned theories that explain the size scale plasticity, several other factors may also affect the behaviors of samples especially when they are small:

1. Thin film texture effect:

Strong texture is usually developed when thin film is deposited on the substrate.

Up to 90% volume fraction of textured structure was found in the aluminum thin film by Kang et al.[22]. The developed texture can greatly affect the measured strength in different locations.

2. Grain size effect:

When thin film is deposited on the substrate, the thickness of the film restricted the size of the grains that can grow, so the grain size of the thin film is usually less than the thickness of the film. So if the thickness of the thin film is in sub-micron level, the size of the grains of the film must be sub-micron too, thus higher strength is expected.

3. Intrinsic stresses

The deposited thin films often exhibit intrinsic stresses [23] when they are deposited onto the substrates due to different in thermo expansion coefficients of the substrate and the film. When testing these thin films, the intrinsic stresses may increase the stress that required for them to yield.

Small volume tensile tests were done mostly on the thin films, and more or less the afore mentioned factors may affect the measured results. To minimize those errors and find the true hardening effect due to change in sample sizes, it is essential to test small samples in different sizes directly machined from one bulk material. In this study, small tensile samples were machined from Ti-1100 and Inconel 625 sheets. The cross-sectional areas of small samples varied from 2000 μm^2 to 400μm^2. These samples were relatively larger than thin films samples (cross-sectional area ~10μm^2) but much smaller than the conventional test samples (cross-sectional ~10mm^2). Strong size effect was found in small samples through series of microscopic tensile tests. Measured stress-strain curves of the tested small samples gave very different mechanical properties than those of large

samples. Strain burst phenomenon discovered by Ghosh [24] was observed during the tests of the small samples. The size effect found in small samples is believed to be caused by the thickening of the mantle areas of the samples, which is caused by continuous strain bursts, and repeated slips occurred at the same slip step. The fabrication and dimension of small samples as well as the test apparatus will be described in the following sections.

6.2 Fabrication of small samples

The base materials used in the tests were 0.1mm thick Ti-1100 sheet and 0.27mm thick Inconel 625 sheets. The chemical compositions of Ti-1100 and Inconel 625 are tabulated in Table 6.1 and Table 6.2. Optical metallography of both Ti-1100 and Inconel 625 are shown in Fig 6.2(a) and 6.2(b). Ti-1100 sample was etched by Kroll's reagent (1~3ml HF, 2~6 HNO_3, 90ml DI water) and Inconel 625 sample was etched by Aqua regia (20ml Nitric acid with 100ml Hydrochloric acid) to reveal the grains. The average grain size of original Ti-1100 sheet is 22.3μm and the grain size of original Inconel 625 sheet is 15.7μm.

Two types of small samples were machined from the Ti-1100 and Inconel 625 sheets; type 1 and type 2 samples. Type 1 small sample has a two-finger shape with an average cross-sectional area around 400-800μm^2 as shown in the schematic illustration in Fig 6.3(a). Type 2 small sample has elongated shape and larger cross-sectional areas in gauge section (around 1000-2000μm^2) as shown in the schematic illustration in Fig 6.3(b).

20mm x 6mm rectangular strips were cut from the Ti-1100 and Inconel 625 sheets. Both type 1 and type 2 samples were further machined from these strips to give small gauge sections. For type 1 samples, three 1.76mm diameter holes were drilled parallel to each other on the strips and the spacing between holes were kept for 50-75 μm. These spacing between holes are the gauge sections (test areas) of the samples. The spacing between the holes and the edges of the strip are served as protection arms which protect the test fingers from breaking during transportations. These supportive arms would be cut open before the tests. Two 3mm diameter pin holes were drilled on the left and right of the strip for pins of the test machine to go through. The centers of the pin holes and the 1.76mm diameter hole in the middle are carefully aligned such that load could be equally distributed to two gauge sections. After machining, the middle section of the sample where two fingers located would be etched by the HF solution (10ml HF, 90ml ethyl alcohol) to reduce the size of the fingers. After the diameter of the fingers were etched down to ~30 μm, focused ion beam (FIB) machining would be applied to the fingers and carve a 50 x 20 x 20 μm^3 rectangular gauge section on the fingers. A photo of the type 1 small sample is shown in Fig 6.4(a) and the SEM image of the FIBed gauge section is shown in Fig 6.4(c).

Type 2 samples were made by machining the Ti-1100 strips to a dumbbell-like piece as shown in the schematic illustration in Fig 6.3(b) with four 0.150 x 5 x 0.1mm^3 fingers in the middle and two 0.5 x 5 x 0.1mm^3 supportive arms on the top and bottom. The supportive arms were made to protect the test fingers during the transportation and would be cut open before the tests. HF solution was used to etch the fingers of the machined

samples to reduce the volume of the fingers down to $100\mu m^2$. Subsequent mechanical sanding and polishing was done on the top and bottom of the fingers which reduced the thickness of the fingers down to around 30μm. A 100 x 30 μm^2 rectangular block on the side of the fingers would be cut by the FIB and form a smooth gauge section. A photo of the type 2 small sample is shown in Fig 6.4(b) and the SEM image of the FIBed gauge section is shown in Fig 6.4(d). The curvature on the test fingers of the type 2 small sample may result in a higher flow stress measured than the real effective stress which acts on the sample. The curvature problem can be solved by the Bridgeman correction and the details of Bridgeman correction is given in Appendix 6B.

6.3 Small sample test apparatus

A tensile test apparatus was special designed to test the small samples. Fig 6.5 shows the photo image of the test apparatus. A computer controlled open-loot New Technology Squiggle linear actuator (H) was used to apply load to the loading flange (G), and the load was transferred through the slide stage (E) and mobile crosshead (B) to the test sample(C). The loads registered on the test sample were recorded by a Futek 5lbs load cell (D) and translated to voltage signals and stored in computer through DAQ system. The test apparatus is vacuum proved and can be set up inside a SEM chamber and allowed the test to be monitored under the SEM. Detailed description of the small sample test apparatus is shown in Appendix 6D.

6.4 Calibration of the small sample test apparatus

Calibration of the small sample test apparatus was done by comparing the load-strain curves of the Ti-1100 small sample tested under the small sample test apparatus and conventional tensile sample tested under the Instron machine. The test procedure and sample dimension of the conventional large tensile sample are listed in Appendix 6C. Fig 6.6(a) shows the load-displacement plot of two samples different in sizes tested by the small test apparatus and Instron test machine. The tensile load of the conventional large sample tested under the Instron machine went up to ~290 N so only a small portion of the curve is shown in plot (a). Another load-displacement curve shown in plot (a) is a smaller sample with 1.59x0.1mm^2 in the gauge section tested under the small sample test apparatus. The maximum load of small sample bore was 20N due to the load limitation of the motor. The load displacement curves in plot (a) are transformed to engineering stress-strain curves and re-plotted in plot (b). Also, another stress-strain curve was added into plot (b), which is a large sample tested in small sample test apparatus. Though different samples were tested under different test apparatus, in the engineering stress-strain plot, the young's modulus of all three tests are almost the same. Since young's modulus of same material would not chance with different sample sizes, this gives strong evidence that the readings of the small sample test apparatus are credible and the data collected could be used for analysis.

6.5 Tests of type 1 small samples

The first small sample test was conducted on the type 1 small sample machined from Ti-1100 strips with 20μm x 20μm cross-sectional areas. The cross head speed was controlled

by an open loop squiggle linear actuator with minimum rate of 1μm/s and the load cell was calibrated before tests. Engineering stress-strain curve of the Ti-1100 type 1 small sample is shown in Fig 6.7(a) with the stress-strain curve of a conventional large tensile sample and a stress-strain curve of a type 2 small sample. The stress-strain curves of the type 1 small samples did not give a clear elastic-plastic transition point; instead, it had many small strain bursts (strain steps). The curve of large sample showed strain softening after yielding while the type 1 small sample continued hardened till failure. The hardening rate of the type 1 small sample slowed down after strain reached 0.1 and fewer strain bursts were found in strain between 0.1 and 0.17. The type 1 small sample hardened again after strain reached 0.17 with several small strain bursts. The fracture stress of type 1 small sample reached 2000MPa and is much higher than the fracture stress of the large sample (~800MPa).

The second set of test was done on the type 1 small sample machined from Inconel 625 strip. Fig 6.7(b) shows the stress-strain curves of a tested small sample and a conventional large sample for comparison. Again, no apparent elastic-plastic transition point was found on the stress-strain curve of the Inconel 625 small sample. Also, many strain bursts (strain steps) were found on the stress-strain curve of the Inconel 625 small sample. Both Inconel 625 small sample and large sample stain-hardened till failure, but small sample had a higher hardening rate and failed at 2800MPa, which is about 2 times higher than the failure stress of the large sample. Two plots in Fig 6.8(a) and Fig 6.8(b) show the details of early part and end of stress-strain curves of tested Ti-1100 type 1 small sample. Strain steps on the curve are outlined by horizontal bars. These strain steps

shown in the plots are believed to be early yieldings of the small samples and are believed to correspond to the slip steps formed on the sample surface. And slip steps usually occur at the imperfect surface regions which have higher stress concentration. When each slip step is formed, strain energy of the sample is temporary released and the flow stress is lowered, thus on the stress-strain curve, a flat region (strain step) is formed. When the sample is further deformed, flow stress increases again and keeps increasing until the next slip occurs (ie, ejection of dislocations to the surface). Detailed modeling of slip-associated strain bursts is described in Ghosh [24]. The continuous strain bursts caused the stress-strain curves of both type 1 Ti-1100 and type 1 Inconel 625 small samples to be serrated. The total number of strain steps recorded on the Ti-1100 type 1 small sample is 33. The total number of strain steps found on the Inconel 625 type 1 samples (recorded on the magnified stress-strain curves in Fig 6.9(a) and Fig 6.9(b)) is 54. To further investigate the relation between the strain steps and slip steps that formed on the sample, SEM analysis is required. Fig 6.10(a) shows the SEM image of tested Ti-1100 type 1 small sample at fracture surface. The final cross-sectional area is circled by the black dotted line. The fractured surface still retained its original rectangular shape with small area reduction. Fig 6.10(b) shows another SEM image 45 degrees to the fracture surface. Many slip steps were shown on the side of the sample. The number of the slip steps appeared on the sample is 33, which is identical to number of strain steps found in the stress-strain curve. The matching numbers of the slip steps and strain steps give strong proof that the strain steps on the stress-strain curves were caused by the formation of slip steps. Fig 6.11(a) shows the SEM image of the tested Inconel 625 type 1 small sample looking down from the fracture surface. Heavy slip steps surrounded the

fractured area and formed a pyramid shape. The slip steps propagated from one side of the sample to the other. The final cross-sectional area was greatly reduced from original $400\mu m^2$ to $83\mu m^2$. On the side of the sample, as shown in Fig 6.11(b), a total of 34 slip steps were measured. The number of slip steps measured in Inconel 625 type 1 small sample did not match the number of strain steps (54 strain steps) in the stress-strain curve. The difference in numbers of strain steps and slip steps may be caused by the multiple slips in a single slip step. Fig 6.12(a) shows the SEM image taken on the side of the fractured Inconel 625 type 1 small sample where the strain is about 0.145. Fig 6.12(b) shows the SEM image of the same sample with another region where strain is about 0.324. The thickness of slip steps that formed at higher strain region are ~ 0.4 μm, which are thicker than the slip steps that formed at lower strain region (0.16 μm). Thick slip steps at higher strain region are believed to contain more slips than slip steps in lower strain region. Multiple slips may have occurred in one slip step at high strain region. A schematic illustration of the formation of slips is shown in Fig 6.12(c).

6.6 Tests of the type 2 small samples

The stress-strain curve of the Ti-1100 type 2 small sample is shown in Fig 6.7(a). The type 2 small sample followed similar hardening pattern of the type 1 small sample. There are only three strain steps found in the stress-strain curve of type 2 small sample, which took place at strain 0.02, 0.04 and 0.08, respectively. Type 2 small sample has a larger cross-sectional area (~$2000\mu m^2$) compared to the type 1 small sample (~$400\mu m^2$) and requires higher load to deform the sample such that small load drops when slip steps formed may not be picked up by the load cell, so few strain bursts were recorded. Fig

6.13 shows the fracture surface of the type 2 small sample. Slip steps could be seen on the side of the sample. The slip steps formed in the type 2 small sample are less than slip steps formed in type 1 small sample. The final cross-sectional area of the fractured sample is circled by the dotted line in Fig 6.13. Several Ti-1100 type 2 small samples were tested and the failure stresses of each sample were measured by dividing the load applied to the sample before failure by the sample's final cross-sectional area.

6.7 Result and discussion

The failure stresses of Ti-1100 small samples are plotted in Fig 6.14(a) with the corresponding final strains (measure from the change of cross-sectional area) and extrapolation lines were made to connect the data points. A stress-strain curve of conventional large sample is also plotted in the figure for comparison. The large sample shows much lower yield stress and failure stress than the small samples. The extrapolated stress-strain curves of the type 2 small samples shows higher strength and strain hardening rate than large sample. Type 1 small sample with the smallest cross-sectional area (20μm x 20μm) shows even higher strength and hardening rate than type 1 small samples. The failure stress of the type 1 small sample is 2240MPa (measured from the final cross-sectional area), which is more than two times larger than the failure stress of the conventional large sample (~900MPa).Yield stress (1600MPa) of the type 1 small sample is also much larger than the yield stress of conventional large sample (900MPa). Also, the strain hardening rates of the small samples are higher than the large sample.

The increase in strength of Inconel 625 type 1 small samples is even more phenomenal. In Fig 6.14(b), failure stress of Inconel 625 type 1 small sample is plotted with its corresponding strain and a stress-strain curve of conventional large sample is also plotted for comparison. From the extrapolation, yield stress of the small sample reached 1020 MPa while yield stress of the conventional large sample is 470MPa. The tensile stress of the large sample is 1370MPa while the tensile stress measured from the type 1 small sample is 14.4GPa, about 11 times increments. The strain hardening rates of the Inconel 625 small samples are believed to be much higher than the hardening rates of large sample. By comparing the stress-strain curves of large samples and small samples in both materials, we can find that the stress-strain curves of small sample do not follow the conventional pattern. The curves of small sample have no apparent yielding point but consist of many small strain steps. Therefore, it is difficult to determine the yielding strength of the small samples because different yield off-sets we use will give different yield strength. Also, the material hardens after every strain steps forms and this hardening continues till sample fractures. These step-hardening curves were first found in the tests of small samples.

A plot of cross-sectional area versus failure stress of Ti-1100 small sample is shown in Fig 6.15. The failure stress of the conventional large sample ($4x10^{11}nm^2$) is around 1000MPa. With the size of the samples decreases, the failure stress increases up to ~2000Mpa. Strong size scale plasticity is shown in the plot. Size scale plasticity is also found in the Inconel 625 small samples, as shown in the plot in Fig 6.16. The stress at failure increased from 950 MPa for a conventional large sample to 10500 MPa for a type

1 small sample and the yield stress increased from 450 MPa for a conventional large sample to 1000MPa for a type 1 small sample.

6.8 Factors which may cause the size scale plasticity

From the SEM analysis and test results, there is no doubt that size scale plasticity exists in small samples. It is believed that two factors caused the increase in flow stress in small samples.

1. Hardening of the mantle area (skin) of the small sample:

The mantle area of the sample hardens during plastic deformation, thus higher stress is required for the dislocations to pass through the mantle area of the sample when it is hardened. In large sample, the volume of the mantle area is small compare to the overall volume of the sample. An illustration is shown in Fig 6.17. However, if sample is small, the number of atoms in the mantle area is close to the total number of atoms in the sample, thus the strengthening from the mantle area becomes more prominent. In SEM image taken from Inconel 625 tested small sample, as shown in Fig 6.11(a), the final cross-sectional area reduced from original 400 μm^2 to 78μm^2 and the perimeter of the sample reduced from 112 μm to 36 μm. The cross-sectional area to perimeter ratio equals the volume fraction of mantle area. So the volume fraction of mantle area of small sample increased from 0.28 before test to 0.46 after test. The strengthening from the mantle area became more prominent when the small sample was elongated.

2. Continual slip on the previously formed slip steps:

The slip steps shown in Fig 6.12 indicated that more than one slip occurred at one slip step in small samples. The flow stress required for slip to occur on the same slip step is higher than slip to occur elsewhere. Since slip steps found in Fig 6.12 showed multiple slips occurred on same slip steps, higher flow stresses must be applied in these regions.

Perimeter (inverse proportional to the volume fraction of mantle area) and width of slip steps of Inconel 625 small sample with deformation strain is plotted in Fig 6.18. It is believed that both increase in mantle area and multiple slips attributed to the increased strength in Inconel 625 small sample.

6.9 Imperfect surface regions from the machining.

Due to the machine limit, the focused ion beam machining may cause small surface defect on the small sample (~0.5μm since the resolution of the Focused Ion Beam machining is 0.5μm). This defect may be neglected in large samples for their massive volume. However, in small samples, the cross-sectional areas in gauge sections are very small and defects even in micron-scale may lead to stress-concentration. These surface defects are the regions where slip steps prefer to occur. It is believed that because slip steps formed on the defect regions, strain steps showed up and formed the unique serrated stress-strain curve. The defects have more prominent effect on type 1 small sample than type 2 small sample since cross-sectional area of type 1 small sample is much smaller than type 2 small sample, and this is believed to be the reason why less strain steps were found on the type 2 small samples. The radius on the shoulders of FIB'd gauge sections

may also affect the stress distribution of the sample. The detailed discussion is tabulated in Appendix 6B.

6.10 Summary and conclusions

Ti-1100 and Inconel 625 type 1 small samples with ~400μm^2 cross-sectional areas and type 2 small samples with cross-sectional areas ~1000-3000 μm^2 were successfully machined from metal strips by series of cutting, chemical etching and focused ion beam (FIB) trimming. Tensile tests were done on the small samples with special designed small sample test apparatus. The fracture surfaces of tested type 1 and type 2 small samples showed extensive slip lines. Numbers of the dislocation lines formed on the Ti-1100 small samples matched the strain steps formed on the stress-strain curves. It is believed that for each slip step formed, a corresponding strain step formed on the stress-strain curve. A trend was found in the tests of small samples that with reduce in cross-sectional areas, flow stresses increased. This strengthening effect is believed to be caused by the hardening from the mantle area and the multiple slips that occurred in same slip steps. The tests of small samples can be summarized by the followings:

1. Micron-level small samples can be machined from the bulk materials via precise mechanical machining, chemical etching and focus ion beam machining.
2. Strain steps were found in the type 2 small sample tests and were believed to be caused by the slips formed on the sample surface.
3. Multiple slips may occur on the same slip steps and increase the required flow stress.
4. Hardening of the mantle area caused the strengthening in small samples.
5. Higher flow stresses were found in the small samples compare to the conventional

large samples.

6. Samples with smaller cross-sectional areas exhibited higher flow stresses.

7**.** Surface imperfections may be responsible for the premature slips to occur in the small samples, which lead to the formation of strain steps on the stress-strain curves.

Table 6.1 Chemical composition of the Ti-1100 alloy.

Alloy	Sn	Zr	Al	Mo	Si	C	Ti
Weight %	2.85	4.09	6.04	0.45	0.36	0.006	Balance

Table 6.2 Chemical composition of the Inconel 625 Ni-based alloy.

Alloy	C	Mn	Si	P	S	Cr	Mo	Al	Cu	Ti	Iron	Ni
Weight %	0.024	0.05	0.13	0.004	0.0006	21.31	8.67	0.18	0.03	0.2	3.47	balance

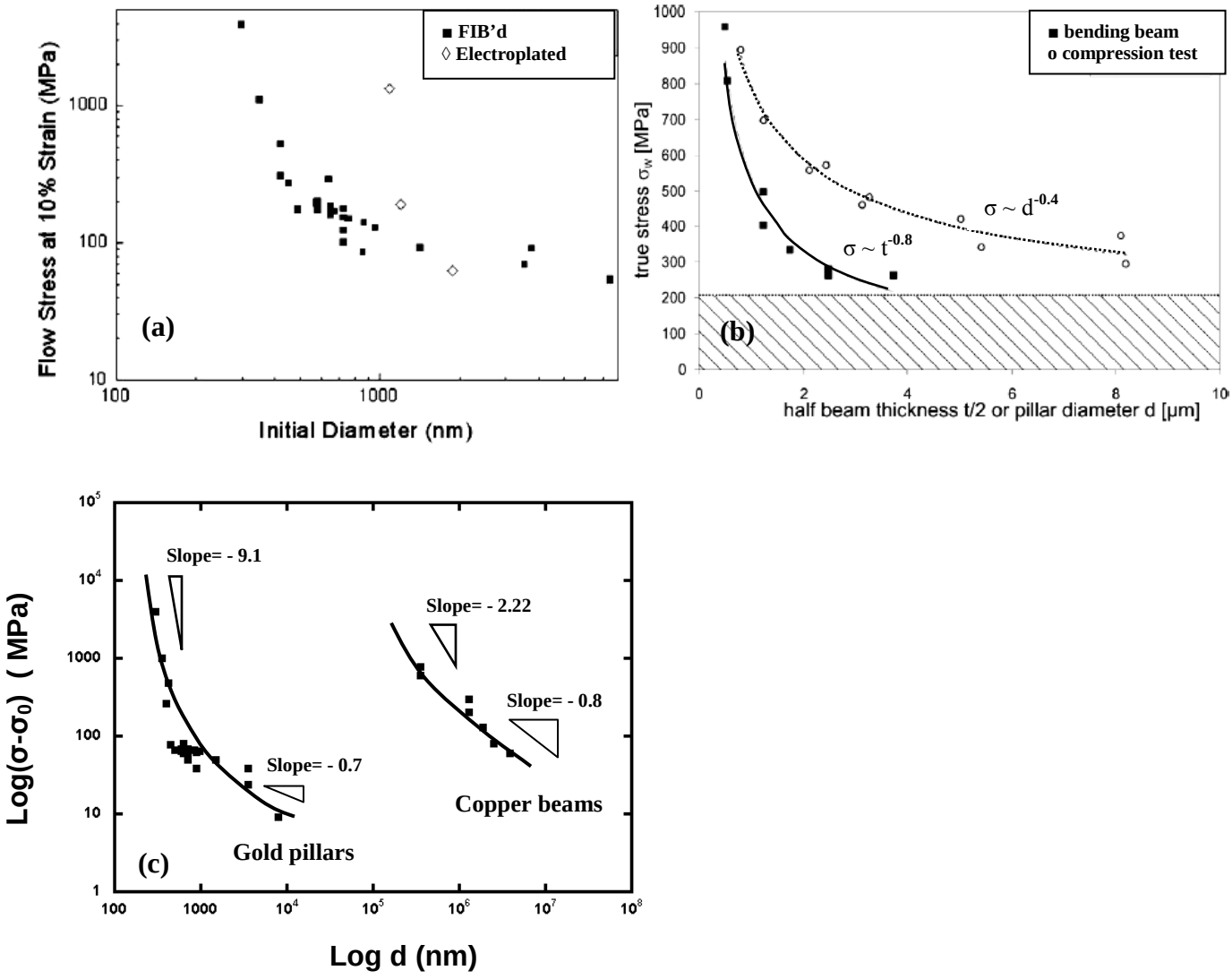

Figure 6.1 (a) Plot of flow stress versus pillar diameter of the micro-compression tests on the gold pillars. (b)Plot of stress versus beam thickness of micro-bending tests on the copper beams. It is evident in both plots that samples with smaller volumes exhibit higher strength. (c). Reconstruction of plot and (b) by changing the flow stress σ to the stress increment due to the size scale plasticity (σ-σ_0). The slops of both curves increase with reducing specimens size.

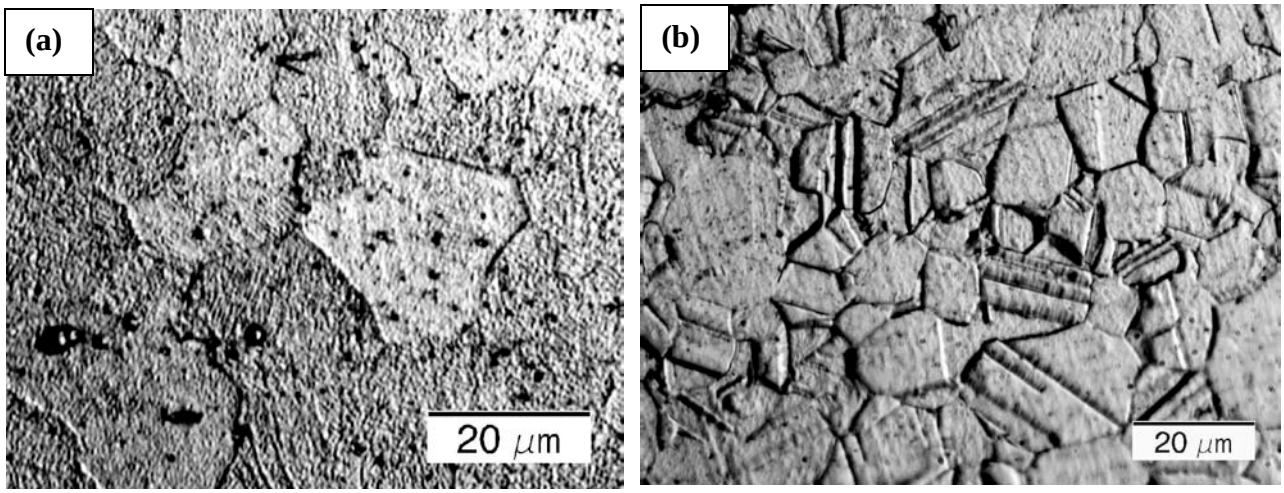

Figure 6.2 (a) Optical microscopic image of microstructure of Ti-1100 thin metal sheet. The average grain size is 22.3μm. (b) OM image of microstructure of Inconel 625 thin metal sheet. The average grain size is 15.7μm.

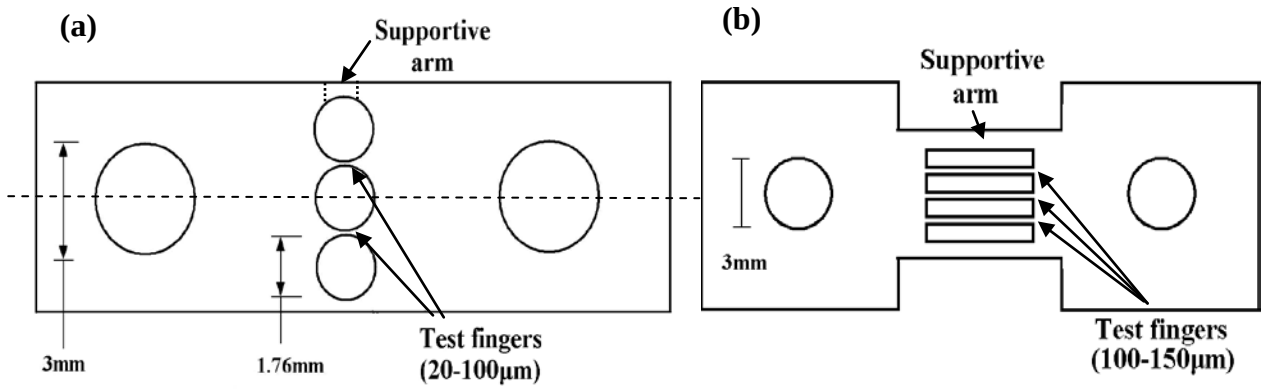

Figure 6.3 (a) Schematic illustration of the type 1 small sample. The spacing between three 1.76 mm diameter holes in the center of the sample is where the test fingers located. Two 3mm diameter holes on left and right are the pin holes for the gripping of the sample. The centers of two pin holes and the small hole in the middle are precisely aligned thus upon loading, the load would be equally distributed to the two test fingers. (b) Schematic illustration of the type 2 small sample. Rectangular cuts were made at the gauge section to form the elongated fingers. The finger width was kept in between 100-150μm. One larger spacing (500-600μm) at each side between the edges of the sample and the outer cuts would server as the supportive arms which would be cut open before the test. Two 3mm holes on the left and right are the pin holes for the gripping.

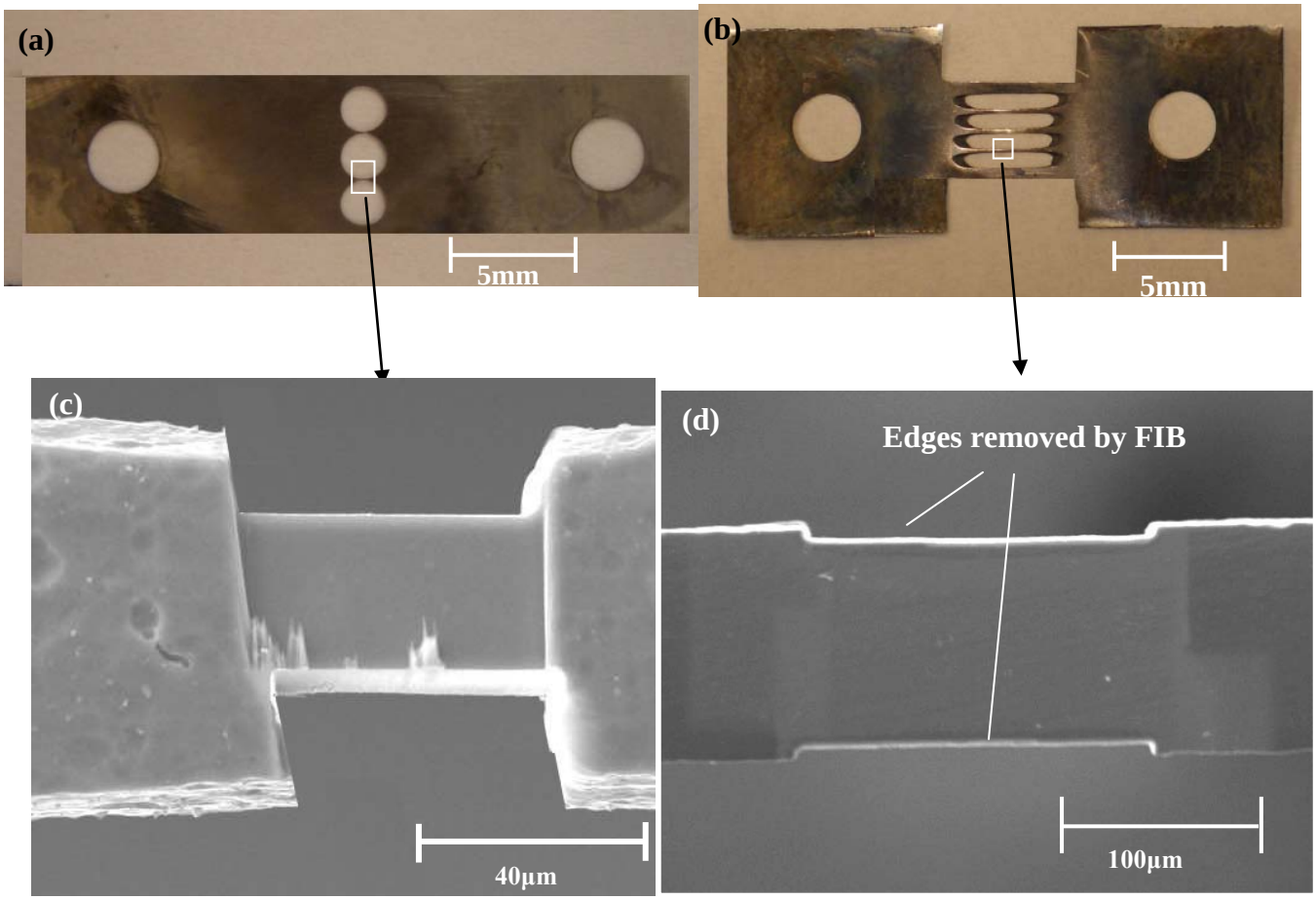

Figure 6.4 (a) Photo of the type 1 small sample. (b) Photo of the type 2 small sample. (c) SEM image of the gauge section of the type 1 small sample. A 50 x 20 x 20 μm^3 rectangular portion was carved by the FIB. (d) The SEM image of the gauge section of the type 2 small sample where two 200 µm long stripes on both sides of the sample were removed by the FIB.

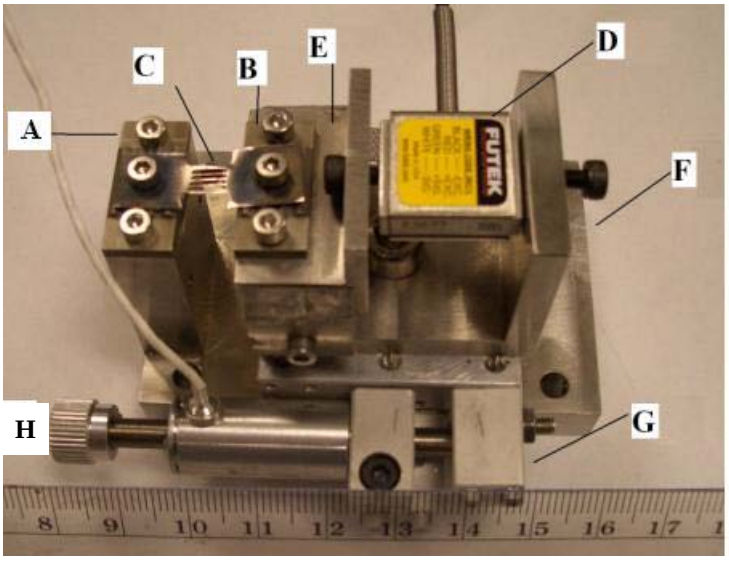

Figure 6.5 The small sample test apparatus. (A)Fixed crosshead (B) Mobile crosshead (C) small sample (D) Futek 5lbs loadcell (E) slide stage (F) Stainless steel frame (G)Loading flange (H) New Technology squiggle linear actuator.

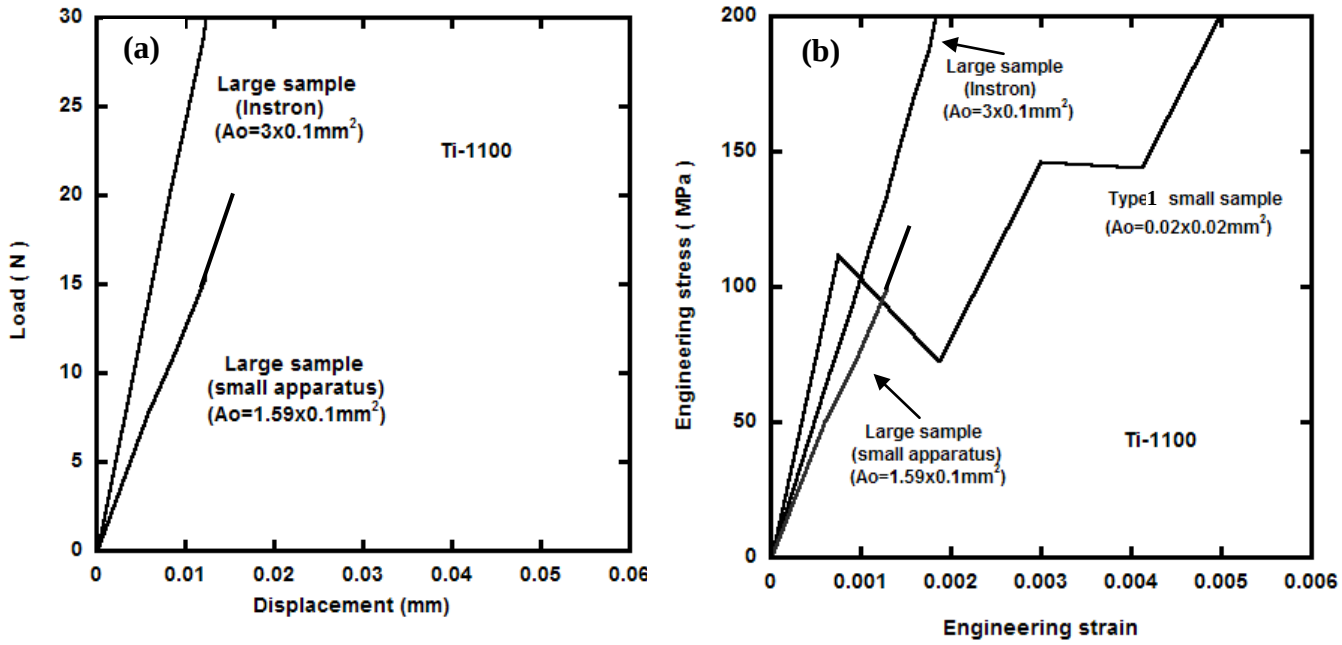

Figure 6.6 (a) Ti-1100 Load-displacement curve of the large sample tested under the small sample test apparatus compared with the load-displacement curve of the large sample tested under the Instron test machine. The maximum loading capacity of the small sample test apparatus is 20N where the curve ceased growing. (b) Ti-1100 Engineering stress-strain curves. Type 1 small sample was tested under the small test apparatus, large samples were tested under the small test apparatus and Instron machine. In both plots, the tests done in the small apparatus followed the similar slopes of the test done in the Instron machine, which verified the credibility of the data collected from the small sample test apparatus.

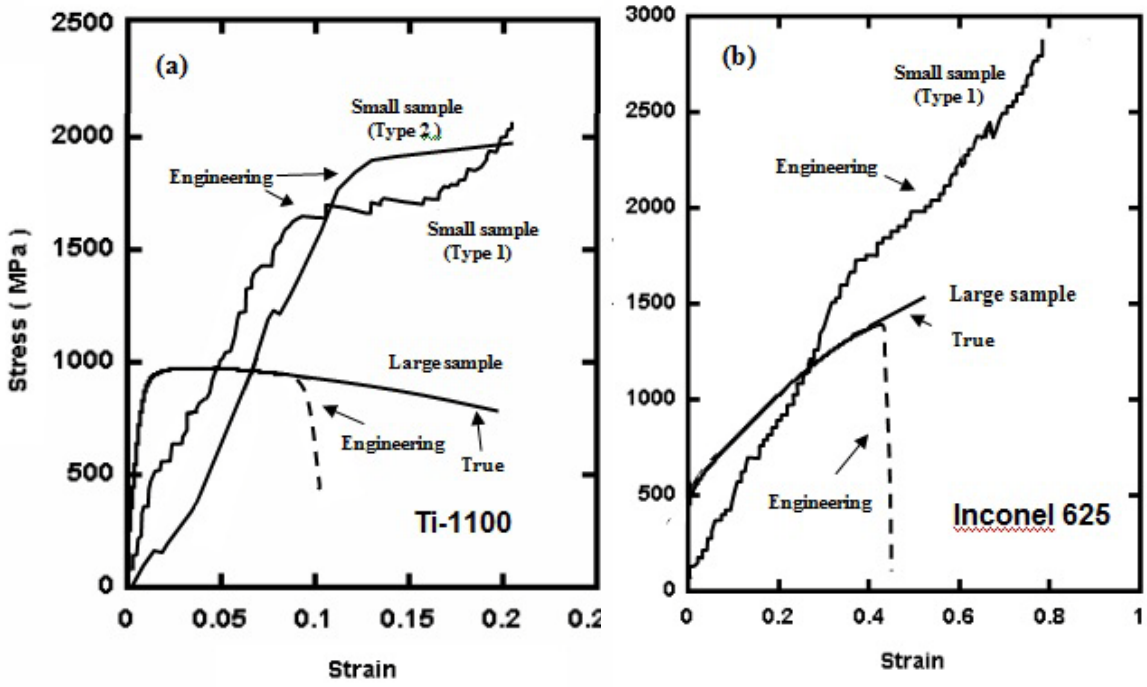

Figure 6.7 (a) Stress-strain curves of the Ti-1100 type 1 and type 2 small sample vs large sample. The yielding of the small samples started much earlier than the large sample but continued hardened with the increasing strain till failure. Strain softening was observed in the large sample after reaching the ultimate tensile stress. (b) Stress-strain curves of the Inconel 625 type 1 small sample vs large sample. The same early yielding occurred to the small sample. Strain hardening was found in both samples, but the small sample exhibits a higher hardening rate than the large sample.

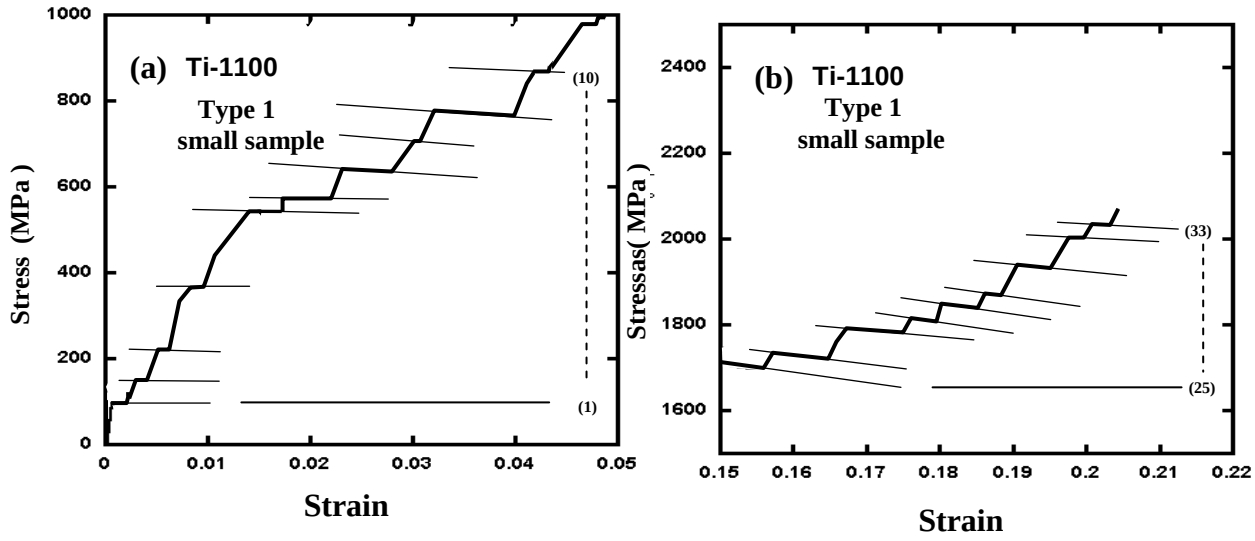

Figure 6.8 Magnified stress-strain curve of the Ti-1100 type 1 small sample in the early stage of the test (a) and right before failure (b). The horizontal lines indicate the strain steps that formed during the test. A total 33 steps were measured.

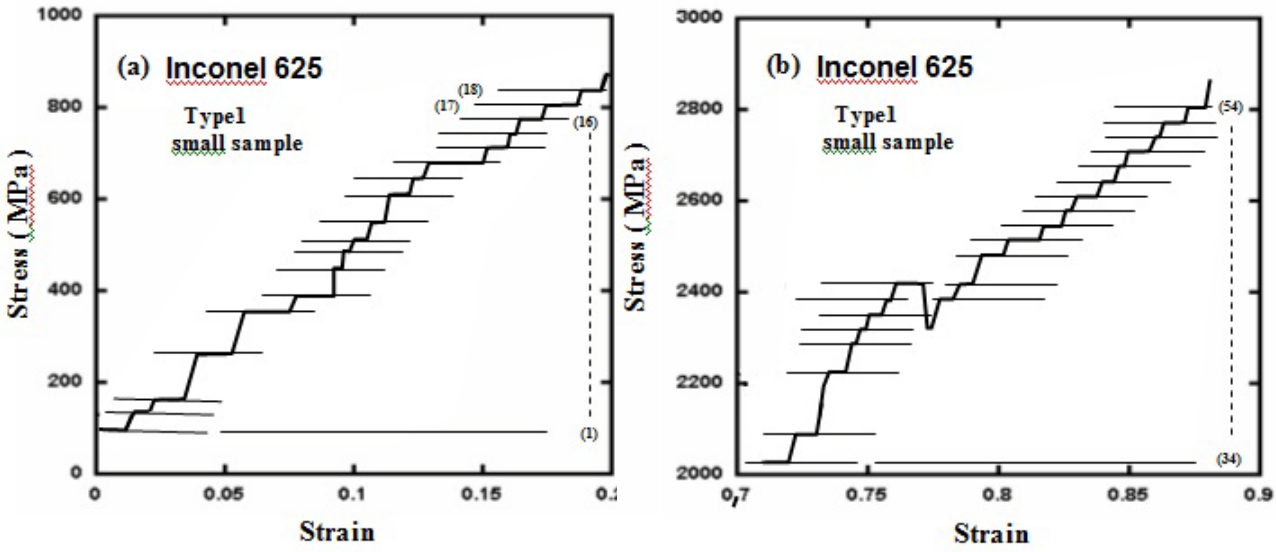

Figure 6.9 Magnified stress-strain curve of the Inconel 625 type 1 small sample in the early stage of the test (a) and right before failure (b). The stress increments of each strain step in Inconel 625 small sample were smaller than the Ti-1100 small sample. But the number of the strain steps in Inconel small sample is much more than the Ti-1100. A total 54 steps were measured.

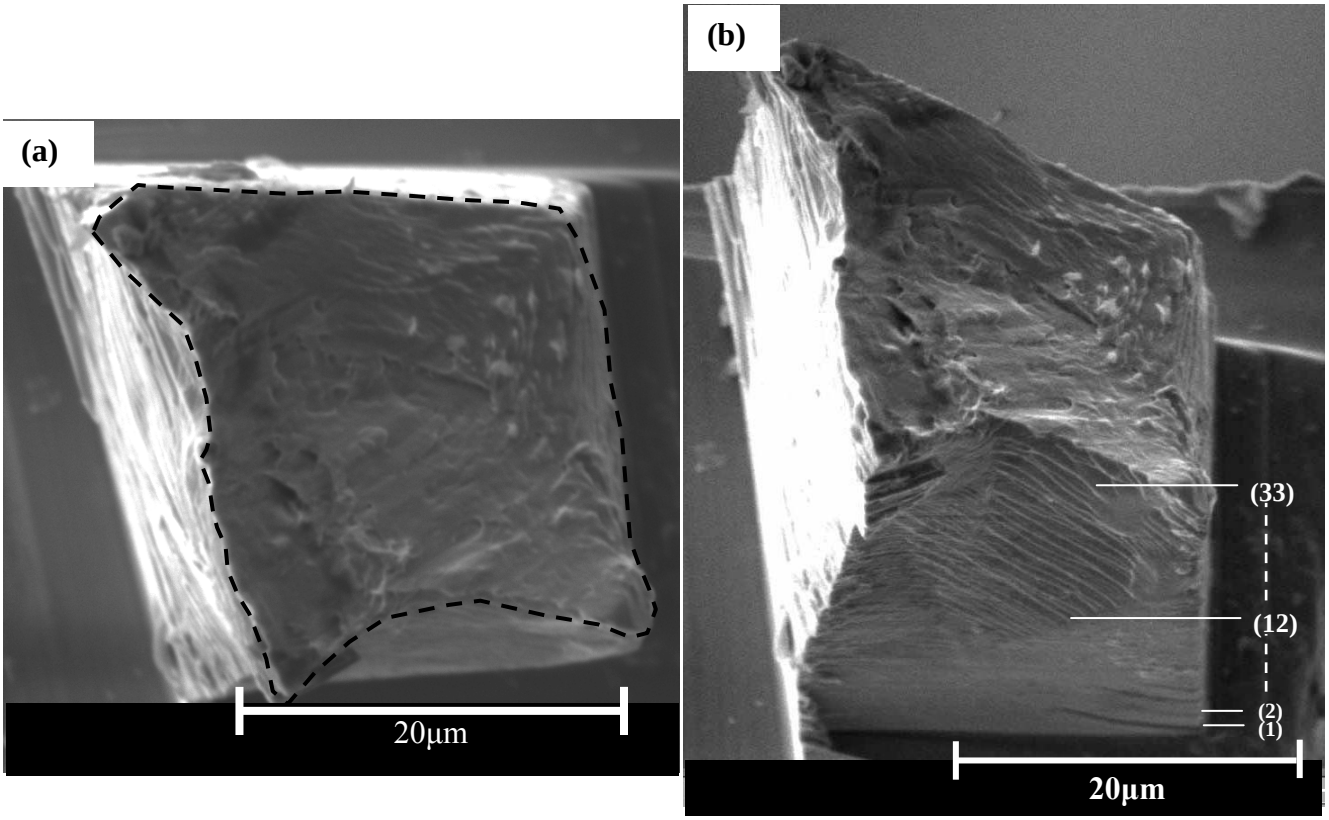

Figure 6.10 SEM images of the fractured Ti-1100 type 1 small sample (a) looking from the project direction of the fracture surface, the final cross-sectional area is circled by the dotted lines (b) looking 45° from the fracture surface, slip lines appears at the edge of the sample. A total 33 slip lines were measured.

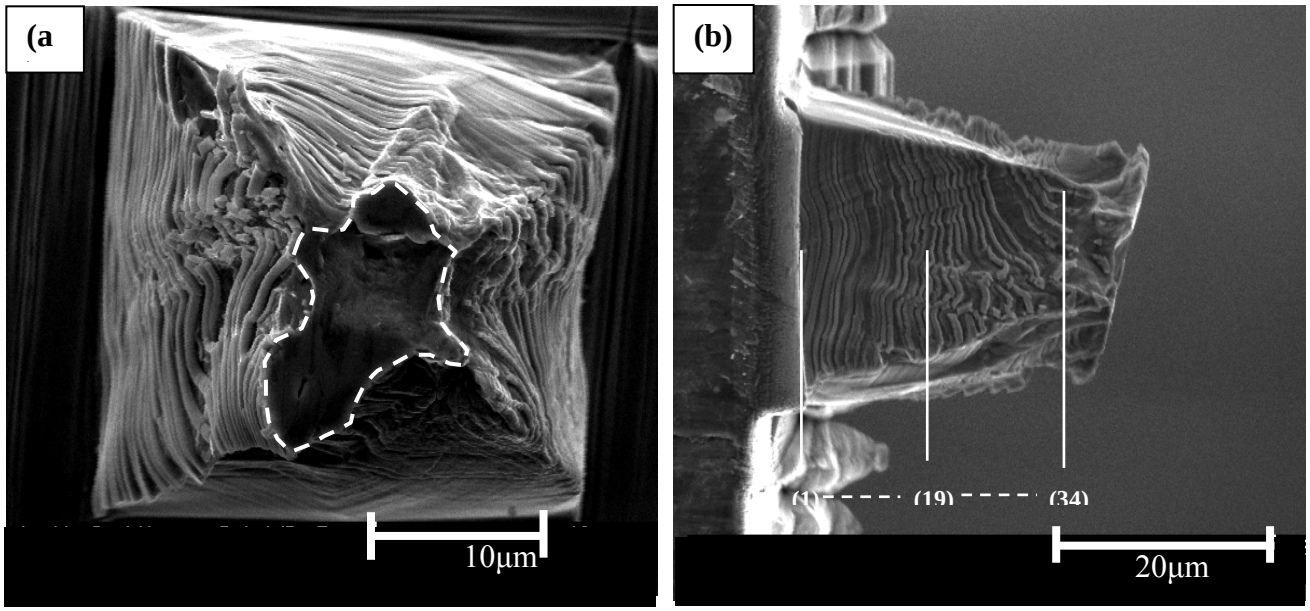

Figure 6.11 SEM images of Inconel 625 type 1 small sample (a) looking from the project direction of the fracture surface, the final cross section area is circled by the dotted line. Compared to the original area (rectangular shape in the background), large area reduction was obtained. Two white arrows indicated the thicker slip lines where the multiple slips may have occurred. (b) looking from the top of the fractured small sample, heavy slip lines are visible. Spacing between slip lines are small near the base of the samples and grow larger toward the fracture surface. A total 34 slip lines were measured.

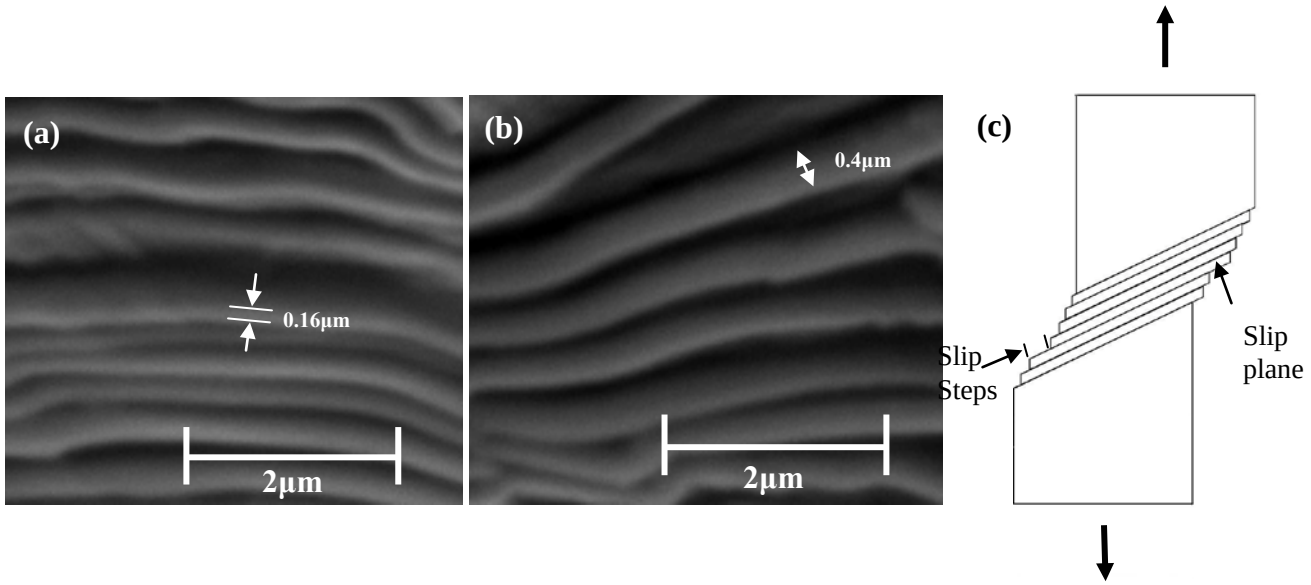

Figure 6.12 SEM image on the side of the Inconel 625 type 1 small sample at (a) ε=0.145 and (b) ε=0.324. Width of the slip lines grow larger with the higher strain. (c) Schematic illustration of slip step formation for single slip

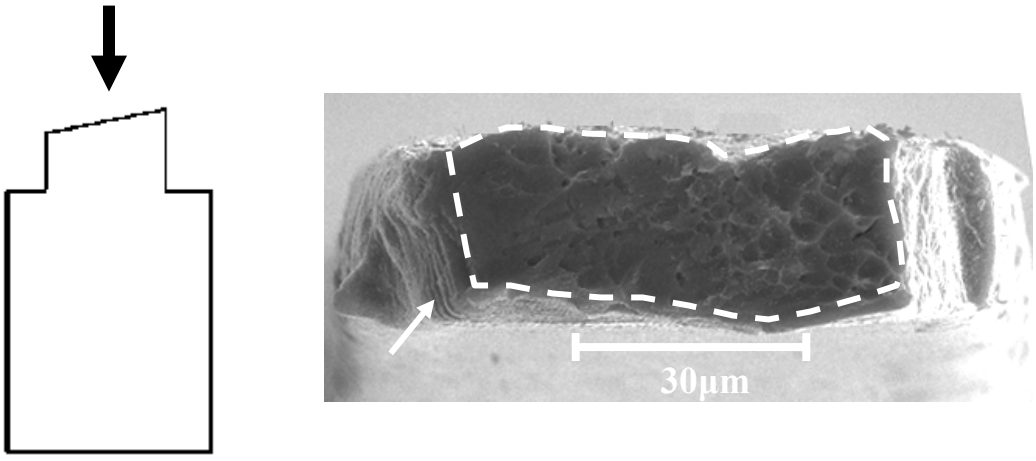

Figure 6.13 SEM image looking from the project direction of the fracture surface of the Ti-1100 type 2 small sample. Dimples appeared on the surface are the evident of the ductile failure. Slip steps created during the test are pointed out by the white arrow. The final cross section area which used in the calculation of fracture stress- strain is circled by the dotted line.

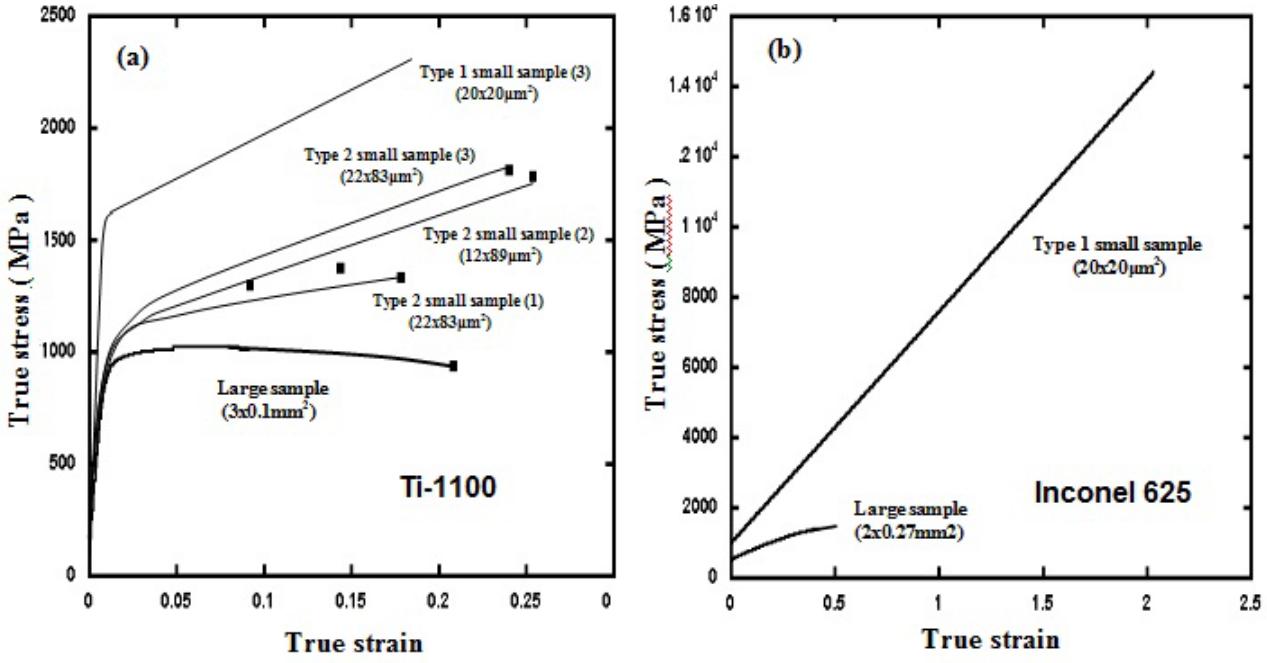

Figure 6.14 Stress-Strain plots of (a) Ti-1100 and (b) Inconel 625. The data points of the small samples were calculated by the final cross section areas and it is evident that samples with smaller cross section areas have higher stress values. The strain hardening rates of small samples were also found higher than the large sample from the extrapolated curves.

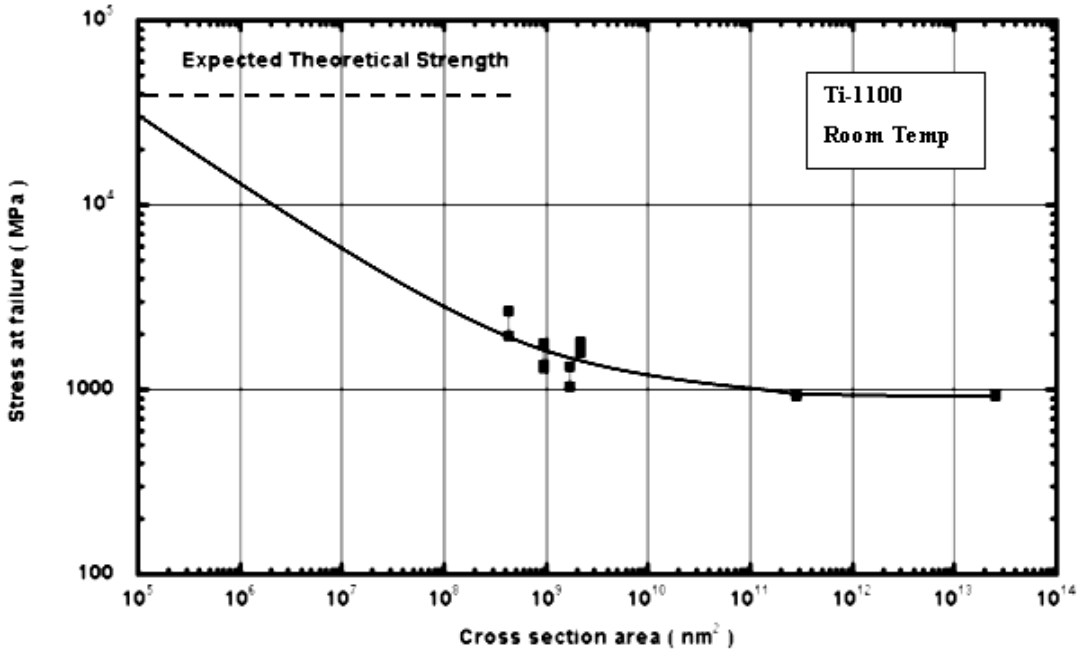

Figure 6.15 Relation ship between the cross-sectional area of the Ti-1100 samples and measured flow stress. An extrapolated curve was made to fit the experimental data. Samples with smaller cross-sectional areas exhibit higher stresses.

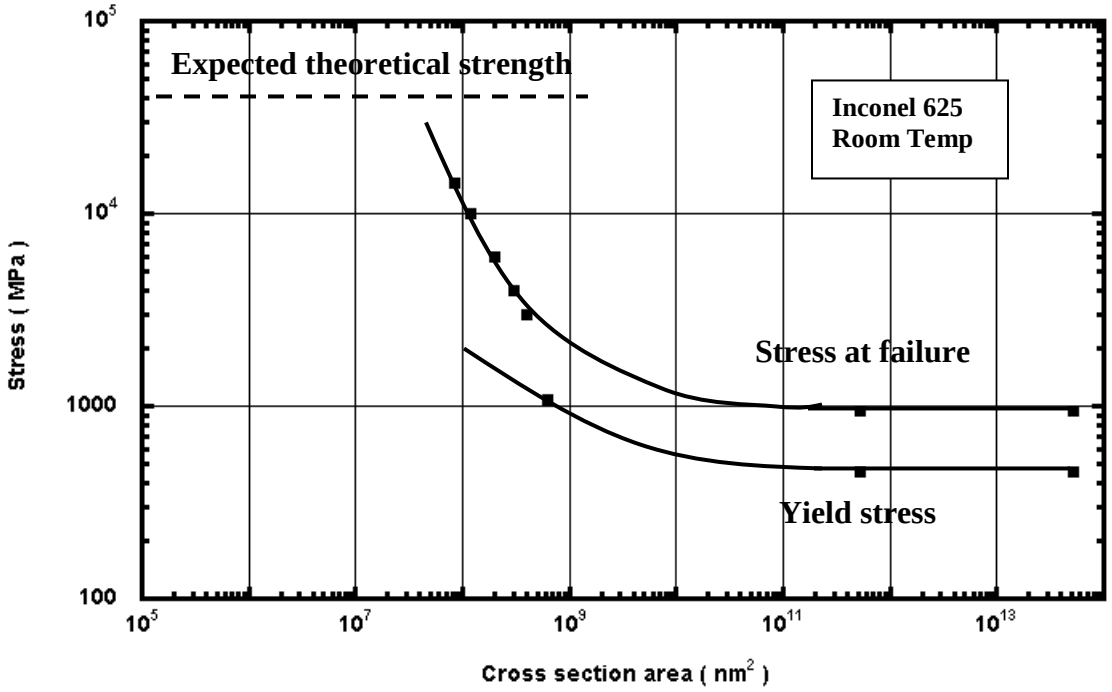

Figure 6.16 Stress vs cross section area plot of the Inconel 625 tensile samples. The stress at failure increased rapidly with the cross-sectional area reduced to less than 10^9 nm^2. The yield stress also increased with the smaller cross section area but with a more gradual slope.

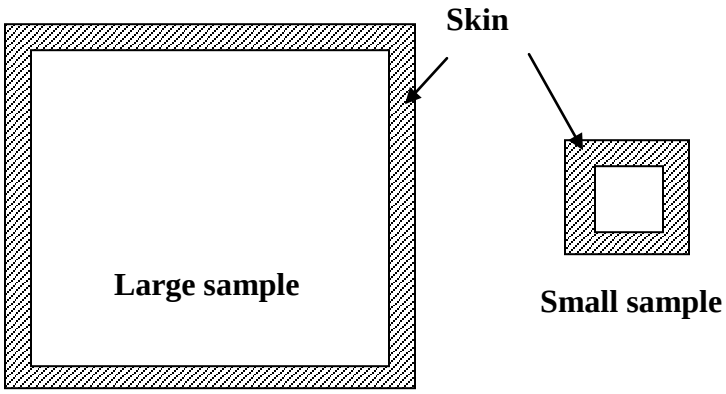

Figure 6.17 Schematic illustrations of skin areas in the sample. When the sample is large, flow stress increase from the skin area has little effect on the overall strength of the sample. When the sample is small, the number of atoms in the skin area is almost the same as numbers of atoms in the body of the sample. Hence the stress increase from the skin area becomes more prominent for the overall strength.

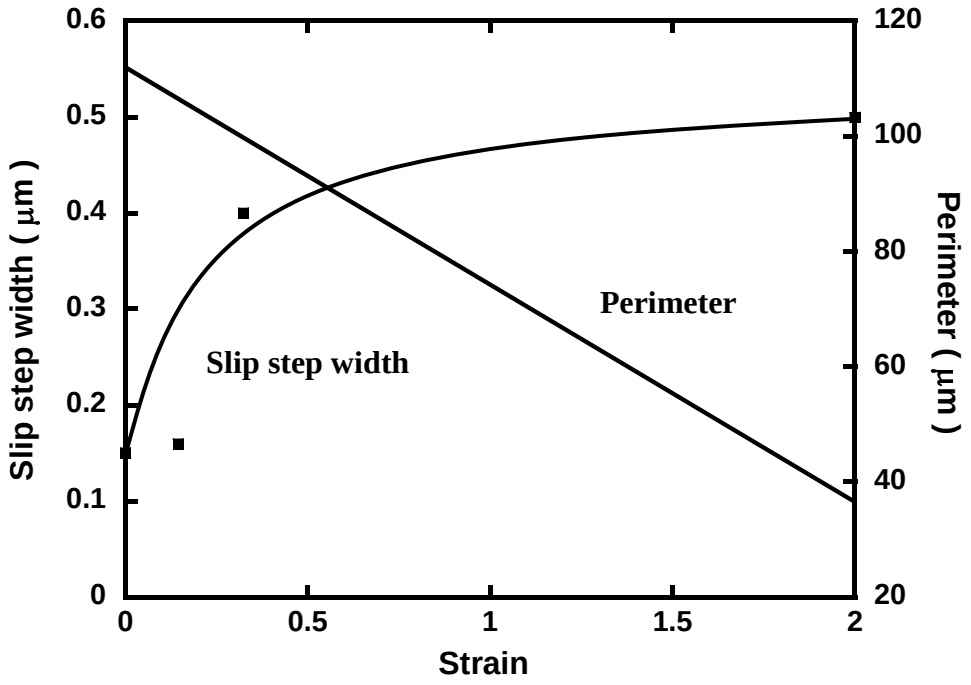

Figure 6.18 Correlation between strain and slip step width and sample perimeter of Inconel 625 type 1 small sample. As strain increases, slip step width increases from 0.15 μm to 0.5μm and perimeter decreases from 112μm to 36μm.

Appendix 6 A

Size effect in pure nickel microcrystals.

Dimiduk et al. [2] introduced a method of testing small Ni single crystal pillars based on the FIB machining and nanoindentation. The dimensions of the Ni pillars varied from 0.1 μm to 40 μm and had length-to-diameter ratio of 2:1-3:1. An SEM image of the FIB machined micro-pillar is shown in Fig 6.A.1. Compression test was done by the modified nanoindentor with flat diamond tip. The loading is control by the close loop voice-coil loading system and the displacement rate is controlled in between 0.2 to 5 nm/s. A schematic illustration of the configuration of the nanoindentation system is shown in 6.A.2. With decrease in sample size, the stress-strain curves of the samples start to deviate from the conventional single crystal stress-strain behavior. A plot of stress-strain of Ni pillars with diameter less than 2.5 μm is shown in Fig6.A.3. There are no distinct yieldings among these samples and many large strain bursts are shown in the stress-strain curves. The shape of the stress-strain curves also changed from conventional convex upward to concave upward. Fig 6.A.4 shows the plot of the relationship between the engineering stress and pillar diameter. It is clear that stress increases with the decreasing sample diameter and the lowest stress for the small pillar is higher than the CRSS for the macroscopic crystal. The size-dependence of the strength for single Ni small pillars is attributed to the lack of dislocation intersections due to the sample sizes smaller than the mean free path length (~50-300μm) of the dislocation. With the continuous escaping of the dislocations from the sample surface, the dislocation density of the small sample approached to the dislocation-free whiskers and resulted in the consequent strengthening and high flow stress of the small samples.

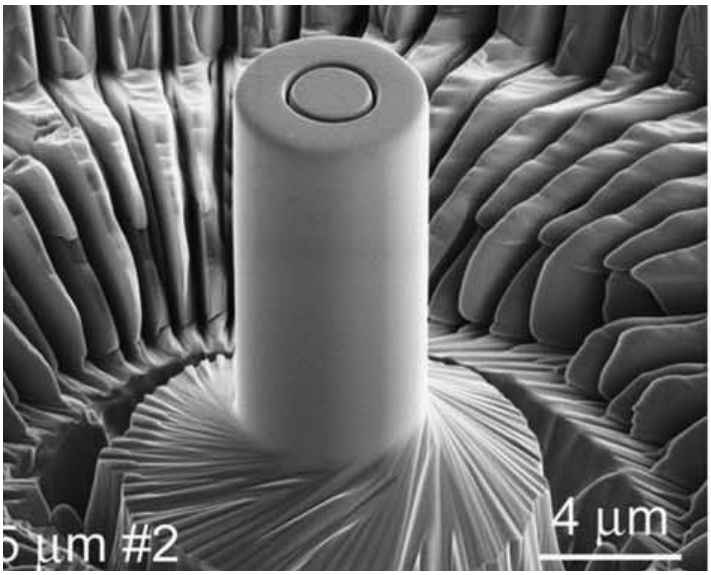

Figure 6.A.1 SEM image of the FIB'd small nickel pillar used in the compression test. The length to- diameter ratio is 2:1-3:1

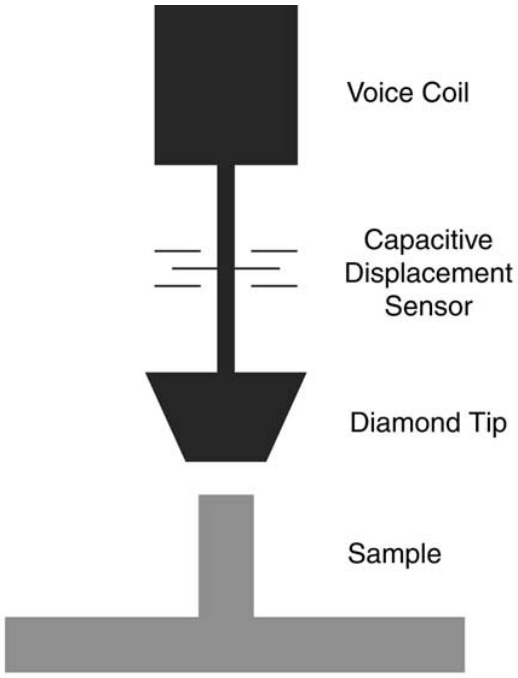

Figure 6.A.2 Schematic illustration of the nanoindentation system used in the nickel pillars compression tests.

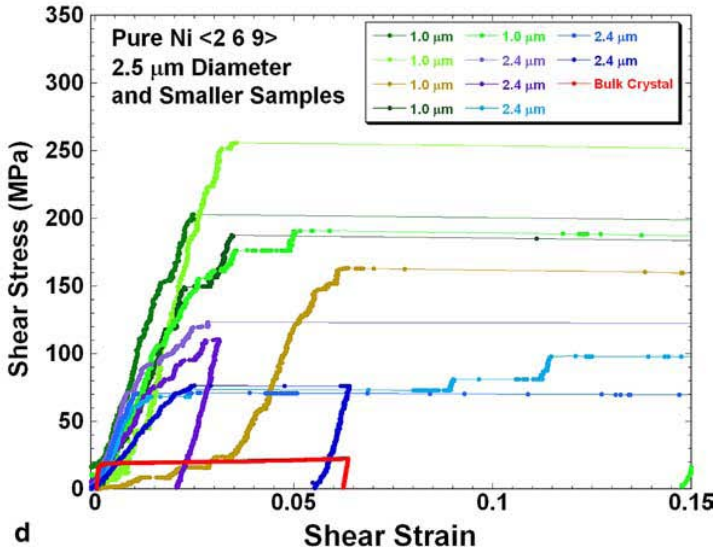

Figure 6.A.3 Stress-strain curves of the nickel pillars with diameter less than 2.5μm. Many strain bursts are shown in the curves with slopes concave upward..

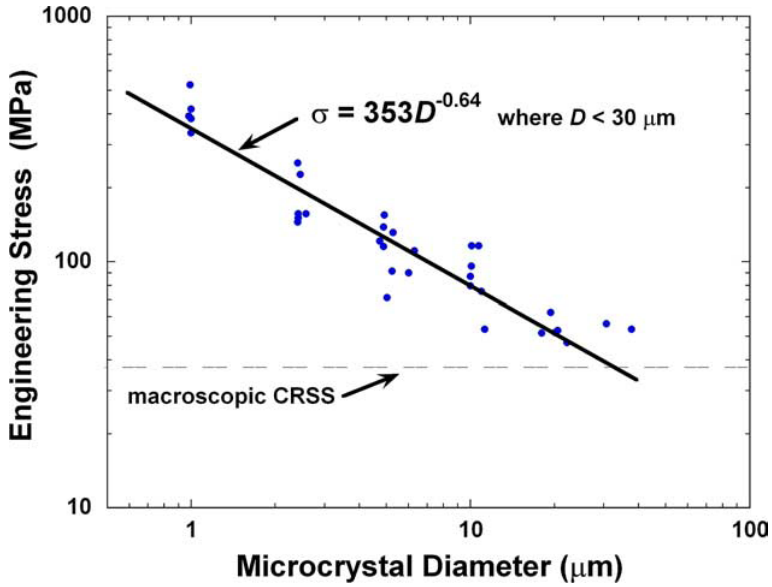

Figure 6.A.4 Engineering stress vs sample diameter plot of the small nickel pillars. The stress increases with the decreasing sample diameter. The dashed line shows the CRSS of the macroscopic nickel single crystal.

Appendix 6 B

Bridgman correction

The stresses at the center of neck is not uniaxial tension but also compression from the lateral contraction during the tensile deformation. The effective tensile stress that causes yielding is the total tensile stress minus the compression stresses from the lateral contraction and the curvature on the neck affects the state of the lateral compression stresses. Bridgman's correction for the effective stress for the tensile deformation is,

$$\bar{\sigma}/\sigma = 1/[1 + 2R/a)\ln(1 + a/2R)] \quad \text{(B1)}$$

where $\bar{\sigma}$ is the measured stress, R is the radius of curvature at neck, a is the radius of the neck.

Fig 6.B.1. showed the Bridgman correction factor as a function of the curvature of the neck region. The radius of curvature of the type 2 small sample used in this study is around 30mm and the radius of the finger is ~50μm. The Bridgman factor of the type 2 small sample is 0.9996, which means the effective stress for tensile deformation is almost equal to the applied tensile stress. Furthermore, the curvature of the sample is only outside the gauge section since the curvature in the gauge section is removed by the focused ion beam. So that it can be concluded that the load applied to the sample can be used as the tensile stress with little/no corrections.

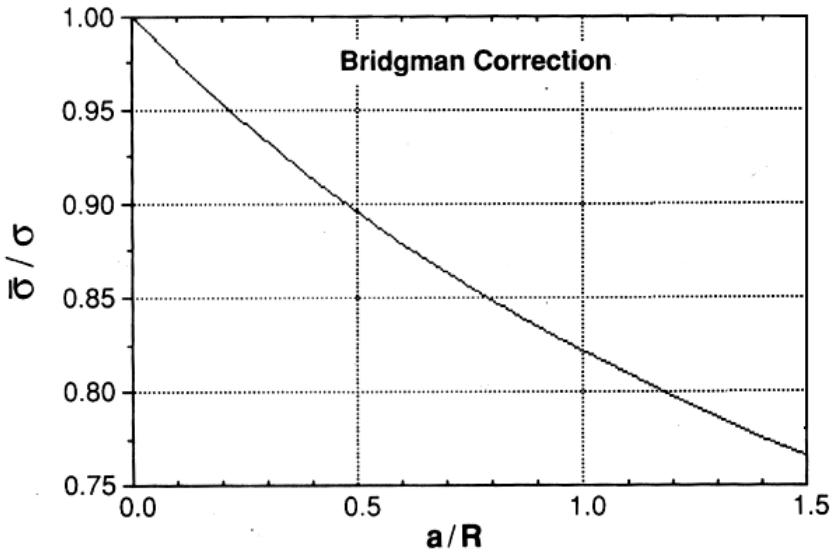

Figure 6.B.1 The Bridgman correction factor as a function of the curvature of the neck

Appendix 6 C

Conventional tensile tests on the large samples

Conventional large samples were machined from Ti-1100 sheet and Inconel 625 sheets with dimensions of 15mm long and 3mm wide in gauge section. A 4505 Instron frame was employed in the test and the strain rate was set at 0.5mm/min. The pulled samples compared with the untested sample is shown in Fig 6.C.1. and the stress-strain curves of the test are shown in Fig 6.C.2. The stress-strain curves of the Ti-1100 large sample (Fig 6.C.2(a)) showed a little strain hardening in the beginning and then dropped to zero following the dotted line. An extrapolation of the true stress-strain was made to connect the original Ti-1100 curve to the stress-strain at fracture, which was calculated from the load at failure and the final cross-section area of the sample. Some strain softening was found from the extrapolation. The tensile strength of the large sample is around 1000MPa and the tensile elongation measured from the gauge section is about 9.3%. Compared to Ti-1100, Stress-strain behavior of the Inconel 625 large sample (Fig 6.C.2(b)) showed a much stronger strain hardening effect and no strain softening was found. Same true stress-strain extrapolation was made on the Inconel 625 plot. The sample yielded at 470 MPa but the flow stress continued grew to 1400 MPa. Elongation of the Inconel 625 sample is about 45%.

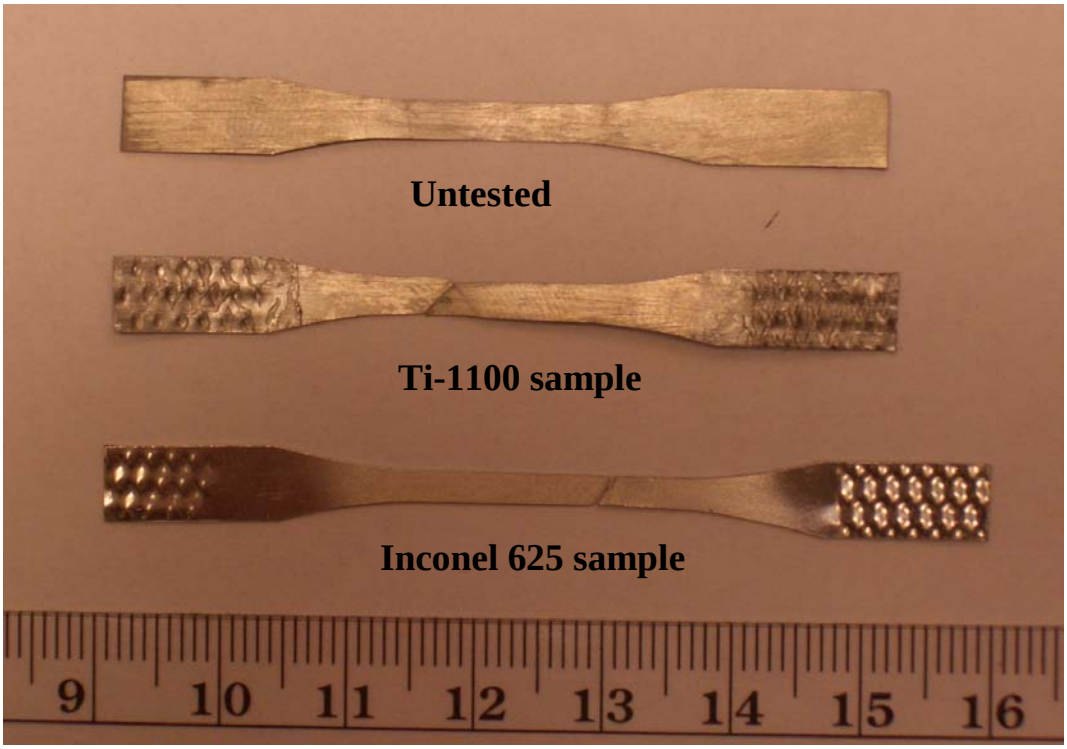

Figure 6.C.1 Photo of the large samples. The top one is the unstrained sample, middle one is the tested Ti-1100 large sample and bottom one is the tested Inconel 625 sample. The cross section of the Ti-1100 and Inconel 625 samples are $3x0.1mm^2$ and $3x0.27mm^2$ respectively. Elongation of 9.3% was found in the tested Ti-1100 sample and 45% in the tested Inconel

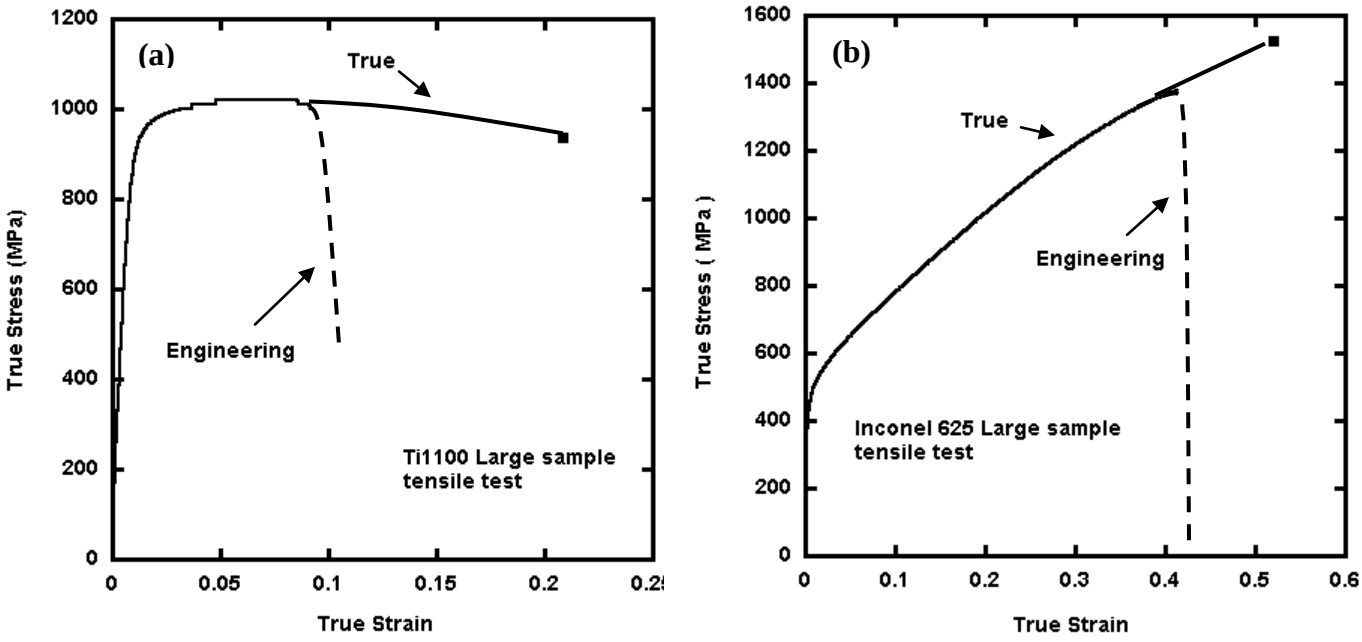

Figure 6.C.2 True stress-strain curves of the (a)Ti-1100 large sample and (b) Inconel 625 large sample. The dashed lines are the engineering stress-strain obtained from the tensile tests where the true stress-strain of the curves were extrapolated by connecting the original stress-strain curves to the failure stress-strain points of the samples. The failure stress-strain were measured by dividing the load before failure by the final cross section area of the samples. The strain rates were set at 0.5mm/min. Strain hardening was found in the Inconel 625.

Appendix 6 D

Step-by-step assembling and standard operation procedure of small sample test apparatus.

The small sample test apparatus is consisted of 4 major systems: The stage, feed through, data acquisition (DAQ) system and motor control. The basic assembling steps of each component in each system are described in the following:

Stage system

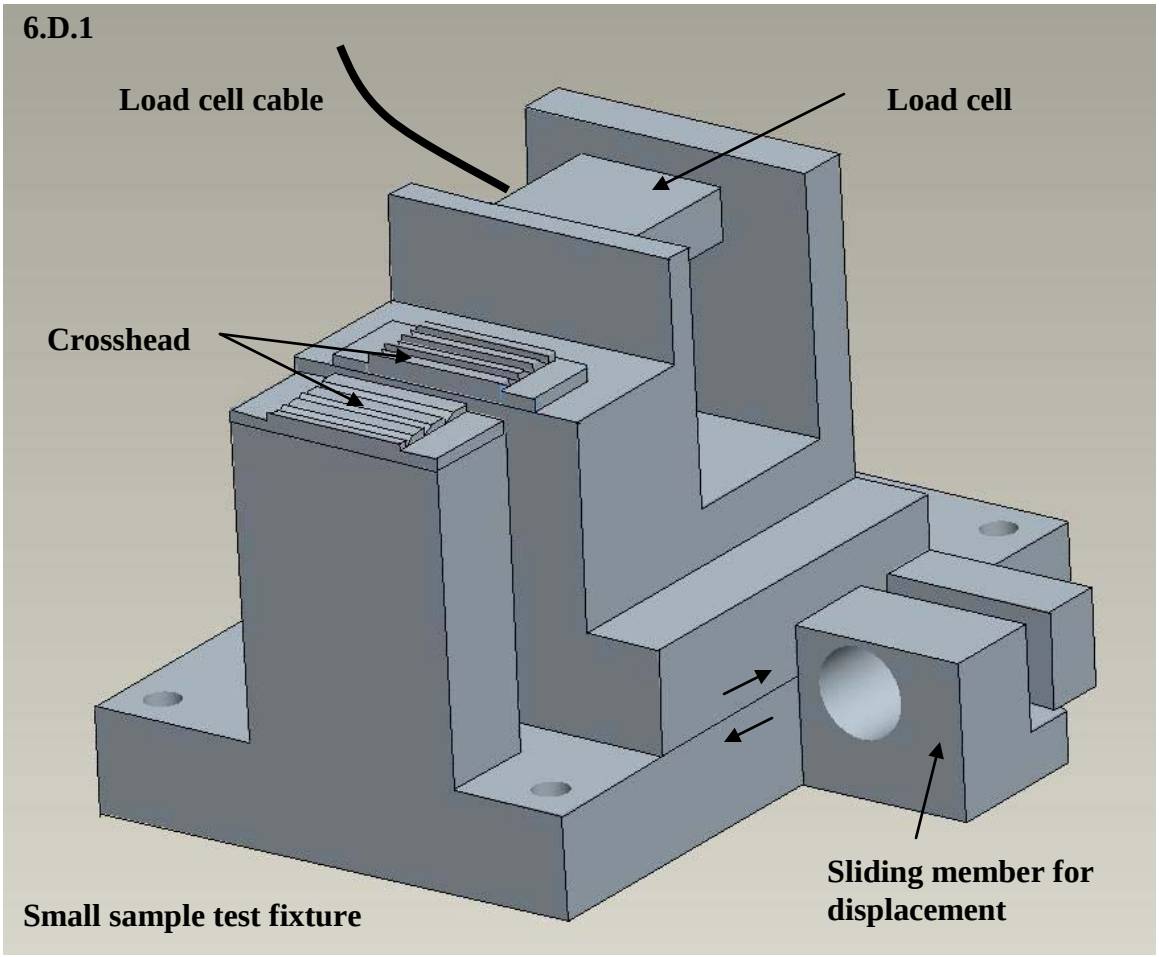

6.D.2

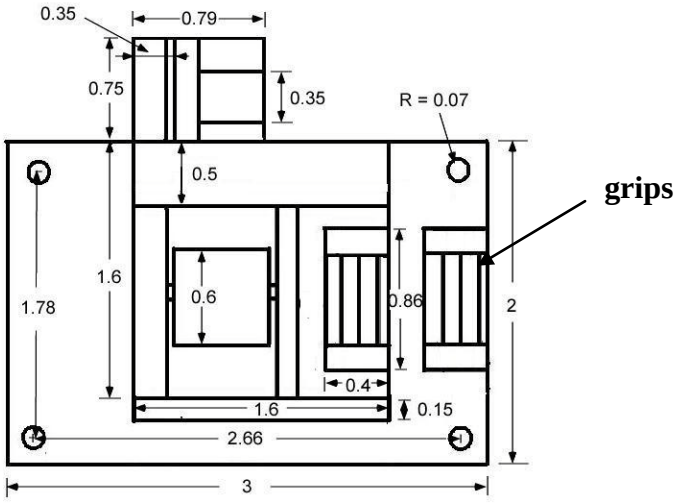

Part # 1 Drawing (304. Stainless steel)

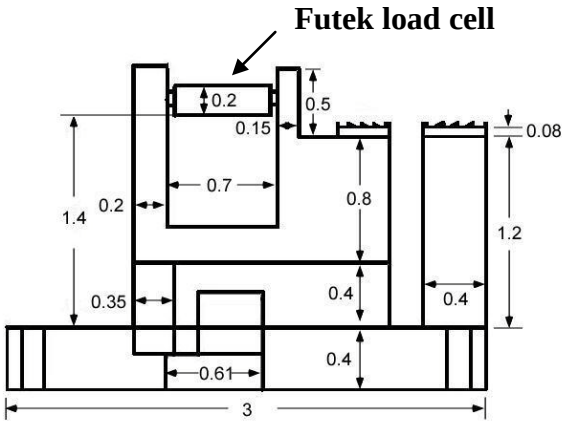

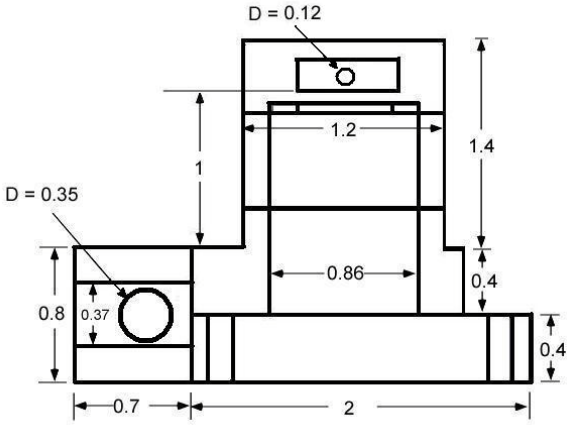

Small sample test fixture without squiggle motor shown

Unit: inch

Figure 6.D.1 shows the components of small sample test fixture including Futeck load cell, cable of the load cell, cross head, body of the stage and sliding member. The detailed scales of each part are illustrated in Fig 6.D.2. Figure 6.D.3(a) and (b) shows the front side and back side of the mounting fixture of the stage.

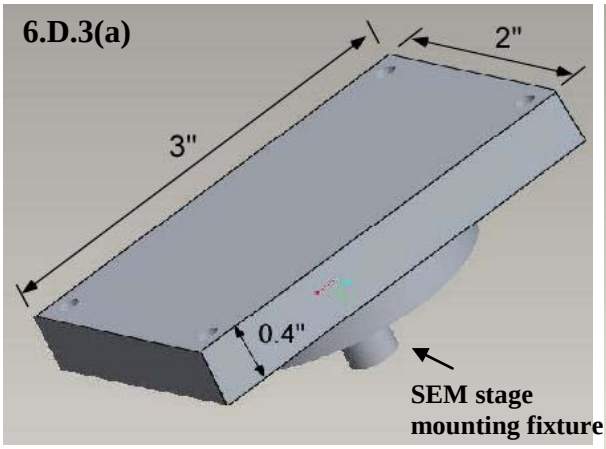

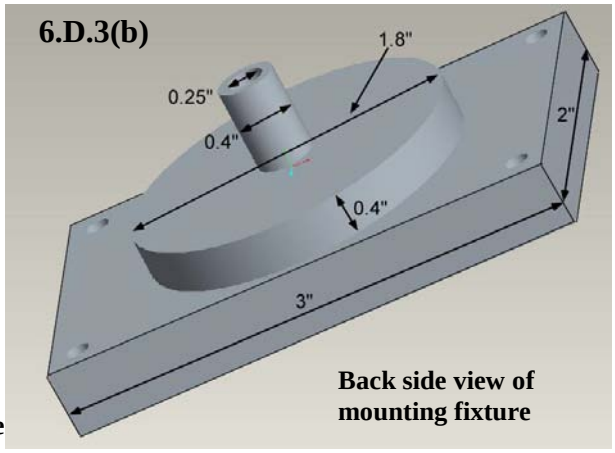

Combine the mounting fixture to the small sample test fixture as shown in Fig 6.D.4 (a) Front view and 6.D.4 (b) Back view.

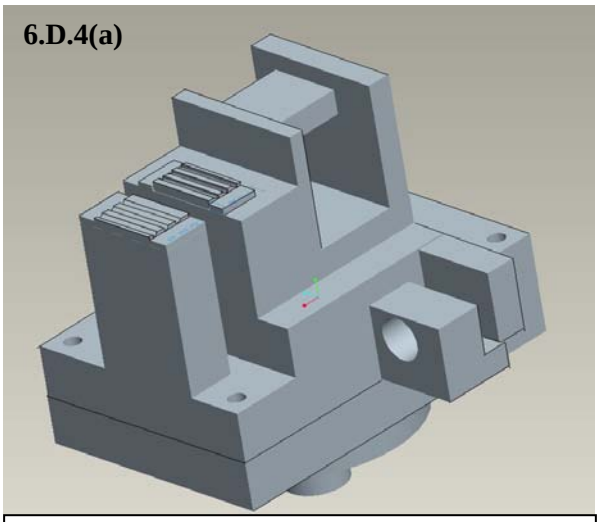

Small sample stage body with mounting fixture

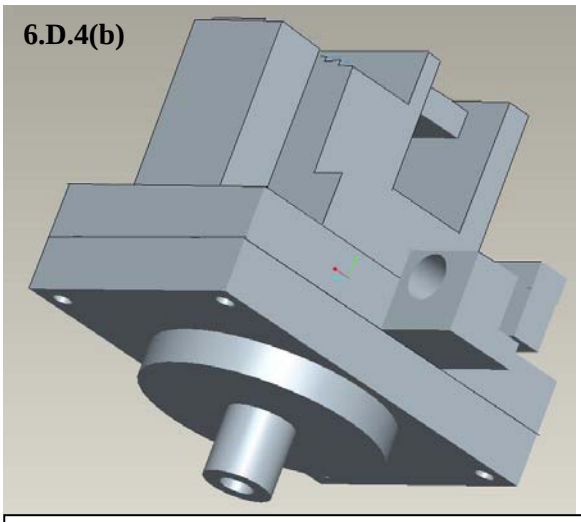

Backside view of small sample stage body with mounting fixture

Attach squiggle motor to the sliding member and the stage system is completed as shown in schematic in Fig 6.D.5 (a) and photo 6.D.5(b).

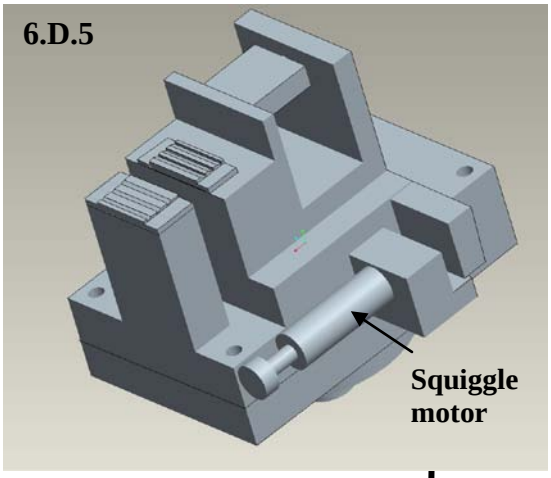

Part # 1 (schematic)

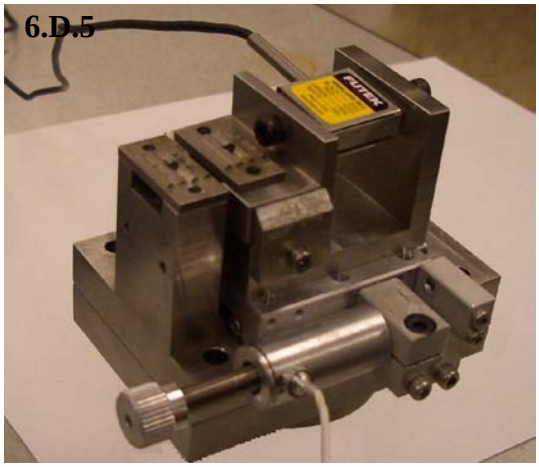

Part # 1 (photo)

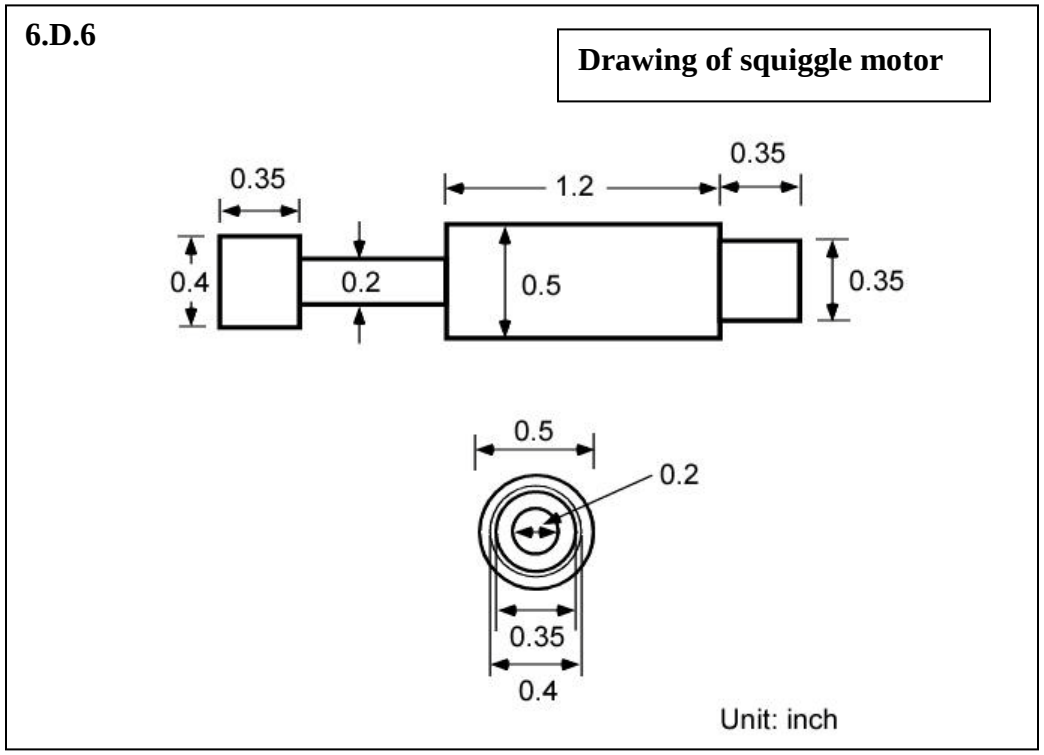

Feed through system

Fig 6.D.7 shows the schematic of the side plate of SEM chamber with two feed through installed. One feed through has two wires and another has eight wires attached to it.

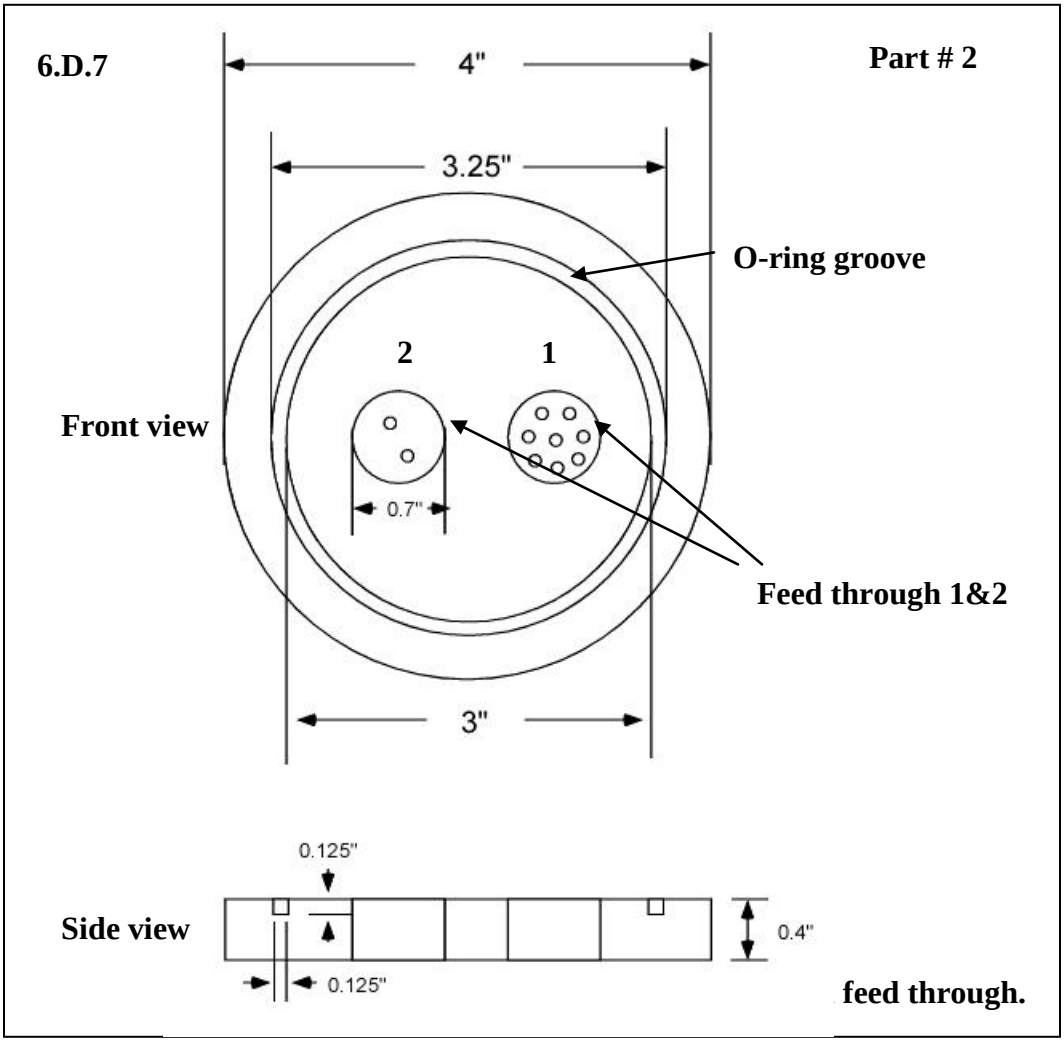

Four wires of feed through 1 are used for motor control and the other four wires of feed through 1 are used to collect signals from load cell. The connections between systems in and out of the feed through are illustrated in Fig 6.D.8. The stage system is connected to the feed through system and the motor control system (control box + motor control) is also connected to the feed through system. Data acquisition (DAQ) board connects to

four wires through feed through to the load cell and collects signals, which are stored in the computer.

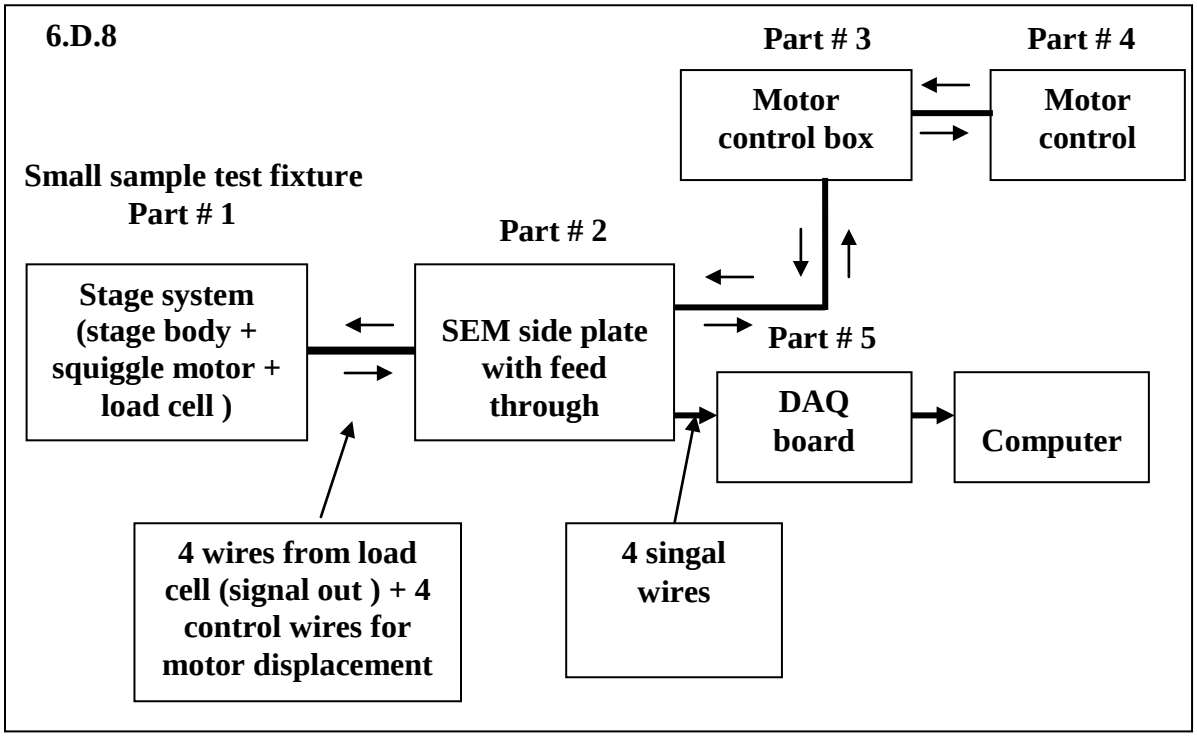

6.D.9

Control box part # 3

Motor control part # 4

DAQ board part # 5

Photos of control box (#3), motor control (#4) and DAQ board (#5).

Standard operation procedure (SOP) of small sample test apparatus.

1. Load cell and DAQ system.

The load cell should be connected to the amplifier and the amplifier is connected to one end of the feed through. The numbers on the cords of feed through correspond to different signals that load cell provides.

#5 positive excitation to the amplifier (12v~24V)

#6 negative excitation to the amplifier

#7 grounds

#8 positive voltage signals from the load cell

Connect # 5 and #6 to the power supply which gives constant voltage of 12~24V

Connect # 7 and # 8 to the ground and CH1IN port of the DAQ board

2. DAQ board and computer

Use USB cable to connect DAQ board to the laptop.

Install the tracer DAQ program from the “NEW SCALE TECHNOLOGY” blue cd (blue cd shown in figure 6.D.10).

Open the software and enable the selected board, then change vol to big20V

Start recording the voltage and change data point to 1000 or more

Save data after finish the test.

3. Extensometer and the stage assembly

Connect the extensometer of the Instron 5505 to the stage.

Measure the displacement based on 12.7mm gauge length.

The displacement measured from Instron machine needs to be converted by the following equation:

Displacement of the small sample (mm) = (((%strain/100)+1)12.7)-12.7

4. Voltage signal – load conversion

Each 1V change in signal corresponds to 0.5 lb change of load.

The base voltage DAQ board gives is 1.4 V, which decreases with increasing load.

To convert the voltage signal into load (N), follow the equation below.

Load (N) = ((volt signal)*(-1)+1.4)*0.5*0.454*9.8

5. Check all measurement equipments are calibrated and ready for recording.

Put small sample on the stage and secure with screws through pin holes

Increase the load by advancing the motor through the control knob of the motor system.

Continue increase the load till sample fails.

Save all the data collected and convert into stress-strain values.

References

[1] N.A. Fleck, G.M. Muller, M.F. Ashby, Hutchinson: *Acta Metallurgica et Materialia*, v 42, n 2, Feb, 1994, p 475-487

[2] D.M. Dimiduk, M.D. Uchic, T.A. Parthasarathy: *Acta Materialia*, v 53, n 15, September, 2005, p 4065-4077

[3] J.R. Greer, W.C. Oliver, W.D. Nix: *Acta Materialia*, v 53, n 6, April, 2005, p 1821-1830

[4] D. Kiener, C. Motz, T. Schoberl, M. Jenko and G. Dehm: *Advanced Engineering Materials*, v 8, n 11, November, 2006, p 1119-1125

[5] M.A. Haque and M.T.A Saif: *Experimental Mechanics*, v 42, n 1, March 2002, p 123-8

[6] J.A. Ruud, D. Josell and Spaepen: *Journal of Materials Research*, v 8, n 1, Jan. 1993, p 112-17.

[7] H. Huang and Spaepen: *Acta Materialia* v 48 3261-3269 (2000)

[8] B. Yuan, and Sharpe: *Experimental Techniques*, v 21, n 2, Mar-Apr, 1997, p 32-35

[5] M.A. Haque, and M.T.A. Saif: *Journal of Microelectromechanical Systems*, v 10, n 1, March 2001, p 146-52

[10] H.D. Espinosa, B.C. Porok, B. Peng: *Journal of the Mechanics and Physics of Solids*, v 52, n 3, March 2004, p 667-89

[11]H.D. Espinosa, S.Berbenni, M.Oanico, K.W. Schwarz: *Proceedings of the National Academy of Sciences of the United States of America*, v 102, n 47, 22 Nov. 2005, p 16933-8

[12]J. Michler, K. Wasmer, S. Meier, F. Ostlund: *Applied Physics Letters*, v 90, n 4, 22 Jan. 2007

[13]M.D. Uchic, D.M. Dimiduk, J.N. Florando, W.D. Nix: *Science*, v 305, n 5686, 13 Aug. 2004, p 986-9

[14] K. Lu, W.D. Wei, J.T. Wang: *Scripta Metallurgica et Materialia*, v 24, n 12, Dec, 1990, p 2319-2323

[15] S. Greek, F. Ericson, S. Johansson and J. A.Schweitz: *International Conference on Solid-State Sensors and Actuators, Proceedings*, v 2, 1995, p 56-59

[16] E. Arzt:*Acta Materialia*, v 46, n 16, 9 Oct. 1998, p 5611-26

[17] B.V. Blanckenhagen, P. Gumbsch and E. Arzt: *Philosophical Magazine Letters*, v 83, n 1, Jan. 2003, p 1-8

[18] S. Suresh, T.G. Nieh, B.W. Choi: *Scripta Materialia*, v 41, n 9, 8 Oct. 1999, p 951-7

[19] W.W. Gerberich, N.I. Tymiak, J.C. Grunlan: *Journal of Applied Mechanics, Transactions ASME*, v 69, n 4, July, 2002, p 433-442

[20] W.D. Nix, H.Gao: *Journal of the Mechanics and Physics of Solids*, v 46, n 3, March 1998, p 411-25

[21] R. Sedlacek: *Materials Science & Engineering A (Structural Materials: Properties, Microstructure and Processing)*, v 393, n 1-2, 25 Feb. 2005, p 387-95

[22] Y. S. Kang, P.S. Ho: *J, Electr. Mater*, Vol 26, no. 7, pp 805-813, 1997

[23] C.V. Thompson R. Carel: *Journal of the Mechanics and Physics of Solids*, v 44, n 5, May 1996, p 657-73

[24] A.K. Ghosh: *Acta Mater* (2008)

Chapter 7

Summary and recommendations for future work

The focus of this work is mostly on the thermo-mechanical processes of hard-to-deform metal alloys. The process techniques include ABRC, angle die extrusion followed by hot rolling and biaxial extrusion. Materials processed by these thermo-mechanical processes all showed great grain refinement with improved mechanical properties. ZK60 Mg alloy processed by ABRC 3 cycles (cumulative strain = 7.5) has final grain size of 6.39μm and yield strength of 274MPa and maximum elongation of 207%. ZK60 alloy processed by biaxial extrusion (cumulative strain = 7.92) has bimodal final grain size with large grain ~29μm and small grain ~1.57μm with higher yield strength 355 MPa and maximum elongation of 252%. Though the cumulative strain of ZK60 processed by ABRC (7.5) and biaxial extrusion (7.92) were similar, the resulting microstructures differ due to their different processing routes.In ABRC processed ZK60, no bimodal grain distribution was observed but bimodal grain distribution was shown in biaxial extruded ZK60. The uniform fine-grained microstructure of ABRC processed ZK60 is believed to be attributed to the repeated deformation induced recrystallizations at ambient temperature (most of the deformations were done above 250ºC). On the contrary, the biaxial extruded ZK60 at 150ºC lacks the driving force for recrystallization (low temperature) thus the big grains were not able to break down to smaller grains. However, low temperature deformation and unique extrusion route in biaxial extrusion helped further break down the small grains into near submicron size (1.57μm grain size with many ~500nm

segments) where warm deformed ABRC ZK60 has relatively larger final grain size (6.39 μm). The difference in developed grain structures also affected the mechanical behaviors. Higher yield strength was found in biaxial extruded ZK60 with smaller grain size (smaller grains in fine grained area compare to ABRC processed ZK60).

Two processing techniques were used to process Ti-6Al-4V alloy; angle die pressing followed by hot rolling and biaxial extrusion. In Ti-6Al-4V processed by angle die pressing and rolling, ultra-fine grain size of 0.31 μm was found with equiaxed microstructure. The biaxial extruded Ti-6Al-4V also has fine equiaxed grains with average grain size of 0.7μm. The microstructures of Ti-6Al-4V processed by these two techniques do not differ too much. However, the ductility of biaxial extruded Ti-6Al-4V (724%) is much higher than angle die processed Ti-6Al-4V (450%). This higher ductility in biaxial extruded Ti-6Al-4V is believed to be attributed to the higher β phase content (~ 25% compare to ~20% in angle die pressed Ti-6Al-4V) due to its one shot processing step.

From the experience learned from processing Ti-6Al-4V and several magnesium alloys in different thermo-mechanical routes, there are few recommendations for the future works

1. For magnesium alloys, precipitates play important roles in the mechanical properties as well as grain sizes. The stability of grain sizes under elevate temperature deformation is also of concern. So far, the optimal processing route that gives highest strength and good ductility of ZK60 is via biaxial extrusion

with processing temperature set at 150ºC. It is of interest to discover the effect of biaxial extrusions on other magnesium alloys (AZ series and AM series as well as rare earth containing Mg alloys).

2. For Ti-6Al-4V alloy, the mechanical properties are deeply affected by the volume percent of α-β content and grain size. It is believed with higher β phase present, higher ductility could be achieved. Various processing route should be tested to adjust the α-β content of the processed work piece.
3. For small sample tests, TEM works should be done on the tested samples to examine the microstructure of mantle area and bulk area to verify the dislocation pile-up theory that causes the increase in strength of small samples.